AD-A143 594

NAVAL POSTGRADUATE SCHOOL
Monterey, California

DTIC
S **ELECTE** **D**
JUL 27 1984
D

THESIS

MEASUREMENT OF RANGE-RESOLVED WATER VAPOR
CONCENTRATION BY COHERENT CO_2 DIFFERENTIAL
ABSORPTION LIDAR

by

Robert Michael Hardesty

March, 1984

Dissertation Supervisor: John P. Powers

84 07 27 026

REPORT DOCUMENTATION PAGE		READ INSTRUCTIONS BEFORE COMPLETING FORM
1. REPORT NUMBER	2. GOVT ACCESSION NO. AD-A143 594	3. RECIPIENT'S CATALOG NUMBER
4. TITLE (and Subtitle) Measurement of Range-Resolved Water Vapor Concentration by Coherent CO_2 Differential Absorption Lidar		5. TYPE OF REPORT & PERIOD COVERED Ph.D. Dissertation March 1984
		6. PERFORMING ORG. REPORT NUMBER
7. AUTHOR(s) Robert Michael Hardesty		8. CONTRACT OR GRANT NUMBER(s)
9. PERFORMING ORGANIZATION NAME AND ADDRESS Naval Postgraduate School Monterey, California 93940		10. PROGRAM ELEMENT, PROJECT, TASK AREA & WORK UNIT NUMBERS
11. CONTROLLING OFFICE NAME AND ADDRESS Naval Postgraduate School Monterey, California 93940		12. REPORT DATE March 1984
		13. NUMBER OF PAGES 311
14. MONITORING AGENCY NAME & ADDRESS(if different from Controlling Office)		15. SECURITY CLASS. (of this report) Unclassified
		15a. DECLASSIFICATION/DOWNGRADING SCHEDULE

16. DISTRIBUTION STATEMENT (of this Report)

Approved for public release, distribution unlimited.

17. DISTRIBUTION STATEMENT (of the abstract entered in Block 20, if different from Report)

18. SUPPLEMENTARY NOTES

19. KEY WORDS (Continue on reverse side if necessary and identify by block number)
differential absorption
laser radar
species concentration measurement
remote sensing

20. ABSTRACT (Continue on reverse side if necessary and identify by block number)

The feasibility of DIAL species concentration measurements using a coherent CO_2 lidar was examined. A computer simulation estimated errors in coherent and incoherent CO_2 DIAL measurements due to speckle, noise, turbulence, and atmospheric inhomogeneities. Results indicated that direct-detection is the preferable mode at shorter ranges while heterodyne detection provides better sensitivity behond a few km. The NOAA pulsed lidar was used to investigate statistical properties of the aerosol backscattered returns which are

Block No. 20 (continued)

processed to obtain DIAL measurements. Fluctuations due to speckle and noise necessitate averaging of returns from multiple pulses for accurate concentration estimates. Other atmospheric effects can be minimized by judicious signal processing. The first reported range-resolved coherent DIAL water vapor measurements were made with the lidar to ranges beyond 10 km. Estimates compared reasonably with those from rawinsondes, although some tendency to overestimate relative to the sondes was observed. Wind velocity profiles were also obtained, demonstrating the feasibility of simultaneous concentration and wind velocity measurements.

```
Accession For

NTIS   GRA&I        X
DTIC TAB            ☐
Unannounced         ☐
Justification

By
Distribution/

  Availability Codes

        Avail and/or
Dist      Special

A
```

Measurement of Range-Resolved Water Vapor Concentration
by Coherent CO_2 Differential Absorption Lidar

by

Robert M. Hardesty
NOAA/ERL Wave Propagation Laboratory
B.S., Virginia Polytechnic Institute and
State University, 1971

M.S., University of Colorado, 1972

Submitted in partial fulfillment of the
requirement for the degree of

DOCTOR OF PHILOSOPHY

from the

NAVAL POSTGRADUATE SCHOOL
March 1984

Author: _Robert M. Hardesty_

Approved by:

D. E. Kirk
D. E. Kirk
Professor of Electrical Engineering

K. L. Davidson
K. L. Davidson
Professor of Meteorology

J. B. Knorr
J. B. Knorr
Professor of Electrical Engineering

P. Wang
Professor of Mathematics

J. P. Powers
J. P. Powers
Professor of Electrical Engineering
Dissertation Supervisor

Approved by _____
Acting Chairman, Department of Electrical and Computer
Engineering

Approved by _____
Academic Dean

2

ABSTRACT (differential absorption lidar)

The feasibility of DIAL species concentration measurements using a coherent CO_2 lidar was examined. A computer simulation estimated errors in coherent and incoherent CO_2 DIAL measurements due to speckle, noise, turbulence, and atmospheric inhomogeneities. Results indicated that direct-detection is the preferable mode at shorter ranges while heterodyne detection provides better sensitivity beyond a few km. The NOAA pulsed lidar was used to investigate statistical properties of the aerosol backscattered returns which are processed to obtain DIAL measurements. Fluctuations due to speckle and noise necessitate averaging of returns from multiple pulses for accurate concentration estimates. Other atmospheric effects can be minimized by judicious signal processing. The first reported range-resolved coherent DIAL water vapor measurements were made with the lidar to ranges beyond 10 km. Estimates compared reasonably with those from rawinsondes, although some tendency to overestimate relative to the sondes was observed. Wind velocity profiles were also obtained, demonstrating the feasibility of simultaneous concentration and wind velocity measurements.

3

TABLE OF CONTENTS

ACKNOWLEDGEMENTS

I. INTRODUCTION

The measurement of atmospheric gas species concentrations by differential absorption lidar (DIAL) has been widely demonstrated since the technique was first suggested in the middle 1960's. Over the past decade concentration measurements made using DIAL systems operating in the ultraviolet, visible and infrared regions of the electromagnetic spectrum have been reported. In some cases, DIAL technology has been advanced to the point where mobile systems installed in both vans and aircraft are routinely used for pollution monitoring. At present however, DIAL systems have not been demonstrated which can produce concentration profiles from ranges beyond a few km in the middle infrared spectral region. This dissertation describes an effort to determine the feasibility of measuring species concentrations at longer ranges by employing a pulsed coherent CO_2 laser transmitter and heterodyne detection of the backscattered radiation.

In order to measure gas concentration by the DIAL technique, the lidar ust be operated at a frequency which coincides with a discrete spectral absorption line of the gas. The infrared region of the spectrum, especially the region with wavelengths ranging between 2.5 and 25 μm, is rich in species absorption lines. Unfortunately, the sensitivity of conventional lidar systems, which employ direct detection of backscattered or reflected radiation, is less at infrared wavelengths than in the visible or ultraviolet spectral regions. This

6

degradation at longer wavelengths is a result of the limitations imposed by current detector technology, as well as the increased level of optical background which exists in the middle infrared.

Reduced detection sensitivity of lidar systems in the infrared is especially significant because atmospheric backscatter coefficients in that region are substantially lower than at visible or ultraviolet wavelengths. As a result of this combination of detrimental effects, lidar systems operating at wavelengths in the region around $\lambda = 10$ μm require many orders-of-magnitude more transmit power to obtain aerosol backscattered signals comparable to those obtained with from more modest systems at shorter wavelengths. To date, reported DIAL concentration measurements estimated from aerosol-backscattered returns have employed pulsed CO_2 lasers and direct detection to probe the 9-11. μm spectral region. Maximum ranges obtained for these measurements have been on the order of 2-3 km despite transmit pulse energies of 2 J or more. In order to extend the range capabilities of these incoherent DIAL systems beyond 10 km, as much as 10 J of pulse energy would be required.

An alternate technique to improve DIAL measurement sensitivity in the CO_2 region without constructing larger lasers is to use optical heterodyne detection on the backscatter radiation. In principle, a heterodyne (also known as coherent) CO_2 DIAL system provides as much as a 30 dB increase in sensitivity over a direct detection system because the detector can be operated in a quantum-noise limited mode. The

notion of employing heterodyne detection to increase infrared DIAL sensitivity was first suggested in the mid 1970's. Since then, a number of analytical studies have been performed which examined the performance capabilities of coherent DIAL systems. To date however, actual coherent DIAL measurements are limited to continuous-wave (CW) or low-energy pulsed applications using solid targets. The absence of results describing coherent detection of aerosol returns is due primarily to the relative difficulty and complexity involved in constructing a pulsed coherent system. Because the state-of-the-art technology required to make such a system perform adequately entails high costs, research on coherent IR systems has advanced slowly in the absence of a well-defined benefit or application.

Recently coherent lidar technology has moved ahead to the point where pulsed systems exist or are under development at a number of locations. The primary impetus for this proliferation is the potential application of coherent CO_2 systems to measure atmospheric winds from ground-based or space-based platforms. Results of pulsed coherent system measurement programs have demonstrated wind-velocity and back-scatter coefficient measurement capabilities to beyond 15 km, despite pulse energies on the order of 10 mJ (less than 1/10 the energies of pulsed CO_2 systems used in incoherent DIAL measurements). Although much data have been gathered regarding Doppler applications, no measurements have yet been taken which examine the capabilities of these new pulsed coherent systems for DIAL measurements. The potential benefits of coherent CO_2 DIAL are substantial: long range (tens of

kilometers) sensitivity in the 9-11 μm spectral region obtainable with nominal pulse energies; and a capability to simultaneously measure radial velocity as well as gas concentration. Measuring both radial velocity and concentration simultaneously offers the possibility of measuring species fluxes over a specific measurement area. This capability could be useful in applications such as identification and tracking of poisonous gases, research involving moisture entrainment into convective storms, or pollution monitoring.

The primary contribution in this dissertation is the first range-resolved DIAL measurement of an atmospheric species using a pulsed coherent lidar. The measurements were one segment of a comprehensive study of coherent DIAL, which included analysis and formulation of primary sources of error in DIAL measurements, simulation of ground-based system capabilities, and statistical characterization of pulsed lidar returns backscattered from atmospheric aerosols. The overall objective of the research was to evaluate coherent DIAL both analytically and experimentally. To reach this goal, the following secondary objectives were established:

1. Analyze in detail potential error sources in ground-based DIAL measurements. Develop quantitative expressions for the errors in order to determine which parameters are the most critical and which can be neglected.

2. Model ground-based lidar measurements of a particular species as a function of lidar system parameters and atmospheric conditions.

9

3. Measure statistical properties of aerosol-backscattered lidar returns, and compute effects of the observed signal fluctuation characteristics on DIAL measurement technique and accuracy.

4. Demonstrate coherent range-resolved DIAL measurements of atmospheric water vapor.

5. Examine feasibility of combined species and wind velocity measurements.

The dissertation is organized roughly along the lines of the objectives listed above. Chapter II contains background information describing lidar remote sensing, direct versus heterodyne detection, the DIAL technique, and previous DIAL research. In Chapter III a detailed discussion of error sources for measurements using CO_2 lasers in both coherent and incoherent DIAL systems is presented. Uncertainties due to the primary error sources are quantified and used in a simulation to estimate ground-based DIAL capability for range-resolved water vapor measurement. Chapter IV describes measurements of the statistical characteristics of coherent lidar returns. Following a description of the NOAA pulsed lidar, the ensemble and temporal properties of backscattered signals are presented and related to DIAL measurement capabilities and selection of processing techniques.

In Chapter V the actual DIAL measurements are described. Range-resolved estimates of water vapor concentration along both horizontal and elevated atmospheric paths are presented and compared with values

10

measured by comparison sensors. The errors and analomies which appear in the results are discussed with regard to uncertainties predicted by theory. Also included in Chapter V are measurements ot radial wind velocities estimated simultaneously with the concentration estimates, followed by a discussion of optimal design criteria for combined DIAL/Doppler systems. The entire dissertation is summarized in Chapter VI. The capabilities of coherent DIAL as shown in the experimental measurements are.compared with those predicted by the simulation described in Chapter III, and an overall evaluation of the coherent DIAL technique is presented. Finally, a recommendation for future research on the topic is offered.

II. DIAL BACKGROUND INFORMATION

This chapter presents background material describing lidar remote
sensing, heterodyne detection of optical radiation, and differential
absorption lidar (DIAL) species concentration measurement. It is
intended to provide a brief overview of the current state of DIAL-
related technology and capabilities, to acquaint the reader with the
important characteristics associated with heterodyne detection, and to
show under which conditions the use of coherent DIAL can potentially
improve measurement capabilities beyond those which currently exist.
The first section contains a very fundamental discussion on use of
lidars for remote sensing of atmospheric parameters, including a brief
description of typical transmitter and receiver characteristics. In
Section B the lidar equation for return signal strength is presented
and explained. Also included in Section B are equations for direct and
heterodyne detection signal-to-noise ratio (SNR) which illustrate the
sensitivity advantages of heterodyne detection at long wavelengths.
Section C shows the mathematical basis for the DIAL method, then pre-
sents a brief history of DIAL measurements from 1964, when the tech-
nique was first suggested, up to the present. The potential benefits
to be gained through application of coherent CO_2 DIAL, i.e., improved
sensitivity and wind measuring capability, are discussed in Section D.
Section E provides a brief chapter summary.

12

A. LIDAR FUNDAMENTALS AND EXAMPLES

The term lidar, for LIght Detection And Ranging, was first applied to pulsed light techniques by Middleton and Spillhaus [1]. Except for the frequency of the transmitted radiation, lidar as used in remote sensing applications is conceptually identical to standard electromagnetic radar. In its basic form a lidar transmitter produces a pulse of optical radiation, which is directed into the medium of interest by the system optics. Although lidar techniques can be applied in the vacuum of space as well as in water, most lidar work employs the terrestial atmosphere as the propagation and scattering medium. In the remaining discussion in this chapter, the assumption will be made that the lidar measurements are performed in the Earth's atmosphere.

As the transmitted optical energy propagates, it is affected by the characteristics of the region of atmosphere through which it passes. Gas molecules and particles or droplets cause some of the energy to be scattered. A small fraction of this scattered energy is backscattered, i.e., directed back toward the lidar system. This energy can be detected at the lidar receiver. Since energy which is not directed back along the path of propagation is lost, scattering also produces attenuation in the optical field. Additional attenuation occurs from absorption by the gases and particles which occur along the path.

In general the atmosphere is a spatially and temporally random medium with respect to its scattering and absorptive properties. Although it can be characterized in a statistical sense, its exact

13

characteristics during the instant in which it interacts with the optical energy are not precisely known. This random characterization also applies to refractive index. Inhomogenieties in refractive index perturb the phase of a propagating wave, producing bending, decoherence and scintillations in the wave intensity. A more detailed discussion of refractive index turbulence as it effects CO_2 lidar systems is included in Chapter III.

In lidar applications, the signal of interest is usually the energy backscattered by the atoms and particles within some segment of the propagation medium. In some cases, when the atmospherically backscattered signal is too weak to be detected, the energy reflected from a solid target at one extreme of the propagation medium is used. The returned energy is collected by the receiver optics and directed onto a photodetector, which produces an electrical signal proportional to the intensity of the optical radiation incident at the detector. In a pulsed lidar, the time elapsed between the transmit pulse and the return signal is proportional to the range from which the return originates.

Since lidar system performance characteristics are affected by particular properties of the propagation medium and target, analysis of the received signal yields information on these properties. The magnitude of the signal from a given range is a function of the backscatter characteristic at that range as well as the attenuative properties of the intervening medium. In order to estimate one parameter, e.g.,

backscatter, information on the other parameters (propagation-path characteristics) must be known or estimated. For the most part, both backscatter and transmission properties are a strong function of operating wavelength.

Absorption of energy increases sharply when the operational wavelength coincides with a resonance absorption line of an atmospheric gas. Backscatter and turbulence effects also vary with wavelength; at shorter wavelengths molecular scattering and turbulence effects are both enhanced. By appropriately selecting the operating wavelength one can often deliberately emphasize the effects of one parameter relative to another in order to perform a particular function.

Although the term "lidar" originally applied to any system which employed an optical source, almost all present-day systems use a laser as the system transmitter. The monochromatic radiation produced by laser transmitters enables the operating wavelength to be exactly specified, and provides transmit beams which remain collimated over long distances. In remote sensing applications the minimal dispersion of the beam permits measurements to be made at low elevation angles where typical radar systems would be hampered by ground clutter effects [2,3].

Lidar systems for remote sensing have been demonstrated at a number of wavelengths ranging from the ultraviolet through the infrared. To obtain energy in the UV region, radiation from a Nd:YAG laser is frequently employed to pump a dye laser, the output of which is frequency

15

doubled in a crystal to produce the desired wavelength [4-9]. The Nd:YAG laser can also be tripled to yield radiation at $\lambda = 355$ nm [9]. Since dye laser systems used in the UV spectral region are hampered by low efficiency and limited pulse energy, much work has been done in recent years to develop rare-gas halide excimer lasers for remote sensing applications [10, 11]. Use of pulsed XeCl excimer lasers for ozone monitoring has been reported [12].

Dye lasers are also commonly employed as sources for remote sensing in the visible. As in the case when UV radiation is generated, most systems are pumped by a flashlamp [13,14] or a doubled Nd:YAG laser [7,8,15]. Dye systems pumped by nitrogen lasers [13] and excimer lasers [16] have also been reported. For high power applications using dye lasers Nd:YAG and excimer lasers are typically the excitation sources of choice because of the high conversion efficiency (as high as 40% [11]) which can be achieved. This increased efficiency over flashlamp pumping comes about primarily because the output radiation is spectrally narrow with low divergence. Ruby ($\lambda = 694.3$ nm) and argon ($\lambda = 514.5$ nm) lasers have also been used as sources in visible atmospheric gaseous species measurements [16,17]. These transmitters provide high pulse energies, but have limited tunability relative to dye lasers. Tuning is obtained in ruby lasers by thermal pressure or interferometric techniques. Recently, an argon laser operating on multiple lines was reported in an atmospheric gas monitoring application [17]. The multi-line output provided simultaneous radiation at two desired wavelengths.

In the IR region of the spectrum the most commonly used sources for remote sensing are Nd:YAG and CO_2 lasers. Carbon dioxide lasers offer relatively high efficiency, and can be operated in either a continuous wave (CW) or pulsed mode. For pulsed operation, a TEA (transverse-excited-atmospheric) laser is often employed. Such lasers can provide many Joules of energy per pulse. Recently much effort has been applied to development of high pressure CO_2 lasers. High pressure lasers potentially offer tunability across the entire 9-11 μm CO_2 spectral region through pressure broadening of the discrete CO_2 gain lines. This capability is especially desirable in atmospheric spectroscopy, since absorption lines of many interacting gases are contained within the 9-11 μm gain. By doubling the CO_2 radiation frequency with a non-linear crystal, gases with absorbing lines near $\lambda = 5$ μm can be examined [18].

The other commonly-used IR lidar transmitter, Nd:YAG, can also be operated in either a CW or pulsed mode to obtain radiation at $\lambda = 1.06$ μm. Although there is not an abundance of absorption lines in the immediate spectral region, Nd:YAG lasers are frequently used to measure aerosol densities [19] or to observe smoke plumes [20]. By using a Nd:YAG laser to pump an optical parametric oscillator (OPO) source, tunability over the 1.4 − 4 μm spectral region can be obtained [21]. This region offers good potential to measure water vapor concentrations at $\lambda = 1.9$ μm.

By injection locking or hybrid (combined CW and pulsed) techniques, CO_2 lasers can be made to produce ultra-high purity pulses with from

17

100 mJ to as much as 2 J of energy. These lasers are used in systems which employ optical heterodyne detection. The sensitivity advantages and wind-measuring capability of the heterodyne detection technique are outlined in the next section; this dissertation is primarily concerned with the application of heterodyne detection in range-resolved species concentration measurement. Although the majority of demonstrated heterodyne lidar systems have employed CO_2 laser transmitters, recent work has suggested that sufficient frequency stability for heterodyne measurement of Doppler shifts can be obtained using a Nd:YAG laser [22]. Heterodyne detection at $\lambda = 1.06$ μm offers the potential for wind velocity measurements with improved backscatter and better spatial resolution than at CO_2 wavelengths.

Another source of optical radiation in the infrared for remote sensing applications is the tunable diode laser. Because of the low power output of these devices, their use is generally restricted to applications as local oscillators in heterodyne systems in situations where a double-ended path or retroreflector can be employed. One example of a diode laser application is the measurement of average humidity using derivative spectroscopy as reported by Taylor [23]. In this experiment a retroreflector was used to reflect the low signal energy back to the receiver.

A potentially promising new source of optical radiation for remote sensing is a tunable laser made from transition-metal-doped crystals. Although still in a research stage these devices are continuously

18

tunable and can be Q-switched to generate high-peak-power output. An example of such a device is the Co:MgF$_2$ laser [24], which is tunable across the 1.6 to 2.3 μm region. This spectral region contains strong absorption bands due to H_2O and CO_2.

The discussion to this point has centered primarily on laser transmitters, since these are the principal elements which distinguish one lidar system from another. However, other characteristics, such as optical configuration and receiver type, also differ among lidar systems. Most single-ended lidars operate in either a monostatic or bistatic configuration. In a monostatic system the transmitted and backscattered signals follow a common optical path, hence alignment is simplified. However, in the case where the transmitter and receiver also share the same optics, some kind of transmit/receive switch is usually necessary to prevent saturation or damage to the signal detector from leakage of the transmit energy back along the receiver path. This problem can be reduced by the use of a 2-mirror coaxial system, such as the one employed in the University of Hull coherent lidar system [25]. Mounting the transmit mirror coaxially in the middle of the receiver provides isolation as well as monostatic operation, although alignment difficulties are increased. Isolation is also improved for single transmit/receive mirror monostatic systems when the telescope employs an off-axis configuration, such that no transmit energy reflects back into the detector from the system primary mirror. Bistatic configurations alleviate isolation problems at a cost of increased alignment difficulty.

In the receiver, the choice of a system detector and electronic bandwidth is a strong function of both the transmitter characteristics and the system performance requirements. Photomultiplier tubes provide high sensitivity from the ultraviolet region of the spectrum through the visible to the near infrared. If applications necessitate operation at longer wavelengths in the infrared, photoconductive and photovoltaic semiconductors are employed. Materials from which these detectors are fabricated include silicon, germanium, InSb, PbSnTe, PbSnSe, InAsSb and HgCdTe. In general HgCdTe has become the preferred material because detector response can be peaked at any wavelengath from 0.9 μm to 40 μm by using the appropriate alloy of HgTe and CdTe. Because photons at longer wavelengths possess less energy, detectors in the IR portion of the spectrum must be cooled to reduce the effect of thermal excitation. Since this property is often a disadvantage in certain applications, room temperature detectors have been developed. Their performance is at least 10 dB poorer than appropriately cooled detectors [26].

A key element in a lidar receiver, especially at longer wavelengths, is the detection mode; i.e., direct detection or heterodyne detection. These two detection configurations are characterized in the following section, which examines some of the fundamental expressions describing lidar system operation.

B. BASIC LIDAR THEORY

Many aspects of lidar operation are included in the lidar equation [27] for signal power backscattered by single particles:

$$P_r(R) = P_t(\frac{c\tau}{2}) \ \beta(R)A_r R^{-2} \ \exp[-2 \int_0^R \alpha(r)dR] \qquad (2.1)$$

where $P_r(R)$ is the instantaneous received power at time $(\tau-t_o)$ P_t is the transmitted power at time t_o, c is the velocity of light, τ is the pulse duration, $\beta(R)$ is the volume backscattering coefficient of the atmosphere, R is range, A_r is the effective receiver area and α is the volume extinction coefficient of the atmosphere. Equation 2.1 assumes that a rectangular pulse was transmitted, and that effects such as turbulence do not affect the intensity of the signal.

The volume backscatter coefficient β in Eq. (2.1) is defined as the fractional amount of energy scattered per unit solid angle in the backward direction per unit atmospheric length. A point often overlooked when applying Eq. (2.1) is that the value of β is usually specified as a mean value. In reality the instantaneous energy fraction varies considerably over time and space due to coherent fading (speckle). This phenomena, which is discussed in detail in Chapter III, comes about because the intensities of the signals backscattered from the individual particles within the scattering volume do not add instantaneously to produce a resultant intensity. In actuality the fields are superposed in a vector addition; hence as the relative phases of the individual signals vary the signal alternately fades and surges. As a

21

result, the instantaneous β as calculated from the fractional energy measured at a point is in essence a random variable. By recognizing β as such and taking expected values, misinterpretaions of Eq. (2.1) resulting from a failure to include potential signal fluctuations can be reduced. Note that Eq. (2.1) also neglects turbulence, which can produce additional random scintillations in signal intensity.

In a lidar system the optical power collected by the receiver aperture is directed back to the system detector. Detection of the radiation can at that point be either incoherent (direct detection) or coherent (heterodyne detection). In either case, the signal-to-noise ratio (SNR) following detection is given by

$$SNR = \frac{F_s P_r}{NEP} \tag{2.2}$$

where F_s is a system dependent constant which takes into account losses between the receiver aperture and the detector, η is the detector quantum efficiency and NEP is the noise equivalent power of the detector. In the following paragraphs SNR expressions for both coherent and incoherent detection are discussed. A more detailed look at noise-equivalent-power for lidar measurements in the 10.6 μm spectral region is contained in Chapter III.

1. Direct Detection

For the most part, optical detectors used in remote sensing applications are characterized by the property that the electric signal out of the detector is proportional to the rate at which charge carriers are

22

excited by the optical field. Given an optical field $\vec{E(t)}$, where $\vec{E(t)}$ is represented in phasor form, the transition rate of current-carrying electrons is proportional to the intensity of the field, i.e.,

$$W \propto \vec{E(t)} \; \vec{E^{\star}(t)} \;.\tag{2.3}$$

When direct detection of lidar radiation is employed, the incident field on the detector is simply the backscattered optical energy. The output detector current is proportional to the power in the backscattered signal, i.e.,

$$i_d(t) \propto P(t)$$

where $P(t)$ is the incident optical power.

SNR of the detector output current differs as a function of type of detector employed. Photomultipliers are the most widely used detectors in the visible and ultraviolet spectral regions. For a photomultiplier used in a direct detection mode, the SNR (assuming a constant signal) is

$$SNR = \frac{2(P_r e\eta/h\nu)^2 G^2 \; F_s}{2G^2 e i_d \Delta\nu + \dfrac{2G^2 e^2 \eta}{h\nu} \Delta\nu F(P_r + P_B) + 4k_B T_e \Delta\nu/R_L}\tag{2.4}$$

where P_r is optical power, from Eq. (2.1)

P_B is optical background power

e is electron charge

η is quantum efficiency

23

$h\nu$ is photon energy

G is total current multiplication between anode and cathode

F_s is one way system optics loss

i_d is dark current

$\Delta\nu$ is receiver bandwidth

k_B is Boltzmann's constant

T_e is receiver equivalent temperature

R_L is load resistance.

The signal-to-noise ratio in Eq. (2.4) is computed from the average detector current as the mean signal power divided by the mean noise power, and assumes no fluctuation in signal intensity. Since detector current is proportional to optical signal intensity, the power in the detector current is actually proportional to the square of the optical power. Because of this, the voltage SNR, equal to the square root of the SNR in Eq. (2.4), is frequently used.

The numerator in Eq. (2.4) comes from the mean signal power at the detector, while the various denominator terms are the result of different noise sources. The leftmost denominator term comes from dark current, the middle term is quantum noise due to optical signal and background, and the righthand term includes the effects of Johnson noise. Usually the dark noise is the dominant noise source for direct detection using photomultipliers. By working with a small photocathode, the dark current can usually be made small enough that the detector noise is of no consequence, so that the detector operates in a quantum noise limited mode.

In the infrared spectral region, lidar system detectors are usually either of the photovoltaic or photoconductive type. When connected to a bias voltage, photoconductive detectors respond to optical intensity by lowering the resistance across a semiconductor crystal, so that by monitoring the detector current the optical signal is extracted. In a direct detection mode the photoconductor SNR is

$$SNR = \frac{2\left(\frac{e\eta\tau_o F_s P_r}{h\nu\tau_d}\right)^2}{\frac{4e^2\eta F(\tau_o/\tau_d)^2(P_r+P_B)\Delta\nu}{h\nu} + 2ei_d\Delta\nu + 4k_B T_e\Delta\nu/R_L} \tag{2.5}$$

where τ_o is the average carrier lifetime, τ_d is the drift time across the photoconductor crystal and other terms are as described previously. The denominator in Eq. (2.5) contains noise terms from dark current and Johnson noise identical to those in the photomultiplier SNR expression; the leftmost denominator term is due to generation/recombination noise. In most applications employing direct detection, the noise in Eq. (2.5) is dominated by the Johnson or background noise terms.

Photodiodes are the most commonly used IR detector in lidar systems. When a photon is absorbed by a photodiode, it generates a charge carrier which contributes to the signal current as it traverses the p-n junction. The noise mechanisms for a photodiode are similar to those in a photoconductor, except that the individual carriers do not recombine within the crystal. The SNR for a photodiode operated in the direct detector mode is

25

$$SNR = \frac{2(P_r e\eta F_s/h\nu)^2}{(3e^2(P_d + P_B)F\eta\Delta\nu/h\nu) + 2ei_d\Delta\nu + 4k_B T_e\Delta\nu/R_L} \qquad (2.6)$$

where all terms have been described previously. As in the photoconductor case the dominant noise sources are typically thermal and background shot noise. Because signal energy is higher than in the photovoltaic case, the relative NEP due to Johnson noise is lower. A typical value of direct detection NEP for photodiodes is 2×10^{-11} w at $\lambda = 10.6$ μm, assuming a receiver bandwidth of 10 MHz [26].

Examining the SNR expressions for each of the three detectors discussed above, substitution of representative values shows that quantum or shot-noise limited operation is difficult to obtain in the middle infrared using direct detection. Even the use of cooled amplifiers does not generally reduce the thermal noise to a point where it can be neglected. To obtain shot-noise limited operation it is necessary to employ heterodyne detection. This important mode of detection is discussed in the following paragraphs.

2. Heterodyne Detection

The fundamental optical arrangement for heterodyne detection is shown in Fig. 2-1. The radiation from the local oscillator laser and the backscattered signal radiation impinge normally on the photodetector, such that the total electric field is given by

$$E_t = E_s \cos \omega_s t + E_L \cos \omega_L t \qquad (2.7)$$

where E_s and E_L are the amplitudes of the signal and local oscillator fields (assumed constant for this discussion), and ω_s and ω_L are the
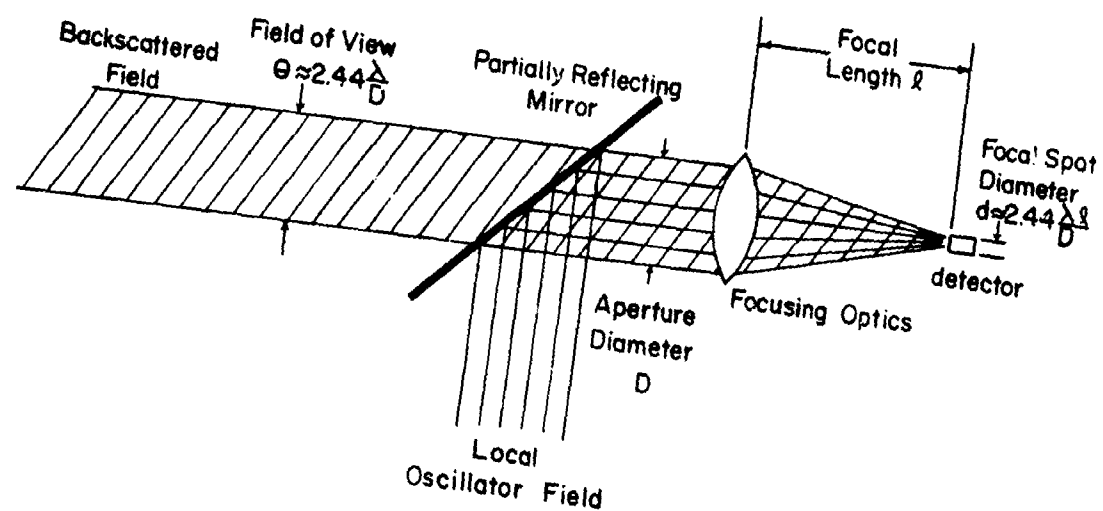
26

Fig. 2-1 - Optical heterodyne receiver.

27

field frequencies. The detector response is proportional to the intensity of the radiation in the total electric field

$$i(t) \propto E_t^2 = E_s^2 \cos^2 \omega_s t + E_L^2 \cos^2 \omega_L t$$

$$+ E_s E_L \cos(\omega_s - \omega_L)t + E_s E_L \cos(\omega_s + \omega_L)t . \qquad (2.8)$$

Since the detector cannot follow the instantaneous intensity at infrared frequencies, it responds to the average values of the first, second and fourth terms in Eq. (2.8). Assuming however, that the detector has sufficient bandwidth to respond to the $(\omega_s - \omega_L)$ difference frequency, Eq. (2.8) becomes

$$i(t) \propto \frac{E_s^2}{2} + \frac{E_L^2}{2} + E_s E_L \cos(\omega_s - \omega_L)t \qquad (2.9)$$

By filtering the detector current about a bandwidth centered on the difference, or intermediate frequency (IF), the DC terms are eliminated. Inserting the quantity $e\eta/h\nu$ as a proportionality term, we get

$$i_s(t) = \frac{E_s E_L \ e\eta}{h\nu} \cos(\omega_s - \omega_L)t . \qquad (2.10)$$

The sensitivity advantage gained when heterodyne detection is employed becomes apparent when the quantum noise term in the SNR expressions is examined. For a photomultiplier or photodiode. The quantum noise power, $i_N^2(t)$, is given by

$$\overline{i_N^2} = \frac{e^2 \overline{E_t^2} \eta \Delta \nu}{2h\nu} \qquad (2.11)$$

where E_t^2 is the mean intensity of the optical field in Eq. (2.7). By making $E_L \gg E_s$, the first, third and fourth terms become negligible in Eq. (2.8) relative to the second term so that

$$\overline{i_N^2} = \frac{e^2 E_L^2 \eta \Delta \nu}{2h\nu} . \qquad (2.12)$$

It is obvious in Eq. (2.12) that the noise power due to quantum noise can be adjusted by varying the local oscillator (LO) intensity. Note from Eq. (2.10) that signal power $i_s^2(t)$ is also proportional to E_L^2. Thus, by increasing E_L to a point where the shot noise term is much larger than other noise sources, such as Johnson or dark current noise, the detector can be operated in a shot-noise limited mode. The only limitation on this procedure is the observation that E_L cannot be increased indefinitely in an attempt to make the shot-noise dominate the other sources, since eventually the detector saturates. Practically, attainment of full shot noise limited operation through heterodyning was demonstrated in the visible and infrared portions of the spectrum as early as the 1960's [28].

When shot noise is the dominant term, the signal-to-noise ratio expressions in Eqs. (2.4) through (2.6) become

$$SNR = \frac{F_s P_r \eta}{h\nu\Delta\nu} \qquad (2.13)$$

for both photoemissive and photovoltaic type detectors, and

$$SNR = \frac{F_s P_r \eta}{2h\nu\Delta\nu} \qquad (2.14)$$

for photoconductors. It is seen from the above equations that signal-to-noise ratio in the heterodyne case is proportional to the optical signal intensity, in contrast to direct detection where SNR varies as the square of the optical intensity.

Most early interest in heterodyne lidar was concerned more with the phase measurement capability of the technique than with its potential sensitivity benefits. The first measurements of atmospheric winds using coherent lidars were made by Jelalian and Huffaker [29] using a CO_2 continuous wave system. Subsequently, results of comparisons between CO_2 lidar wind measurements and those from a cup anemometer showed good agreement [30] indicating the feasibility of such devices. A coherent infrared lidar system used for satellite tracking and identification was developed at Lincoln Laboratory in the late 1960's and is still operational [31]. Because this system occupied several rooms, a program to develop a transportable radar for tactical military operations was initiated. By early 1982, the major components of this portable system were nearly complete [32].

In the late 1970's, a number of groups reported using coherent CW CO_2 lidar systems for remote sensing of winds [33], backscatter [34] and stack plumes [35]. Such systems employed conventional or waveguide CO_2 lasers in either homodyne or heterodyne configurations. Although CW lidar systems are still employed today for military remote sensing

30

applications such as imaging and short range wind and backscatter moni-
toring, an important thrust of coherent lidar technology in recent
years has been toward development of pulsed systems capable of range-
resolved measurements from longer distances.

During the summer of 1981 the NOAA lidar employed for the experi-
ments described in this dissertation was the first high-peak-power
pulsed system to be used for atmospheric remote sensing. Developed by
United Technologies Research Center, the system has been used in a
variety of wind-monitoring applications [2,36]. Additional information
describing the NOAA lidar is presented in Chapter IV.

A number of "second-generation" pulsed CO_2 lidar systems are
currently near operation or under development. Such systems typically
generate pulse energies on the order of 1 J or more and maintain
necessary transmitter frequency stability by injection-locking the main
ty; in contrast to the hybrid TEA configuration used in the NOAA
li. . The abundance of these newer systems, combined with the capabi-
lity demonstrated in recent years to operate lidar systems in battle
field or other hostile environments, indicate that coherent CO_2 lidar
technology should continue to mature in the future. This available
technology provides a good reason to pursue potential new applications
of CO_2 lidar such as the measurements described in this dissertation.

3. Trade-Offs Between Coherent and Incoherent Systems for Atmospheric Remote Sensing

Optical heterodyne detection is characterized by two important properties which make it potentially attractive for atmospheric remote sensing: (1) the frequency and phase of the optical field can be measured and (2) the receiver can be made to operate in a shot-noise-limited detection mode. The capability to measure frequency is extremely valuable for remote monitoring of wind velocities through estimation of the Doppler shift of the backscattered radiation. Although other optical techniques, such as the so-called "fringe" system, have been demonstrated for measurement of wind velocities at limited ranges [37], pulsed-Doppler lidars using optical heterodyne detection provide a demonstrated means of measuring radial wind velocities to ranges beyond 15 km. One would normally employ these heterodyne systems when longer range measurements are desired.

For monitoring of atmospheric parameters which require measurement of backscattered signal intensity, the type of detection technique employed is usually a function of wavelength. At wavelengths below approximately 3 μm, where photoemissive devices can be used, direct detection can be made to approach quantum-noise-limited operation by using narrow spectrum optical filters and restricting the receiver field of view. Conversely at wavelengths above 3 μm, where solid state detectors are necessary, the average signal-to-noise ratio of a direct detection receiver is usually orders of magnitude below that of a

32

heterodyne receiver. This is especially true in the 10 μm spectral region, which is characterized by a high level of background radiance. When heterodyne detection is employed, the detected signal can be electronically filtered so that the receiver bandwidth is matched to the information bandwidth (typically on the order of 10 MHz). Over this narrow spectral region noise due to background radiance is negligible.

Although much more sensitive at longer wavelengths, employment of a coherent lidar system entails an enormous increase in complexity and precision over a similar direct-detection system. The transmitter and local oscillator optical sources must have sufficient frequency stability to prevent the optical beat signal from drifting out of the detector bandwidth. Unless a homodyne configuration is employed, this normally entails the use of closed-loop servo mechanisms on both lasers to maintain their appropriate frequency relationship. When the backscattered signal is directed by the receiver optics on to the detector, its phase fronts must be precisely matched with those of the local oscillator radiation to prevent degradation in sensitivity. Additionally, the backscattered signal must be transversely coherent across the entire surface of the detector where it mixes with the LO oscillation. For a distributed-type target, such as the atmospheric aerosol, this necessitates the use of a diffraction limited field of view in both transmitter and receiver for maximum SNR. Such narrow fields of view increase the difficulty of system alignment, especially when separate transmitters and receivers are employed. Because of the need for

33

transverse coherence, atmospheric processes such as turbulence can reduce sensitivity in coherent systems. Turbulence typically has a negligible effect on direct detection systems operating in the infrared.

The brief discussion above is intended to outline those factors which must be considered when considering coherent or incoherent detection for a proposed lidar system. In the visible or near IR, direct detection is probably the preferred technique unless a requirement exists for phase and frequency measurements. Farther into the IR region, heterodyne detection has a definite sensitivity advantage in terms of SNR. The complexity entailed when employing heterodyne detection, combined with the degradation possible because of turbulence and speckle effects on the return, however, tend to make one hesitate before employing a coherent technique. Chapter III examines the trade-offs between techniques with regard to a specific application: measurement of species concentration in the 10.6 μm region. The method for performing such measurements is described in the next section.

C. THE DIAL TECHNIQUE

1. DIAL equation

Measurement of gaseous species concentration by differential absorption lidar was first suggested by Schotland [38]. From Eq. (2.1), it is seen that the optical power received from the atmosphere by a lidar system is a function of the transmitted power, the volume back-

scatter coefficient, the receiver characteristics, the range to the scattering volume and the total absorption. Since system parameters can be specified, Eq. (2.1) contains two unknown quantities, backscatter and absorption, which are dependent on the state of the atmosphere. To remove the backscatter coefficient dependence in DIAL species measurements, radiation is transmitted at two wavelengths. The wavelengths are selected such that radiation at one wavelength is strongly absorbed by the atmospheric gas to be monitored, while radiation at the other wavelength, which essentially serves as a reference, is minimally absorbed by the candidate gas.

The expression used to calculate concentration in range-resolved DIAL measurements is derived from Eq. (2.1) as follows. The backscattered power at frequency ν from range R is

$$P_\nu(R) = \frac{P_0 c \tau \beta_\nu(R) \; A_r \; \exp\left\{-2 \int_0^R [\gamma(R) + \rho(r)K_\nu(r)]dr\right\}}{2R^2} \qquad (2.15)$$

where $\gamma(R)$ is the absorption coefficient of the atmosphere due to all gases except the species of interest, $\rho(r)$ is the concentration of the candidate species and $K_\nu(r)$ is absorption cross section of the species at frequency ν. Equation (2.15) assumes that pulse lengths are relatively short, such that $\beta_\nu(R)$ is constant over the pulse volume. Effects of longer pulses on measurement results are further discussed in Chapters III and IV.

DIAL measurements are performed by observing the backscattered signal power from two ranges (R and R+ΔR) and two frequencies (ν_a and

35

ν_w where ν_a corresponds to an isolated absorption line of the gas under study, and ν_w is in a spectral region on the absorption line wing). An expression for $\rho(R)$ averaged over the distance ΔR is obtained from Eq. (2.15) by forming the difference of the logarithm of $P_\nu(R)$ evaluated at R and $R + \Delta R$ for each of the two wavelengths. The equations are [38]

$$\ln \frac{P_a(R)}{P_a(R+\Delta R)} = -\frac{2\Delta R}{R} + \ln \beta_a(R) - \ln \beta_a(R+\Delta R)$$
$$+ 2\bar{\gamma}_a \Delta R + 2\bar{\rho}\, \bar{K}_a \Delta R$$

$$\ln \frac{P_w(R)}{P_w(R+\Delta R)} = \frac{2\Delta R}{R} + \ln \beta_w(R) - \ln \beta_w(R+\Delta R)$$
$$+ 2\bar{\gamma}_w \Delta R + 2\bar{\rho}\, \bar{K}_w \Delta R \qquad (2.16)$$

where $\nu = a$ and $\nu = w$ represent frequencies corresponding to line center and line wing, respectively, and the overbar indicates a spatially averaged quantity over the distance ΔR. The concentration is obtained from (2.15) and (2.16) as

$$\bar{\rho}(R) = \frac{1}{2\bar{K}_m \Delta R} \left[\ln \frac{P_a(R)}{P_a(R+\Delta R)} - \ln \frac{P_w(R)}{P_w(R+\Delta R)} + B + T \right] \quad (2.17)$$

where

$$T = -2\left[\bar{\gamma}_a - \bar{\gamma}_w\right]\Delta R$$

$$B = \ln \frac{\beta_a(R+\Delta R)}{\beta_a(R)} - \ln \frac{\beta_w(R+\Delta R)}{\beta_w(R)} \qquad (2.18)$$

$$\bar{K}_m = \bar{K}_a - \bar{K}_w \ .$$

It is seen that in order to evaluate $\bar{\rho}$ in Eq. (2.17), it is necessary to know the magnitudes of B, T and $\bar{K}_m$. The differential absorption cross section K_m can be estimated from line parameter estimation routines, such as the commonly-used Air Force Geophysical Laboratory (AFGL) absorption program [39]. The quantities B and T are, in general, unknown. It is generally assumed that if the on-line and off-line frequencies are close together and the measurements are taken nearly simultaneously then B and T can be taken to be zero. Errors due to uncertainties in $\bar{K}_m$, B and T and other factors were estimated by Schotland [40] for water vapor DIAL measurements using a tunable ruby system operating at 694 nm. In Chapter III these errors are discussed for DIAL measurements using CO_2 lasers in the 9-11 μm spectral region.

2. History of DIAL Species Measurements

Initially, DIAL measurements were performed in the visible region of the spectrum, hence direct detection was usually employed to measure the optical radiation. Following his suggestion of the technique, Schotland reported water vapor profile measurements using a ruby lidar in 1966 [16]. Although theoretical analyses examined the feasibility of the DIAL technique during the late 1960's and early 1970's [41,42], very little experimental work was reported until 1974, when Rothe et al. [43] described measurements of NO_2 using a tunable dye laser with 1 mJ output. They gathered data on a number of wavelengths to effectively map out the NO_2 absorption spectra between 4550 and 4670 Å.

37

Later in 1975 Grant et al. [14] measured NO_2 concentration in a sample chamber using atmospheric aerosols as a backscatter source. By comparing the DIAL results with those from an in situ sensor, they estimated uncertainties in the measurements to be 0.05 ppm km.

In a subsequent experiment, Grant and Hake made measurements of SO_2 and O_3 in the UV portion of the spectrum by doubling the output from a tunable diode laser in a non-linear crystal [4]. Integration of 8 laser pulses at each of the sequentially-tuned wavelengths resulted in uncertainties of .06 ppm km for SO_2 and .12 ppm km for O_3. Also in 1975, measurements of SO_2 at a smokestack exit were reported by Kuhl and Spitschon [44]. Output from a frequency doubled dye laser operating near 300 nm was directed to a retroreflector on the opposite side of the stack.

An early species measurement in the IR was made by Hennigsen et al. [45] who remotely measured CO concentration in plastic bags. Using an optical parametric oscillator as a source, they monitored differential absorption from a topographical target at wavelengths near 1.3 μm. Ku et al. [46] performed a similar measurement of CO concentration using signal transmitted by a diode laser and scattered by a retroreflector.

The concept of employing heterodyne detection to increase sensitivity for DIAL measurements in the infrared spectral region was first proposed by Kobayashi and Inaba [47] in 1975. One year later Menzies and Shumate [48] employed homodyne detection to measure concentrations of O_3, C_2H_4 and NO along 0.8 km and 3.75 km paths near

38

Pasadena, California. Continuous-wave radiation from CO and CO_2 lasers was reflected by a rotating hard target. The rotation of the target provided the necessary Doppler shift in the backscattered signal for homodyne detection. Measurements taken over a busy highway showed good correlation between expected gas concentrations and increase or decrease in traffic volume. Reported uncertainties were on the order of .03 ppm for the NO measurements; the authors predicted a minimum detectable concentration for ozone of 2 ppb.

Also, in 1976, Murray et al. [49] reported range-resolved measurement of water vapor using a pulsed CO_2 laser and incoherent detection. A pulse output energy of 1 J with 30 cm optics produced measurements out to a range of 1.5 km which agreed reasonably well with that from a point monitor. Murray et al., recognized the need for better range capability; they estimated that 15 J of transmit energy would be required to extend maximum range to 5 km.

The SRI pulsed CO_2 lidar was also used by Murray and van der Laan [50] to measure path-integrated ethylene concentrations. Returns from a topographic target were processed to produce ethylene measurements with uncertainties on the order of 0.4 ppb. The measurements showed that water vapor interference was significant on the P(14) laser line used as the absorbing wavelength, producing an error equivalent to 7.6 ppb of ethylene if not corrected for.

Path-integrated, direct detection DIAL measurements of HCl, CH_4 and N_2O concentrations using a chemical laser were reported by Murray et

al. [51] in 1976. The DF laser produced 100-150 mJ of energy in the wavelength region between $\lambda = 3.6$ and $\lambda = 3.9$ μm. Sensitivities of the gases were determined to be 50 ppb-km for HCl, 240 ppb-km for N_2O, and 6 ppm-km for CH_4.

During 1978 construction of airborne lidar systems for range-resolved species measurements was reported by groups from Battelle Frankfurt Laboratory [52] and the Jet Propulsion Laboratory [53]. Both systems performed conceptually in the same manner. Dual CO_2 lasers operated in CW mode at the on-line and reference wavelengths. From the airborne platform the colinear beams were directed downward such that the radiation reflected from the surface was used to obtain path-averaged estimates. By pointing the transmit beams slightly forward of vertical, a Doppler shift was imparted to the backscattered signal. This permitted the use of homodyne detection of the backscattered signals. A limited range-resolving capability for the JPL system was obtained by use of waveguide lasers which could be tuned around the center of the CO_2 gain lines. This enabled matching to pressure-broadened gas absorption lines at different altitudes.

Both systems were widely used. The JPL system monitored O_3 and NH_3 during at least 7 measurement programs between 1977 and 1981 [54]. The Battelle system has been employed for examination of differential albedo effects [55] as well as for gas species monitoring [56]. The concept of differential albedo, in which mineral identification could in principle be carried out by analysis of reflected lidar returns in

the 8-12 μm region, may open up the possibility of remotely sensing the uncovered Earth's surface.

During 1979, Asai et al. [57] reported on ground-based, range-resolved ozone measurements using a 5.5 J pulsed CO_2 laser. Measurements were obtained to 3 km range after 30 minutes of averaging. Estimated uncertainty in the measurements was 40 ppb at 1.5 km range. The observed maximum range is roughly consistent with the scaling predicted by Murray et al. [49] for aerosol-backscattered returns using direct detection.

Thus far in the 1980's, progress in DIAL technology has occurred on many wavelengths within the IR, visible and UV portions of the spectrum. An attempt to measure stratospheric ozone using a UV DIAL system had been first described by Fegley [58] in 1978. The attempt was unsuccessful, primarily due to insufficient laser output energy. In 1982, however, Pelon and Megie [59] measured ozone distributions to heights of 40 km using ultraviolet DIAL. Comparisons of these results with sonde measurements showed good agreement. Hawley et al. [5] have incorporated a mobile UV DIAL system into a van. The dual laser-pumped dye laser system is used primarily by utility companies to study diffusion of stack emissions such as SO_2, O_3 and NO_2.

In a similar application, a mobile Nd:YAG-pumped tunable dye laser system operating in both the visible and UV was described by Fredericksson et al. [8]. This system measured NO_2 and SO_2 emitted from industrial stacks. Typical maximum range for the range-resolved

41

measurements was on the order of 1500 m with 50-100 mJ of output pulse energy.

The mobility demonstrated in the two previously-discussed systems was extended by Broweil et al. [60] who mounted a multipurpose DIAL system in a NASA aircraft. The NASA system uses tunable Nd:YAG pumped dye lasers to measure O_3, SO_2, NO_2, and water vapor, as well as temperature, pressure and aerosol backscatter. Operating wavelength is tunable from 280 to 1064 nm. Designed following earlier ground-based measurements of water vapor and SO_2 [61,62], ozone profiles obtained using the NASA system were within 10% of comparative in situ measurements. Measurements of aerosol backscatter profiles with the system also have shown reasonable results.

Zuev [63] recently described humidity profiling using a ruby lidar transmitting 100 mJ of pulse energy at a 0.25 Hz repetition rate. Measurements obtained to heights of 17 km showed good comparisons with radiosonde measurements. Although the measurements had to be taken at night to minimize background noise, the technique gave both good range resolution and excellent maximum range capability.

In the IR spectral region, a substantial amount of DIAL work in recent years has been performed at Lincoln Laboratory by Killinger, Menyuk, and associates [64]. They have developed a dual laser system employing two mini-TEA CO_2 lasers as primary radiation sources. The technologically advanced mini-TEA lasers produce pulses with 20 mJ of energy at repetition rates greater than 500 Hz, and can be separately

42

triggered with a time delay between the two laser firings of from 2 μs to 200 ms. This system has been used in direct detection DIAL measurements of C_2H_4 and hydrazine using returns from topographical and reflective targets. The output radiation was doubled to estimate NO and CO in the 5 μm band. In addition, experimental studies were performed which examined key DIAL-related points such as correlation between target-reflected returns as a function of time delay and wavelength, and comparison of performance for heterodyne and direct detection. These studies are discussed in more detail in Chapter IV of this dissertation, where statistics of the returns from aerososl targets are discussed.

Other recent DIAL systems using CO_2 lidars have been reported by Bufton [65], Baker [66] and Lundquist et al. [67]. Bufton described a dual pulsed TEA-laser system in a NASA P3 aircraft designed to sample O_3 and other trace species. The lasers were pulsed 25-50 μs apart to enable use of a single detector. System capability has been demonstrated in preliminary backscatter measurements from the ocean surface. Baker employed an incoherent CO_2 lidar to profile water vapor in the boundary layer. The system produced water vapor profile measurements to approximately 1500 m range using output pulses of 4 J. Baker also examined the effect of long pulses on profile measurements, concluding that the tail in the longer pulses produced erroneous backscatter power estimates at ranges fairly close to the lidar.

Lundquist et al. [67] reported the first use of heterodyne detection in a pulsed CO_2 DIAL system. The lidar transmitter employed a Q-

43

switched laser to produce output pulses at a 20 kHz rate; average power was 1.5 W. Because of the low single pulse energy (.075 mJ), sensitivity was not adequate to examine returns from aerosols, however, the high pulse repetition frequency enabled rapid averaging of the speckle fluctuations. Returns from a topographical target were used to monitor ethylene emissions from a petrochemical plant.

In addition to the CO_2 work, DIAL measurements in the 1-4 μm region using optical parametric oscialltors (OPO) as radiation sources have been described by Endemann and Byer [68] and Brassington [21]. Brassington measured water vapor on a weak absorption line near 1.73 μm to ranges approaching 1 km. Endemann and Byer used measurements on water vapor lines near 1.9 μm to measure both temperature and humidity according to the method described by Mason [69]. The 10 mJ/pulse OPO was tuned to three wavelengths; two of which coincided with water vapor line centers while a third corresponded to relatively low absorption spectral regions. Humidity and temperature measurements were obtained by analyzing returns reflected from a nearby building. Additional analysis of Mason's method for simultaneous measurement of temperature and humidity has been performed by Rosenberg and Hogan [70] and Schwenner and Wilkerson [71]. A ground-based system employing Alexandrite lasers is being constructed at NASA Goddard for measurements of temperature and pressure in the spectral region near 700 nm [72].

Because of the potential of DIAL for range-resolved or long path remote monitoring, a number of studies have examined the feasibility of

making DIAL measurements from a satellite or space-Shuttle based platform. NASA has proposed a series of Shuttle lidar experiments which would include tunable dye lasers pumped by successive harmonics of a Nd:YAG laser, grating tunable CW CO_2 lasers, and discretely-tuned pulsed CO_2 lasers, and discretely-tuned pulsed CO_2 lasers [73]. The primary advantage of a spaceborne lidar system is the capability for global measurements. Spaceborne systems are also aided by the fact that, in general, extinction and turbulence effects are much less than are encountered by ground-based systems. Various studies have indicated the feasibility of spaceborne DIAL measurements of ozone, e.g., [74] as well as other constituents with absorption lines in the visible and UV spectral regions.

D. POTENTIAL USES OF COHERENT CO_2 DIAL

As the discussion in the previous section illustrates, the DIAL techno was has been amply demonstrated at a number of wavelengths rang. from the UV through the IR portion of the spectrum. Because of the availability of laser-pumped tunable dye lasers as sources, and of photomultiplier tubes to serve as high quality detectors, much of the work has been performed at visible and ultraviolet wavelengths. Nevertheless, the middle infrared region between 2.5 and 25 µm is probably the most fertile for DIAL work because of the large number of gases which absorb radiation at those wavelengths. In this region absorption is due to fui ental and combination vibrational-rotational bands, and strong lines of a number of important pollutant gases can be

45

distinguished from lines of other significant atmospheric absorbers—an important factor for high specificity. An interesting segment of the 2.5-25 µm region is the spectral window between 9-11 µm, which can be measured using CO_2 lasers. Table 2.1 lists some of the gases with absorption lines in the 9-11 µm region which can potentially be monitored using CO_2 lidar.

The primary difficulty associated with atmospheric monitoring in the 9-11 µm region is obtaining sufficient sensitivity. Typical aerosol backscatter coefficients at $\lambda = 10$ µm are at least an order of magnitude lower than at $\lambda = 1$ µm [75]. In addition, detector sensitivities are lower, so that the SNR of a lidar operating in a direct detection mode at 10 µm can be expected to be decreased by as much as 40 dB relative to that of an equivalent quantum-noise limited system operating at $\lambda = 1.06$ µm. Because of the lack of sensitivity, incoherent DIAL measurements using aerosol-backscattered returns have only been possible to ranges of 1 or 2 km or less, despite laser pulse energies of 1-5 J. Murray [49] predicted that a lidar would require 15 J/pulse of transmit energy and a 90 cm diameter receiver to be able to sense returns from 15 km away.

Table 2.1. Gases with absorption lines in the 9-11 μm CO_2 region including isotope lasers). From [56].

Ammonia	Trichloroethylene
Benzene	Vinyl chloride
Butane	Acetaldehyde
Carbon dioxide	Butadiene-1,3
Chloroprene	Carbon monoxide
Ethylene	Formaldehyde
Freon 11	Nitric oxide
Freon 13	Nitrogen dioxide
Methanol	Nitrogen tetroxide
Ozone	Nitrous oxide
Perchloroethylene	Propylene
Sulfur dioxide	Water vapor
Sulfur hexafluoride	

Therein lies the attraction of coherent DIAL in the 9-11 μm spectral region. The ability to operate in a quantum noise limited mode gives coherent DIAL an advantage of approximately 30 dB in terms of average SNR (defined as average signal power divided by average noise power). Although this advantage is negated somewhat by an increased susceptibility to laser speckle and refractive turbulence, the fact remains that the backscattered signal energy is available to be measured at ranges well beyond those where the direct detection signal is totally obscured by noise. Hence, for species monitoring at long ranges, coherent DIAL offers the capability to obtain measurements using low-energy transmit pulses. As an example, the NOAA coherent lidar system has measured both intensities and wind velocities in the boundary layer to ranges beyond 15 km, using only a 100 mJ pulse.

The other principal advantage of coherent CO_2 DIAL is the capability to measure the radial wind velocity as well as the concentration.

Wind velocity measurements using pulsed coherent CO_2 lidar have been reported by groups at NOAA and NASA, and the technique is well established. By measuring the phase of the detected signal as well as the intensity, information on both the movement and concentration of the target gas can be obtained. Such a capability is potentially valuable in such applications as hazardous gas detection and tracking, pollution diffusion studies, and severe storm moisture entrainment. In a tactical battlefield environment a coherent DIAL system could conceivably detect clouds of chemical or biological agents at ranges up to 10 km or more, and provide information on the rate of movement of the cloud toward the lidar.

Although a number of feasibility studies have looked at the capabilities of coherent CO_2 DIAL for range-resolved species measurement, very little experimental work has yet taken place. In the following chapters the first comprehensive examination of the coherent DIAL problem is performed. Chapter III uses atmospheric models to analyze the potential accuracy of ground-based DIAL measurements and includes a detailed discussion of the significant error sources which degrade measurments in the 9-11 μm spectral region. In Chapter IV the statistical properties of aerosol-backscattered returns are examined in detail with respect to their effect on range-resolved species measurments. Actual DIAL measurements of atmospheric water vapor are described in Chapter V and compared with values measured by in situ sensors. The important results are summarized and discussed in Chapter VI, which also includes a recommendation for future work on the coherent DIAL problem.

48

E. SUMMARY

This chapter has served to provide a perspective on the coherent DIAL problem through a general discussion and history of lidar fundamentals as well as DIAL applications. Species concentration measurements have been reported using a wide variety of laser sources with wavelengths ranging from the ultraviolet to the middle infrared. Through the use of photomultipliers, quantum-noise-limited performance can be obtained at wavelengths shorter than the near IR, where tunable dye lasers are the most widely-employed laser source. This sensitivity eliminates the need to employ heterodyne detection to enhance sensitivity, although background can still be a problem. At longer wavelengths, where photon energies are relatively small (typically beyond 3 μm), detector dark noise and thermal noise dominate quantum noise. In these circumstances, such as at $\lambda = 10.6$ μm, SNR observed using direct detection is degraded by as much as 30 dB relative to that which can be obtained using quantum-noise limited operation. As a result incoherent DIAL systems operating in the IR typically have maximum ranges of a few km.

DIAL measurements in the atmosphere have been used to estimate concentration of a number of gases, including water vapor, NO_2, SO_2, O_3, CO, C_2H_4, NO, HCl, CH_4, N_2O, NH_3 and hydrazine, as well as to estimate temperature profiles. For the most part, these measurements have occurred at short ranges or through the use of topographic or other hard targets. Two notable exceptions are ozone profiles measured to

40 km height in the ultraviolet, and water vapor profiles measured to 17 km using a ruby lidar in the visible spectral region.

Coherent DIAL using CO_2 lasers offers the potential to estimate both gas concentrations and wind velocity at ranges to 15 km or more using relatively low (~100 mJ) pulse energies. Through the use of heterodyne detection, quantum-noise limited operation is obtained in a spectral region (9-11 μm) which is particularly rich in species absorption lines. Additionally, contamination of signal by background optical radiation is virtually non-existent. The capability to measure both species and wind velocity available with coherent CO_2 DIAL could be useful in pollution transport studies, detection and tracking of hazardous gases, and severe storm water entrainment research.

III   FEASIBILITY ANALYSIS OF DIAL WATER VAPOR MEASUREMENTS

This chapter describes a feasibility analysis into the capabilities of DIAL water vapor measurements using ground-based heterodyne CO_2 lidar. Some of the results covered in this chapter were published earlier in a NOAA Technical Memorandum [76]. The first part of the chapter deals with the mechanisms of the error producing parameters in DIAL measurements. Because of a general interest in the comparative capabilities of coherent and incoherent systems, uncertainties in both types of measurement are examined. Expressions for the effects of each mechanism on the concentration-measurement error are developed, and the results compared.

Following the general discussion of errors in DIAL measurements, a simulation is described to compare the measurement capability of the coherent and incoherent CO_2 DIAL techniques. Models for atmospheric variables used in the simulation such as backscatter, turbulence, transmission, temperature and pressure are described. Simulations were performed for both "standard" and "optimized" system parameters over a variety of atmospheric conditions. The results of these simulations are discussed in the latter part of the chapter.

A. ERROR SOURCES IN DIAL MEASUREMENTS

As described in Chapter II, range-resolved DIAL measurements require measurement of the transmitted power backscattered from two

51

different ranges at each of two laser wavelengths. In practice, these measurements would typically be made in one of three ways:

1) Transmit and receive radiation at the on-line and off-line wavelengths simultaneously. Such a concept would probably require separate transmitters and receivers for each wavelength.

2) Rapidly tune the system transmit wavelength back and forth between the two desired wavelengths. A method for doing this has been proposed using a hexagonal rotating grating [77]. This approach is probably impractical for coherent DIAL, due to the increased precision required in frequency stabilization. Both system transmitter and local oscillator frequencies have to be tuned and stabilized within the inter-pulse interval.

3) Transmit and receive a sequence of pulses at one wavelength, then tune the system to the other wavelength and repeat the procedure. This is the least complex method, in terms of equipment required; however the measurement errors inherent with this technique are expected to be larger because of changes in the key atmospheric characteristics during the wavelength switching interval.

In the following examination of the error-inducing processes in DIAL measurements the relative effects for both sequential and simultaneous measurements will be discussed. The error analysis follows that of Schotland [40]. As explained in Chapter II, the gaseous species concentration $\bar{\rho}$ is obtained from estimates of the power backscattered from

52

ranges R and R + ΔR at each of the absorbing (λ_a) and non-absorbing (λ_w) wavelengths as follows

$$\tilde{\rho}(R + \Delta R/2) = \frac{1}{2\bar{K}_m \Delta R} \ell n \frac{\hat{P}_a(R)}{\hat{P}_a(R+\Delta R)} - \ell n \frac{\hat{P}_w(R)}{\hat{P}_w(R+\Delta R)} + B + T \qquad (3.1)$$

where

$$B = \ell n \frac{\beta_a(R+\Delta R)}{\beta_a(R)} - \ell n \frac{\beta_w(R+\Delta R)}{\beta_w(R)}$$

$$T = 2(\bar{\gamma}_a - \bar{\gamma}_w)\Delta R$$

and other terms have been defined previously. The terms B and T in Eq. (3.1) represent the effect of differential backscatter and differential absorption by background species on the measurement. A bar over the parameter indicates a spatially averaged quantity over the range interval ΔR. One basic premise of the DIAL technique is that the B and T terms can be ignored when the time between the on-line and off-line measurements is short and the wavelengths are chosen to be close together. Conversely, when the measurement time interval is long, random changes in β or γ are expected to increase the total measurement error. This point is discussed in more detail in Sec. D.

The hat superscripts over the power terms in Eq. (3.1) are necessary because the instantaneous measured power output from the system detector at a given range is not necessarily proportional to the average backscattered signal power. In general the measured power is a random process as a result of both variability in the atmosphere and receiver noise added during detection. Thus averaging, filtering, or

53

some other form of processing is typically necessary to estimate the mean power for insertion into Eq. (3.1).

In addition to measuring the mean backscattered power values, the differential absorption cross section $\overline{K}_m$ in Eq. (3.1) must be known to calculate concentration. The absorption cross-section is a function of both temperature and pressure, which generally are not precisely known for remote measurements. Typically a value for $\overline{K}_m$ is estimated using absorption line parameter data such as that archived by McClatchey [39], or from published tables of results.

Following Schotland, an expression is derived for the fractional variance of $\overline{\rho}$ in terms of the variances of the aforementioned variables by expanding the logarithms of Eq. (3.1) in differential form about the mean values of the independent variables. The fractional variance becomes

$$
\frac{\sigma_{\overline{\rho}}^2}{\overline{\rho}^2} = \frac{\sigma_{\overline{K}_m}^2}{\overline{K}_m^2} + \frac{1}{4\overline{K}_a^2\overline{\rho}_c^2(\Delta R)^2} \left[\frac{\sigma_{\hat{P}_a}^2(R_1,t_1)}{\langle \hat{P}_a(R_1,t_1)\rangle^2} + \frac{\sigma_{\hat{P}_w}^2(R_1,t_2)}{\langle \hat{P}_w(R_1,t_1)\rangle^2} + \frac{\sigma_{\hat{P}_a}^2(R_2,t_1)}{\langle \hat{P}_a(R_2,t_1)\rangle^2} \right.
$$

$$
+ \frac{\sigma_{\hat{P}_w}^2(R_2,t_2)}{\langle \hat{P}_w(R_2,t_2)\rangle^2} - \frac{2\mathrm{cov}\{\hat{P}_a(R_1,t_1)\hat{P}_w(k_1,t_2)\}}{\langle \hat{P}_a(R_1 t_1)\rangle\langle(\hat{P}_w(R_1,t_2)\rangle} - \frac{2\mathrm{cov}\{\hat{P}_a(R_2,t_1)\hat{P}_w(R_2,t_2)\}}{\langle \hat{P}_a(R_2,t_1)\rangle\langle \hat{P}_w(R_2,t_2)\rangle}
$$

$$
- \frac{2\mathrm{cov}\{\hat{P}_a(R_1,t_1)\hat{P}_A(R_2,t_1)\}}{\langle \hat{P}_a(R_1,t_1)\rangle\langle \hat{P}_A(R_2,t_1)\rangle} + \frac{2\mathrm{cov}\{\hat{P}_a(R_1,t_1)\hat{P}_w(R_2,t_2)\}}{\langle \hat{P}_a(R_1,t_1)\rangle\langle \hat{P}_w(R_2,t_2)\rangle}
$$

$$
+ \frac{2\mathrm{cov}\{\hat{P}_a(R_2,t_1)\hat{P}_w(R_1,t_2)\}}{\langle \hat{P}_a(R_2,t_1)\rangle\langle \hat{P}_w(R_1,t_2)\rangle} - \frac{2\mathrm{cov}\{\hat{P}_w(R_1,t_2)\hat{P}_w(R_2,t_2)\}}{\langle \hat{P}_w(R_1,t_2)\rangle\langle \hat{P}_w(R_2,t_2)\rangle}
$$

$$
+ \sigma_B^2(t_1,t_2) + \sigma_T^2(t_1,t_2) \tag{3.2}
$$

where σ^2 is the variance of the subscripted parameter, $\langle \hat{P}_1(R_j, t_K) \rangle$ is the ensemble mean of the estimated average power estimated at time t_K from range R_j with wavelength i, and $cov(\hat{P}_1, \hat{P}_2)$ represents the covariance between the fluctuations of power estimates $\hat{P}_1$ and $\hat{P}_2$. A time variability has been added in the power estimate, backscatter, and transmission terms in Eq. (3.2) in order to model the estimates as random processes. Since errors in absorption cross-sections tend to be more systematic, the parameter is modeled as a random variable in Eq. (3.2) rather than a random process.

We see from Eq. (3.2) that errors occur as a result of uncertainties in four key parameters: average power estimate, backscatter coefficient, background extinction and species absorption cross-section. For the most part, differences between coherent and incoherent DIAL system performances are centered around their comparative capabilities to measure average power. Errors due to the other parameters are generally similar for the two techniques. In the following sections we examine and quantify the effect on measurement accuracy of uncertainties in each of the four error terms. A simulation is then developed assuming typical atmospheric conditions to predict measurement accuracy for direct and heterodyne detection DIAL. These predicted uncertainties are compared with actual measurement results in Chapter VI.

B. POWER MEASUREMENT CERTAINTIES

It is seen from Eq. (3.2) that errors in measurement of average

power for each of the four cases $\hat{P}_a(R,t_1)$, $\hat{P}_a(R+\Delta R,t_1)$, $\hat{P}_w(R,t_2)$,

$\hat{P}_w(R+\Delta R,t_2)$ lead directly to concentration estimate errors. By power

measurement uncertainties we refer to effects of random fluctuations in

the estimate which occur even when other parameters in Eq. (3.2) are

held constant. Thus, fluctuations in irradiance due to temporal or

spectral variability in backscatter or path extinction are not dis-

cussed in this section, but rather considered separately.

For constant β, γ, and $\bar{\rho}$ conservation of energy constraints re-

quire that the average irradiance incident at the system receiver

remain constant. Instantaneously, however, the irradiance varies as a

stochastic process due to random fluctuations in the atmosphere. The

primary sources of random fluctuations in receiver irradiance are

target speckle and atmospheric turbulence. Target speckle results

because of the distributed nature of the aerosol target. Since the

individual particles are randomly positioned, the field at a point in

space results from the superposition of the individual backscattered

fields and thus has random amplitude and phase. The irradiance level

is therefore also random. Atmospheric refractive index turbulence

along the path produces a conceptually similar effect. In turbulence

the eddies of refractive index inhomogeneities along the path randomize

the phase of the propagating field, resulting in random fluctuations of

irradiance at points downstream of the propagation path. Turbulence
and speckle are examined in more detail in Sections B.1 and B.4.

In addition to the uncertainties caused by fluctuation of instan-
taneous irradiance, additional error is introduced into the mean
backscattered signal power estimate by noise in the detection and esti-
mation process. Since detection noise is an additive process, the
actual power at the output of the receiver increases as the noise level
goes up. Thus, noise adds both bias and increased variability to the
estimate.

To avoid confusion when discussing errors caused by fluctuation in
the irradiance as opposed to errors caused by relatively high levels of
detection noise, it is useful to define the terms carrier-to-noise
ratio (CNR) and signal-to-noise ratio (SNR). From here on, CNR is de-
fined as the ratio of mean signal power to mean detection noise power.
Thus CNR is a function of the fluctuations in the power estimate due
only to detection noise (including quantum noise). Fluctuations caused
by variation in signal irradiance are not included in this term. To
account for this additional uncertainty the SNR of the estimate is
defined as the ratio of the mean of the desired parameter to its stan-
dard deviation, i.e.,

$$SNR = \frac{\langle X \rangle}{\sigma_x} . \tag{3.3}$$

Thus, SNR is the reciprocal of the normalized or fractional standard
deviation, and is a measure of expected error in a single measurement

57

of the mean of X. The definition of SNR includes effects of signal
fluctuations as well as noise on the mean estimate. The reader should
be cautioned that the above definition of CNR as used in lidar litera-
ture corresponds to the standard definition of SNR used in communica-
tion theory.

In the following sections the effects of the above-mentioned
error-producing phenomena are examined for coherent and incoherent DIAL
systems. Since in general the effects are not independent, we will
first discuss the phenomena separately, then examine the measurement
error caused by the combined effects.

1. Target Speckle Effects

Effects of speckle, or coherent fading, which results due to the
extended, distributed nature of the aerosol backscattered target are
examined first. The general problem of speckle in lidar measurements
has been addressed by a number of authors, e.g., [78]. In this section
we describe the phenomenon, discuss its effect on DIAL species measure-
ments, and illustrate methods to reduce speckle contribution to DIAL
measurement error. Speckle results because of the random placement of
the individual aerosol particles within the scattering volume. Upon
being irradiated by the lidar transmit field, each scatterer acts as an
individual source radiating a field with random phase. At a given
point in space, the resulting field is the vector addition of the
fields produced by the individual scatterers. Since various degrees of

58

constructive or destructive interference between the fields take place at different points in space, a random spatial pattern of high and low intensity regions results from the total backscattered energy.

The relative spatial size of the individual speckles in the speckle pattern is a function of the transverse dimensions of the distributed target and the intensity distribution of the incident field across the target. From the van Clttert-Zernicke theorem [79], the mutual intensity function of the field in the observation plane can be calculated. For a Gaussian-distributed intensity field across a diffuse target, the transverse mutual intensity function at the receiver is also Gaussian; the approximate size or lateral coherence distance of a single region is on the order of $\lambda L/D_s$, where D_s is the diameter of the illuminated spot, λ is the wavelength, and L is the distance to the observation point (assumed to be roughly perpendicular to the scattering plane).

If the atmosphere were perfectly still and the illuminating source perfectly coherent, a single speckle pattern would be frozen in space. Because the atmosphere is in constant motion, at least on the scale of a laser wavelength, the speckle pattern continuously varies with time as the individual scatterers change their relative distance to the observation point. The characteristic time constant τ_s of the speckle pattern fluctuations is a function of the standard deviation of the radial velocity of the scatterers (σ_v) as $\tau_s \approx \lambda/\sigma_v$.

59

Since the superposition of individual scattered fields with random phase is analogous to the classical random walk problem, the amplitude of the field at a point is ideally a Rayleigh distributed random variable [80]. In a Rayleigh phasor model the resulting random intensity field has a negative exponential distribution. Since the exponential distribution is characterized by the standard deviation being equal to the mean, estimates of the mean taken from a single measurement of the irradiance over a single speckle have an expected error of 100%, even in the absence of noise. Thus, the expected error of a single DIAL concentration measurement due to speckle from Eq. (3.2) is

$$\frac{\sigma_{\bar{\rho}}}{\langle \bar{\rho} \rangle} = \frac{1}{\bar{K}_m \bar{\rho} \, \Delta R} \quad . \tag{3.4}$$

Equations (3.2) and (3.4) are valid when $\sigma_{\hat{p}}/\langle \hat{P} \rangle \ll 1$, as would be the case when multiple samples are averaged. The exact error expression is calculated from the probability distribution of the $\hat{P}$ terms. Assuming an exponential distribution Ostberg [80] finds the error for m samples averaged per power estimate, to be

$$\frac{\sigma_{\rho}}{\bar{\rho}} = \frac{1}{\bar{K}_m \rho \Delta R} \frac{\pi^2}{6} - \sum_{\nu=1}^{m-1} \frac{1}{\nu^2} \tag{3.5}$$

which is approximately 50% higher than predicted by the approximation in Eq. (3.4) for $m = 1$ samples. As the number of averaged samples increases $\sigma_{\hat{p}}/\langle \hat{P} \rangle$ decreases and the approximation in Eq. (3.2) becomes

60

more valid. Since $\sigma_P^2/\langle\hat{P}\rangle$ for a single measurement in the presence of speckle is unacceptably high, throughout the rest of the analysis some form of averaging is assumed to have been employed to reduce the standard deviation of the power measurement. Estimates of concentration error will be generally calculated using Eq. (3.2) under this assumption.

Signal averaging to reduce speckle can be performed either in the spatial, temporal or frequency domains. Spatial averaging is employed by sampling multiple speckles across the receiver aperture. This is relatively easy in a direct detection system. One employs a large receiver aperture, such that a portion of the speckle pattern containing multiple speckles is imaged onto the detector. A large receiver in this sense means that the diffraction-limited receiver field of view θ_{R_d} is smaller than the transmitter beam divergence θ_T, such that the number of speckles across the receiver aperture is approximately θ_T/θ_{R_d}. This ratio is increased by making the transmitter smaller than the receiver and/or allowing the transmitter to operate on higher-order transverse modes. Since direct detection responds to total irradiance, in a "light bucket" sense, enlarging the receiver aperture improves speckle averaging while at the same time increasing the detected signal level. The effective number of speckles contained across the aperture can be calculated from [82]

$$m_a = \frac{[\,|\vec{J}_s(0)|\,\int d^2r w(r)]^2}{\int d^2r \,|\vec{J}_s(r)|^2 R_w(r)} \tag{3.6}$$

61

where $\vec{J}_a(r)$ is the signal spatial mutual intensity function [79], $w(r)$ is the weighting function across the aperture and $R_w(r)$ is the auto-correlation function of the aperture weighting function. Gardner and Mecherle [82] have evaluated m_a for a number of receiver weighting and mutual intensity functions.

Spatial averaging is physically more difficult in coherent systems. Because the signal must mix coherently with the local oscillator across the entire surface of the detector to avoid inter-ference, multiple spatial speckles cannot be imaged on a single detec-tor, but must be directed to separate detectors with spacings approxi-mately equal to the transverse coherence length. The IF beat signals from each detector are then square-law detected and combined to produce the desired speckle averaging. The number of independent samples M_a under such a configuration is approximately, from Appendix A,

$$M_a = m_a \qquad N_d > m_\infty$$
$$= N_d \qquad N_d < m_\infty \qquad (3.7)$$

where

$$m_a = \frac{[\langle I \rangle \int w(r)d^2r]^2}{\langle I^2 \rangle \int B_I'(r)R_w(r)d^2r}$$

is the number of independent samples assuming an infinite number of detectors, N is the number of detectors, I is the optical intensity, $B_I'(r)$ is the normalized autocovariance function of intensity across the aperture, w is the aperture weighting function and $R_w(r)$ is its

62

spatial autocorrelation function. The number of heterodyne samples is basically equal to that of the direct detection case for large number of samples. The only difference between Eqs. (3.6) and (3.7) is the form of the expression; Gardner substitutes $|\vec{J}(r)|^2$ for the autocorrelation function of intensity fluctuations.

Temporal speckle averaging takes place when the time scale of the irradiance fluctuations is shorter than the equivalent time increment of a range gate. By filtering or integrating the power time series the fluctuations are smoothed. The time scale of the temporal fluctuations is a function of both the speckle time scale and the bandwidth of the transmitted pulse, and can be roughly approximated by an inverse root-sum-square relationship

$$(\frac{1}{\tau})^2 \approx (\frac{1}{\tau_s})^2 + (B_t)^2 \qquad (3.8)$$

where τ_s is speckle time scale and B_t is transmit pulse bandwidth. Temporal averaging is employed in the same manner for both incoherent and coherent systems. For incoherent detection the number of independent samples of the speckle fluctuations has been developed by Gardner and Mecherle [82], as

63

$$m_t = \frac{[|\vec{J}_T(0)| \; R_{p_t}(0) \int_{-\infty}^{-\infty} h(\tau) \, d\tau]}{\int_{-\infty}^{\infty} |\vec{J}_T(\tau)|^2 \; R_{p_t}^2(\tau) \; R_h(\tau) \, d\tau} \qquad (3.9)$$

where $\vec{J}_T$ is the temporal mutual intensity function, R_{p_t} is the autocorrelation function of the transmit pulse, and R_h is the autocorrelation function of the receiver filter which serves to average. A derivation of the corresponding equation for coherent detection is developed in Appendix B, and is shown to be identical to Eq. (3.9) when no noise is present at the detector. Gardner and Mecherle also computed m_t for incoherent systems with various filter responses and transmit pulse characteristics; many of these calculations are also valid for coherent detection.

Finally, frequency diversity can be employed in coherent systems by transmitting pulses with large bandwidths. It can be shown that when pulsed radiation of different frequencies interacts with the same distributed scattering medium, the speckle patterns associated with the backscattered field are independent when the frequency separation is more than $2/\tau_p$ Hz, where τ_p is pulse duration. Thus, by passing the detector output signal through a bank of bandpass filters, then computing the power in each filter and summing the results, speckle averaging is obtained. It should be noted that frequency diversity and temporal diversity techniques are not independent. For example, consider a case in which the transmit pulse bandwidth is $N * 2/\tau_p$, where

64

the time equivalent of the desired range resolution is T. For frequency diversity one employs N bandpass filters, each with a bandpass of $2/\tau_p$ Hz, to get N simultaneous independent samples. Additional independent samples are produced when T is greater than the temporal response of each filter, so that the total number of independent samples of the speckle fluctuations over a time increment T is $2NT/\tau_p$. Note that this is equivalent to simply filtering the output power estimate, since the time scale of the fluctuations in the detector output signal is approximately $\tau_p/2N$. Thus, in essence, a frequency diversity receiver adds complexity without a corresponding increase in performance. The only exception to this might be a case where the transmit pulse is comprised of discrete frequencies, as would be the case when transmission occurs on multiple longitudinal modes. Under this condition some CNR advantage might be incurred by narrow bandpass filtering around each discrete mode frequency.

The preceding discussion shows that although diversity techniques can be utilized in both coherent and incoherent systems to reduce speckle errors, implementation is typically less complex for incoherent systems. Furthermore, as will be shown in Part 3, the trade-off in sensitivity which occurs when diversity techniques are employed is usually less severe with incoherent systems.

2. Effects of Detection Noise

Next the uncertainty added to the power measurement process by detection and background noise is examined. It is assumed in this section that the signal is deterministic rather than a random process. In heterodyne systems the noise adds to the signal-induced current as narrow band Gaussian noise and the detector output current is given by

$$i_d(t) = K_d \{A_s(t) \cos \nu_{IF}t + A_{nc}(t) \cos \nu_{IF}t + A_{ns}(t) \sin \nu_{IF}t\} \quad (3.10)$$

where $A_s(t)$ is the amplitude of the optical received signal, ν_{IF} is the IF frequency determined by the LO offset, $A_{nc}(t)$ and $A_{ns}(t)$ are random uncorrelated quantities with zero mean representing the in-phase and quadrature noise components, and $K_d = A_L e \eta / h \nu$ is a proportionality constant. Following Yariv [83] the average total power is given by

$$\langle P \rangle = \langle i_d^2 \rangle$$
$$= K_d^2 \{ \frac{\langle A_s^2 \rangle}{2} + \frac{1}{2} [\langle A_{nc}^2(t) \rangle + \langle A_{ns}^2 \rangle] \} \quad . \quad (3.11)$$

A_{nc} and A_{ns} are zero mean Gaussian; their mean square values are represented by σ_n^2. Thus, for shot noise limited detection

$$\frac{K_d^2}{2} [\langle A_{nc}^2(t) \rangle + \langle A_{nc}^2(t) \rangle] = K_d^2 \sigma_N^2 = \frac{e^2 P_L \eta \Delta \nu}{h \nu} \quad . \quad (3.12)$$

The total measured power in the detector output is

$$\langle i_d^2 \rangle = \frac{K_d^2}{2} \{ \langle \hat{P}_s \rangle \div \langle P_n \rangle \} \quad (3.13)$$

where

66

$\langle P_s \rangle = \langle A_s^2 \rangle$ = signal power

$\langle P_n \rangle = 2\sigma^2$ = Noise Equivalent Power (NEP).

Since $K_d^2/2$ is a system constant, valid for all measurements, it can be dropped without affecting the results. It can be seen from Eq. (3.13) that the estimate of the detector output power $\hat{P} = \langle i_c^2 \rangle$ is a biased estimate of the signal power due to the presence of the noise. Hence an estimate of the mean noise power must be subtracted to get

$$\hat{P}_s = \hat{P} - \bar{P}_n. \tag{3.14}$$

It is obvious from Eq. (3.14) that errors in signal power estimate result from (1) random fluctuations in $\hat{P}$ due to noise (remember that signal power is assumed deterministic) and (2) inexact estimate of the mean noise power $\bar{P}_n$. It is generally not unrealistic to assume that noise power can be well established in a stabilized system by observing the noise-only detector output for a sufficient period to reduce the variance to a negligible value. Under this condition the estimate is unbiased and its error is due entirely to random fluctuations in the noise. The estimate error is then given by

$$\sigma_{\hat{P}_s}^2 = 2\langle \hat{P}_s \rangle \langle \bar{P}_n \rangle + \langle \bar{P}_n \rangle^2 . \tag{3.15}$$

The relative uncertainty is

$$\frac{\sigma_{\hat{P}_s}^2}{\langle P_s^2 \rangle} = \frac{2\langle \bar{P}_n \rangle}{\langle \hat{P}_s \rangle} + \left(\frac{\langle \bar{P}_n \rangle}{\langle \hat{P}_s \rangle}\right)^2 = \frac{2}{CNR} + \frac{1}{CNR^2} \qquad (3.16)$$

where $CNR = \langle \hat{P}_s \rangle / \langle \bar{P}_n \rangle$ Going back to the definition of K_d in Eq. (3.12) it is easily shown that $\langle \bar{P}_n \rangle = h\nu B/\eta$, which is the noise equivalent power (NEP) for heterodyne systems. For a CO_2 laser system with a matched filter receiver whose bandwidth is matched to a 1 μs pulse, and which has a detector quantum efficiency of 50%, $NEP = 3.76 \times 10^{-14}$ W.

A treatment of incoherent DIAL systems differs in that the detector current is proportional to the total incident optical power on the detector. That is,

$$i(t) = K_d[P_s(t) + P_b(t)] + i_n(t) + i_d(t) \qquad (3.17)$$

where $P_s(t)$ is signal power incident on the detector, $P_b(t)$ is optical background power, K_d is a proportionality constant equal to $e\eta/h\nu$, $i_d(t)$ is dark current and $i_n(t)$ is current due to various noise sources (Johnson noise, shot noise, etc). As in the heterodyne case the estimate of power directly from the detector current is biased, i.e.,

$$\langle i_d(t) \rangle = \langle P \rangle = K_d[\langle \hat{P}_s \rangle + \langle \hat{P_b} \rangle] + \langle \hat{i_d}(t) \rangle + \langle i_n(t) \rangle . \qquad (3.18)$$

An estimate of P_s is thus obtained by subtracting the best estimate of background and noise contributions, such that

68

$$K_d \langle \hat{P}_s \rangle = \langle i_d(t) \rangle - K_d \langle \hat{P}_B \rangle - \langle i_d \rangle - \langle i_n(t) \rangle . \qquad (3.19)$$

Again, assuming that signal power is constant and errors in the background and dark current estimates are negligible, fluctuations in the power estimate are due only to fluctuations caused by the noise current $i_n(t)$. Thus

$$\sigma_{\hat{P}_s} = \frac{\sigma_{i_n}}{K_d} \qquad (3.20)$$

and the normalized variance is

$$\frac{\sigma_{\hat{P}_s}^2}{\langle \hat{P}_s \rangle^2} = \frac{\sigma_{i_n}^2}{K_d^2 \langle P_s \rangle^2} = \left(\frac{1}{CNR}\right)^2 ; \qquad (3.21)$$

where CNR is a voltage signal to noise ratio.

In direct detection systems, dominant noise sources are shot noise due to signal, shot noise due to background, and Johnson noise. These terms are given by [83]

$$\sigma_{i_n}^2 (\text{Johnson}) = \frac{4 k_B T_e \Delta \nu}{R_L} \qquad (3.22)$$

where T_e is equivalent temperature, $\Delta \nu$ is receiver bandwidth, k_B is Boltzmann's constant, and R_L is load resistance of the system preamplifier; and

69

$$\sigma_{i_n}^2 \text{ (shot)} = \frac{2e^2\eta}{h\nu} (P_s + P_B) . \qquad (3.23)$$

These expressions can be used to estimate NEP for comparison with that for heterodyne detection. Assuming a 1 MHz receiver bandwidth, background radiance of 1000 μW cm^{-2} sr^{-1} [84], input resistance of 1 MΩ noise temperature of 300°K, and 30 cm receiver aperture, the various noise equivalent powers are

$$NEP_{Johnson} \approx 3 \times 10^{-11} \text{ W}$$

$$NEP_{background-shot} \approx 5.3 \times 10^{-11} \text{ W}$$

$$NEP_{signal-shot} \approx 3.76 \times 10^{-14} \text{ W} .$$

It is seen that for typical conditions background shot noise and Johnson noise are the dominant noise sources. Adding the NEP values, the incoherent system NEP is roughly 8.3×10^{-11} W or more than three orders of magnitude greater than the NEP in a signal shot noise-limited heterodyne system. This translates directly into much poorer mean power measurement sensitivity when uncertainties resulting from a fluc-tuating signal are small. In atmospheric DIAL measurements, however, the instantaneous irradiance is nearly always a random process whose fluctuations dominate the variance, hence this apparent 3 order-of-magnitude heterodyne sensitivity advantage is rarely realized.

3. Power Measurement Uncertainties in the Absence of Turbulence

The combined effects of speckle-induced signal fluctuations and detection noise on power measurements are now examined. Consider a heterodyne system operating in a nonturbulent environment, such that power-measurement uncertainties are caused by speckle and detection noise effects only. Because of the complexity of spatial averaging, it is assumed that only a single detector is employed. A typical configuration for estimation of the received power is shown in Fig. 3-1. The amplitude of the received field, $|\vec{E}_r(t)|$ is a Rayleigh-distributed random process modulating a sinusoid of frequency ν_d, where ν_d is the difference frequency between the received signal and the local oscillator. During detection, shot noise is added to $\vec{E}_r(t)$; this noise component can be modeled as white Gaussian noise. The detector output is band-pass filtered and fed into a complex demodulator, which removes any frequency shift due to local oscillator offset to produce the estimate of average received power. The resulting quadrature outputs are squared, summed, and low-pass filtered.

For power estimation, a complex demodulator has an advantage over a demodulator that produces only a single quadrature component in that it enables a power estimate to be made instantaneously, regardless of the frequency variation in the received signal. With a single component, the output has to be averaged over a number of cycles to accurately estimate the mean power. In the absence of the low-pass filter the single component square-law detector produces a mean power
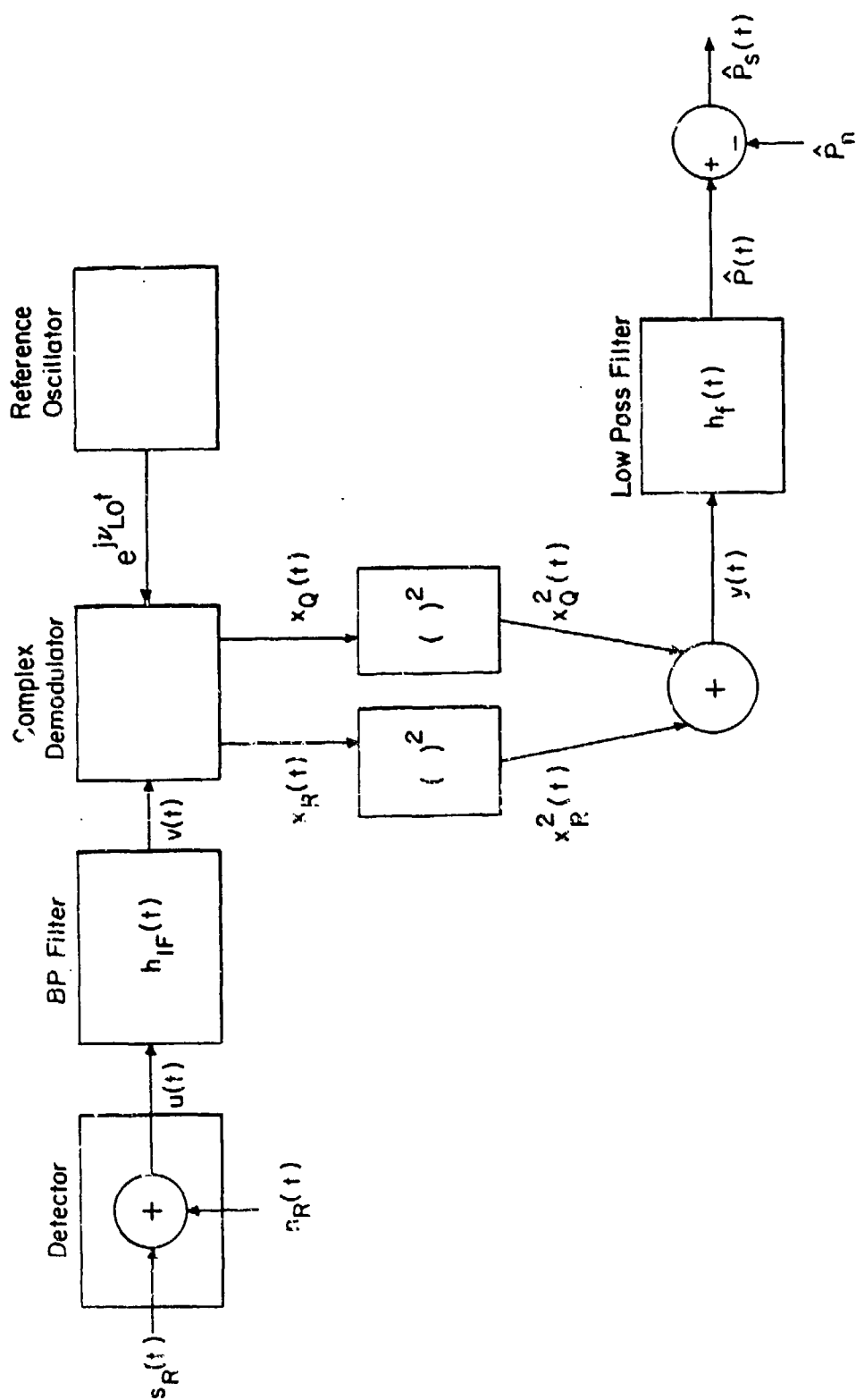
Fig. 3-1 — Schematic of heterodyne receiver optical power estimator.

72

estimate of a time-varying Rayleigh process which has twice the variance of the comparable estimate using both quadrature components. When the square law detector output is low-pass filtered, the normalized variance of the single component estimate is identical to that of the quadrature component estimate.

The estimate of received signal power, $\hat{P}_s$, is equal to the integrator power output, $\hat{P}$, less the estimated mean noise power $\bar{P}_n$, determined by observing $\hat{P}$ in the absence of signal. It can be shown (Appendix A) that at the output of the integrator, the normalized variance of the estimate for a single pulse is

$$\frac{\sigma_{\hat{P}_s}^2}{\langle \hat{P}_s \rangle^2} = \frac{1}{m_s} + \frac{1}{m_n}\left[\frac{1}{CNR}\right]^2 + \frac{2}{m_c CNR} \qquad (3.24)$$

where

$$m_s = \int_{-\infty}^{\infty} R_f(\tau)d\tau / \int_{-\infty}^{\infty} R_s'^2(\tau)R_f(\tau) \qquad (3.25)$$

$$m_n = \int_{-\infty}^{\infty} R_f(\tau)d\tau / \int_{-\infty}^{\infty} R_n'^2(\tau)R_f(\tau)d\tau, \quad \text{and}$$

$$m_c = \int_{-\infty}^{\infty} R_f(\tau)d\tau / \int_{-\infty}^{\infty} R_s'(\tau)R_n'(\tau)R_f(\tau)d\tau$$

are the equivalent number of independent samples of the signal, noise, and cross (multiplicative signal and noise) components, respectively, over the filter response time; CNR is the average signal-to-noise ratio

73

at the output of the bandpass filter, $R_s'(\tau)$ and $R_n'(\tau)$ are the normalized autocorrelation functions of the inphase signal and noise waveforms following the demodulator, and $R_f(\tau)$ is the autocorrelation function of the lowpass filter impulse response $h_f(t)$, given by

$$R_f(\tau) = \int_{-\infty}^{\infty} h_f(t) \, h_f(t+\tau) \, dt \; . \tag{3.26}$$

The smoothing filter h_f smoothes the fluctuations in the power estimate $z(t)$. The response of h_f is chosen to provide maximum smoothing while still achieving the desired range response. A simple smoothing filter often used is a running average, where

$$h_f(t) = 1/T, \; 0 < \tau < T$$
$$0 \text{ otherwise.} \tag{3.27}$$

The autocorrelation function for this filter is

$$R_f(\tau) = 1 - |\tau|/T \qquad |\tau| < T$$
$$0 \qquad |\tau| > T \; . \tag{3.28}$$

A running-average type smoothing filter shall be employed in most of the subsequent analyses.

It can be seen from Eq. (3.24) that the variance in the power estimate is due to a signal fluctuation term, a detection noise fluctuation term, and a noise cross signal term resulting from the nonlinearity of the square-law detector. The terms m_s, m_n, and m_c are

74

equivalent to the number of independent samples of the fluctuating noise terms over a filter response interval. By decreasing the bind- width of the smoothing filter, thereby increasing the response time constant, more independent samples are obtained and normalized variance is reduced. The trade-off is a reduction in system range resolution, since the slower filter cannot respond to rapid changes in signal vs. range. An increase in the equivalent number of independent samples also comes about by increasing the bandwidth of the fluctuation terms, i.e., producing more fluctuations per unit time. Received signal band- width can be increased by increasing the bandwidth of the transmitted pulse, either by shortening the pulse duration or chirping the pulse. Since a broader signal bandwidth necessitates a wider matched IF filter, the signal.fluctuation noise term is reduced at the expense of the CNR (detection noise) term in Eq. (3.24).

The CNR in Eq. (3.24) for a heterodyne system in the absence of turbulence with bandwidth matched to the pulse duration is calculated from [85]

$$CNR = \frac{\pi F \eta J \beta c \tau_p D^2 e^{-2\bar{\gamma}R}}{8h\nu R^2} \tag{3.29}$$

where J is the transmit energy, F is the beam shape compensation fac- tor, η is the overall system efficiency, β is the backscattering coef- ficient, c is the speed of light, τ_p is the pulse duration, D is the diameter of the transmit/receive optics, $\bar{\gamma}_p$ is average path absorption coefficient, R is the range, $h\nu$ is the photon energy, and the effects

of atmospheric turbulence are neglected. Equation (3.29) is valid for a system with the telescope focused at range R or for a collimated beam in the far field.

Heterodyne lidar systems used primarily for measurements of Doppler shift are typically designed such that the transmit pulse duration is equivalent in time to the desired range resolution, i.e., $\tau_\rho = 2\Delta R/c$, and chirping in the signal is minimized. This is the maximum CNR case. When CNR is high, however, this is generally not the minimum power estimate variance (maximum SNR) case. Since signal correlation time is roughly equivalent to range resolution, $m_s = m_n = m_c = 1$ in Eq. (3.24) for a matched IF filter. Thus the first term in Eq. (3.24) is unity. Since this term dominates the normalized variance expression at high CNR, little improvement is gained by increasing CNR.

Under this condition the estimate normalized variance can be decreased by widening the signal bandwidth. This has the effect of increasing the number of independent samples of m_s, m_n, and m_c within the smoothing filter response time. The cost one incurs for this adjustment is the previously mentioned decrease in CNR which comes about because of the necessary widening of the receiver bandwidth. To illustrate this tradeoff, consider the following simplified example. Assume the bandpass filter in Fig. 3-1 has a Gaussian-shaped autocorrelation function. If the filter is roughly matched to signal bandwidth, then both signal and detection noise spectra equal the filter response and

76

$$R_s(\tau) = R_n(\tau) = e^{-\tau^2/4\tau_p^2} \ . \tag{3.30}$$

Assuming a Gaussian shaped smoothing filter

$$m_s = m_n = m_c = \frac{1}{T} \ \frac{\int_{-\infty}^{\infty} R_f(\tau)d\tau}{\int_{-\infty}^{\infty} e^{-\tau^2/4\tau_p^2} R_f(\tau)d\tau} \tag{3.31}$$

where

$$R_f(\tau) = e^{-\tau^2/4\tau_f^2} \ .$$

Thus

$$m_s = m_n = m_c = \frac{\int_{-\infty}^{\infty} e^{-\tau^2/4\tau_f^2} \ d\tau}{\int_{-\infty}^{\infty} e^{-\tau^2(4\tau_f^2 + 4\tau_p^2)/16\tau_f^2 \tau_p^2} \ d\tau} \tag{3.32}$$

$$= \frac{(\tau_f^2 + \tau_p^2)^{1/2}}{\tau_p} \tag{3.33}$$

and the carrier to noise ratio is given by

77

$$CNR = CNR_o (\frac{\tau_p}{\tau_f})$$

where CNR_o is the carrier to noise ratio where $\tau_p = \tau_f$, i.e., signal bandwidth matched to range resolution.

The equation for the normalized variance is

$$\frac{\sigma_{\hat{P}}^2}{\langle \hat{P} \rangle^2} = \frac{\tau_p}{(\tau_f^2 + \tau_p^2)^{1/2}} [1 + \frac{2\tau_f}{\tau_p \, CNR_o} + \frac{\tau_f^2}{\tau_p^2 \, CNR_o^2}] \quad . \qquad (3.34)$$

Defining r_f as the ratio τ_b/τ_p (equivalent to B_p/B_f where B_f is equivalent bandwidth), Eq. (3.34) becomes

$$\frac{\sigma_{\hat{P}}^2}{\langle \hat{P} \rangle^2} = \frac{1}{(1+r_f^2)^{1/2}} [1 + \frac{2r_f}{CNR_o} + \frac{r_f^2}{CNR_o^2}] \quad . \qquad (3.35)$$

By differentiating the right hand side of Eq. (3.35) and setting the derivative equal to zero, we can find $r_{f_{opt}}$, the ratio τ_f/τ_p which minimizes the normalized variance. The optimal ratio $r_{f_{opt}}$ is a root of the cubic equation

$$4K r_{f_{opt}}^3 + (4K-K^2) \, r_{f_{opt}}^2 + (4K^2-2K) \, r_{f_{opt}} + 4K-1 = 0 \qquad (3.36)$$

where $K = 1/CNR_o$. Equation (3.36) can be solved analytically using a published formula for roots of a cubic equation. The minimum achievable normalized variance is found by substituting $r_{f_{opt}}$ in Eq. (3.35).

Figure 3-2 shows a plot of the optimum ratio $r_{f_{opt}}$ versus CNR_o. When $CNR \gg 1$, $r_{f_{opt}}$ is approximately equal to CNR_o; i.e., the minimum variance is achieved when CNR is reduced to 1 by widening the pulse bandwidth. When $CNR < 1$, R_{opt} approaches 1, implying that no additional improvement can be gained over the matched receiver. Since in this regime the detection noise is the dominant source of error, the system parameter choice which minimizes the detection noise-related uncertainties is preferred. This is, of course, the matched filter.

Also plotted in Fig. 3-2 is the measurement error that results when the pulse duration is shortened to the optimum length. Every 2 dB increase in CNR_o can be "traded off" for speckle noise reduction to bring about a 1 dB improvement in measurement accuracy. Thus, if the bandwidth of a heterodyne system is adjustable, increasing the transmit energy in order to increase CNR_o is worthwhile as long as the optimum pulse bandwidth can also be obtained without degrading other aspects of the system.

When the ratio B_p/B_f is limited by design considerations the effect on measurement capability can be determined from Fig. 3-2. For example, suppose the smallest pulse length attainable is 1/10 the original pulse length, i.e., $B_p/B_f = 10$. This length is optimum for an CNR_o of approximately 10 dB, producing a power measurement error of about 0.45. Any additional increase in CNR_o has little effect on measurement capability, since the pulse cannot be shortened to its optimum duration. Thus 0.45, less about 1.25 dB, is the best measure-
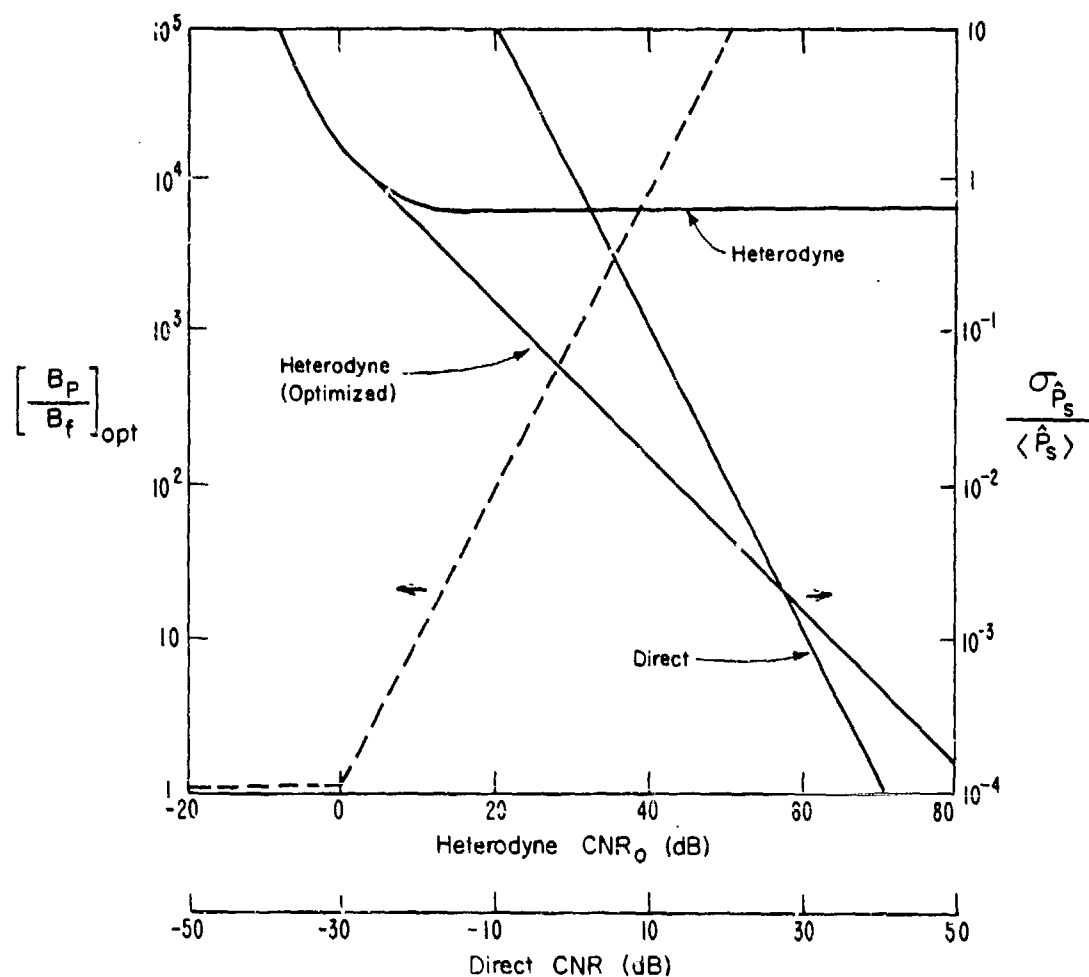
79

Fig. 3-2 — Optimum ratio B_p/B_f versus CNR_o, where CNR_o is carrier-to-noise ratio when $B_p = B_f$. Also plotted are heterodyne single-pulse measurement error for $B_p/B_f = 1$ and B_p/B_f optimized, and direct detection measurement error assuming heterodyne gain = 30 dB.

80

ment the system can make. The limit on pulse duration provides a design criterion for the system. There is no advantage in increasing the transmit energy or receiver optics beyond the value necessary to produce 10 dB of CNR_o.

In contrast, increasing the transmit signal bandwidth for direct detection systems to reduce speckle effects does not necessarily reduce CNR. The basic model of Fig. 3-3 is employed to illustrate this point. Since the detector output current is proportional to incident irradiance, the signal is simply filtered to reduce noise and average speckle. The normalized variance is calculated in Appendix B as

$$\frac{\sigma_{\hat{P}}^2}{\langle \hat{P} \rangle^2} = \frac{1}{m_t m_a} + \frac{1}{CNR^2} \tag{3.37}$$

where m_a and m_t are the number of independent spatial and temporal modes during the filter response time and CNR is the direct-detection voltage carrier-to-noise ratio. The number of temporal modes m_t is

$$m_t = \frac{\displaystyle\int_{-\infty}^{\infty} R_f(\tau)d\tau}{\displaystyle\int_{-\infty}^{\infty} B_I'(\tau)R_f(\tau)d\tau} \tag{3.38}$$

where B_I' is the normalized temporal autocovariance of the optical field intensity due to signal at a point in space and $R_f(\tau)$ is the filter autocorrelation function as defined previously. Similarly, the number of spatial modes is
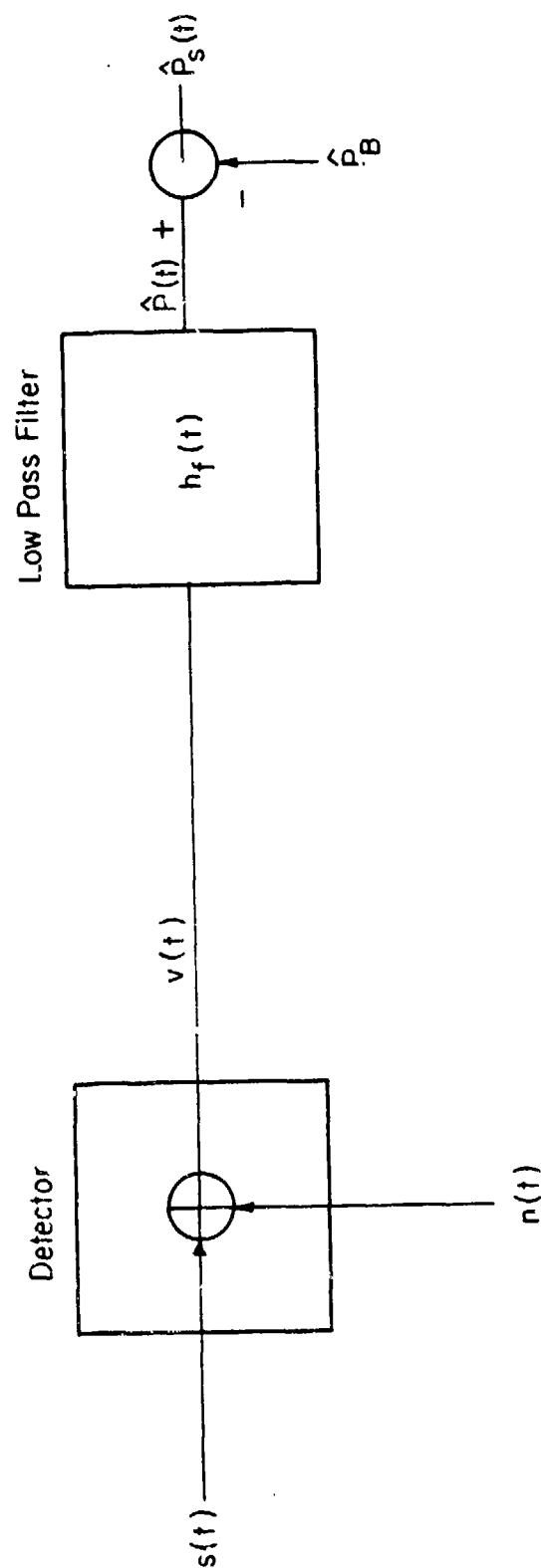
Fig. 3-3 – Schematic of direct detection receiver optical power estimator.

32

$$m_a = \frac{\int rw(r)d^2r}{\int J'_s(r)R_w(r)d^2r} \,. \tag{3.39}$$

Here $J'_s(r)$ is the normalized spatial mutual intensity function across the receiver aperture $w(r)$ is the aperture weighting function, and $R_w(r)$ is its autocorrelation.

The CNR is

$$CNR = \frac{I_s}{NEP} \tag{3.40}$$

where I_s is the optical intensity due to signal and NEP must be calculated by taking into account the various sources of noise discussed in Part 2.

It is seen from Eq. (3.37) that the normalized variance contains a speckle-induced fluctuation term and a general additive noise term which includes thermal, background and shot noise. There is no cross term as in the heterodyne case. The effect of speckle averaging can be illustrated with a simple analogous example to that put forth for heterodyne detection. Our discussion follows an example given by Gardner [86]. Assume that the temporal autocovariance function, spatial mutual intensity function, receiver weighting function, and filter response function are all Gaussian such that

$$J_s'(r) = e^{-r^2/2\rho_c^2}$$

$$B_I'(\tau) = e^{-\tau^2/\tau_c^2} \tag{3.41}$$

$$h_f(\tau) = e^{-B^2 t^2}$$

$$W(r) = e^{-r^2/R^2}$$

where

ρ_c = transverse spatial coherence length of signal

τ_c = coherence time of signal

B_f = receiver bandwidth

R = receiver aperture radius.

Then, from Eqs. (3.38) and (3.39)

$$m_a = 1 + \frac{R^2}{\rho_c^2}$$

$$m_t = [1 + \frac{1}{B_f^2 \tau_c^2}]^{1/2} . \tag{3.42}$$

Note that the expression for m_t is identical to that derived in Eq. (3.33). As discussed previously, to minimize speckle, it is desirable to increase m_a and m_t. Since receiver bandwidth B_f is determined by the required range resolution, m is increased by reducing τ_c, the temporal correlation time of the backscattered intensity. For pulse durations less than ~1 μs, the temporal correlation time due to

pulse bandwidth is much less than that due to scatterer motion, thus it is the dominant parameter for determination of the signal correlation time. Shortening the pulse decreases the speckle fluctuations without affecting CNR as long as peak power is correspondingly increased to maintain constant energy. Obviously there are practical limitations to this approach, and at some point shortening the pulse duration will begin to decrease the CNR.

The transverse correlation length ρ_c is a function of the transmitter field of view such that

$$\rho_c = \frac{\lambda}{\theta_t} \qquad (3.43)$$

where θ_t is the beam divergence from the transmitter. If the transmitter is operating at the diffraction-limited divergence, then

$$\theta_t \sim \frac{\lambda}{a} \qquad (3.44)$$

where a is the transmitter aperture radius. In diffraction limited, monostatic operation $m_a \approx 2$. To increase m_a, the transmitter field of view is increased; however the receiver FOV must also be increased such that the entire scattering volume can be observed. This increases background power and background shot noise. If background shot noise is the dominant noise source, the situation is identical to the hetero-dyne case, where speckle and CNR fluctuation terms are directly traded off. When background noise is negligible, the transmitter field-of-view can be increased without cost to CNR until the background shot noise becomes significant.

85

For a simple comparison with heterodyne system power measurement capability, the speckle fluctuations are assumed to be negligible in Eq. (3.37), and the normalized variance of a single-pulse incoherent measurement is plotted in Fig. 3-2 versus heterodyne CNR_o. The assumed heterodyne gain is 30 dB. We see that in situations where direct-detection CNR exceeds 0 dB, direct detection systems are superior to non-optimal heterodyne systems. When a fully optimized heterodyne system is employed, it is superior to a direct detection system for CNR_{het} < 50 dB (CNR_{dir} < 20 dB). It can be seen from Fig. 3-2 that the direct detection normalized variance reduces as the square of the CNR, compared with a linear relationship with CNR_o in the optimized heterodyne case. This is because some of the increased CNR_o is traded off for speckle noise reduction in the optimal case.

4. Refractive Turbulence Effects

In this section the effects of refractive-index turbulence on DIAL measurements are discussed. The general subject of optical system performance in the turbulent atmosphere has received much attention in recent years due to the potential applications of such systems in remote sensing, target ranging and imaging, and high data rate communications.

Turbulence is manifested as random patches of refractive-index variations in the free atmosphere. Although both the absorptive, or imaginary, part and dispersive (real) part of the refractive index

86

vary, the effects of fluctuation in the imaginary part are small in comparison with those of the real part and can generally be neglected [87]. At optical wavelengths, the fluctuations in the real part of the refractive index are due to atmospheric temperature variations. For clear air turbulence it is generally reasonable to assume that the temporal variations in refractive index at a point result from advection of the spatial refractive index field by atmospheric winds [88], i.e., Taylor's frozen-flow hypothesis is valid in most situations.

Physically, the effect of medium refractive index variations on a propagating optical wave is to produce random fluctuations along the wavefront. These fluctuations produce intensity scintillation further along the propagation path due to interference effects. The overall effect is a function of the relative size of the inhomogeneity (often referred to as a turbulent eddy). When the turbulent eddy size is less than $\sqrt{\lambda L}$ where L is the propagation path length, the primary mechanism contributing to scintillation is diffraction. For larger eddies, refraction is the dominant scintillation-producing process. Clifford [87] has shown that eddies of size $\sqrt{\lambda L}$ are the "most effective" in producing scintillations.

The turbulent atmosphere contains refractive index variations of all sizes. The most widely used model of the distributor of the turbulent eddy scale sizes in the atmosphere is that developed by Kolmogorov [89], which models the mean-squared difference in the refractive indexes at points r_1 and r_2 as

$$\langle[n(r_1) - n(r_2)]\rangle^2 = C_n^2 |r_2 - r_1|^{2/3}, \qquad \ell_o \ll |r_1 - r_2| \ll L_o$$

$$= D_n(r) \tag{3.45}$$

where ℓ_o and L_c are called the inner and outer scales of turbulence, C_n is the refractive index structure constant, and the angular brackets denote ensemble average. In the atmosphere ℓ_o is of the order of a few millimeters to a centimeter and, in the lower troposphere, L_o is of the order of the height above the ground. The structure parameter C_n^2 is a measure of turbulence; values range from $10^{-12} \, \bar{m}^{2/3}$ near the ground to $10^{-17} \, \bar{m}^{2/3}$ in the free troposphere. For turbulent eddy sizes of characteristic length ℓ, such that $\ell_o \ll \ell \ll L_o$, the Kolmogorov 2/3 law implies that the mean square fluctuation associated with the scale size increases as the 2/3 power of the scale size.

When Taylor's hypothesis is valid, the time scale of fluctuations in signal irradiance due to the turbulence is roughly equivalent to the time required for the most effective eddy to move one diameter transverse to the path or [90], i.e.,

$$\tau_t \approx \frac{\sqrt{\lambda L}}{v_c} \tag{3.46}$$

where v_c is the mean crosswind and L is the distance between transmitter and receiver. For typical values of L and v_c, τ_t is on the order of tens of milliseconds. Thus, the atmosphere is effectively frozen during the round trip travel time for a pulse in a representative lidar system (round trip time $\approx$ 200 μs for 30 km range). Note

also that the turbulence time scale is 3 orders of magnitude larger than the speckle time scale.

Physically, turbulence affects lidar systems on both transmit and receive paths. On the outward path, the refractive index fluctuations produce a phase decoherence along the propagating wavefront. The net effect of this decoherence is to reduce the effective transmit aperture diameter, causing an enlargement in the diameter of the irradiated spot at the atmospheric target. The degree of beam spreading is related to the plane-wave phase coherence length ρ_o, where

$$\rho_o = [1.46 \frac{k^2}{z} \int_0^1 dt \ C_n^2(t) \ t^{5/3} \ dt]^{-3/5} \tag{3.47}$$

In Eq. (3.47) $k = 2\pi/\lambda$, z is path length to the scattering volume, and $t = 0$ at the scattering volume and 1 at the transmitter. By definition ρ_o is the distance in the receiver plane at which the expected mutual coherence function is reduced by $1/e$. When transmit diameter D is much smaller than ρ_o, very little spreading occurs; however when $\rho_o \ll D$, beam spreading can be significant. Equation 3.47 can be used to compute ρ_o versus pathlength for various degrees of turbulence, assuming 10.6 μm radiation. Results are shown in Table 3.1. It is seen that when turbulence is strong (i.e., $C_n^2 > 10^{-13} \ m^{-2/3}$), lateral coherence is reduced to a scale comparable to that of a typical receiver aperture over distances as short as a few hundred meters. In weaker turbulence ($C_n^2 < 10^{-15} \ m^{-2/3}$), ρ_o remains greater than half a meter or so for distances approaching 10 km. Typically values of C_n^2 as high as 10^{-13}

89

$m^{-2/3}$ are present only when an extended portion of the path lies just above the ground. When turbulence is not uniform along the path, it is seen from Eq. (3.46) that turbulence nearer the lidar is weighted more heavily.

Table 3.1. Computed values of plane-wave coherence length ρ_o versus pathlength and turbulence structure parameter, assuming constant turbulence along the path and 10.6 μm radiation.

		C_n^2 ($m^{-2/3}$)				
		10^{-12}	10^{-13}	10^{-14}	10^{-15}	10^{-16}
	100	.17	.67	2.7	11.	43.
z(m)	500	.065	.26	1.0	4.1	16.
	1000	.0425	.17	.67	2.7	11.
	5000	.016	.065	.26	1.0	4.1
	10000	.011	.043	.17	.67	2.7

For heterodyne lidar systems a larger spot size at the target causes a reduction in CNR at the receiver relative to the diffraction-limited value, since by the Van Cittert-Zernicke theorem the transverse coherence across the receiver aperture is reduced. Received signal coherence is further reduced as the backscattered signal encounters the turbulence on its return trip, producing additional CNR degradation. As in the speckle case, reduction in lateral coherence at the receiver has very little effect on the CNR of direct detection lidars when receiver aperture is sufficiently large.

Since turbulent eddies tend to focus and defocus the propagating optical energy, turbulence on the transmit path produces scintillation in the irradiance at the target. When the turbulence is weak, such that ρ_o is large, the scintillation effectively modulates the irradiance across the entire target spot. This produces an additional temporal variation in received irradiance on top of any fluctuation resulting from speckle. At the other extreme, when turbulence is strong, the scale size of the individual spatial irradiance fluctuations is smaller. Under these conditions $\rho_o \ll D$, so that the fields of view of both transmitter and receiver are expanded. For sufficiently strong turbulence the receiver cannot resolve the spatial variations in irradiance at the target, hence the variations are effectively averaged out. In strong turbulence the field at the target is analogous to the speckle case even when the target is specular, since the backscattered field is incoherent across the receiver field of view. Because no lensing of the spatially incoherent field occurs, scintillations in the limit of strong turbulence have the identical ensemble characteristics as in the speckle only case.

In weak turbulence, the amplitude of the intensity of the incident field at a point has been predicted and experimentally verified to be lognormally distributed. In this regime the variance of the log amplitude is given by

$$\sigma_\chi^2 = 0.56 \ k^{7/6} \int_o^L dz \ C_n^2(z) \ (z/L)^{5/6} \ (L-z)^{5/6} \qquad (3.48)$$

which reduces to $\sigma_\chi^2 = 0.124 \ C_n^2 \ k^{7/6} \ L^{11/6}$ for uniform C_n^2. The weak turbulence regime is defined as that in which σ_χ^2 is predicted by Eq. (3.48). Experimental data have shown that σ_χ^2 saturates at a value of approximately 0.5 in strong turbulence. This is the so-called saturation regime, where σ_χ^2 predicted by Eq. (3.48) is greater than 0.5. Here the statistics deviate widely from lognormal. A number of mathematical models have been proposed to fit observed data in this regime; the most useful is probably the K distribution since it fits many of the data [91]. Table 3.2 lists σ_χ^2 calculated from Eq. (3.48) vs. propagation path length and strength of turbulence, assuming constant turbulence along the path and 10.6 μm radiation. Note that σ_χ^2 approaches the saturation value only when turbulence is extremely high ($C_n^2 > 10^{-13} \ m^{-2/3}$) for path lengths on the order of 5 km. In general, such large values of C_n^2 would exist along 1 km paths only when the path is very close to the ground (i.e., within the surface layer) over its entire length.

92

Table 3.2. Log amplitude variance σ_χ^2 calculated from Eq. (3.46) versus pathlength and turbulence strength, assuming constant turbulence along the path and 10.6 μm radiation. Asterisks indicate regions where observed value will saturate at approximately 0.5.

L (meters)	C_n^2 (m$^{-2/3}$)				
	10^{-12}	10^{-13}	10^{-14}	10^{-15}	10^{-16}
100	3.1×10^{-3}	3.1×10^{-4}	3.1×10^{-5}	3.1×10^{-6}	3.1×10^{-7}
500	6.0×10^{-2}	6.0×10^{-3}	6.0×10^{-4}	6.0×10^{-5}	6.0×10^{-6}
1000	2.1×10^{-1}	2.1×10^{-2}	2.1×10^{-3}	2.1×10^{-4}	2.1×10^{-5}
5000	4.1*	4.1×10^{-1}	4.1×10^{-2}	4.1×10^{-3}	4.1×10^{-4}
10000	14.5*	1.45*	1.45×10^{-1}	1.45×10^{-2}	1.45×10^{-3}

The preceding phenomenological discussion illustrates that atmospheric turbulence degrades the anticipated performance of a coherent DIAL system in two basic fashions: 1) scintillations increase the normalized variance of the backscattered signal such that the SNR of the average irradiance estimate is decreased, and 2) decoherence effects tend to reduce CNR, which also reduces measurement SNR by enhancing the effects of detection noise. This uncertainty introduced into the power measurements by turbulence necessitates a modification of the uncertainty expressions developed in Part 3. The single-shot heterodyne lidar error expression for a distributed target becomes

93

$$\frac{\sigma_{\hat{P}}^2}{\langle\hat{P}\rangle^2} = \gamma + \frac{1}{m_s} + \frac{1}{m_n}\left[\frac{1}{F \times CNR_o}\right]^2 + \frac{2}{m_c}\left[\frac{1}{F \times CNR_o}\right] \tag{3.49}$$

where γ is the additional scintillation variance due to the turbulence, CNR_o is the carrier to noise ratio when no turbulence exists, F is a factor accounting for the reduction in CNR due to turbulence, and m_s, m_n and m_c are as defined previously. Since turbulence is frozen over the time scale of a pulse, no intrapulse averaging occurs in the turbulence fluctuation term γ.

Estimation of the heterodyne CNR reduction factor F in Eq. (3.49) was initially addressed by Murty [92] and Thomson and Dorian [93]. Their approaches, which invoked the modified Huygens-Fresnel principle, assumed that the turbulence encountered by the incoming and outgoing wave was independent, and that the phase structure function could be approximated by a quadratic. Under these assumptions, Murty calculated the CNR reduction factor F to be

$$F = \frac{1}{1 + (\frac{D}{r_a})^2} \tag{3.49}$$

where $r_a \approx 1.5\ \rho_o$ is the transverse correlation length defined by Fried and Myers [94]. In 1980 Wandzura [95] showed that use of a quadratic structure function in essence takes into account only those perturbations due to wavefront tilt. Based on this rather significant observation, Clifford and Wandzura [96] reexamined the problem using the appropriate structure function. Their results showed that when the

94

assumption of a quadratic structure function was employed in a calcula-
tion where the assumed dependence between transmit and receive paths
was included, no effect due to turbulence was predicted. When both of
the previous assumptions were dropped, the predicted degradation in CNR
due to turbulence was less than in the previous calculations.

Results of Clifford and Wandzura's calculations as well as results
obtained assuming a quadratic struct e function are shown in Fig. 3-4,
versus Fresnel number Ω, where $\Omega^2 = [kD^2/4(f^{-1} - Z^{-1})]^2$, and f is focal
distance. The abscissa varies with $N_0 = D/\rho_0$, the number of coherent
spots across the aperture, while the ordinant represents the CNR reduc-
tion factor F. If we assume $D_0 = 0.3$ m and $Z = 10$ km in Fig. 3-4, the
curves correspond to CNR reduction vs. C_n^2 for returns from 10 km for
beams focused at 770 m, 2.5 km and 10 km. The appropriate values of
C_n^2 given this assumption are shown under the coordinate label. Note
that in some cases, increasing turbulence actually results in an
increase in CNR relative to the nonturbulent case for a collimated
beam. This is physically due to lensing effects of the turbulence.
Since the scintillation varies lognormally the effect of an intensity
increase due to a focusing eddy is more than that of an intensity
decrease. At higher levels of turbulence the scintillation saturates
and transmit beamspreading becomes a factor, serving to degrade the
CNR.

The effect of the turbulence on the intensity fluctuations from a
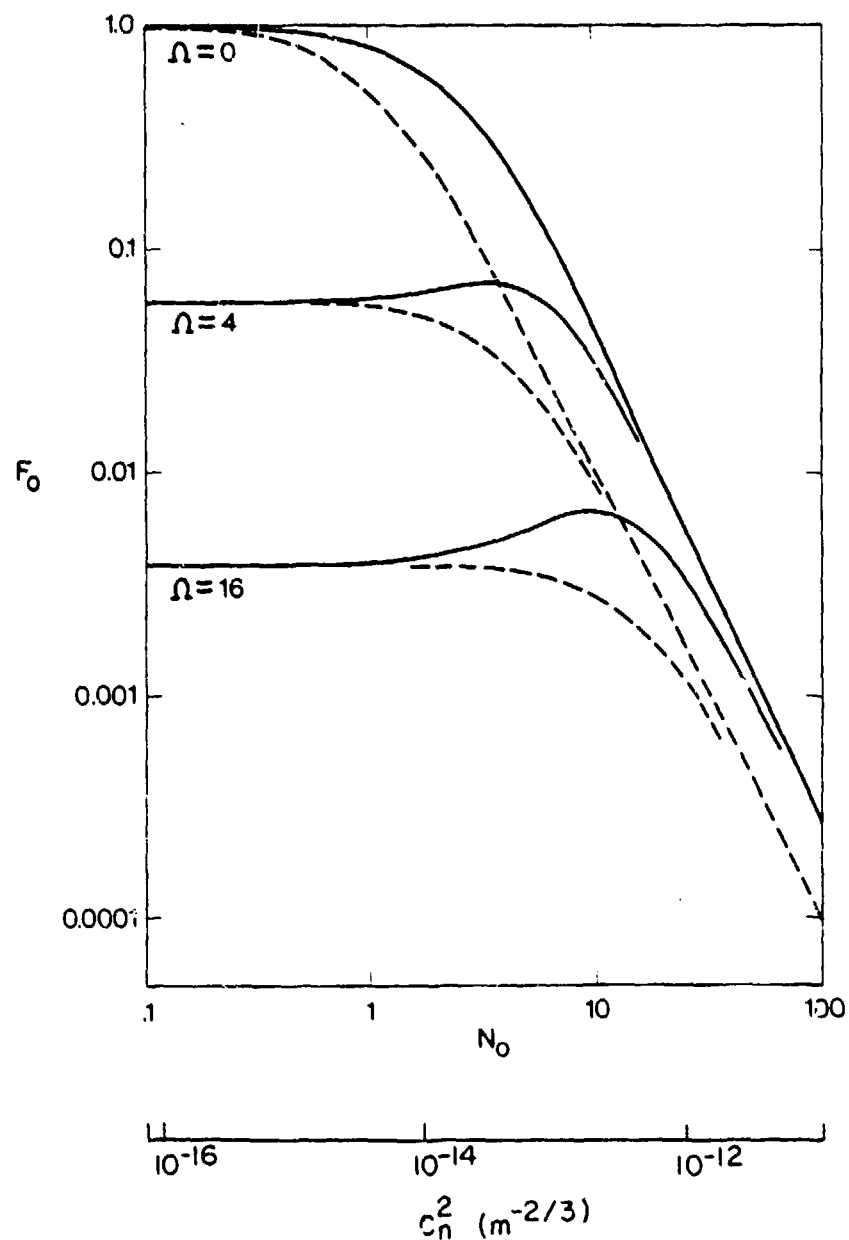speckled target ' is been examined by Holmes et al. [97], and Shapiro et

Fig. 3-4 - Reduction in heterodyne CNR versus $F_0 = D_0/\rho_0$ for original (dashed lines) and updated (solid lines) monostatic turbulence theory. Top trace applies to returns from focal volume; lower 2 traces pertain to returns from points increasingly separated from focus. Also plotted on abscissa are C_n^2 values for $D_0 = 0.3$ m, $Z = 10$ km. From Clifford and Wandzura[96].

96

al. [98]. Both analyzed the problem of a signal propagating through refractive turbulence, scattering off of an incoherent target, and returning through the same medium to the receiver. We will follow the derivation of Holmes et al., since Shapiro makes assumptions on weak turbulence which may not be valid at longer ranges. As previously discussed, most of the scintillation should be produced on the outward leg, since the randomization of the phase front upon scattering reduces the effectiveness of the eddies in producing scintillation on the return path. Holmes et al., derive the formula

$$\frac{\sigma_I^2}{\langle I \rangle} = (\frac{k}{2})^2 \int_{L_o}^{\infty} dr \; r \int d\rho\rho \; [2e^{4C_\chi(\rho)} - 1] \; J_o(k/L_o\rho r)f(r) \qquad (3.51)$$

where J_o is the zero order Bessel function of the first kind and C_χ is the log amplitude covariance function for a spherical wave propagating through turbulence.

The coordinates ρ and r in Eq. (3.51) describe the surface of the target and transmitter, and

$$f(r) = \exp\{-r^2[\frac{2}{D_o^2} + 2(\frac{kD_o}{4L})^2 \; (1 - L/f)^2 - (R/\rho_o)^{5/3}\} \; . \qquad (3.52)$$

In Eq. (3.52), R is transmitter telescope radius, f is focal length and ρ_o is turbulence-induced coherence length. Figure 3-5 shows the predicted scintillation in the return due to turbulence and speckle for a point receiver, assuming a focused beam, as a function of integrated turbulence along the path σ_χ^2, where σ_χ^2 was calculated from
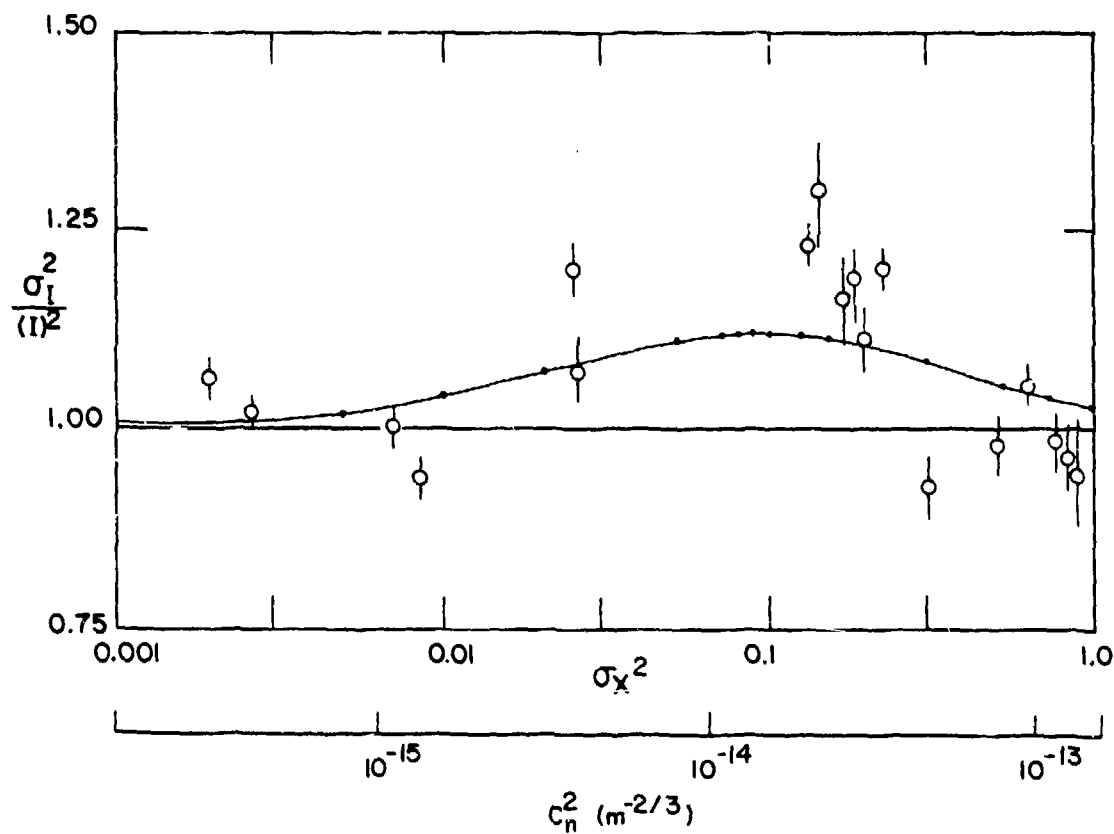
97

Fig. 3-5 – Predicted (dots) and measured (circles) increase in normalized variance of signal fluctuations from diffuse target versus integrated turbulence. Also plotted on abscissa are C_n^2 values computed for $Z = 10$ km. From [97].

Eq. (3.48). The abscissa is also calibrated as a function of C_n^2 computed for returns from a 10 km range. In the absence of turbulence ($\sigma_\chi^2 < .001$) the normalized variance of received power fluctuations, $\sigma_P^2 / \langle \hat{P} \rangle^2$, essentially is unity with the power exponentially distributed, as in the speckle-only case. When integrated turbulence is moderate ($\sigma_\chi^2 \approx .01$), the phase variations produced by the inhomogeneities result in irradiance scintillations at the scattering volume, which are seen in Fig. 3-5 to increase the received signal variance above the unity speckle value. Under these conditions the scintillations result from the speckle interference effects further amplified by the modulation of irradiance of the illuminating field.

Additional increases in turbulence beyond this point cause the irradiance scintillations at the scattering volume to further increase. However, the relatively strong turbulence also produces significant reduction in the transverse scale size of the irradiance fluctuations. Thus, the beam incident on the scattering volume has regions of high and low intensity with scale size $\sim \rho_0$. In strong turbulence these regions are decreased in size to the point where they cannot be resolved by the receiver, and source aperture averaging becomes important. The slope of the curve in Fig. 3-5 thus level off. At this point the fluctuations are becoming larger in magnitude and smaller in scale size.

With further increases in integrated turbulence, the aperture averaging effect dominates the irradiance fluctuations causing the normalized variance of fluctuations at the receiver to peak at a value of

99

approximately 1.25. At this peak in the normalized variance the received signal statistics are a combination of lognormal and exponential distribution. Any additional increase in turbulence along the path produces a decrease in normalized variance; the scintillation statistics eventually become exponentially distributed as in the nonturbulent case. This effect occurs for values of integrated turbulence below those which result in saturation of the scintillations.

Because the effects in Figs. 3-4 and 3-5 are both plotted as a function of C_n^2 for returns from 10 km, the two results can be compared. Examining the case in Fig. 3-4 where $f = 10$ km, which is most typical of long-range measurements, it is seen that the roll-off in CNR occurs in the region around $C_n^2 \sim 10^{-14}$ $m^{-2/3}$. Higher values of uniform turbulence produce sharp decreases in CNR, while lower values produce negligible effects. In Fig. 3-5 the effect of turbulence on signal fluctuation variance is seen to be maximized around the same point; i.e., $C_n^2 = 10^{-14}$ $m^{-2/3}$. In this case, however, both increasing and reducing turbulence lessens the effect, which at its worst adds 10-20% to the scintillation-induced variance. Such an effect should generally be negligible, except in cases where speckle effects dominate the power measurement error. Since generally CNR is the limiting factor determining sensitivity at longer ranges, the CNR reduction factor shown in Fig. 3-4 is potentially much more detrimental. Note, however, that a uniform C_n^2 value approaching 10^{-14} $m^{-2/3}$ over a 10 km path would typically exist only within horizontal paths a few meters above

100

the surface. The abscissa parameter N_o is directly proportional to optics diameter; therefore, increasing the system telescope increases its sensitivty to turbulence at longer ranges, as would be expected.

Since averaging or filtering is necessary to reduce power measurement SNR, the differences in relative time scales of the error components in Eq. (3. `` should also be noted. The CNR-based fluctuations caused by noise take place at a time scale inversely proportional to the noise bandwidth of the system. For a matched filter receiver this would be identical to the signal (speckle) bandwidth, although in many cases the noise bandwidth is larger than the signal bandwidth to account for Doppler shift in the signal. The bandwidth of the turbulence fluctuation term γ is at least 3 orders of magnitude smaller than the signal and noise bandwidth. Thus, if the system could be pulsed rapidly enough, many independent samples of speckle and noise could be obtained for a single equivalent turbulence sample. For high pulse-repetition-rate systems turbulence fluctuations, although smaller in magnitude than the other terms, may be the limiting parameter at longer ranges.

One method of reducing the sensitivity to turbulence is to transmit the two probing pulses at the absorbing and nonabsorbing wavelengths simultaneously. If the pulses are sufficiently close in frequency, the atmosphere will appear "frozen", and the scintillations of the two received intensities will be correlated. Because the covariance terms in Eq. (3.2) become nonzero, an improvement in the

101

overall measurement accuracy results. Kjelaas et al. [99] have exa-
mined the correlation of the two pulses as a function of both wave-
length and temporal separation assuming a Kolmogorov spectrum of
turbulence. They present expressions showing that the total variance
of the logarithmic differences in Eq. (3.1) decreases as the frequency
and temporal separation of the pulses are reduced. However, it should
be noted that simultaneous operation at the two wavelengths does not in
general reduce the portion of the uncertainty caused by speckle at CO_2
wavelengths. The speckle patterns produced by the absorbing and nonab-
sorbing wavelengths are usually independent, since the frequencies
typically differ by more than $2/\tau_p$, where τ_p is the pulse duration.
Thus, the reduction in the variance of the logarithmic difference in
Eq. (3.1) which can be realized by simultaneous operation is related to
the proportion of the total variance caused by turbulence and other
temporally-varying atmospheric parameters which are correlated between
the two wavelengths.

In an incoherent receiver, which is essentially a light bucket,
the average CNR is minimally affected by turbulence-induced loss of
coherence. Although the irradiance scintillations are still present,
their effects can often be reduced by receiver aperture averaging. The
number of independent samples of the scintillations which are averaged
at the detector is inversely proportional to the integral of the spa-
tial covariance function of intensity $C_\chi(\rho)$ across the receiver. In
weak or moderate turbulence the scale size of irradiance fluctuations
is on the order of a Fresnel zone $\sqrt{\lambda L}$ [87], such that the number of

102

independent spatial samples is approximately $(D/\sqrt{\lambda L})^2$. As turbulence increases, the spatial covariance function of the scintillations acquires a longer tail, as seen in Fig. 3.6. This tail diminishes the effectiveness of aperture averaging under strong turbulence conditions.

Taking into account the turbulence-induced scintillations, an expression equivalent to Eq. (3.49) for single-pulse direct detection power-measurement uncertainty is

$$\frac{\sigma_{\hat{P}}^2}{\langle\hat{P}\rangle^2} = \frac{1}{m_s}\left[\frac{1}{m_t m_f} + \gamma_d\right] + \frac{1}{[(CNR_o)]^2} \tag{3.53}$$

where all terms are as defined previously. Here m_s is the number of spatial samples of the irradiance fluctuations due to the combined effects of speckle and turbulence. Equation (3.53) assumes no temporal or frequency diversity in the turbulence scintillation term. The ineffectiveness of temporal diversity is obvious in that the turbulent time scale is much longer than the single-pulse observation window. Frequency diversity is also ineffective since turbulence-produced fluctuations at two different frequencies are highly correlated when the wavenumber ratio approaches unity [99], as it typically does for DIAL measurements. It is assumed in Eq. (3.52) that effects of turbulence on mean CNR are negligible and that the spatial averaging term is calculated from the expected scale size of the fluctuations at the receiver aperture due to both speckle and turbulence. If the system is
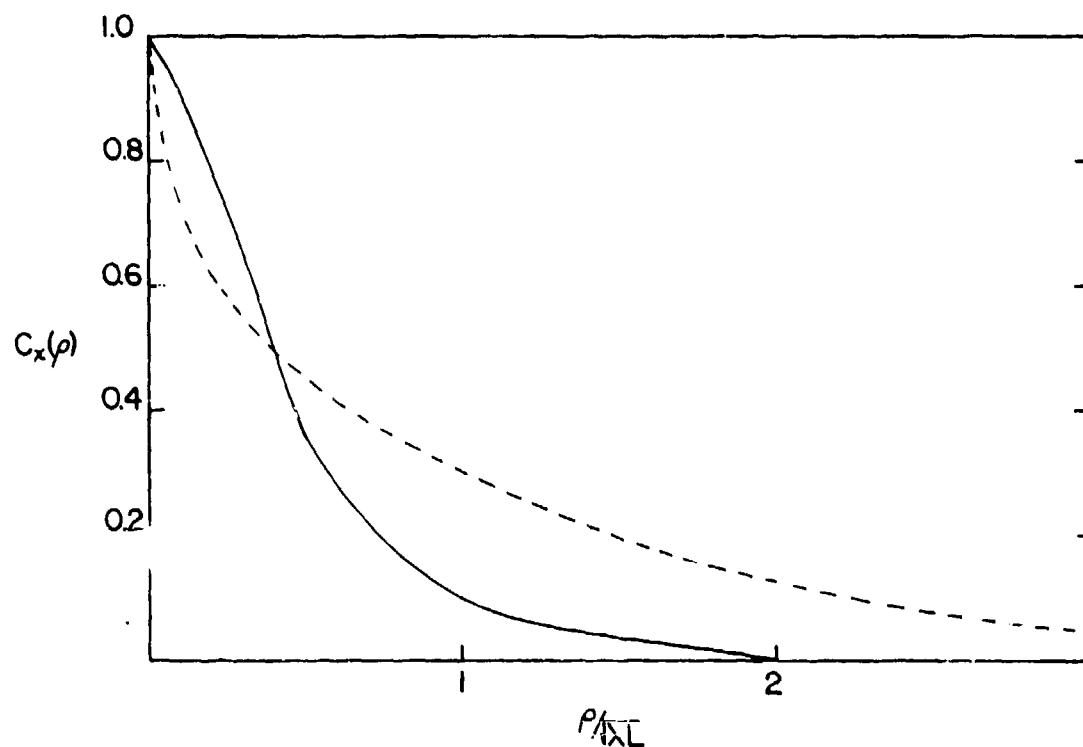
103

Fig. 3-6 - Normalized spatial log-amplitude covariance function for weak
(———) and strong (-----) scintillation versus spacing in Fresnel
zones. From Clifford [87].

designed so that receiver field of view is much greater than trans-
mitter field-of-view as would be the case when speckle reduction is a
primary concern, effective source averaging at the scattering volume
will tend to average out most irradiance fluctuations as the turbulence
increases. Hence γ_d approaches 0 and Eq. (3.52) reduces back to Eq.
(3.35), the nonturbulent case.

C. ABSORPTION COEFFICIENT UNCERTAINTIES

We now examine the absorption coefficient term $\sigma_{K_m}^2 / \langle K_m \rangle^2$, in Eq.
(3.2). The accuracy of the concentration measurement is limited by the
relative error in absorption coefficient uncertainty; that is, a 10%
error in the knowledge of K_m translates into a 10% error in the con-
centration measurement even if the backscattered power is estimated
perfectly.

It is assumed that most ground-based DIAL applications will be
limited to the lower or mid-troposphere. Thus, the absorption lines of
the various species will be pressure broadened with absorption coef-
ficients at frequency ν given by

$$K_\nu = \frac{S\alpha}{\pi(\nu-\nu_o)^2 + \alpha^2} \tag{3.54}$$

where S is the linestrength, ν_o is the line center frequency, and α is
the line width. Both S and α are temperature dependent, and α is also
pressure dependent. The linestrength is determined from [39] as

$$S = \frac{S_o Q_v(T_o)(T/T_o)^j}{Q_v(T)} \; \text{exp} \; \left\{ \frac{1.439 E''(T-T_o)}{T \, T_o} \right\} \tag{3.55}$$

where S_o is the linestrength at standard temperature, $Q_v(T)$ is the vibrational partition function, T is the temperature, T_o is the standard temperature (196 K), j is a parameter related to the temperature dependence of the rotational partition function, and E'' is the energy of the lower state of the transition resulting from the absorbed energy. Since ground-based measurements will be made in the troposphere, Doppler broadening effects can be neglected. Thus the half-width α is the collisional halfwidth α_c given by Gates et al. [100] as

$$\alpha_c = \alpha_{co}(p/p_o)(T_o/T)^d \tag{3.56}$$

where α_{co} is the collisional halfwidth at standard conditions, p is the pressure, p_o is the standard pressure, and d is a species- and transition-dependent parameter.

From Eqs. (3.54) through (3.56) it is seen that to determine K_v, the quantities S_o, α_{co}, ν, ν_o, j, d, T, p, Q_v, and E'' must be known. Inaccuracies in the specification of these parameters result in inaccuracies in K_v, and subsequently, in the concentration measurements. To estimate K_v, one would typically rely on published data for values of S_o, α_{co}, j, d, Q_v, and E''. Temperature and pressure at the measurement range R could be estimated from available meteorological data obtained either by radiosonde or satellite. Finally, the wavelength of the radiation, ν, is a function of the type of laser employed and its stability.

In addition to inaccuracies in the knowledge of pressure and temperature, some lack of precision in the determination of the species-dependent line parameters might also be expected. The effects of imprecise knowledge of S_o, α_{co}, $E"$, p, and T can be examined by expanding Eqs. (3.54) through (3.56) in differential form about the mean values of each of the parameters. Assuming that the fluctuations are uncorrelated with zero mean, this yields

$$\left(\frac{\delta K_\nu^2}{\bar{K}_\nu^2}\right) = \left(\frac{\delta S}{S}\right)^2 + \left(\frac{\pi\Delta\nu^2 - \bar{\alpha}_c^2}{\pi\Delta\nu^2 + \bar{\alpha}_c^2}\right)^2 \left(\frac{\delta\alpha_c}{\bar{\alpha}_c}\right)^2 \qquad (3.57)$$

where

$$\Delta\nu = \nu - \nu_o . \qquad (3.58)$$

$$\left(\frac{\delta\bar{\alpha}_c}{\bar{\alpha}_c}\right)^2 = \left(\frac{\delta\alpha_{co}}{\bar{\alpha}_{co}}\right)^2 + \left(\frac{\delta p}{\bar{p}}\right)^2 + d^2 \left(\frac{\delta T}{T}\right)^2 , \qquad (3.59)$$

$$\left(\frac{\delta S}{S}\right)^2 = \left(\frac{\delta S_o}{S_o}\right)^2 + (1.439E")^2 \left(\frac{1}{T} - \frac{1}{T_o}\right)^2 \left(\frac{\delta E"}{E"}\right) + \left(\frac{1.439\langle E"\rangle}{\bar{T}} - j\right)^2 \left(\frac{\delta T}{\bar{T}}\right)^2 , \qquad (3.60)$$

and the overbar denotes the mean value of the parameter.

Given the error in $E"$, S_o, α_{co}, T, or p, at each wavelength one can estimate the relative error in differential absorption coefficient $\sigma_{K_m}^2/\bar{K}_m^2$ from the above relationships. In general, errors in DIAL measurements due to inexact knowledge of the absorption coefficient parameters are systematic errors. That is, the error in the parameter will be approximately constant over the time scale of a measurement

107

(typically 5-10 minutes). Averaging of returns from pairs of pulses does not reduce the measurement error resulting from these effects.

One additional source of absorption coefficient errors for incoherent systems is the inexact knowledge of the distribution of the transmitted energy among the various possible longitudinal laser cavity modes. Ideally, if one knew this exactly, a weighted average $K_{m_{ave}}$ could be calculated from

$$\bar{K}_{\nu_{ave}} = \frac{\bar{K}_{\nu}(\nu_1)J(\nu_1) + \bar{K}_{\nu}(\nu_2)J(\nu_2) + \ldots + \bar{K}_{\nu}(\nu_n)J(\nu_n)}{\sum\limits_{n} E_i} \quad (3.61)$$

where $K_{\nu}(\nu_i)$ is calculated for the frequency ν_i as before, and $J(\nu_i)$ is the laser pulse energy at frequency ν_i. In general some uncertainty will be introduced by the unknown distribution of energy about the modes. The effect of this is a function of the total variation of K_{ν} over the range of frequencies $(\nu_n - \nu_1)$. Over flat regions of the absorption curve K_{ν}, (region A in Fig. 3-7) where $|dK_{\nu}/d\nu|$ is small, uncertainties in the distribution of energy will have less effect than at frequencies where K_{ν} changes more rapidly (region B in Fig. 3-7). In the previous section, the advantage of transmitting several longitudinal laser modes simultaneously (frequency diversity) for reducing instantaneous power fluctuations in incoherent systems has been shown. The accompanying potential increase in absorption coefficient uncertainty, however, limits the range of modes that one can reasonably expect to employ. This effect is examined numerically in the example of Sec. E.
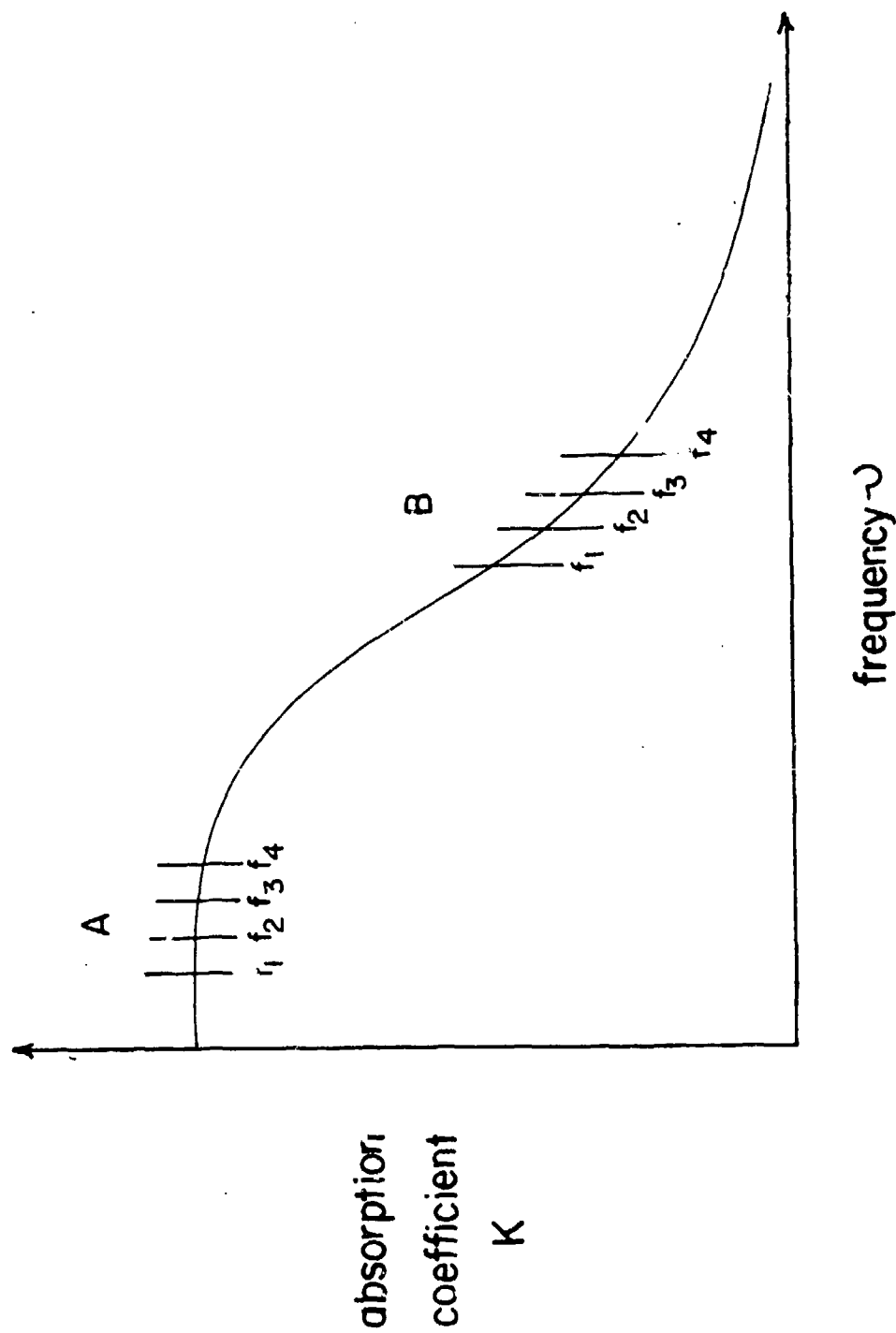
Fig. 3-7 – Longitudinal cavity modes superimposed on typical species absorption line. Uncertainties in distribution of the transmitted energy among the laser modes will have less effect on absorption cross-section uncertainty if the lasing line lies in region A as opposed to region B.

D. EFFECTS OF DIFFERENTIAL BACKSCATTER AND TRANSMISSION

A potentially significant source of error in DIAL measurements results when backscatter coefficient β and range-gate averaged background absorption coefficient $\overline{\gamma}$ differ for the on- and off-line measurements. The effect on the measurements can be seen in Eq. (3.1). Errors come about when backscatter coefficient varies as a function of wavelength, time, and/or range such that the B and T terms have random uncertainties associated with them. Note that errors only occur for non-predictable fluctuations in the parameters; differential effects do not in themselves cause an error if they can be accurately estimated.

The backscatter and background absorption error terms are calculated by expanding the expressions for B and T around their mean values to get

$$\sigma_B^{\;2} = \sum_{j=1}^{2} \sum_{i=1}^{2} \frac{\sigma_{\beta_{\nu_1 R_j}}}{<\beta_{\nu_1 R_j}>^2} \pm \text{cov terms} \tag{3.62}$$

and

$$\sigma_T^{\;2} = 4\Delta R^2 \left[\sigma_{\overline{\gamma}_{\nu_1}}^2 + \sigma_{\overline{\gamma}_{\nu_2}}^2 - 2 \, \text{cov}(\overline{\gamma}_{\nu_1} \, \overline{\gamma}_{\nu_2}) \right]$$

where ν_1 signifies the absorbed wavelength and ν_2 the non-absorbed wavelength, and the covariance terms are a function of time between the on-line and off-line measurements $t_1 = t_2$.

It is seen that the variance in the backscatter and transmission terms is a function of the variance in the terms for each individual measurement and the covariance between the terms. If fluctuations in β and γ were exactly correlated during the on-line and off-line measurements, the covariance terms would exactly cancel the variance terms and $\sigma_B^2 = \sigma_T^2 = 0$. In reality correlation is not unity because of random fluctuations in B and T, which result from two mechanisms. The first comes about because of unknown spectral variability in β_ν and γ_ν as the transmit laser frequency is changed between absorbing and non-absorbing wavelength. The second is caused by transport of non-uniform distributions of aerosol particles and absorbing molecules over the time scale required to change wavelengths. These two effects are discussed in the following paragraphs.

First the spectral variability in β and γ as the transmit wavelength varies between absorbing and non-absorbing lines is examined. The data set on variability of both these parameters is extremely limited. Schotland [40], estimated that $\Delta\beta_\nu/\beta_\nu = 4 \Delta\nu/\nu$ for molecular backscattering in the visible region. A similar effect for aerosol backscattering at CO_2 wavelengths was predicted by Yue et al. [101], who show figures indicating that $\Delta\beta_\nu/\beta_\nu < 10 \Delta\nu/\nu$ for backscatter from different aerosol materials and different size distributions. For a CO_2 lidar operating on adjacent gain lines $\Delta\nu/\nu \sim .001$, which produces a value of σ_B^2 of approximately 10^{-4}. An error of this magnitude is negligible relative to other terms in Eq. (3.2). A similar conclusion

111

was reached by Megie and Menzies [74], who sought to determine the maximum separation allowable between lines in the UV and IR before differential backscatter became significant. Citing the work of Collis and Russel. [102] they determined that a frequency separation of as much as 2000 GHz (≈ 65 cm^{-1}) could be tolerated without significantly degrading the measurement.

These results are disputed somewhat by Petheram [103], who assumed a bimodal size distribution to estimate backscatter coefficients in different tropospheric air masses. He determined that differential backscatter could be as high as 5% in CO_2 DIAL measurements of ethylene, ammonia and ozone. The magnitude of the effect was found to vary with relative humidity and assumed air mass characteristics. It should be reinforced here that differential backscatter in itself does not cause errors if it can be predicted; errors result from uncertainties in the differential backscatter measurement. It is probably reasonable to assume that spectral differential backscatter errors are on the order of 1%, which results in $\sigma_{\beta_\nu}^{2} \sim 10^{-4}$. Such an error is probably a systematic error, since the parameters on which these numbers are calculated (air mass type and relative humidity) would not typically change over the course of a measurement.

Turning to the effects of differential absorption by interfering species, it is seen that experimental data on this subject are also somewhat limited. Schotland [40] estimated that this error is negligible at visible wavelengths. At IR wavelengths under normal

atmospheric conditions the interfering gases for water vapor measurements are primarily CO_2, ammonia, and ozone. The errors due to background absorption result from uncertainty in both the relative concentrations of the interfering gases and the resulting absorption. Given the absence of a locally-obtained data set, interference effects must be estimated using some global atmospheric model, such as that developed at AFGL [39].

Spectral variabilities in both β and γ generally fluctuate over long time scales, since the factors which cause the variability (atmospheric composition, temperature, pressure) usually remain relatively constant over the time scale of a single measurement. Over the short term (<1 hour) errors due to these effects are generally systematic, as in the case of errors due to uncertainty in the estimate of the primary species absorption coefficient. Averaging multiple measurements does not reduce such errors.

In addition to these long-time-scale variations, however, short-term uncertainties arise when the atmospheric properties which determine β_ν and γ_ν change during the time required to switch wavelengths. Such a situation occurs if atmospheric inhomogeneities are advected across the optical path. Temporal and spatial fluctuations in the atmospheric aerosol produce errors in the B term in Eq. (3.1). In the absence of local sources aerosol is often considered to be a passive dditive, such that the one dimensional spectral distribution of energy as a function of inverse length follows a $k^{-5/3}$ distribution, where

113

$k = 2\pi/L$ is the wavenumber. Post [104] measured the structure function of aerosol returns using a CW lidar. His results generally support the passive additive model, although he reported irregularities in the observed outer scale versus that predicted by standard turbulence theory.

The assumed $k^{-5/3}$ distribution which occurs under isotropic conditions is modified by local sources of aerosol concentration, such as pollution plumes, dirt roads, etc., which tend to produce transient, non-stationary fluctuations in β. During convective conditions aerosols from sources near the surface can be carried upward to heights of 3 km [40]. Thus, one might easily assume that in the region of thermals the aerosol concentration aloft would resemble that at the surface, which on the average is usually twenty times higher than at heights of 3 km [105]. Experimental data has shown temporal variations of as much as 20% in both the visible and IR backscatter coefficients at heights of 2-3 km above the surface [40].

This observed temporal variability can be expected to vary as a function of system pulse characteristics and atmospheric properties. Consider a system which has a pulse profile $P_t(t)$. The average return signal power at time t is given by

$$\bar{P}_r(t) = \int_{-\infty}^{\infty} P_t(t - \frac{2R}{c}) \ \beta(R,t) \ dR \qquad (3.63)$$

where the pulse is assumed to exit the laser at $t = 0$, and transmission fluctuations are neglected. The quantity $\beta(R,t)$ is the mean volume backscatter coefficient at range R and time t. Equation (3.63) shows that a long pulse effectively acts as a smoothing filter, filtering out that part of the total variance due to high spatial frequency fluctuations. Since the atmosphere is effectively frozen over the time scale of a single pulse, $\beta(R,t) = \beta(R)$. As an example, consider a Gaussian pulse with a standard deviation pulse duration of 1.67 μs, corresponding to a range resolution of roughly 0.5 km. If the spectrum of backscatter fluctuations is described by a one-dimensional Kolmogorov model with an outer scale of 100 m and Taylor's hypothesis applies, then the filtering effect of the pulse is roughly shown in Fig. 3-8. A large portion of the variance is removed by the spatial filtering.

When a single pulse return is filtered in time, additional spatial filtering of the backscatter occurs as the pulse propagates radially during the observation interval. The expression for return intensity becomes

$$P_f(t) = \int_{-\infty}^{\infty} h_f(t - \tau) \ \left\{ \int_{-\infty}^{\infty} P_t(\tau - \frac{2R}{c}) \ \beta(R) \ dR \right\} \ d\tau \qquad (3.64)$$

where $h_f(t)$ is the impulse response of the receiver filter. Equation (3.64) is identical to an initial convolution of the filter response

115
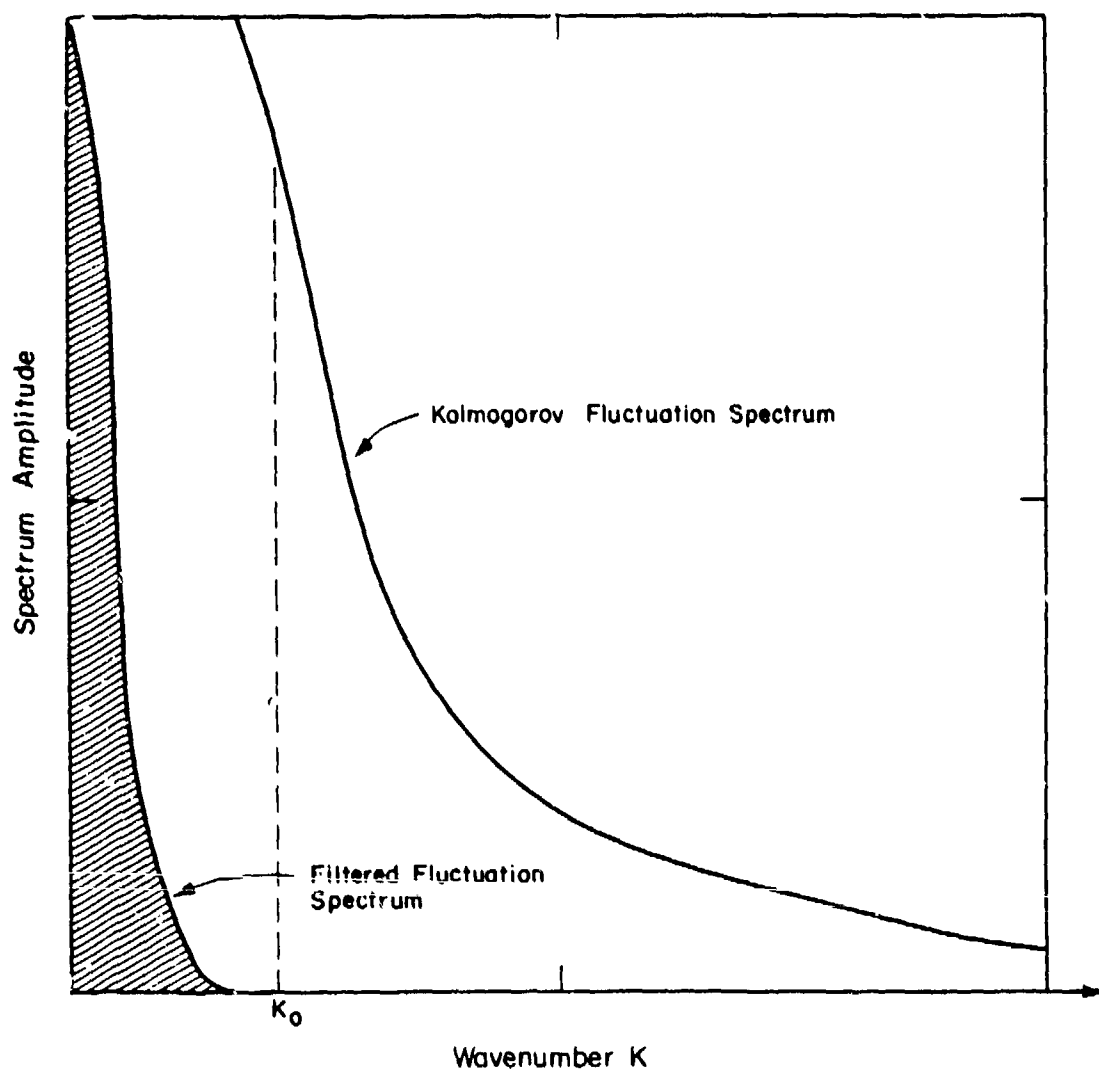
Fig. 3-8 — Spectra of typical atmospheric fluctuation spectrum, where outer scale L_o = 100 m, plotted alongside spatial spectral response of 2 μs wide Gaussian pulse. The long pulse filters out small-scale fluctuations in the return.

116

with the transmit pulse shape, followed by convolution with the radial backscatter function $\beta(R)$. The effect of receiver filters on pulse smearing is discussed in more detail in Chapter IV.

Usually, a measurement is taken over a series of multiple pulses. This may provide additional spatial averaging over length scales of $Nv\Delta t$ where N is the number of pulses, Δt is the pulse repetition period and v is the wind velocity which is assumed to determine the rate of advection of β inhomogeneities. For a system averaging 500 pulses at a 10 Hz pulse repetition rate, the multi-pulse length scale amounts to 500 m when $v = 10$ m s^{-1}. Thus, when pulse duration is less than about 3 μs, additional spatial averaging of backscatter fluctuations can be provided by multi-pulse averaging (which also reduces speckle noise).

The preceeding discussion indicates that temporal fluctuations in backscatter due to a homogeneous, isotropic aerosol structure can be minimized through judicious selection of system parameters. For this type of atmosphere the allowable time between sequentially-switched DIAL measurements over which the measurements are correlated can be estimated from the "length constant" (analogous to time constant) of the measured β fluctuations. If the length constant ℓ_c due to spatial averaging is 500 m, then the allowable switching time is limited by the time required for a new 500 m diameter eddy to advect into the optical path, or $t_{max} = \ell_c/v$. Thus, $t_{max} \approx 50$ s when $v = 10$ m s^{-1}. When the time between measurements is substantially less than the time scale of fluctuations due to β variability t_{max}, sequentially switched-measurements should be highly correlated.

117

Under non-isotropic conditions, when backscatter variability results from random, nonstationary, widely-spaced events, such as periodic emission of pollutants from a stack, sequential operation is acceptable only when the wavelength switching time is less than the advection time scale of the backscatter variability filtered by the spatial pulse filtering function. More measurement data is needed to characterize the expected variability and length scale of backscatter variations in the troposphere.

Temporal variations in the background absorption by interfering species result when differential concentrations of species are advected across the measurement volume over the time required to switch wavelengths. In the absence of local sources of the interfering species, one would expect the gases to be well mixed within the local atmosphere. Additionally, the same averaging factor which holds true for β variations also is applicable here. Thus it is probably reasonable to assume that errors due to temporal fluctuations are negligible relative to other errors considered in this section.

E. SIMULATION OF GROUND-BASED DIAL WATER VAPOR MEASUREMENTS

In this section the expected feasibility of ground-based water vapor DIAL measurements is now examined by modeling performance in a realistic atmosphere. Both direct and heterodyne systems were included in the simulation. The following discussion describes the atmospheric and system parameters assumed in the simulation and the resulting predicted measurement accuracy.

118

1. Model Description

In the model, measurement accuracy as a function of height was estimated from Eq. (3.2). It is seen from the equation that values must be obtained for normalized variances $\sigma_{\hat{P}}/\langle\hat{P}\rangle^2$ and $\overline{\sigma_{K_m}}^2/\langle\overline{K}_m\rangle^2$, variances σ_β^2 and σ_T^2, range resolution ΔR, and mean concentration $\overline{\rho}_o$. To estimate these parameters characteristics of both the atmosphere and the assumed DIAL system must be specified.

It was assumed that the measurements were taken in a midlatitude winter. This assumption results in a somewhat more difficult atmosphere for high relative accuracy water vapor measurements than would exist if a summertime model were employed, since wintertime moisture concentrations are lower. On the other hand, because attenuation due to total water vapor content along the path is smaller, absolute accuracy of the measurements should be generally higher. The mid-latitude winter models employed were identical to those used in the NOAA wind-measuring satellite feasibility study [85]. The backscatter model was developed at NOAA [85], while the temperature and humidity models were taken from the Air Force Geophysical Laboratory (AFGL) mid-latitude winter atmospheric model [106]. Values of the parameters versus height in these models are plotted in Figs. 3-9, 3-10 and 3-11.

For estimates of turbulence-induced effects and absorption cross-section related uncertainties, profiles of atmospheric structure-parameter C_n^2, as well as normalized variances of pressure and

119
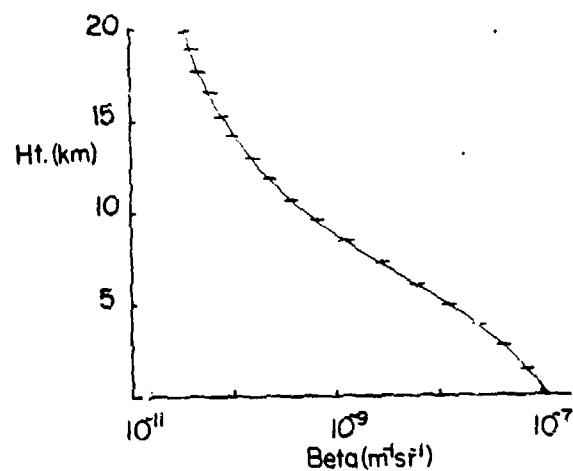
Fig. 3-9 – Midlatitude winter backscatter coefficient model. From [85].
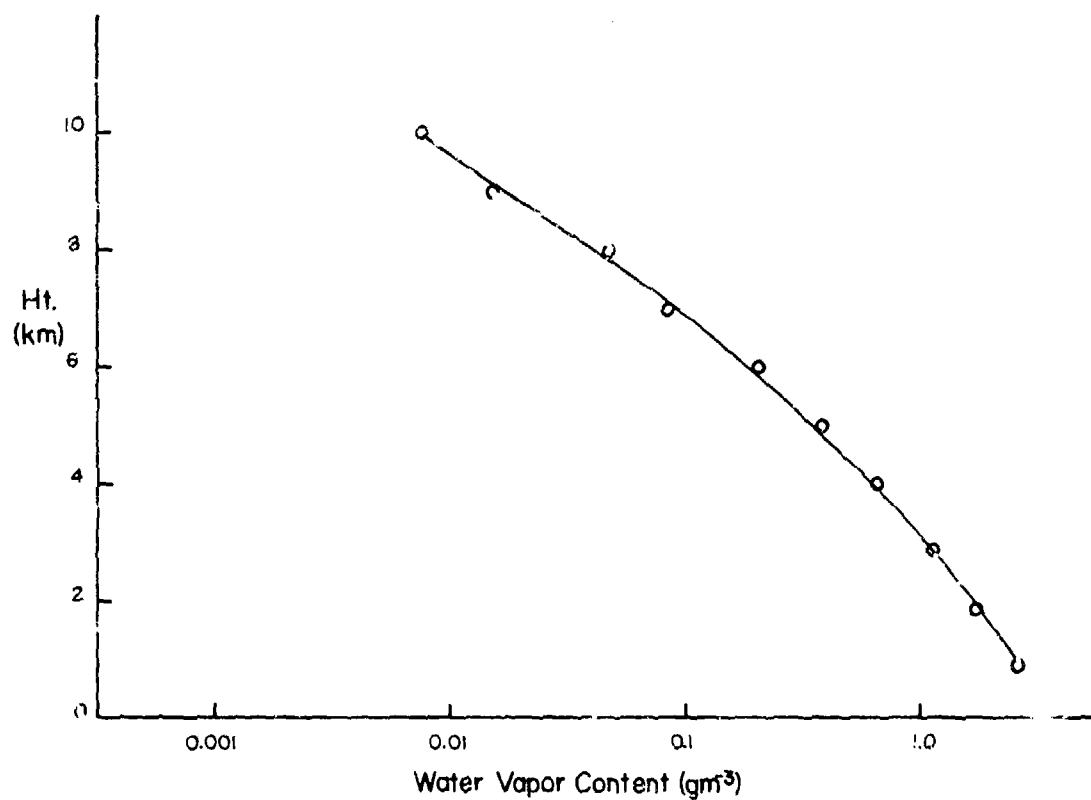

Fig. 3-10 – AFGL midlatitude winter model profile of water vapor concentration. From [39].
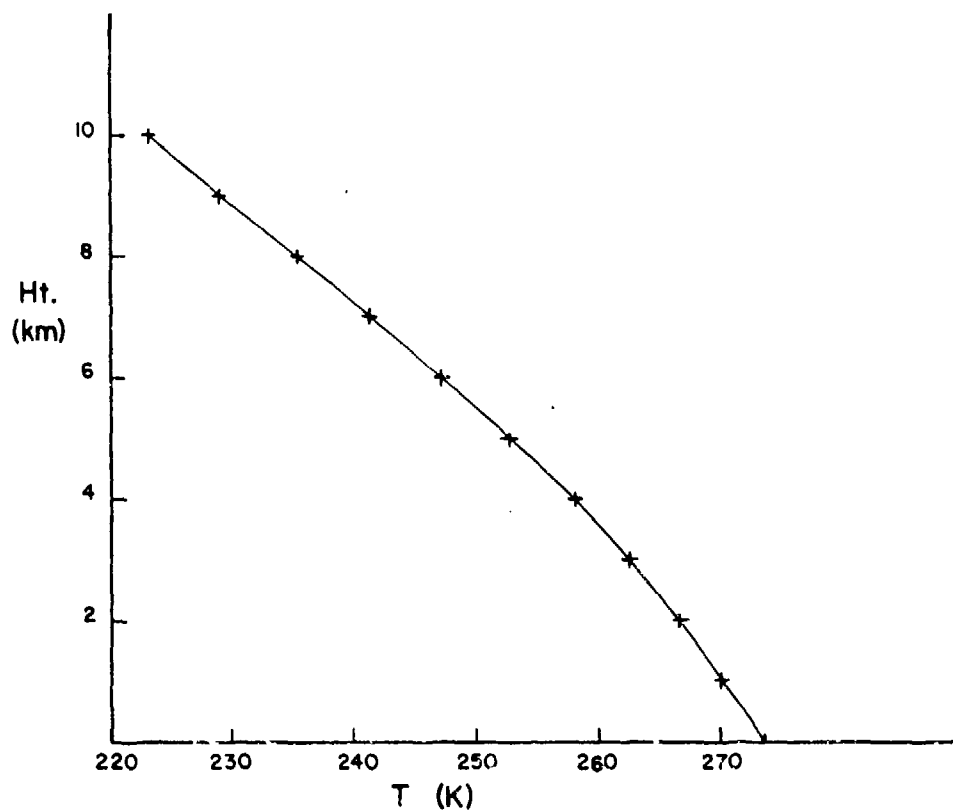
120

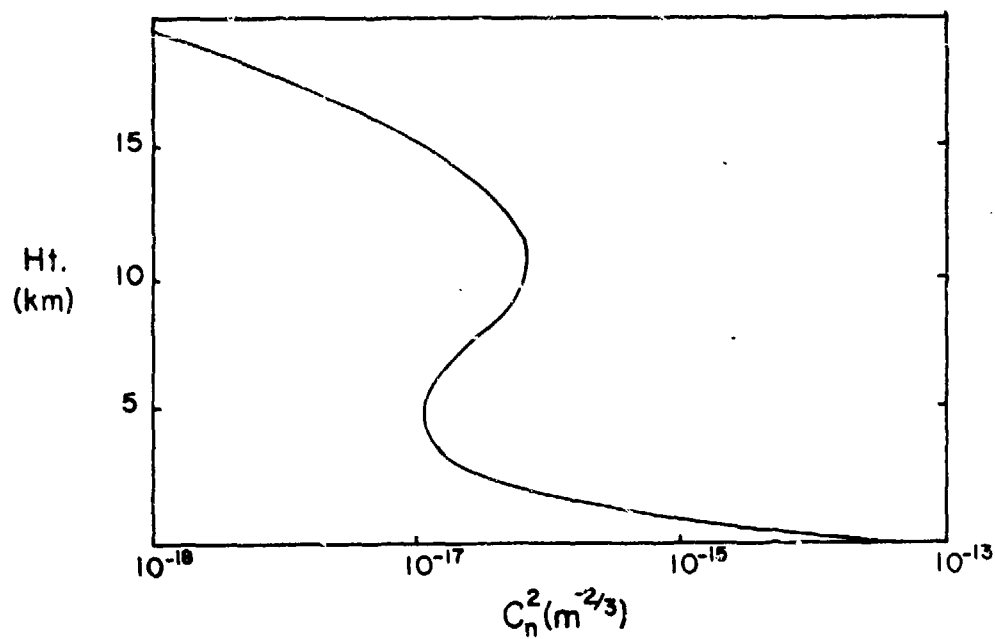Fig. 3-11 - AFGL midlatitude winter temperature profile model. From [39].

Fig. 3-12 - Globally-averaged C_n^2 profile model. From [107].

temperature uncertainties $\sigma_p^2/\langle p\rangle^2$ and $\sigma_T^2/\langle T\rangle^2$, were also required. Estimates of C_n^2 are derived from an approximate form of Hufnagel's globally averaged profile [107], as shown in Fig. 3-12. To characterize $\sigma_p^2/\langle p\rangle^2$ and $\sigma_T^2/\langle T\rangle^2$ a measurement scenario was assumed whereby the most recent and closest radiosonde sounding data were obtained and used to estimate absorption cross-section K_m. Errors can thus be introduced when the atmosphere at the time and place of the measurement differs from that of the sounding. In order to approximate an upper bound for this error, climatological data obtained from atmospheric circulation statistics were employed [108]. The normalized variances in specification of pressure and temperature used in the simulation were estimates of the variances in these parameters which occur during passage of a transient atmospheric eddy at latitude 40°N during winter, as shown in Figs. 3-13 and 3-14.

The system parameters assumed for the calculations are shown in Table 3.3. The specified transmit pulse energies were 10-J for the incoherent system and 1-J for the coherent system. These values are representative of current, or soon-to-be-achieved laser technology. The diffraction-limited field of view of the incoherent receiver aperture was assumed to be 1/1000 that of the transmitter antenna, resulting in a reduction in speckle-induced scintillation variance by a factor of 1000. Additional fluctuation reduction for the incoherent system was obtained by means of frequency diversity. It was assumed that three longitudinal TEM_{oo} modes centered around the middle of the
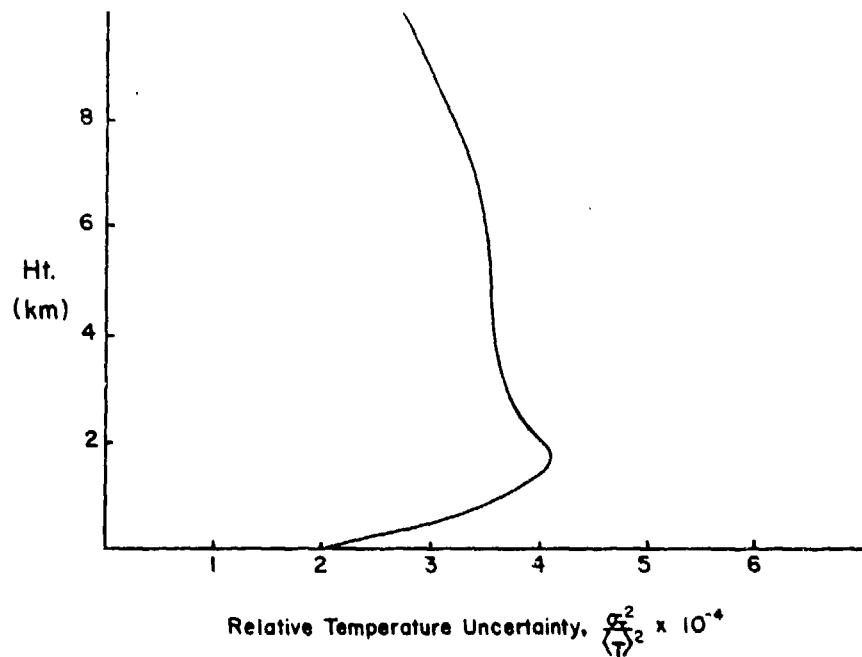
122

Fig. 3-13 – Climatologically-averaged profile of normalized temperature
variance resulting from passage of a synoptic-scale transient eddy
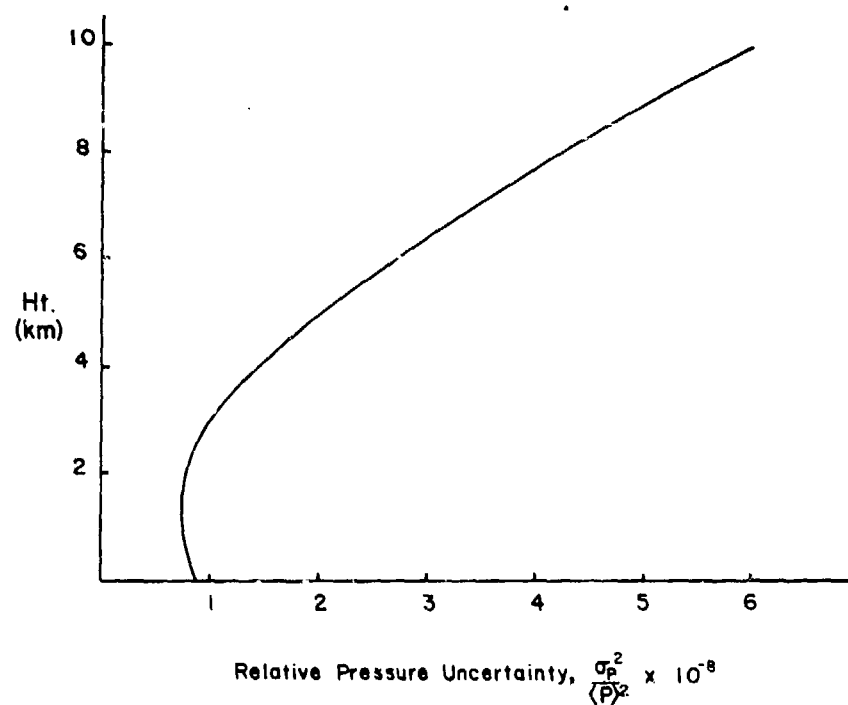during winter. From [108].

Fig. 3-14 – Climatologically-averaged profile of normalized pressure
variance due to passage of a wintertime synoptic-scale transient
eddy. From [108].

123

CO_2 laser line were present in the transmitted pulse. For a CO_2 system with a 2-m cavity, the separation between the longitudinal cavity modes is 75 MHz, which results in a transmit bandwidth of 150 MHz. The variation in absorption coefficient over this frequency range was esti- mated by comparing the 150 MHz bandwidth with the linewidth α_c for the water vapor line nearest in frequency to the R(20) CO_2 line. Because $\alpha_c = 1.26$ GHz for this line ($\nu = 976.012$ cm^{-1}), the transmission band- width was sufficiently narrow that uncertainties in distribution of energies among the lines can be neglected.

Table 3.3. Simulation Parameters

	Direct	Heterodyne
Pulse Energy	10 J	1 J
Optics Diameter	1 m	.5 m
Apodization Factor	---	.47
Focus	---	6 km
NEP	2.6×10^{-10} W	3.76×10^{-14} W*
System Efficiency	0.1	0.1
Pulse length	variable	variable
Bandwidth	150 kHz	matched filter B_f matched to pulse length
CO_2 absorbing wavelength	10.247 μm	10.247 μm
CO_2 reference wavelength	10.260 μs	10.260 μs
Integration time	6.67 μs	6.67 μs
Range resolution	1 km	1 km
Elevation angle	90°	90°

* Assuming 1 MHz IF bandwidth

A block diagram of the model is shown in Fig. 3-15. First, esti- mated values of absorption cross-sections K_ν were calculated vs. height from the McClatchey tapes for the given atmospheric model and elevation
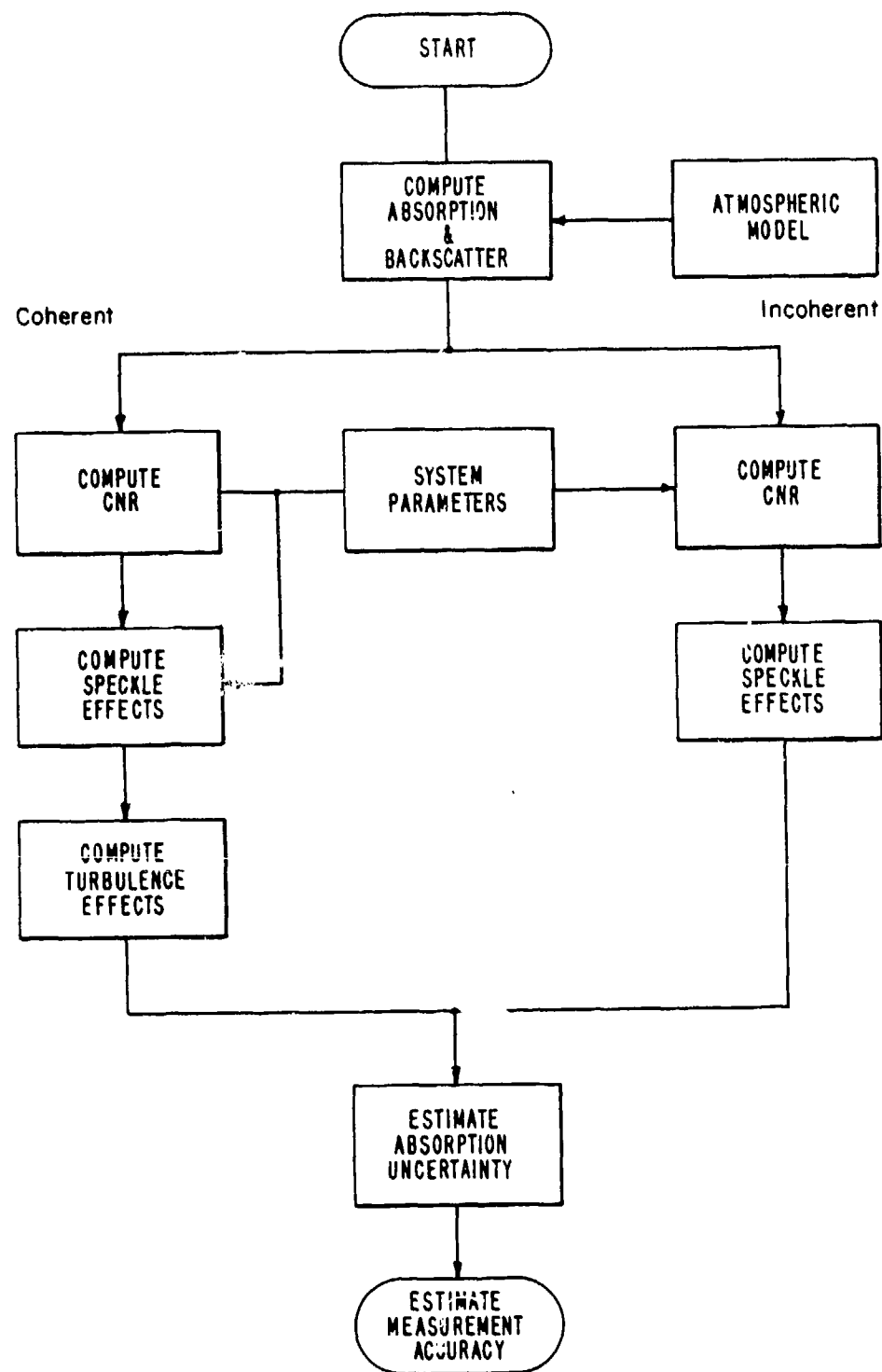
124

Fig. 3-15 — Flow chart of DIAL feasibility computer simulation.

angle. Then, given system parameters, backscatter coefficient profiles, and assumed speckle bandwidth broadening, the mean CNR was computed for each range increment and wavelength. Next, speckle and detection noise fluctuations were included in the estimate of power fluctuations by calculating correlation times τ_s and τ_n based on pulse and total bandwidth considerations, estimating correlation functions, and substituting the results in Eqs. (3.24) and (3.37). The power measurement uncertainties computed from Eqs. (3.24) and (3.37) were modified when turbulence was important. Contributions of turbulence to the power measurement error were estimated by calculating ρ_o and σ_x^2 from Eqs. (3.45) and (3.46), then applying the results of Clifford and Wandzura [96]. If significant, turbulence effects were then included in the γ and F terms in Eqs. (3.49) and (3.53).

Following estimation of the power measurement uncertainty, errors due to lack of knowledge of the absorption coefficient were estimated from Eq. (3.57). The expected measurement errors for both types of system were then calculated from Eq. (3.1). Throughout the analysis it was assumed that the atmosphere was well-mixed and isotropic, and that pulse length and/or observation time were of sufficient duration that backscattering variations were well-averaged. With these assumptions the backscatter uncertainty term σ_B^2 was negligible. The uncertain attenuation due to interfering species was also neglected ($\sigma_T^2 \approx 0$); the validity of this assumption is discussed briefly in Chapter V.

2. Simulation Results

The simulation was initially performed for the given system parameters and atmospheric models. Figure 3-16 shows the estimated value of CNR vs. height on the R(20) line for the 1J coherent system and both 1 and 10J incoherent systems, assuming a matched-filter receiver. Note the improvement gained in CNR by using heterodyne detection is approximately 25 dB for the parameters assumed. Both 1J coherent and 10J incoherent systems produce returns with predicted CNR's above 0 dB from altitudes up to 8 km.

The CNR values plotted in Fig. 3-16 assume that no decoherence of the signal due to refractive-index turbulence occurred for the heterodyne case. The effect of turbulence on lateral coherence and fluctuation is seen in Figs. 3-17 and 3-18. From Fig. 3-17 r_a' was calculated by estimating r_a, then making the approximation $r_a' = 2r_a$ as 'gested by Clifford and Wandzura [96]. Note that since r_a is greater n the assumed .5 m optics diameter for returns from all heights, lateral coherence is maintained and turbulence effect on CNR can essentialy be neglected. Similarly, since σ_x^2 is $\ll 0.1$ for all heights, additional signal fluctuations due to turbulence are negligible according to Fig. 3-5. This result, that refractive-index turbulence does not affect coherent lidar performance for vertically pointing systems, has been shown to hold true even for wavelengths near the visible [109]. When elevation angles are shallow the effects of turbulence must still be considered, although system performance will
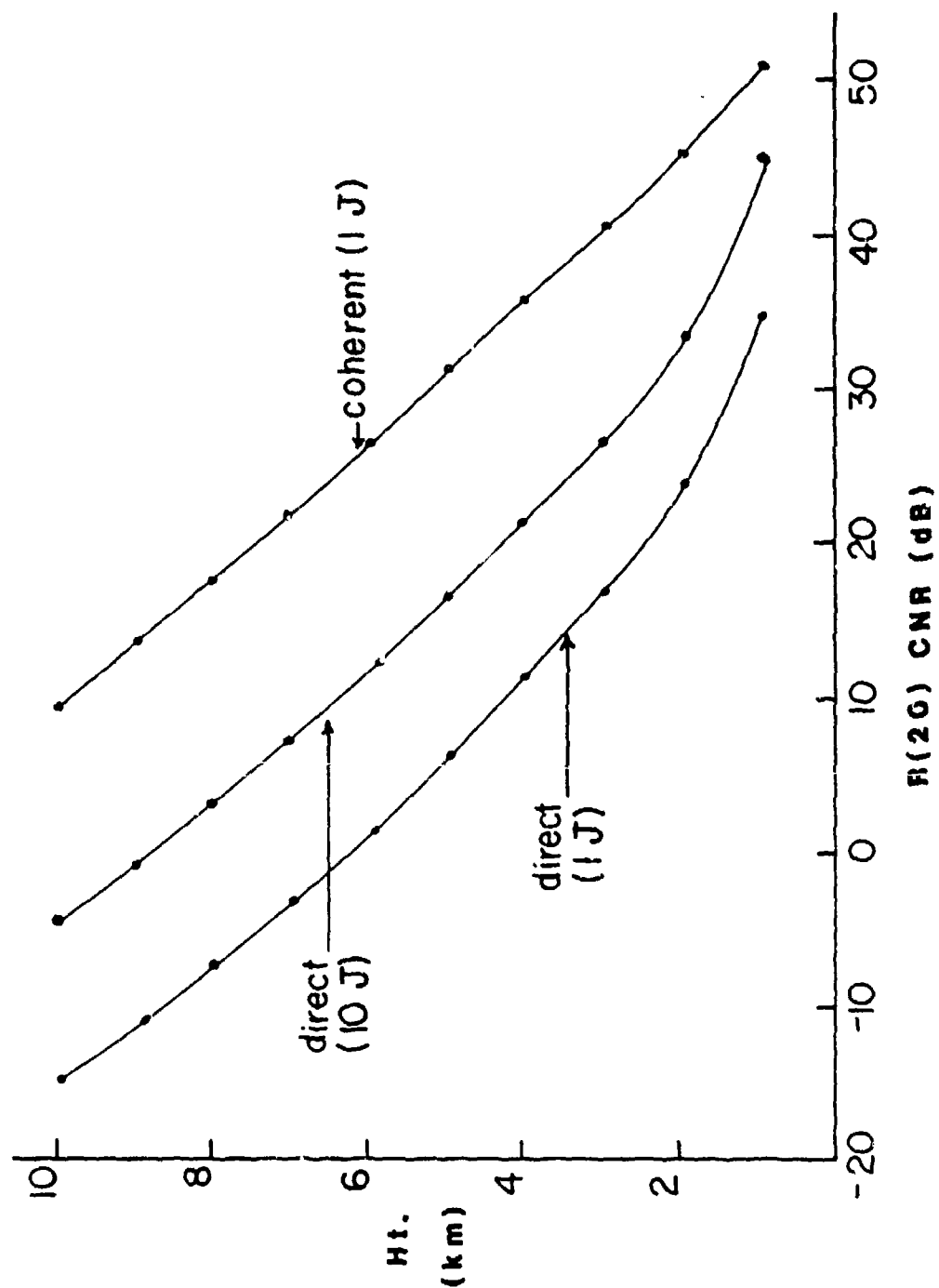
127

Fig. 3-16 – Calculated carrier-to-noise ratio profiles for R(20) measurements using coherent and incoherent systems.
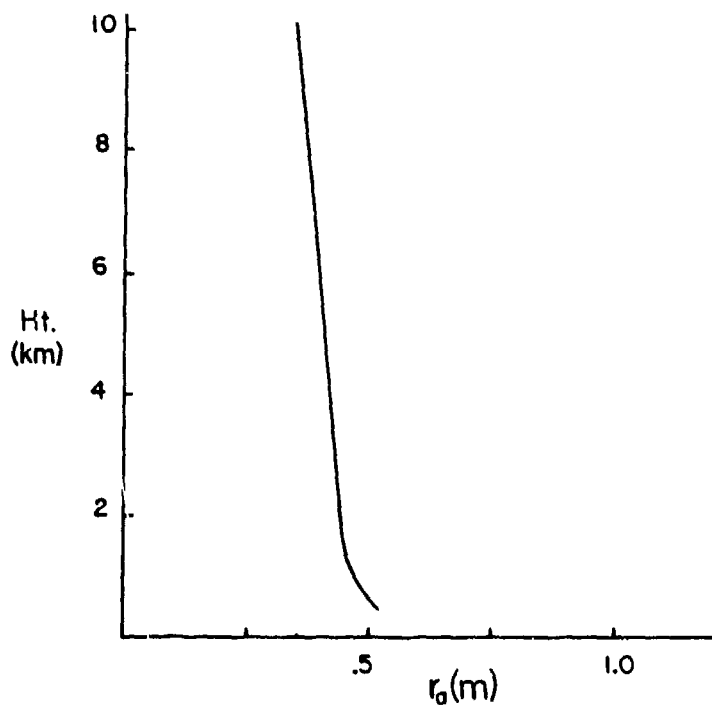
128

Fig. 3-17 – Transverse coherence radius r_a profile calculated from C_n^2 profile of Fig. 3-12.
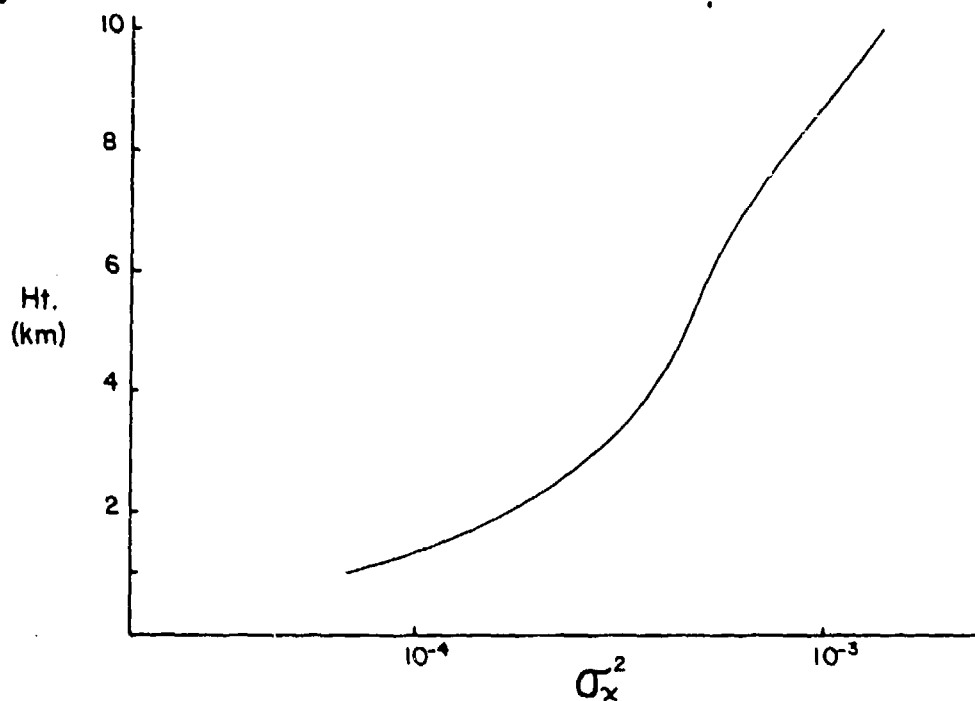

Fig. 3-18 – Profile of signal log-amplitude variance due to turbulence calculated from C_n^2 profile of Fig. 3-12.

typically not be degraded significantly for ranges less than about 10 km.

The uncertainty in power measurements due to fluctuations for a single pulse is shown in Fig. 3-19, where the mean autocorrelation function was assumed to have a negative exponential shape. It is obvious that the entire heterodyne measurement, as well as the 10-J direct detection measurement below 4 km, were limited by speckle noise. From our previous discussion we know that the power measurement error in the speckle-dominated case can be reduced by shortening the transmit pulse if energy is kept constant. From Fig. 3-2 we calculate that a 15 ns pulse will optimize the measurement at 6 km altitude. This conclusion assumes that sufficient detector bandwidth is available (~60 MHz) and that no additional noise sources are introduced in the process. With these assumptions, it is seen in Fig. 3-20 that the heterodyne detection errors can be improved by an order of magnitude through the lower 6 km. The direct detection errors were only improved where speckle noise was significant; at other altitudes the estimates were degraded.

From the error in power measurement, the actual predicted DIAL measurement concentration error (Fig. 3-21) and the resulting percentage error (Fig. 3-22) can be calculated. These errors are based on an average of 2000 pulses (1000 measurements), which, at a pulse repetition rate of 10 Hz, would require about 3 1/2 min. We see that the 1-J heterodyne and the 10-J direct detection systems should measure the
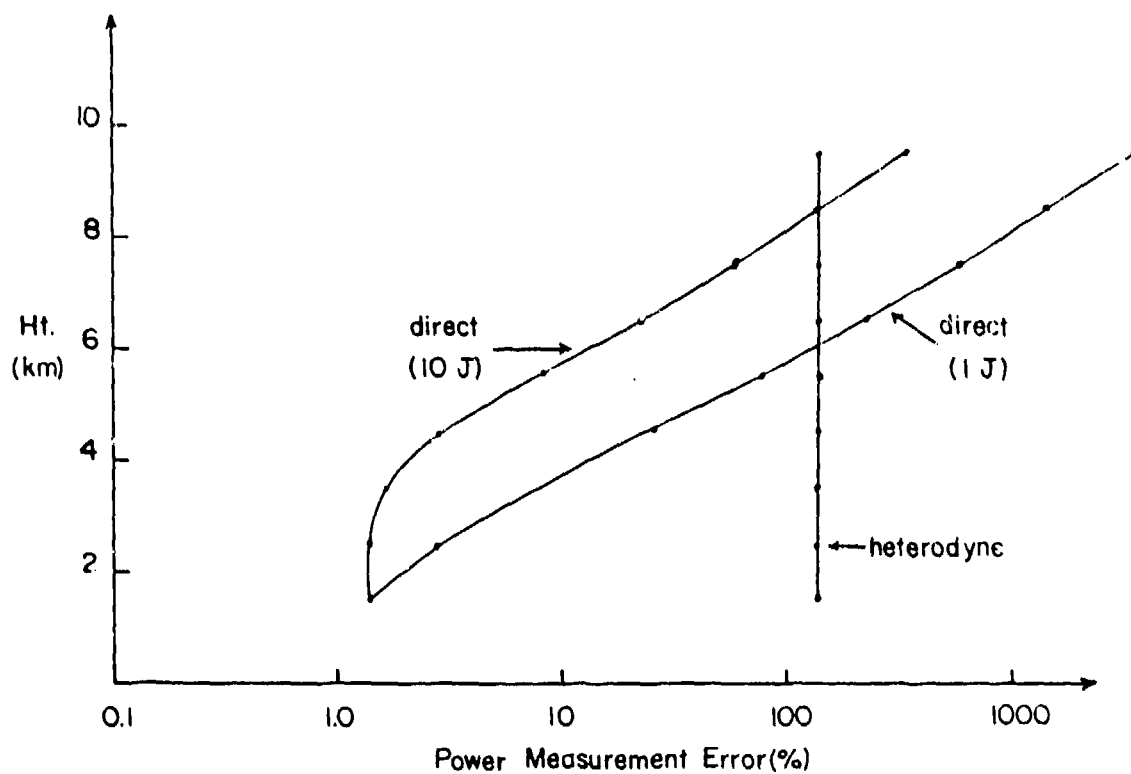
Fig. 3-19 – Estimated single-pulse power estimate error versus height, assuming B_p = 200 KHz.
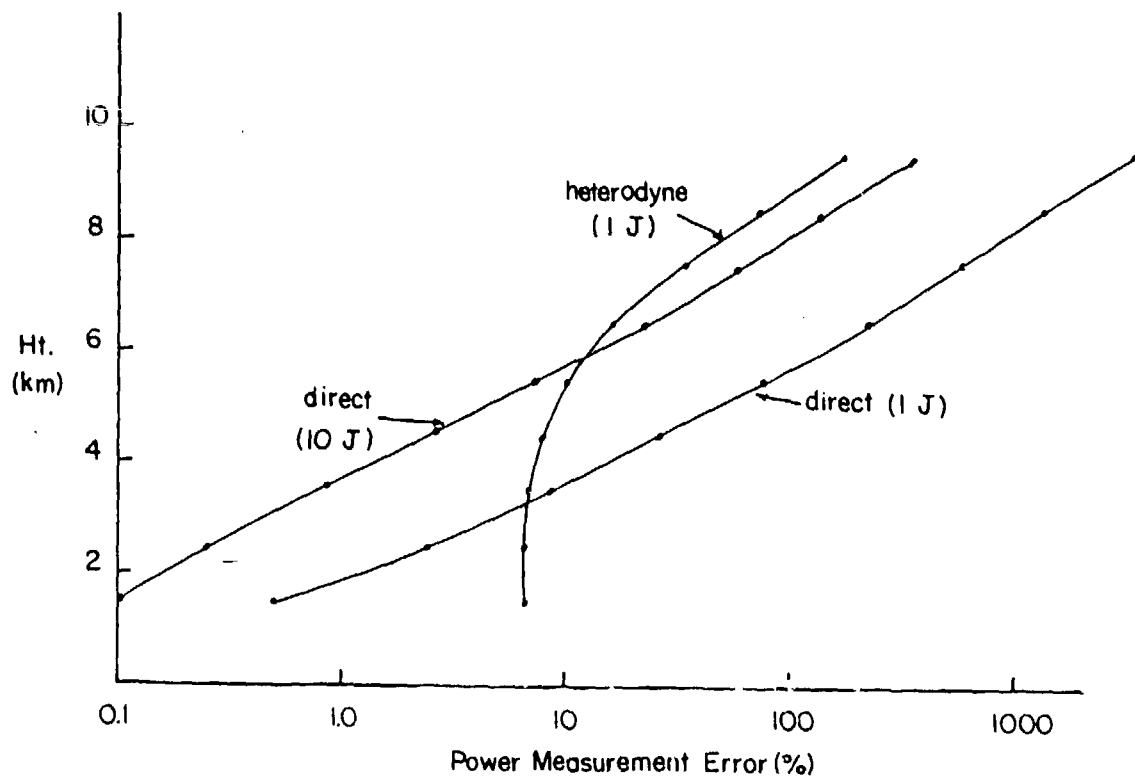

Fig. 3-20 – Estimated single-pulse power estimate error when B_p = 66 MHz.
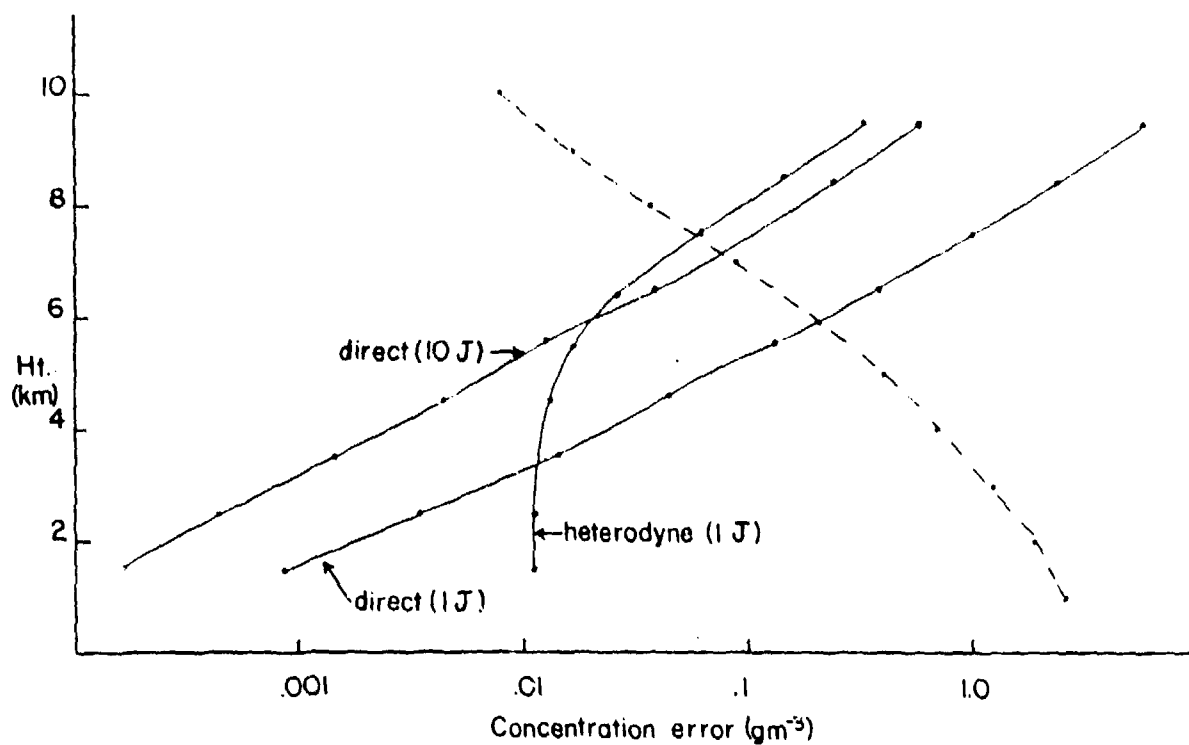
131

Fig. 3-21 - Absolute concentration estimate errors due to power measurement uncertainties where B_p = 66 MHz. Dashed line is mean MLW concentration.
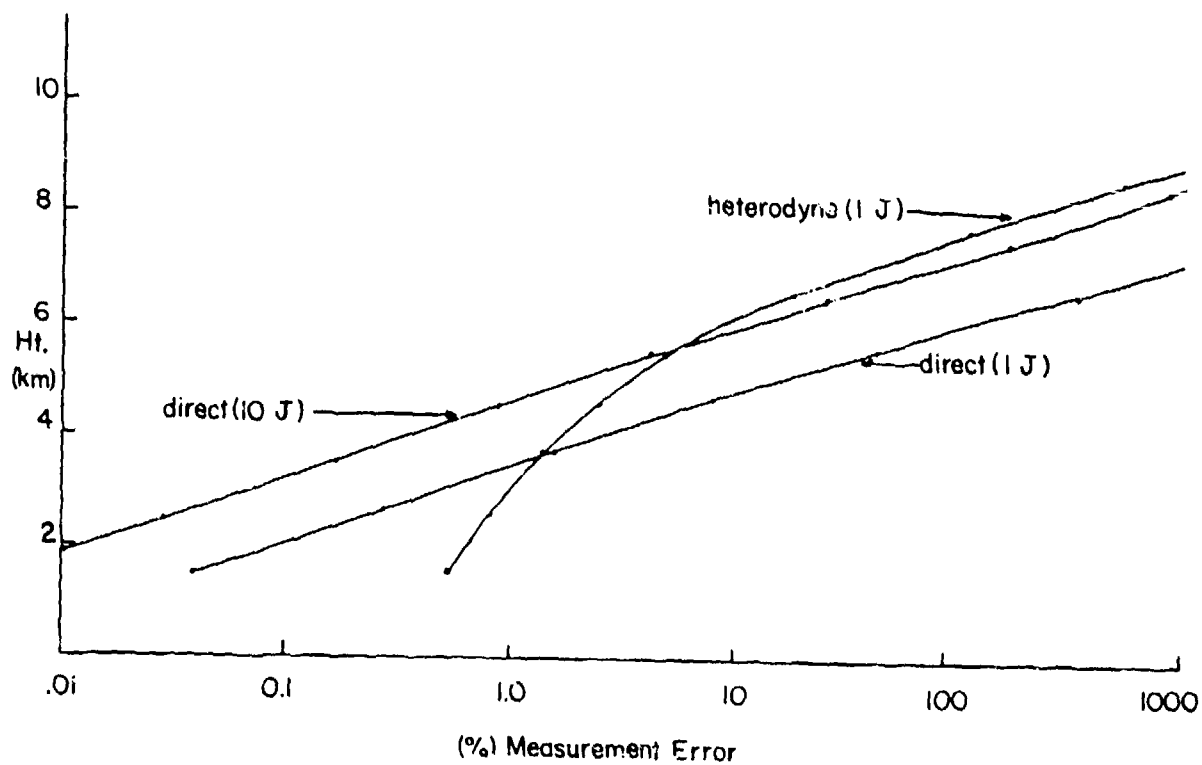

Fig. 3-22 - Relative concentration estimate errors due to power measurement uncertainties, B_p = 66 MHz.

concentration to within 10% to about 6 km. The 10-J incoherent system is superior to the heterodyne system below about 5.5 km, whereas the 1-J incoherent system offers a better measurement below 3.5 km. Obviously, this assessment of performance is closely related to the assumed parameters. However, increasing the number of pulses over which an average is taken should generally lessen the error for both systems. Transmitting more energy will always reduce the direct detection measurement error, while shortening the pulse length will reduce heterodyne errors at lower elevations.

The absorption coefficient uncertainty term $\sigma_{K_m}^{2}/K_m^{2}$ was calculated from Eq. (3.48). The four curves in Fig. 3-23 illustrate the effects of uncertainties in R, p, E", S_o and α_{co}; all include the errors caused by uncertainties in temperature and pressure (solid line in Fig. 3-23). The three remaining curves show the effects of additional uncertainties in the individual line parameters. The temperature uncertainty term turns out to be the dominant parameter. It is seen that for the temperature and pressure uncertainties specified in Figs. 3-13 and 3-14, the absorption coefficient error was about 20%. It can be seen from Eq. (3.53) that the temperature uncertainty couples into the absorption coefficient uncertainty primarily through the ground-state energy E". Thus, it might be advantageous to choose an absorbing line that has a lower ground-state energy, even though it may not be optimum in other respects. These conclusions depend on the
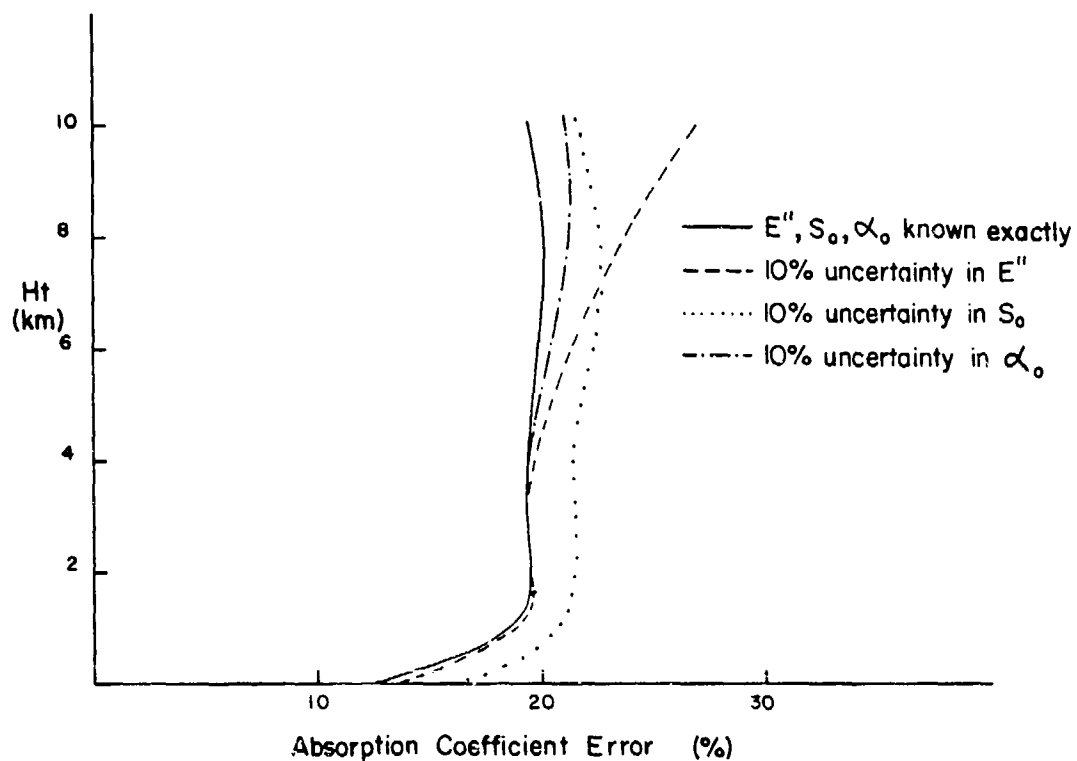
133

Fig. 3-23 - Calculated uncertainties in absorption cross-section
specification, assuming temperature and pressure errors of
Figs. 3-13 and 3-14.

assumed profile of temperature and pressure uncertainties. In prac-
tice, one could probably determine the temperature more accurately than
the temperature indicated by the climatological statistics (Figs. 3-13
and 3-14). For example, by using NWS radiosonde data and simple extra-
polation techniques one would expect to improve on the 4-6 degree error
calculated using the transient eddy statistics.

Combining the absorption coefficient errors with the power
measurement error (Figs. 3-24 and 3-25), we see that reasonably
accurate water vapor concentration measurements should be possible with
the specified DIAL systems to heights of about 6 km. For this simula-
tion the height limitation resulted more from the decrease in measur-
able water vapor than the decrease in system efficiency. Longer time
averaging will improve the power-measurement error term; when pulse-to-
pulse fluctuations are independent the error is reduced by $1/\sqrt{N}$, where
N is the number of pulse pairs averaged. The assumption of in depend-
ent pulse-to-pulse fluctuations is examined further in Chapter IV.
Absorption coefficient errors usually represent a systematic error
which does not average out over the course of a measurement. These
errors can only be improved by better knowledge of the atmospheric and
absorption line parameters. For the R(20)/R(18) line pair used in the
simulations limits on exact specification of absorption cross section
may well represent the ultimate limitation on DIAL concentration
measurement accuracy.

This analysis indicates that incoherent DIAL systems are probably
the choice when range requirements are limited to a few kilometers.
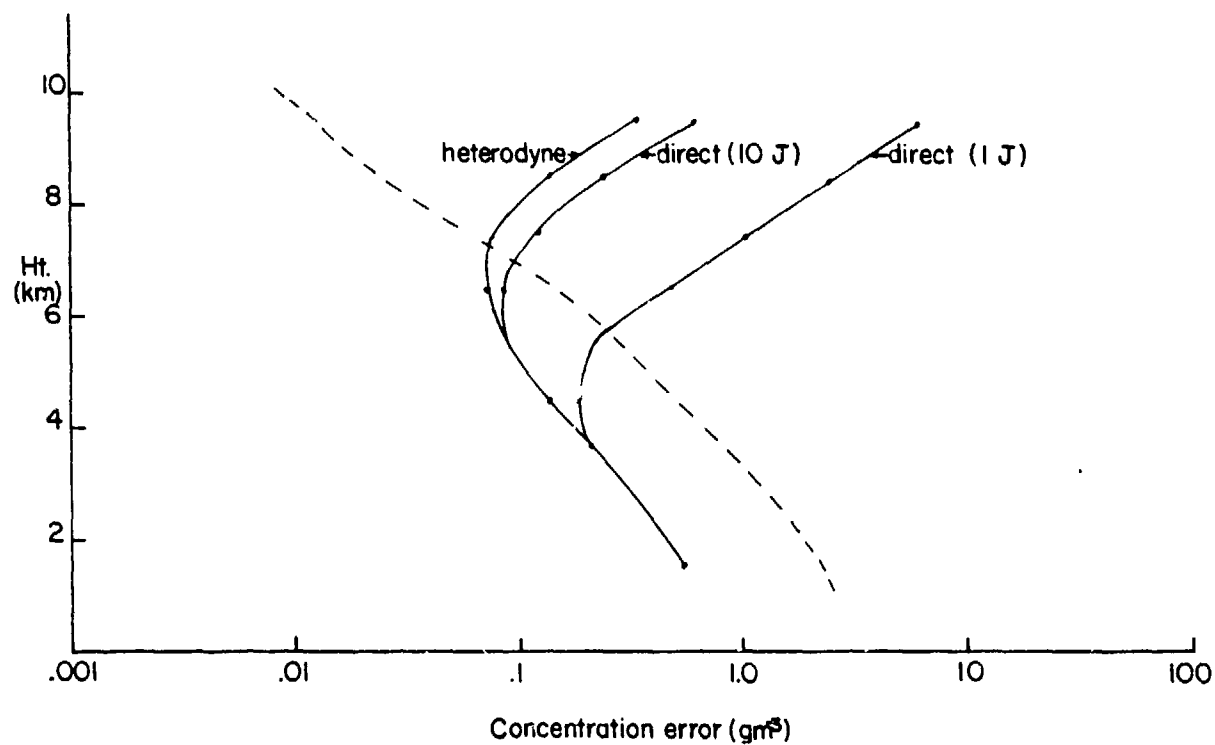
135

Fig. 3-24 – Calculated absolute error of water vapor concentration including absorption cross-section and power measurement uncertainties. Dashed line shows mean MLW concentration; assumed B_p was 66 MHz.
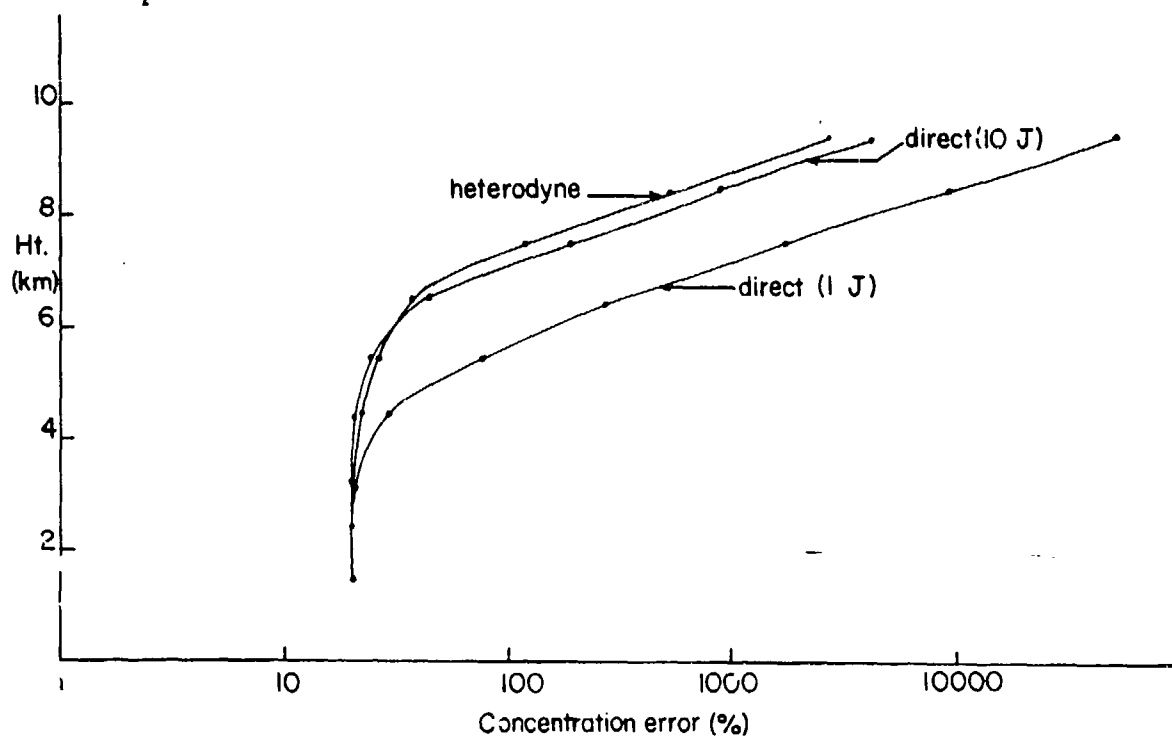

Fig. 3-25 – As in Fig. 3-24, except relative error.

Although maximum range can be extended with higher pulse energies, the exponential decrease in signal due to attenuation at some point makes such a strategy impractical. Coherent systems, on the other hand, offer better sensitivity at long ranges and adequate sensitivity at short ranges when averaging is effective to reduce speckle noise. Additionally, coherent systems offer the opportunity of measuring the Doppler shift and hence the aerosol velocity. Combined measurements of species concentration and radial velocity would be valuable in mesoscale meteorology research (for measurment of moisture flux) as well as in the tactical military scenario for warning of the impending presence of hazardous species.

As moisture concentration in the atmosphere increases, the absorption coefficient must decrease to maintain constant SNR. Ideally, then, one would select a weaker absorption line to maintain good signal. This may not be necessary with heterodyne systems operating in a regime whose error is speckle dominated. Under these conditions, decreasing SNR would have negligible effect on measurement accuracy. This is seen in Fig. 3-26, where power measurement errors were calculated for an atmosphere with twice the moisture of the mid-latitude winter. Although both types of systems were affected, the heterodyne system error was relatively unchanged at the lower levels, where speckle effects dominate the error.

For an operational DIAL system, elevation angles other than the 90° assumed in this simulation will be necessary. An operational
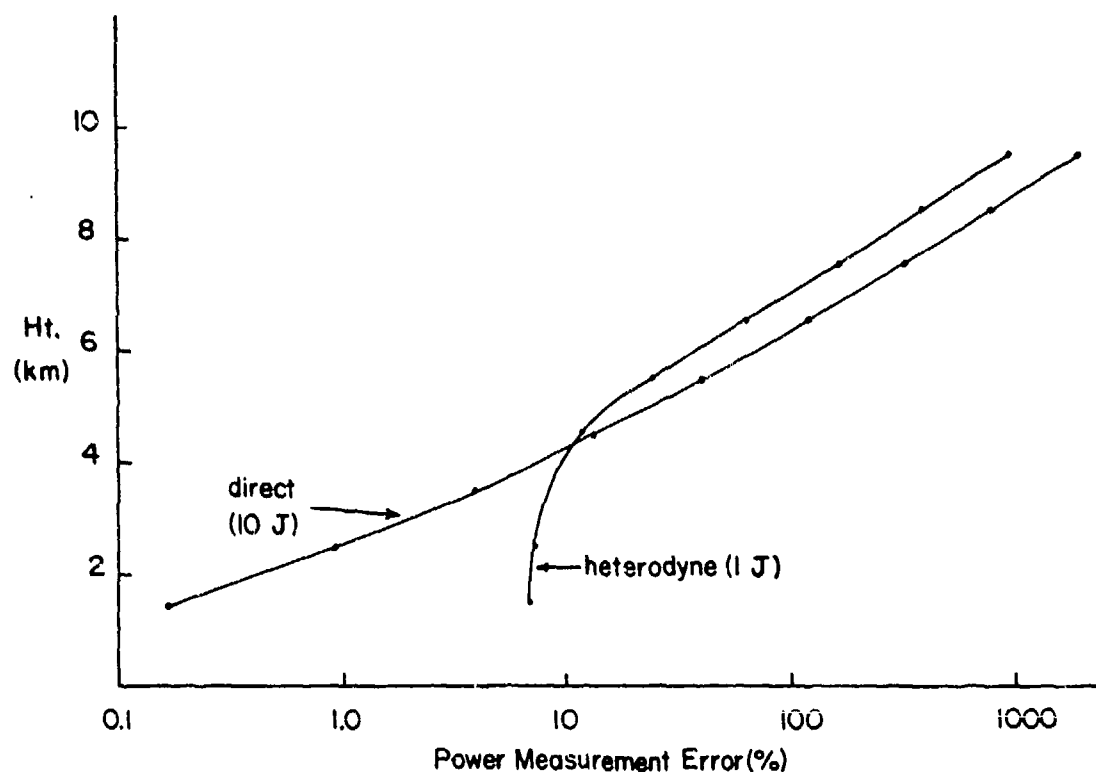
137

Fig. 3-26 — As in Fig. 3-25 assuming a doubled water vapor concentration at all heights.

system should have some scanning capability; for example, it should be able to look for holes in the clouds. As the elevation angle decreases, the path absorption for a given altitude increases and the SNR decreases. This effect is partially offset by the increase in ΔR (for a given height resolution) in the denominator of the uncertainty expression. Using the same system parameters as before, except changing the elevation angle to 60°, a 1.8-dB increase in the error of the water vapor measurement was calculated for the heterodyne system.

The height resolution was held constant at 1 km for this analysis, however, it could be easily varied as a function of the desired measurement accuracy. For example, if 10% accuracy was sought, the height resolution might vary from about 100 m at 1-km altitude to 3 km at 7 km altitude. Above 7 km, the errors become unacceptably large for all range resolution values.

F. SUMMARY

This chapter has been primarily concerned with error sources in DIAL measurements. Both coherent and incoherent systems have been discussed. The major phenomena contributing to measurement errors are coherent fading (speckle), detection noise, and uncertainty in the species differential absorption cross section. The relative importance of each error source varies, depending on whether heterodyne or direct detection is employed. With heterodyne detection speckle fluctuations limit the measurement accuracy when CNR is high; at low CNR quantum

139

noise is a dominant factor. Incoherent systems, on the other hand, can be designed to minimize effects of speckle, hence detection noise usually determines measurement sensitivity for these systems.

Transmission of both the absorbed and reference wavelengths simultaneously is the preferred DIAL pulsing technique. Such an arrangement minimizes errors caused by non-stationarities in atmospheric backscatter and extinction. When sequential measurements (transmit on first one laser line, then the other) must be made, spatial filtering by means of long transmit pulses and averaging times helps to reduce uncertainty.

Refractive index turbulence along the path affects DIAL measurements by degrading the coherence of the propagating energy. For heterodyne DIAL systems this results in both decreased CNR and increased fluctuation. Incoherent DIAL systems are susceptable primarily to the signal fluctuations, which can be reduced fairly easily through aperture averaging. Recent theoretical work [96] has shown that turbulence effects on monostatic lidars are less than was previously thought. Because of this, turbulence effects on DIAL measurements should be significant only when the paths extend just above the ground.

In the latter part of the chapter, a simulation incorporating specific parameters was performed to examine coherent and incoherent DIAL capabilities for measuring water vapor. The simulation assumed speckle

and noise-produced fluctuations were the primary error sources in power measurements. Results of the simulation indicated that for short-range applications where CNR was high for both types of systems, direct-detection DIAL was probably preferable. Although speckle limits coherent lidar accuracy at these closer ranges, superior sensitivity at longer ranges makes a heterodyne system the choice for measurements at ranges beyond 2-3 km. The simulation assumed that an incoherent system could be constructed to make speckle-induced uncertainties negligible. Such an assumption may be overly optimistic.

The two primary error sources in the simulated measurements were inaccuracies in estimate of species absorption coefficient and inexact measurement of average received power. Errors due to absorption coefficient uncertainties are basically system-independent. The errors result from a lack of knowledge of both the absorption line parameters and the temperature and pressure at the point of the measurement. Reasonably accurate values of line parameters can probably be obtained by means of precise measurement experiment. Atmospheric parameters, however, must be estimated at the time of the DIAL measurement. The measurement can be extremely sensitive to errors in the specification of temperature, and less sensitive to pressure. The simulation showed that measurement errors using the $R(20)$ line resulting from absorption coefficient uncertainties could be as much as 10% or more. These are probably systematic errors that cannot be reduced through averaging.

141

The other primary error source, inexact estimate of average received power, can be quite different for heterodyne and direct detection DIAL systems. Power measurement errors result from fluctuations in the instantaneous received signal due to coherent fading (speckle), atmospheric turbulence, and noise added during detection, such as shot, thermal, and background noise. Heterodyne power estimates are sharply degraded by the speckle. One method of reducing this effect is to employ very short pulses and integrate the return over a period equivalent to a large number of pulses. However, short pulses result in a wider received signal bandwidth, hence an increase in bandwidth-dependent shot noise. It is interesting to note that the ideal system probably lies somewhere between a direct-detection system and a CNR-maximized heterodyne system. By continually increasing signal bandwidth in a heterodyne system the relative effects of background, thermal and other noise sources are increased. Eventually the system is no longer shot noise limited, and the sensitivity behaves more and more like a direct detection system. The optimum performance should be somewhere between shot-noise limited and shot noise negligible operation.

Although the simulation parameters differed from the actual NOAA lidar parameters, simulation results can be compared with actual measurements. In Chapter VI these comparisons are analyzed.

IV. SYSTEM DESCRIPTION AND BACKSCATTERED-SIGNAL PROPERTIES

This chapter describes a series of preliminary measurements made using the NOAA pulsed system. These experiments serve to lay the groundwork for the actual DIAL measurements described in the next chapter. The first section briefly describes the NOAA pulsed lidar. Additional information on system capabilities is available in a number of references, see e.g. [110]. Although the NOAA system has been in operation, at the time of this writing, for almost two years, it is still virtually unique in its capabilities. Over the two-year period it has been used to examine such phenomena as tropospheric and stratospheric winds, atmospheric backscatter coefficients, thunderstorm outflows, chinook winds and thermal convective plumes; as well as to measure water vapor, as described in this dissertation. The evaluation of the signal statistical properties discussed in this chapter has been important in a number of those research efforts.

Section B describes the operating characteristics of the NOAA system. Both amplitude and frequency of the transmit pulse were measured, as well as stability in both the transmitter and receiver. Since DIAL measurements taken with the NOAA lidar required approximately 5 minutes to make the sequential measurements on both laser lines, variations or drifts in system performance have a major impact on measurement error. The effects of the instabilities on the measurements are described in this section.

143

In Section C a discussion of range resolution, and how such reso-
lution depends on processing technique as well as pulse duration is
presented. This effect is frequently overlooked when considering
puls·! radiation backscattered from distributed targets. The advan-
tages and disadvantages of using long and short transmit pulses for
DIAL measurements, and the effect of pulse duration and chirp on the
measurement accuracy are also analyzed.

Results of the analysis of atmospheric returns are contained in
Section D. The first part of this section contains a brief analysis of
the sources of temporal fluctuations in the backscattered return, and
shows how the various effects can be analyzed individually. In Part 2
examples of a statistical analysis of the aerosol-backscattered signals
are shown. Ensemble and temporal statistics of the returns from dif-
ferent ranges, at both high and low CNR, are also presented. Because
the need for averaging or filtering of returns is inherent in the DIAL
technique, the expected improvement in measurement accuracy to be
gained is discussed. Range-resolved DIAL measurements require calcula-
tion of power ratios, hence statistics of ratio estimates are also exa-
mined. In all, this section provides a fundamental tutorial on the
properties of coherently-detected lidar returns from atmospheric
targets.

A. EQUIPMENT DESCRIPTION

We first describe the NOAA lidar system components and opera-
tional characteristics. Since the lidar was developed primarily as a

144

wind-velocity measuring sensor, the requirement for frequency stability
in both the transmit pulse and at the receiver had a major impact on
the system design. The transmitter has to operate on a single longitu-
dinal cavity mode so as to limit frequency uncertainty to less than 200
kHz (corresponding to ~ 1 m s^{-1} velocity measuring uncertainty). Fre-
quency instability within the pulse must also be minimized. At the re-
ceiver, the local oscillator laser frequency must stay within 200 kHz
of the transmit pulse frequency over the time interval during which
backscattered data is received (typically about 200 μs). These
requirements necessitate active control of both the transmitter and
local oscillator laser cavities, as well as special considerations in
overall design of the transmitter cavity. If the lidar system had been
designed strictly for coherent DIAL species measurements, frequency
stability constraints could have probably been relaxed. However, since
one important aspect of coherent DIAL is the capability to measure
measuring species movements as well as concentration, an operational
coherent DIAL system would probably be designed to maintain reasonably
tight frequency uncertainty requirements.

The operating specifications of the NOAA system are listed in Table
4.1. As shown in Fig. 4-1, the system employs a hybrid-TE (Transverse
Excited) configuration to maintain tight transmitter frequency stabi-
lity. In this configuration the bulk of the transmit energy is pro-
vided by the UV pre-ionized TE laser, which operates at 490 mm pressure
to produce 60-150 mJ per pulse. A low-pressure continuous-wave (CW)
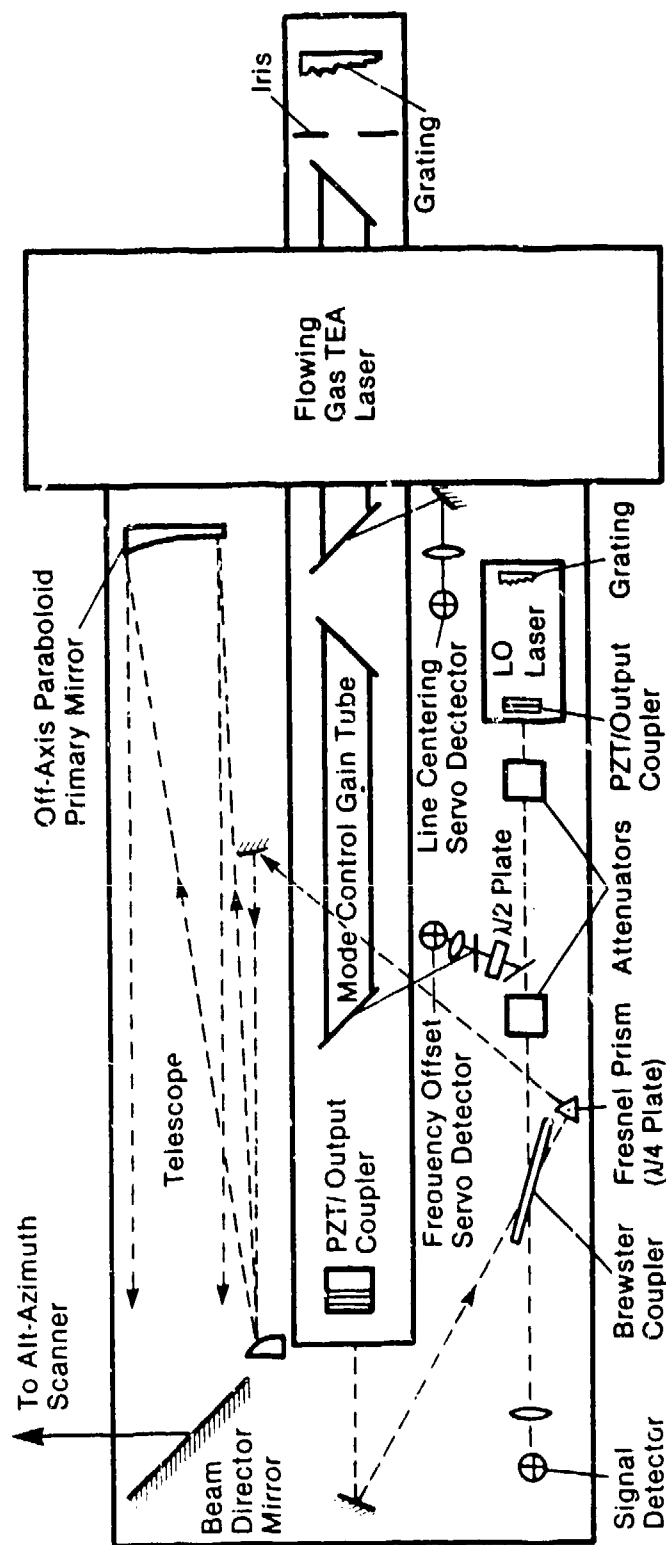
145

PULSED DOPPLER LIDAR OPTICAL CONFIGURATION

Fig. 4-1 – System schematic showing hybrid TEA transmitter, optics, and heterodyne receiver.

laser operates within the TE cavity to provide frequency control. Its frequency is actively maintained on the center of the lasing line by means of a hill-climbing servo-loop, in which a piezoelectric transducer (PZT) is sinusoidally excited at a rate of 8 kHz to modulate the laser cavity length. A detector monitors the CW output power, which varies periodically as the cavity resonance frequency sweeps across the CO_2 gain curve. This detected CW output power signal is compared to the original excitation waveform in a phase-sensitive detector (PSD). When the two waveforms are in-phase (out-of-phase) the cavity PZT is driven to lengthen (shorten) the cavity, such that the cavity resonance frequency coincides with the peak of the CO_2 gain line.

Table 4.1. NOAA lidar system parameters

Transmitter	
Pulse energy	100 mJ
Pulse duration	nominal 2 µs
Pulse repetition frequency	10 Hz
Frequency control	Hybrid-TE configuration; closed loop servo control
Telescope	
Type	Off axis paraboloid
Primary diameter	28 cm
Focal length	202 cm
Receiver	
Detector	HgCdTe photodiode
Local oscillator	Discharge-Excited CO_2 laser
Bandwidth	10 MHz
Intermediate frequency	20 MHz
Computer controlled scanner 2-axis	
Pointing accuracy	.1 degree

Because radiation from the CW laser is present within the TEA cavity when the TE laser is energized, the TE laser output is preferentially seeded to operate on the cavity mode at line center. Insufficient gain is present within the cavity to permit la: ng on other modes. Within the cavity, Brewster-angle windows ensure that the output pulse is linearly polarized. The NOAA laser typically operates at pulse repetition frequencies of 1-15 Hz. Pulse duration and output energy can be controlled somewhat by modification of the gas mixture. Normally a 7:1:1 mixture of $He:N_2:CO_2$ is employed, which produces transmit pulses of approximately 2 μs duration.

The path of the transmit pulse through the system can be traced around the schematic in Fig. 4-1. After exiting the laser cavity, the pulse passes through a germanium Brewster plate that serves as the system transmit-receive (T/R) switch, and into the ZnSe Fresnel prism. The Fresnel prism acts as a quarter-wave plate to change the polarization of the output radiation from linear to right circular by retarding the slow-axis component. Next, the pulse is directed into the parabolic-parabolic off-axis telescope. At this point the beam is expanded at the telescope secondary such that the e^{-2} points of the transverse beam power profile occupy 107% of the 28 cm primary mirror diameter. Rye [111] showed that degradation in CNR due to truncation of the Gaussian shaped beam of the telescope is minimized when the e^{-2} points are at 81.5%; thus the NOAA system is not quite optimal. The off-axis telescope configuration in common with the T/R switch provides

75 dB of isolation between transmitter and receiver. This is suf-
ficient to prevent detector damage.

After passage through the telescope the transmit pulse exits the
trailer through either a roof-mounted scanner or side window, and pro-
pagates outward through the atmospheric aerosol. As the pulse propaga-
tes a portion of its energy is scattered back toward the lidar by the
individual aerosol particles. Upon reaching the system telescope, the
scattered energy is collimated and directed back through the system
transmit/receive optics. Since during the return passage through the
Fresnel prism the slow-axis polarization component is again retarded by
1/4 wavelength, the prism changes the polarization of the backscattered
radiation from circular to vertical. This energy is thus reflected by
the Brewster angle T/R switch and directed onto the signal detector.
By coating the germanium Brewster plate with a reflective coating
approximately 99% reflection efficiency is obtained at the T/R switch.

The typical power across the detector from atmospherically
backscattered signals is on the order of 10^{-12} W. This power is
coherently mixed with the energy from the system LO (local oscillator)
to form a beat signal. In the NOAA system the LO is a low-pressure,
discharge-excited CW laser whose frequency is offset by 20 MHz relative
to that of the transmit pulse. Tight frequency control of the LO is
maintained by means of a second servo-loop. In this loop the radiation
from the LO and CW mode control lasers are mixed on the frequency-
offset detector and capacitively coupled into a frequency modulation

149

(FM) discriminator whose output is zero volts when the input signal frequency is 20 MHz. This discriminator output is used as an error signal to drive a PZT at one end of the LO cavity, maintaining a constant "lock" at 20 MHz offset.

When the TE laser fires, both servo-loop detectors are saturated due to the large peak powers present. To prevent the servo-loop from responding to the resulting transients, the error inputs to the PZT drivers are frozen immediately prior to the transmit pulse output, then held constant for approximately 40 ms. This provides time for the mode control laser to be re-pumped and stabilize (mode cell lasing is quenched by the TE pulse). After 40 ms he loops are closed, providing time for them to stabilize prior to the next pulse.

A liquid nitrogen cooled 2-mm diameter photodiode serves as the system detector. The diode is reverse-biased with 1.5 ma of reverse current in order to enhance system bandwidth. Operating irradiance level of the local oscillator was determined empirically by examining the CW signal reflected from a rotating disk and maximizing the CNR as a function of irradiance level. We also measured the detector response curves as a function of incident LO energy. The optimum operating point was at the edge of the saturation region; i.e., an incremental increase in LO power beyond the operating point pushes the operating point into a nonlinear region. Because of this potential source of error the LO irradiance level is constantly monitored and adjusted during the course of a measurement.

150

The capacitively-coupled detector-output electrical signal is fed into a low-noise (<1 dB noise figure), wide-band preamplifier. This preamplifier is shown along with the rest of the data sampling system in Fig. 4-2. To prevent saturation of the downstream signal amplifiers, the high and low-pass filters in the front-end section limit the noise bandwidth to approximately 25 MHz. After amplification the signal passes into a complex demodulator, where an electrical 20 MHz reference signal is mixed with the backscattered signal to produce in-phase and quadrature components of the Doppler-shifted signal at baseband. This complex demodulator configuration is employed because of its flexibility (the demodulator can be easily adjusted to changes in the IF frequency by tuning the reference signal) and because baseband operation permits the use of commercially available low-pass filters with very flat frequency response (less than 0.5 dB ripple) and sharp cutoffs. A flat system frequency response, such that the noise spectrum is as white as possible, is necessary for good velocity estimation sensitivity at low CNR. The low-pass filters on the demodulator outputs serve as anti-aliasing filters prior to digitization.

The in-phase and quadrature returns from each pulse are digitized at a maximum rate of 10 megawords/s (complex) using dual 8-bit A/D convertors. Since up to 4096 complex samples can be digitized per pulse, the return can be continuously sampled to ranges of 60 km, which is well beyond the maximum system range. The digitized returns are read into the NOVA memory via direct memory access and subsequently dumped

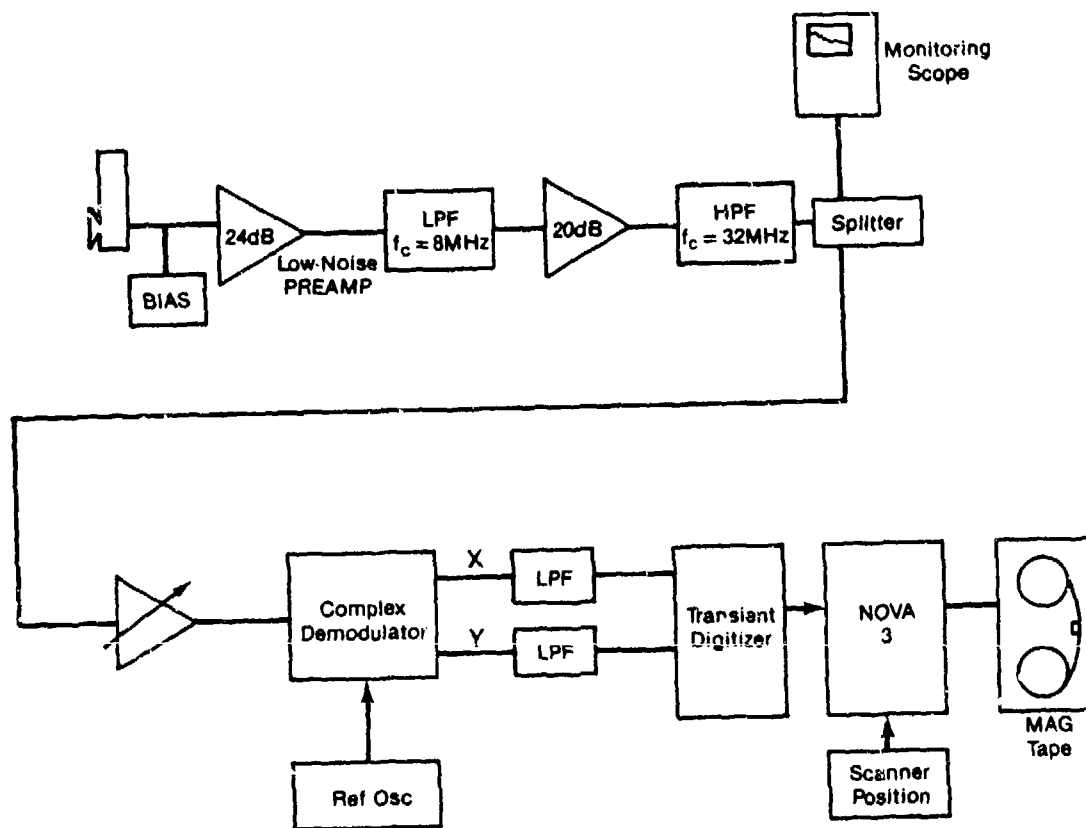151

LIDAR DATA HANDLING SYSTEM

Fig. 4-2 — NOAA lidar data sampling system.

to magnetic tape. Limitations on the speed of the tape-transfer restrict system pulse repetition frequency to a maximum of approximately 12.5 Hz. The use of 8 bit A/D convertors limits system dynamic range to ~45 dB; in the clear air this is generally sufficient, as discussed in Section D.

B. PULSED SYSTEM OPERATING CHARACTERISTICS

In order to predict the measurement capability of the lidar system for any remote parameter measurement, it was first necessary to specify its important operating parameters and stability characteristics. Several measurements were performed on the system to quantify important parameters such as transmit pulse amplitude and phase characteristics, system variability from pulse-to-pulse and over, and absolute calibration. Results of these measurements and their effect on measurement accuracy are discussed in the remainder of this section.

The properties of the lidar pulse were examined by observing the pulse both directly and following reflection from a stationary target. When the transmit pulse travels outward through the system optics, a very small portion of its energy is invariably reflected back along the optical path. This reflection, which occurs because the reflective and transmissive elements are not perfect, typically saturates the detector under normal operating conditions. The presence of this impulse of energy on the detector, and the ensuing time required for the detector to come back out of saturation, determine the minimum range of the

153

system. In the NOAA system detecto recovery time is roughly 10 μs, giving a system minimum range of approximately 1.6 km.

To monitor the pulse it was necessary to reduce the optics-reflected energy so that the signal energy did not saturate the detector. Two Brewster-angle type optical polarizers were inserted directly in front of the laser output coupler to provide the necessary attenuation. Total optical attenuation due to the two polarizers and a third located directly before the detector's focusing lens was approximately 105 dB. Because it was necessary to monitor both amplitude and phase of the transmit pulse, the reflected energy war mixed coherently with the LO field. The resulting 20 MHz beat signal between the two pulses was amplified, demodulated and digitized as described in the preceding section. We carefully monitored the front-end output signal to ensure that the detector did not saturate.

Characteristics of 6000 consecutive pulses transmitted at a 10 Hz rate were digitized providing a data set corresponding to 10 minutes of laser operation. Pulse amplitude was calculated every .1 μs by taking the square root of the sum of the squares of the in-phase and quadrature components. Similarly, frequency was calculated for each sample point from

$$f = \frac{\phi_k - \phi_{k-1}}{\Delta t} \tag{4.1}$$

where

154

$$\phi_k = \tan^{-1} \frac{Y(k)}{X(k)}$$

and $X(k)$ and $Y(k)$ are the digitized baseband in-phase and quadrature
signals.

Figure 4-3 shows the measurements of mean pulse amplitude and fre-
quency vs. time for three 80 s intervals. Each averaging interval was
separated by 80 s. The plots give an indication of the variability in
the pulse properties over time periods roughly equivalent to those
employed when averaging multiple returns for the sequential DIAL
measurements described in the next chapter. The pulse amplitude plot
shows the familiar gain-switched spike and decaying tail common to TE
laser pulses, while the frequency plot shows a u-shaped chirp curve in
which the instantaneous frequency rapidly increases at the beginning of
the pulse, settles back to near the zero, then increases again in the
tail of the pulse to values as high as 2 MHz. This chirp behavior is
similar to that predicted by Willets and Harris [112], who postulated
that the initial chirp results from the presence of free electrons in
the discharge region, while the quadratic-shaped chirp in the pulse
tail is produced by heating of the TE chamber gases. Byron [113] com-
pared the measured chirp characteristics of a number of CO_2 TE systems,
including the NOAA lidar with those predicted by the Willetts and
Harris scaling parameters. In general, the observed chirp closely
followed the predicted values.

Although retaining approximately the same shape, the levels of the
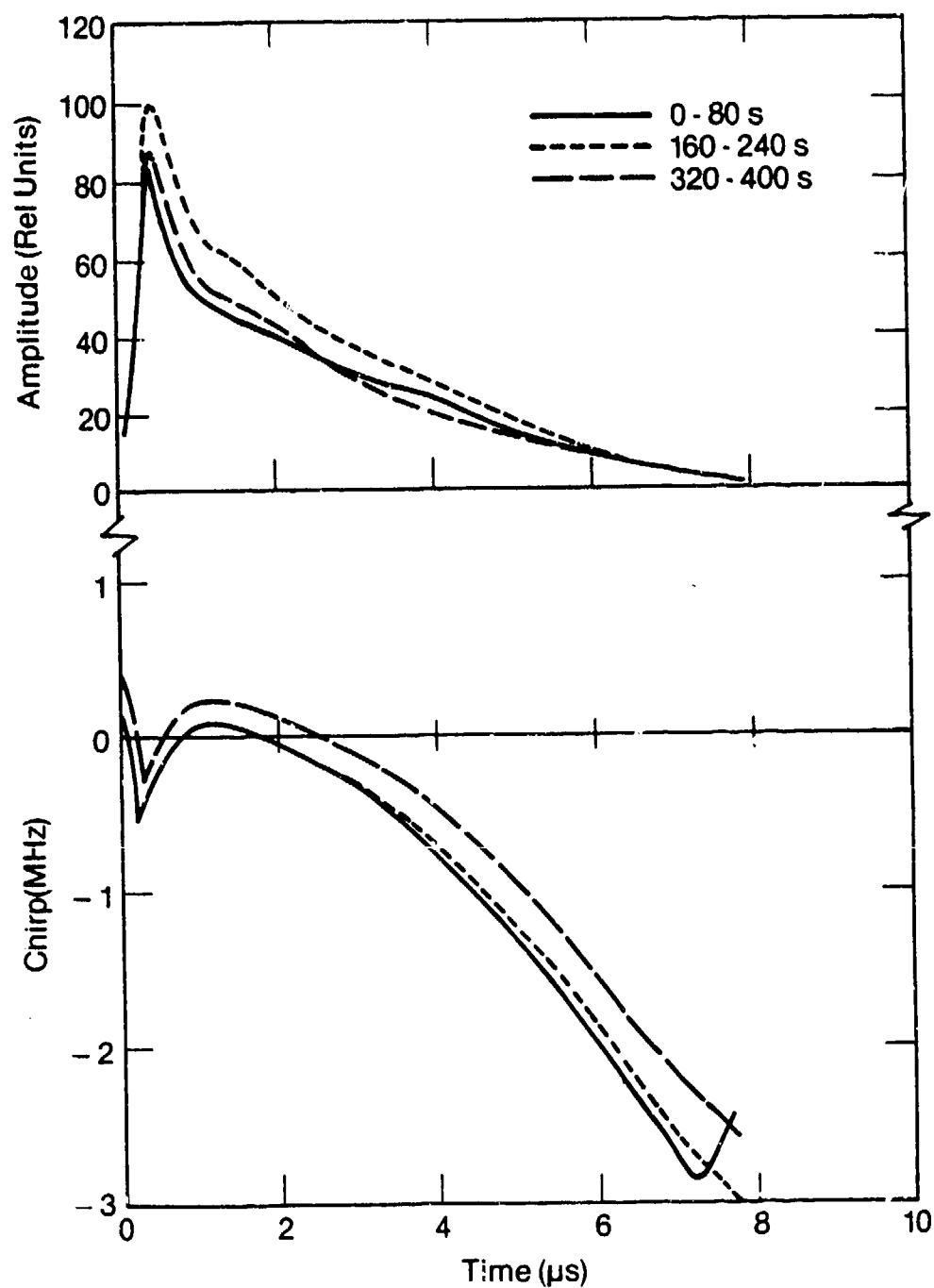curves for the different averaging periods are seen in Fig. 4-3 to vary

155

Fig. 4-3 — 80-s averaged pulse amplitude and frequency for 3 sampling
intervals. Each sampling interval was separated by 80 s.

by as much as 10% of full scale (amplitude) or 200 kHz (frequency). This illustrates the need for pulse-normalization in those measurements which require absolute (as opposed to relative) estimation of backscattered irradiance, such as atmospheric backscatter coefficient β and sequentially tuned path averaged DIAL measurements. For range-resolved DIAL measurements the need for normalization is not so strong, because of the relative nature of the measurement. This point is discussed further in Section D.

Variability of both the pulse energy and mean frequency over longer time scales is shown in Fig. 4-4. Here pulse energy was calculated as the sum of the measured powers in the instantaneous samples, while frequency was estimated using the familiar pulse-pair estimator [114]. Each point represents an average of 10 single-pulse measurements, hence short-term fluctuations are smoothed out. The plots show significant variation in both pulse energy and mean frequency over the 10-minute observation window. Mean energy varies by as much as 40% around the long-term average, while frequency drifts slowly over an interval of approximately 400 kHz ($\sim$2 m s^{-1}). Interestingly, the long-term energy and frequency drifts seem to occur over different time scales during the measurement. As is obvious from the figure, measured energy fluctuated with approximately a 2-minute time scale, while frequency drifts at a rate about 3 times slower. The reasons for these long-term drifts have not been explained at present. In conversations with laser system developers it was suggested that the drifts may be due to fluctuations
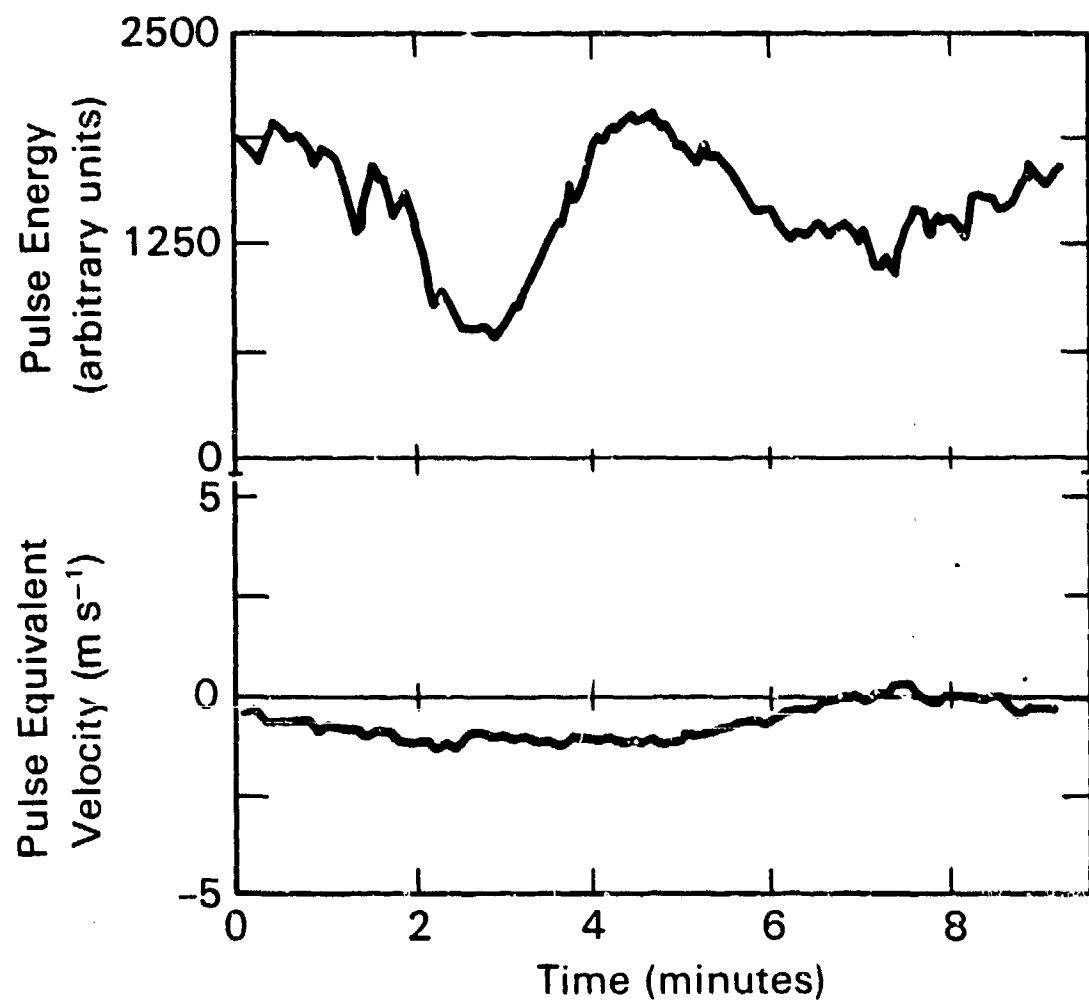
157

Fig. 4-4 – Time series of energy and mean frequency of NOAA transmit
pulse. Each point represents an average of 5 pulses.

in the high-voltage power supply for the TE laser, or changes in the ambient temperature to which the TE laser dumps its heat. These hypotheses are presently being investigated. Because the measurements were performed coherently, changes in LO amplitude could also produce the observed behavior. During these measurements, however, the LO irradiance level and offset frequency were carefully monitored, hence the probability is high that the cause of the drifts is in the TE section of the system. Elimination or compensation for the fluctuation in measured pulse characteristics is crucial for measurement of important meteorological parameters such as structure functions, perturbation spectra, etc.

A second method of examining pulse characteristics, as well as calibrating system performance, was to observe the return from a large sandpaper-covered disk. Calibrations from such targets compared to standards were examined in a previous work [115]. The individual returns from the disk were digitized and power calculated at each point in the digitized return. Because single returns show the effect of speckle, 500 records were averaged in both the time and spectral domains to characterize pulse properties. Figure 4-5 shows the speckle in two individual returns as well as the 500-pulse average reflected power. The pulse power profile agrees well with that measured directly and discussed previously. As shown in similar measurements using a CW transmitter [116], the time scale of the speckle fluctuations varies inversely with the radial velocity gradient across the irradiated spot on the large disk.
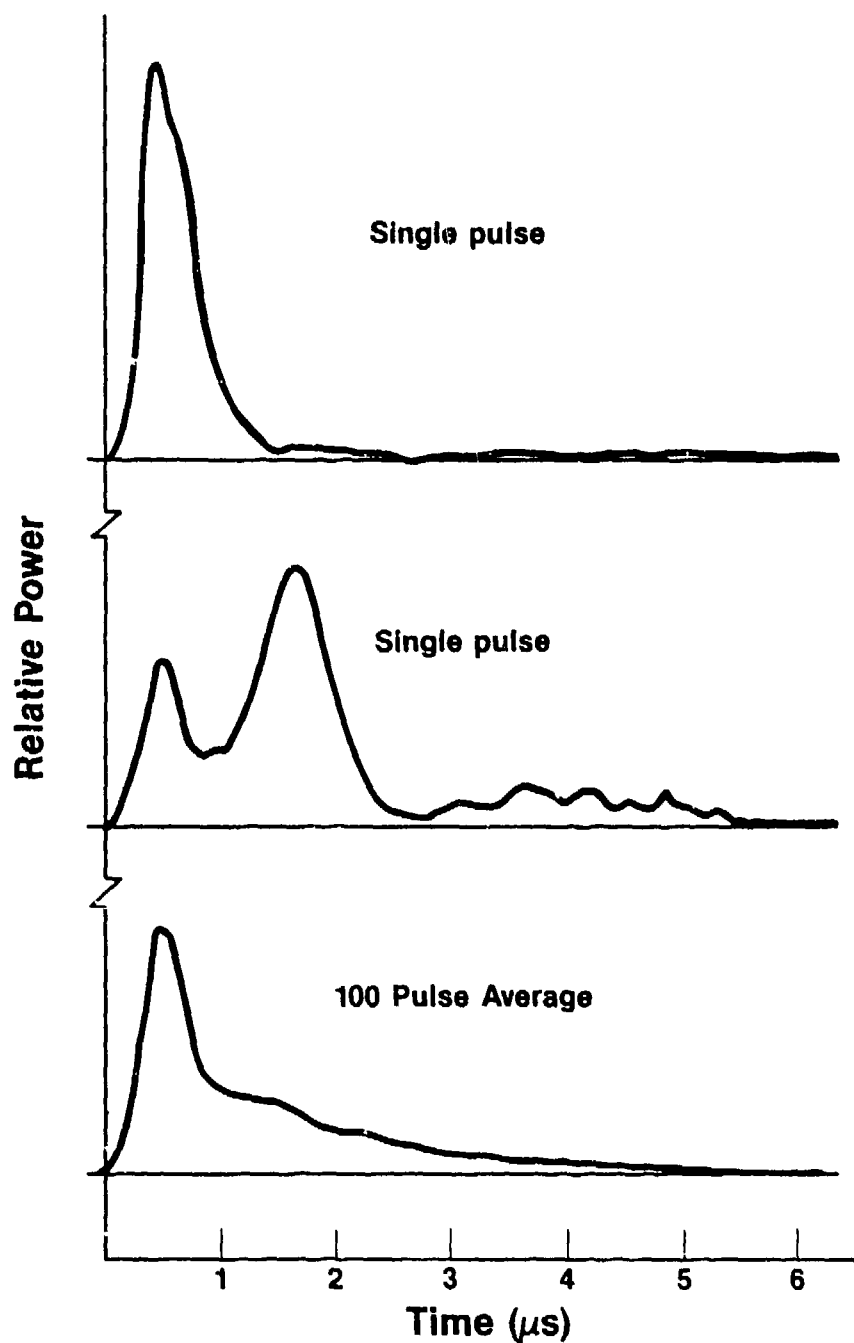
Fig. 4-5 – Received power versus time for signal reflected from large
disk. Top traces are individual returns showing effect of
speckle. Bottom trace is average of 100 returns.

160

By computing the Fourier transform of the disk return and averaging in the spectral domain over 500 shots, the frequency characteristics of the system transmit pulse can be examined. From Fig. 4-6, it is seen that the power spectrum is asymmetric. The bulge in the spectrum on the high frequency side of the main lobe is due to the chirp. Note that because most of the chirp occurs in the tail of the pulse the percentage of total energy in the bulge is small. Graphically, it was determined from Fig. 4-6 that approximately 85% of the energy was contained within a 375 kHz bandwidth. Typically atmospheric returns exhibit a wider bandwidth due to the broadening effects of shear and turbulence. This subject is discussed further in Sec. D.

Returns from the large disk are also used to check system calibration, as described by Post et al. [110]. Essentially, the measured average CNR of the disk return is compared with the expected value calculated from

$$CNR = \frac{\eta P_t A_1 A_2 A_3 A_4 A_5 \ a^2 \rho_r \cos\alpha \ K}{h \nu BL^2} \tag{4.2}$$

where

η =   detector quantum efficiency

P_t =   peak pulse power (3.6×10^4 watts)

A_1 =   round trip optical loss

A_2 = CO_2 gaseous absorption loss factor (.76)

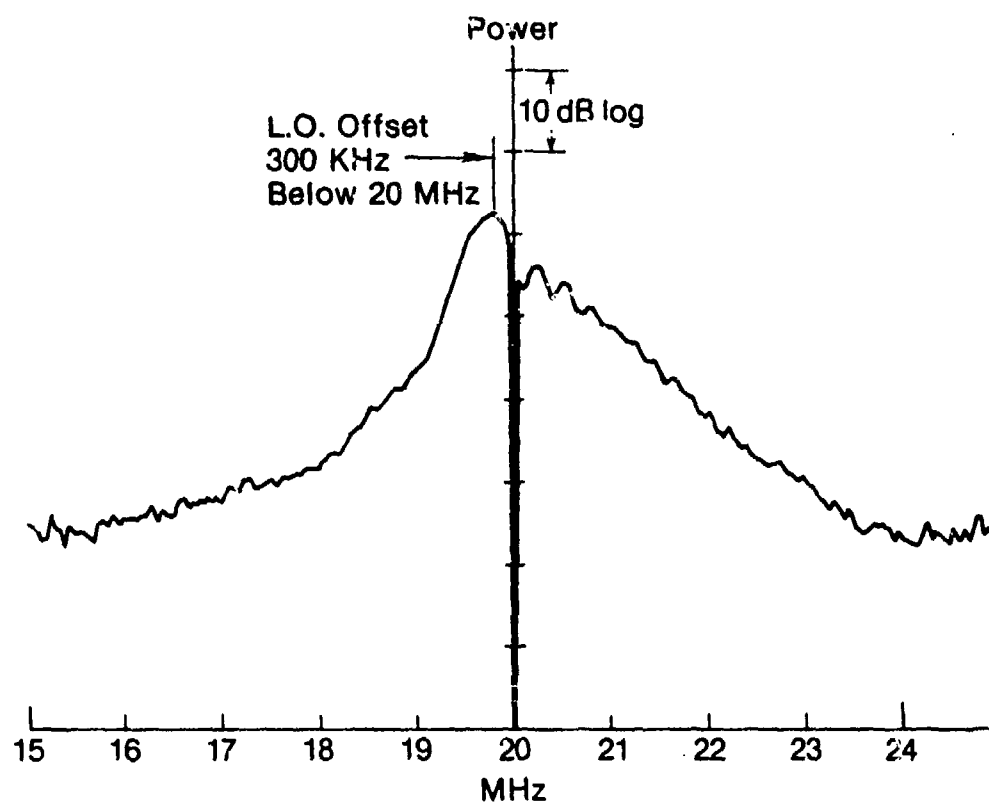A_3 = H_2O gaseous absorption loss factor (.95)

161

Fig. 4-6 - Averaged power spectrum (500 pulses) of return from large
disk showing asymmetry caused by chirp in the tail of the transmit
pulse.

A_4 = Gaussian beam truncation loss factor (.29)

A_5 = shot noise correction loss factor (.5)

a = e^{-2} Gaussian beam radius of telescope output (0.15 m)

ρ_r = total reflectance of target

α = angle of incidence, scattering from target

K = unexplained losses (determined to be 0.2)

$h\nu$ = photon energy (1.88×10^{-20} J)

B = receiver bandwidth (10^7 Hz)

L = range to target.

The measured CNR is consistently 1-2 dB below that predicted in Eq. (4.2). Some of the discrepancy can probably be explained by inexact value of the assumed quantum efficiency of the HgCdTe detector (the manufacturer's specified value was used, which may not be valid for the NOAA system operating conditions) as well as mismatches in signal/LO beam sizes, wavefront matching, etc., which reduce heterodyne efficiency.

The typical mode of operation for data collection is to align the system just prior to commencing measurements, then operate the system and collect data for periods ranging from 15 minutes to a couple of hours. Because thermal control is not perfect within the lidar van, particularly on hot sunny days, changes in optical path lengths may gradually cause the system to go out of alignment. To determine a limit on system degradation due to misalignment, the beam was deliberately misaligned at various points in the optical path. Typical

misalignments were on the order of a cm, much greater than would generally be encountered during operation. Even under these extreme conditions system CNR (as measured from disk returns) was not reduced by more than 3 dB for misalignment at any of the points considered. Although one might expect misalignment errors to be somewhat cumulative, a general observation from these results seems to be that uncertainties in system sensitivity due to misalignment are probably negligible for measurements taken within a reasonable period following an alignment. "A reasonable period" in this case depends on the ambient temperature stability inside the trailer.

C. SYSTEM RANGE RESOLUTION

Having measured properties of the NOAA lidar transmit pulse, the effect on equivalent system range resolution is examined. Range resolution is important in atmospheric DIAL measurements when transmit-pulse lengths are of the same length-scale as the DIAL resolution volume. The standard lidar ranging technique is to time-gate the return signal and assume that uniform temporal separation of points implies uniform range separation. This assumption may not be true when pulses are long, if the backscatter medium is highly structured, or at ranges very near the receiver. To demonstrate this the return at time t is examined as a function of backscatter profile, transmit pulse characteristics and receiver filtering. Since the purpose of this analysis is to examine resolution, errors in measured power due to speckle and other noise sources are neglected.

164

Consider the system transmit pulse profile shown in Fig. 4-3 where
t = 0 at the instant the first power exits the lidar. At time t the
pulse has propagated to a range R = ct/2, backscattered from that
range, and returned to the transceiver. Thus, the mean return power at
time t from range R is given by

$$\overline{P}_r(R,t) = K_s(R) \ \overline{P}_t(\frac{ct}{2} - R) \ \beta(R) \quad , \tag{4.3}$$

where $\overline{P}_t(ct/2 - R)$ is the mean power versus range profile of the trans-
mit pulse, $\beta(R)$ is the mean backscatter coefficient at range R, and
$K_s(R)$ includes system and range-dependent constants in the lidar
equation. Since in general the detector output signal is filtered or
averaged in the receiver, the filtered signal from a given range R is
the convolution of the input signal with the filter impulse response

$$\overline{P}_f(R,t) = \beta(R) \ K_s(R) \ \int h(\frac{c(t-\tau)}{2}) \ \overline{P}_t(\frac{c\tau}{2} - R)d\tau \tag{4.4}$$

$$= \beta(R) \ G(R,t)$$

where $h(ct/2)$ is filter impulse response in range coordinates. The
function $G(R,t)$ may be thought of as the system range-weighting func-
tion at time t, dependent on transmitter and receiver characteristics,
and propagated to range R. Equation (4.4) can be employed to determine
the equivalent range weighting of the return at time t; i.e., answering
the question "where does the return come from?". Given the NOAA lidar

165

pulse power profile measured in Sec. B, the system range–weighting function $\overline{G}(R)$ can be calculated assuming the receiver consists of a block averaging filter of the form

$$h(t) = 1 \qquad 0 < t < \tau_f \qquad\qquad (4.5)$$
$$ 0 \qquad \text{otherwise,}$$

such that

$$h(R) = 1 \qquad 0 < R < c\tau_f/2$$
$$ 0 \qquad \text{otherwise.}$$

Figure 4-7 shows the computed $G(R)$ for τ_f = 2.2 µs, 3.3 µs and 6.6 µs assuming $t = 2R/c$. As the averaging time (observation window) τ_f increases the pulse effectively smears in range and resolution becomes poorer. As τ_f approaches zero the maximum resolution, equivalent to the spatial representation of the transmit pulse, is approached. In actual measurements the backscatter varies with range, and the system range–weighting function $G(R)$ must be multiplied by $\beta(R)$ for the actual range–weighting function. In addition to applicability in irradiance estimation, Eq. (4.4) is valid for determining the range–weighting function of backscattered frequency estimates when the measurement algorithms employed calculate the mean of the Doppler spectrum. Examples of such Doppler estimators are pulse–pair and Fourier transform type processors.

In ground–based DIAL measurements the effect of long pulses is probably most severe at ranges closest to the receiver. Backscatter
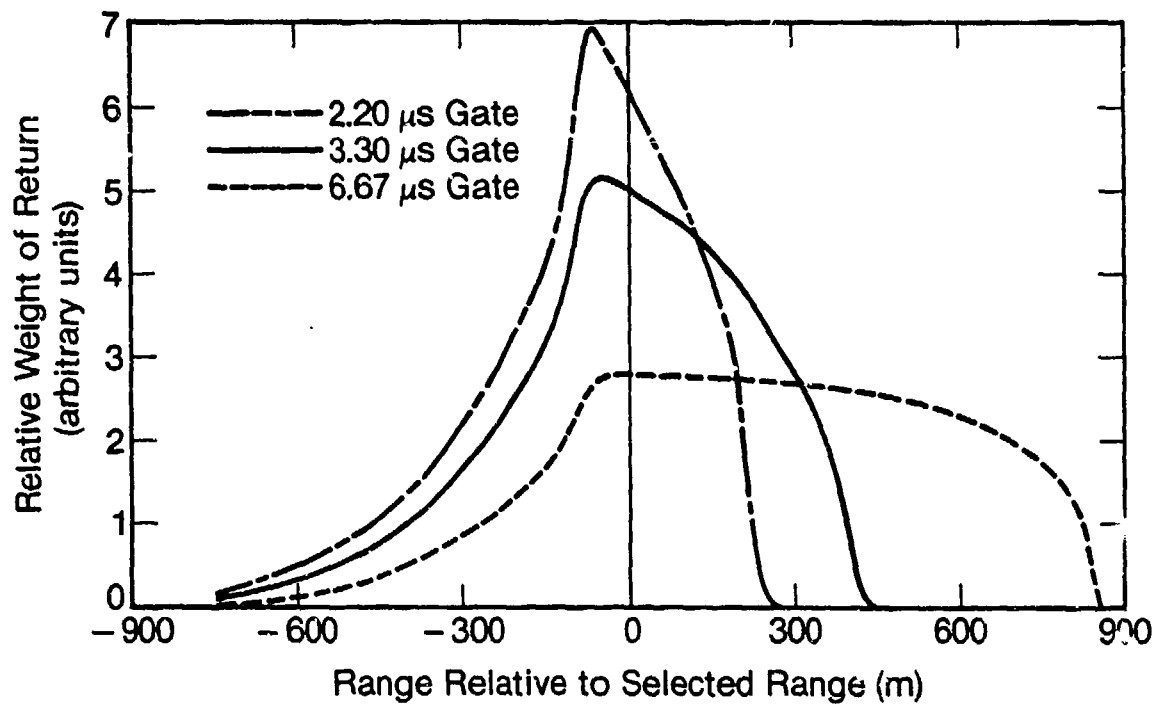
166

Fig. 4-7 – Range weighting function of returns from NOAA lidar, assuming
constant backscatter, for 3 uniformly-weighted processing windows.

167

ficient typically decreases steadily with height above the planetary boundary layer [85]; data collected with the NOAA lidar indicates this falloff may be quite steep. In addition, range-squared effects, which reduce signal level by a factor of 4 with every doubling of range, are most significant close to the lidar. The potential combined effect of these phenomena is to displace toward the receiver the centroid of the first range cell relative to that of the next cell. Thus, the DIAL measurement cell ΔR is lengthened, and more attenuation occurs between the two time-gated samples than is included in the ΔR term of Eq. (3.1). Under such conditions the concentration will be overestimated at closer ranges.

This disadvantage of long pulses is somewhat offset, in sequentially tuned DIAL measurements, by improved spatial averaging of large-scale random backscatter fluctuations. In sequential measurements the mean backscatter power should ideally be measured over a statistically stationary segment, so that the data sampled is representative of the general process statistics. If large-scale backscatter variabilities exist in the atmosphere at times when winds are light, the time required for a single perturbation to advect past a fixed point may be many minutes. For a point sensor to average the sampled measurements of the data in order to obtain a meaningful result, an observation period at least as long as the characteristic advection time of the large-scale variation is required. Spatially-long lidar pulses observe and effectively average returns from a large area during every pulse, reducing the need for long observation windows.

168

Consider a random, homogeneous backscatter field versus range $\beta(R)$ which has a mean associated spatial spectrum $\bar{\phi}_\beta(k)$, where $k = 2\pi/R$. As shown in Eq. (4.4), the instantaneous received signal at time t can be modeled as the output of a linear system whose input is the function $\beta(R)$ and which has a spectral impulse response equal to the spatial profile of the transmit pulse. Then the mean output energy spectrum is

$$\bar{\phi}_{P_r}(k) = \bar{\phi}_\beta(R) \; \left|F_{P_t}(k)\right|^2 \tag{4.6}$$

where $\left|F_{P_t}(k)\right|$ is the amplitude of the Fourier transform of the spatial pulse power profile $P_t(R)$. If a filter or averaging operation occurs at the receiver then the equivalent fluctuation spectrum of the return is

$$\bar{\phi}_{P_f}(k) = \bar{\phi}_\beta(k) \; \left|F_{P_t}(k)\right|^2 \left|F_h(k)\right|^2 \tag{4.7}$$

where $\left|F_h(k)\right|$ is the transform of the filter impulse response translated into spatial coordinates $h(R) = h(t)\big|_{t \,=\, 2R/c}$. Since longer transmit pulses imply narrower bandwidths on $\bar{\phi}_{P_f}(k)$, more filtering of the variations due to random, isotropic fluctuation in backscatter takes place, and the expected variance in the power measurement is reduced for sequentially-tuned measurements spaced in time.

As discussed above further reduction in variance is also obtained when multiple pulses are averaged. During the course of the shot sequence the wind advects large-scale inhomogenieties through the path. Thus, an atmospheric filtering function can be defined as

$$h_A(R) = 1 \qquad R < vT_m \qquad\qquad (4.8)$$
$$ 0 \qquad \text{otherwise}$$

where v is mean wind speed and T_m is total time required for the
multiple pulse measurement. As an example, if $v = 5 \text{ m s}^{-1}$ and $T_m = 100$
s, $h_A(R)$ is equivalent to a 500 m long average. Since this is of the
same order as the pulse spatial filter weighting functions when the
pulse duration is 3.3 μs, the advantage of long pulses for atmospheric
filtering can be seen.

When system range resolution is a primary consideration, the most
direct method is to shorten the transmit pulse duration. Generally
with the TE laser system this is performed by reducing the percentage
of nitrogen in the gas mix. One disadvantage of such a technique is
that output pulse energy is usually reduced as well. A potential
alternative method is to take advantage of the chirp in the pulse by
applying pulse compression and matched filtering techniques commonly
employed in radar processing. In the following paragraphs the feasibi-
lity of employing these techniques to improve resolution of the NOAA
lidar is briefly examined.

In radar processing, the optimum receiver is designed on the basis
of the matched filter criterion. A stored replica of the transmitted
pulse is either correlated with the received signal, or alternatively
used as the impulse response of a filter in the receiver. Either
implementation produces an output signal which is proportional to the

170

cross correlation between the transmit pulse and the received signal. In addressing the capability of a system to resolve returns both in velocity and range, the basic question is that of comparing the receiver output for returns differing in both range and velocity. If returns at different ranges and/or velocities produce a similar receiver response, ambiguity exists and the system cannot resolve the difference in return characteristics.

The commonly used method of specifying the range and velocity resolution capability of a matched-filter receiver is the radar ambiguity function $\chi\ (t_R, f_d)$ defined as [117]

$$|\vec{\chi}(t_R, f_d)| = | \int \vec{E}_t(t)\ E_t^*(t-t_R)\ \exp(j2\pi\ f_d t)dt | \qquad (4.9)$$

where $\vec{E}_t(t)$ is the transmit pulse, and t_R and f_d represent time (range) and frequency (velocity) differences. Figure 4-8 shows $\chi(t_R, f_d)$ for the NOAA lidar transmit pulse. Since plotting the ambiguity function ideally requires three dimensions, contours are used to illustrate magnitude of $\chi(t_R, f_d)$. The value of $\chi(t_R, f_d)$ gives the output of the receiver for a return from range R and velocity v relative to the output for a return of the same intensity for which the receiver is matched. We see that the 3dB (half-power) contour encircles a region bounded roughly by range = ± .2 km and velocity = ± 1 m s^{-1}. The contours follow a slight diagonal tilt from lower left to upper right; this is due to the chirp in the tail of the pulse and is characteristic of FM-chirped waveforms. Neither resolution bandwidth nor spectral resolution is improved significantly over the values
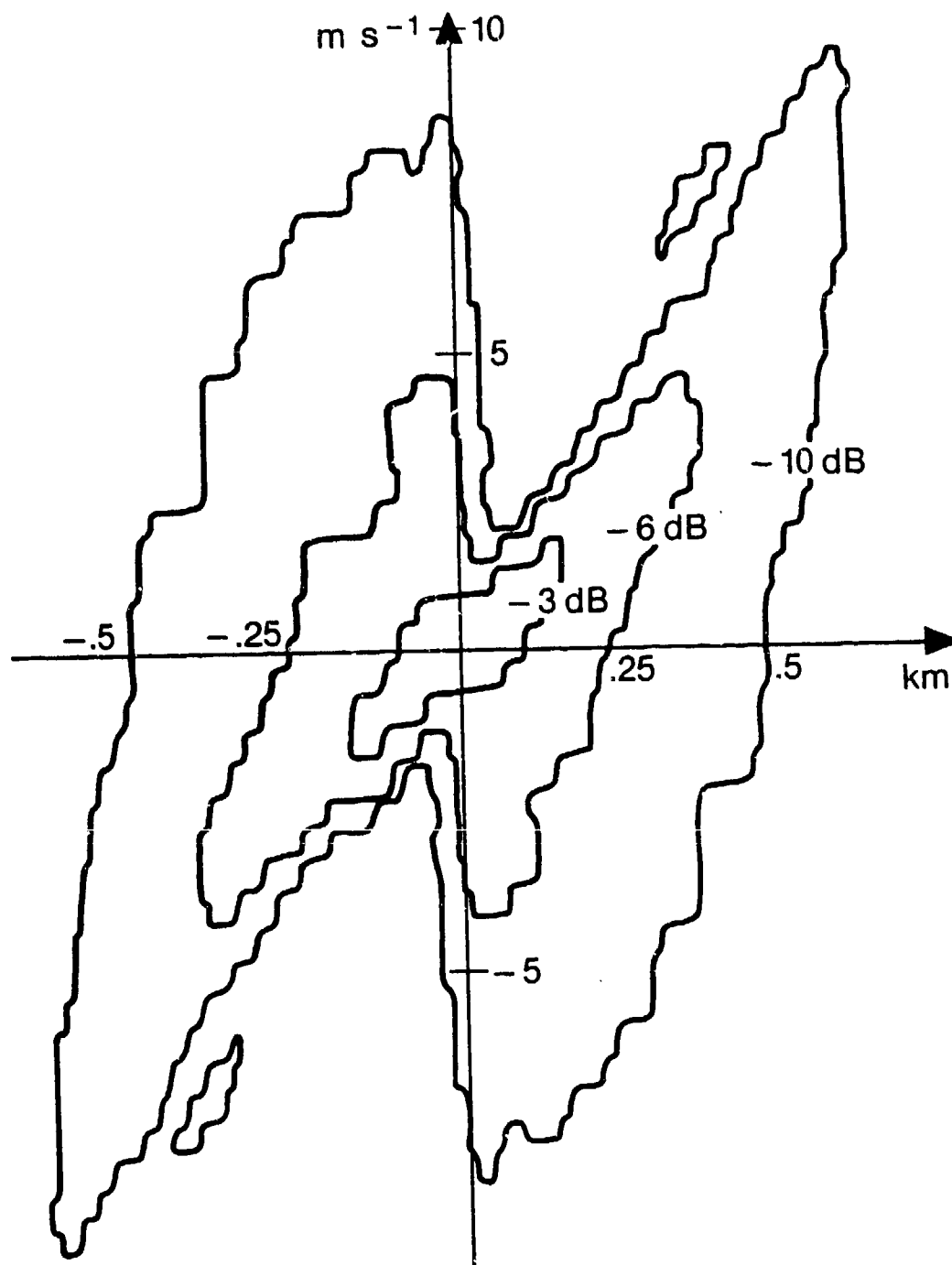
171

Fig. 4-8 – R dar ambiguity function calculated from NOAA lidar transmit
pulse.

172

calculated using conventional time gating (Fig. 4-7) or Fourier spectral processing (Fig. 4-6). Fourier analysis with uniform weighting of the returns, as in Fig. 4-6, is equivalent to matching the return to a rectangular transmit pulse with no chirp, thus it does not represent an optimal receiver for the NOAA pulse. Since the predicted resolution improvement to be gained by using to a matched receiver is minimal, however, the chirp in the pulse tail apparently has a relatively minor effect on overall system performance.

It should be noted that a matched filter does not represent the ideal pulse compression receiver for the NOAA lidar pulse. The ideal filter h(t) is that which gives

$$\vec{E}_t(t) * \vec{h}_t(t) \approx 1$$

where $\vec{E}_t(t)$ is the transmit signal and the star indicates convolution. However such a filter, when calculated for the NOAA pulse, will be very noisy because of large gains at higher frequencies. For practical pulse compression the transmit waveform should be designed so that the matched filter and pulse compression filter are identical.

The ambiguity analysis described above is valid for returns from which the signal coherence time is determined by the pulse characteristics. This is often not the case for lidar returns from the distributed aerosol. As shown in previous work using CW lasers [116], relative movement of the individual aerosols limits coherence of the return signal to a few microseconds. Thus application of classic pulse

173

compression techniques, where long pulses are frequency-modulated to increase bandwidth, is generally limited. In such systems the optimum receiver obtains the range resolution through cross correlation with the return over a long observation window. When velocity turbulence in the atmosphere shortens the coherence time of the return, the effective correlation window is shortened and the range resolution is degraded. Coherence properties of atmospheric returns from the NOAA pulsed lidar are examined in the next section.

D. PROPERTIES OF AEROSOL BACKSCATTERED RETURNS

This section describes measurements of the important ensemble and temporal statistics of aerosol-backscattered returns obtained using the NOAA lidar. Such statistics are important for quantifying the expected error in DIAL measurements due to random scintillation in the measured backscatter power. Ensemble statistics provide information on mean, variance and shape of the power probability distribution function, while temporal properties described by the autocorrelation function are critical for selecting and evaluating averaging techniques to reduce error.

During the period between summer 1981, when the NOAA lidar system was first operated, and summer 1983, an enormous data set of digitized returns from atmospheric aerosols was compiled. In many cases analysis of these data showed a strong consistency in the backscattered return parameters. Because of these similarities, in the following discussion

174

results from the analysis of specific data sets are frequently used to illustrate general aerosol-backscattered signal properties. In general, however, many data were extensively examined to characterize each parameter discussed.

1. Effects of fluctuation

Prior to presenting measurements of the ensemble and temporal characteristics of the backscattered lidar signal, the mechanisms which cause signal fluctuations are discussed briefly. The time scales of the fluctuations are especially important, since temporal averaging or filtering is u ually required to reduce uncertainty in the estimate of mean backscattered power. Effectiveness of the averaging/filtering process is a direct function of the characteristic fluctuation time scale.

When a CW lidar is employed for remote sensing as in [116], the atmospheric measurement volume is continually irradiated with coherent energy. The random motions of the individual scatterers produce a Rayleigh phasor whose intensity fluctuates over a characteristic time scale, typically on the order of a few μsec. The net effect of the velocity turbulence within the scattering volume is to randomly modu-late the backscattered signal. Assuming the radial velocity of an individual particle does not change over the measurement interval, the field at the receiver is the superposition of the fields scattered from the individual particles

175

$$\vec{E}_r(t) = \sum_{i=1}^{N} e^{j[\phi_i + (\nu + \frac{2v_{r_i}}{\lambda})t]} \tag{4.10}$$

where ϕ_i is the phase of the scattered signal from particle i, v_{r_i} is particle radial velocity, and ν is the frequency of the transmitted optical signal. Since the primary intent is to look at fluctuation time scales, Eq. (4.10) assumes for convenience that the amplitude of each backscattered signal is unity and ignores focusing effects. If the IF signal is demodulated to baseband, the complex autocorrelation function of the resultant signal is

$$\vec{R}_E(\tau) = \langle \{\sum_{i=1}^{N} e^{j[\phi_i + \frac{2v_{r_i}}{\lambda} t]}\} \{\sum_{i=1}^{N} e^{-j[\phi_i + \frac{2v_{r_i}}{\lambda}(t + \tau)]}\} \rangle$$

$$= \sum_{i=1}^{N} e^{-j \frac{2\langle v_{r_i} \rangle}{\lambda} \tau} . \tag{4.11}$$

Thus, the expected value of the complex autocorrelation function of the composite signal at a given moment is the superposition of the autocorrelation functions of the signals from the individual particles. Since the Doppler frequency shift of each signal is proportional to the radial velocity of each particle, the magnitude spectrum of the received backscattered signal is equivalent to a histogram of radial velocities within the measurement volume. Therefore, the autocorrelation function of the baseband backscattered signal is calculated from the inverse Fourier transform of the velocity probability density function $f_v(v)$ (i.e., the characteristic function χ) as

$$\vec{R}_E(\tau) = \frac{\lambda}{2} \int_{-\infty}^{\infty} f(v) \, e^{-j \frac{2v\tau}{\lambda}} \, dv \ . \tag{4.12}$$

The autocorrelation function of power fluctuations is then

$$R_P(\tau) = \vec{R}_E(\tau) \, \vec{R}_E^*(\tau) = \frac{\lambda^2}{4} \, \chi_v(v) \, \chi_v^*(v) \tag{4.13}$$

where $\chi_v(v) = 2\vec{R}_E(\tau)/\lambda$ is the characteristic function of the velocity probability density function.

Equations (4.12) and (4.13) relate the turbulent velocity distribution to the received-signal spectrum and power fluctuation time scale, given a constant amplitude and phase CW transmit signal. Thus, velocity turbulence within the scattering volume can be estimated from the measured backscattered signal spectrum.

Suppose a modulation signal $\vec{m}(t)$ is added to the transmit signal, such that

$$\vec{E}_t(\tau) = \vec{m}(t) \, A \, e^{j v t} \ . \tag{4.14}$$

The effect of modulation is to insert range discrimination into the return, with the result

177

$$\vec{E}_r(t) = \int_0^\infty \vec{m}(R) \sum_{i=1}^{N(R)} e^{j[\phi_i + (R)\frac{2v_{r_i}r}{\lambda}]} dR \qquad (4.15)$$

where $R = ct/2$, $N(R)$ is the number of particles at range R, and $v_{r_i}(R)$ and $\phi_i(R)$ are the radial velocity and phase of particle i at range R. It is assumed in Eq. (4.15) that the received signal has been demodulated to baseband, and that focusing effects and backscatter coefficients are constant over the measurement volume. Since returns from different ranges are uncorrelated (different scatterers), the correlation function of the return can be shown to be

$$\vec{R}_{E_r}(\tau) = \vec{R}_m(\tau)\, \vec{R}_v(\tau) \qquad (4.16)$$

where $\vec{R}_m(\tau)$ is the autocorrelation function of the modulation waveform

$$\vec{R}_m(\tau) = \lim_{T \to \infty} \frac{1}{T} \int_0^T \vec{m}(t)\, \vec{m}^*(t+\tau)\, dt \ . \qquad (4.17)$$

Turning to pulsed systems, it is obvious that a pulsed transmit waveform is just a special case of a modulated CW waveform with $\vec{m}(t)$ equal to the transmit pulse $\vec{E}(t)$. Thus, Eq. (4.16) is still valid, and and $\vec{R}_m(t)$ is calculated from

$$\vec{R}_m(\tau) = \frac{1}{T_p} \int_0^\infty \vec{E}_T(t)\, \vec{E}_T^*(t+\tau)\, d\tau \qquad (4.18)$$

where T_p is pulse length and $\vec{E}_T(t)$ is the transmit pulse. We see that for the pulsed case, the fluctuation characteristics are functions of pulse amplitude and frequency characteristics as well as particle radial velocity characteristics. When the pulses are short (~ 1 μs),

fluctuations are usually dominated by the $\vec{R}_m(\tau)$ term and velocity tur-
bulence adds little additional bandwidth to the signal. Conversely,
when pulses are long relative to the velocity correlation time ($\sim 1\text{-}3$
μs) and relatively narrowband, fluctuation bandwidth is determined by
the velocity turbulence characteristics within the pulse volume. As
discussed previously, this limits the practical use of long pulses for
pulse compression.

The preceding analysis neglects the effects of system focusing,
attenuation, and variable backscatter, all of which cause additional
variation in received signal level as the pulse propagates. Usually
these effects vary slowly with range and have a negligible impact on
the backscatter signal correlation function. An exception to this
occurs when the propagating signal encounters a sharp backscatter dis-
continuity, such as a cloud layer. To include these effects the modu-
lation correlation function $\vec{R}_m(t)$ must be modified in Eq. (4.17) as
follows. Assume the signal will be analyzed beginning at time t_1 cor-
responding to range $ct_1/2$. Then the correlation function of the modu-
lation term becomes

$$\vec{R}_m(\tau, t_1) = \frac{1}{T} \int_{t_1 - T}^{t_1} \vec{E}_t(t_1 - t) \; K_s(ct/2) \; \vec{E}_t^*(t_1 - t + \tau) \; K_s(\frac{ct}{2} + \frac{c\tau}{2}) \, dt \quad (4.19)$$

where T is pulse length, t_1 is time elapsed since the transmit pulse,
and $K_s(R)$ is a dimensionless gain versus range factor which includes
the effects of mean backscatter level, absorption, and system effects
such as focusing.

179

The basic analyses in this section show the analytical relationship between pulse characteristics and atmospheric characteristics in determining the temporal statistical properties of the received pulse. In the next section this relationship is illustrated by analyzing actual lidar returns.

2. Measurement of Backscattered Return Statistics

Most data runs sampled with the NOAA lidar consisted of approximately 500-1000 pulses. This is the typical mode of operation for backscatter [118] or velocity measurements. In addition to these runs, several extended-time measurement sets were also gathered in order to obtain data sets with enough samples to be statistically valid for characterizing signal properties. In this mode up to 10000 returns were sampled, usually at a PRF of 10 Hz, yielding data over up to 16-minutes of continuous operations. Typically 1024 samples, corresponding to 15 km range, were digitized per pulse. During the longer runs the temperature control in the van was usually not good enough for the servo control loops to maintain optical stability throughout the entire measurement. To maintain the operation on the center of the CO_2 line, the transmitter-cavity mode control loop (described in Sec. 4.1) continually translates the cavity PZT to adjust for temperature-induced cavity length changes. Because the PZT eventually reached the end of its tuning range, the cavity had to be manually relocked approximately every 10 minutes. Such relocks usually required about 30 seconds and should not have markedly altered the data characteristics.

180

An excellent data set for analysis of statistical properties of returns was taken on February 4, 1983. Atmospheric returns from 6000 consecutive pulses extending over 10 minutes were digitized. Prior to the measurement the lidar was pointed slightly upward, to an elevation angle of 10°, in order to penetrate the boundary layer at longer ranges. Since the day was cold and dry (dew point was near 0°C), attenuation of the signal due to water vapor absorption was minimal. Data were sampled on the P(20) line to maximize signal output and system efficiency. A horizontal water vapor measurement was also performed later on the same day. This measurement is described in Chapter V.

Figure 4-9 shows the calculated wideband CNR versus range for the February 4 extended data set. The CNR was calculated by averaging the power in the return from each range over 1000 pulses and then subtracting the estimated mean noise power. To estimate the noise power the mean power in a reference noise gate (typically selected to be beyond the maximum system range) was calculated. The algorithm for calculating CNR is

$$CNR(R) = \frac{\sum_{i=1}^{N} X_i^2(R) + Y_i^2(R) - \sum_{i=1}^{N} X_i^2(R_N) + Y_i^2(R_N)}{\sum X_i^2(R_N) + Y_i^2(R_N)} \qquad (4.20)$$

where $X_i(R)$ and $Y_i(R)$ are the digitized raw in-phase and quadrature returns from range $R = c\tau/2$ for pulse i; and $X_i(R_N)$ and $Y_i(R_N)$ are the returns from the noise reference range. The noise bandwidth used in Fig. 4-9 was 10 MHz.
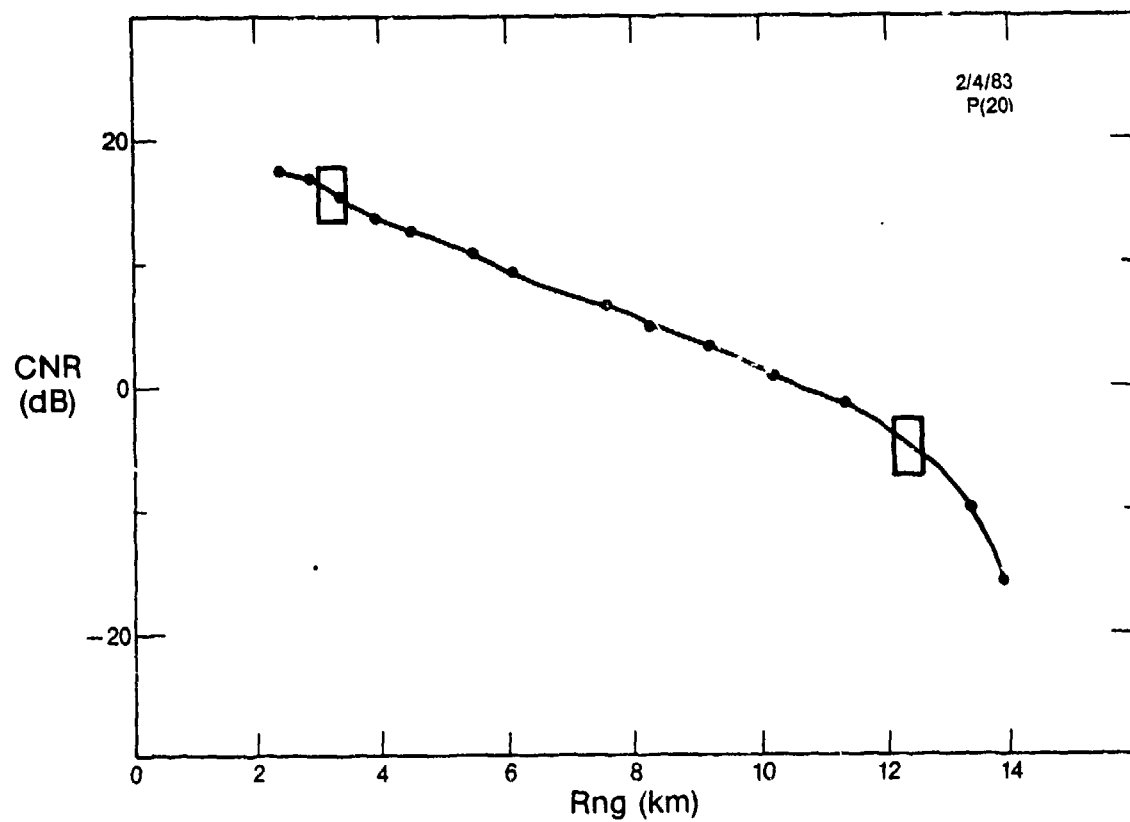
181

Fig. 4-9 - Average carrier-to-noise ratic (CNR) versus range for extended data set taken 2/4/83. Elevation angle of the lidar beam was 10°.

It is seen from Fig. 4-9 that the measured CNR falls off from 17 dB
at the 1.6 km system minimum range to below -12 dB at R = 14 km,
resulting in a dynamic range of <30 dB. Since this value is typical
for reasonably uniform aerosol conditions when the system is focused at
infinity, the 8-bit digitizer, which provides 45 dB of dynamic range,
was generally sufficient. Only during cases where the signal was
backscattered from a cloud or solid target did the receiver dynamic
range limit the analysis capability.

A noise gate between 14 and 15 km was chosen for the calculation
of CNR. The reasonably smooth fall-off in signal versus range shown in
Fig. 4-9 is indicative of lack of structure in the backscatter coef-
ficient, making this data set a good one for looking at signal proper-
ties without having to account for structure-induced range resolution
anomalies. The analysis concentrated on returns from the 2 range cells
in the figure: 3 km range, corresponding to high (13 dB) CNR returns,
and 12 km range, from which the measured CNR was roughly -6 dB.

Figure 4-10 shows returns of signal power versus range for con-
secutive single pulses. The dominating effect of speckle on fluc-
tuations at high CNR is evident even in the near returns. Although
returns from ranges differing by as much as .5 km, with corresponding
differences in intensity, are effectively superposed by the long pulse,
the return still exhibits the large scintillations typical of a
Rayleigh phasor. The validity of the Rayleigh phasor model is further
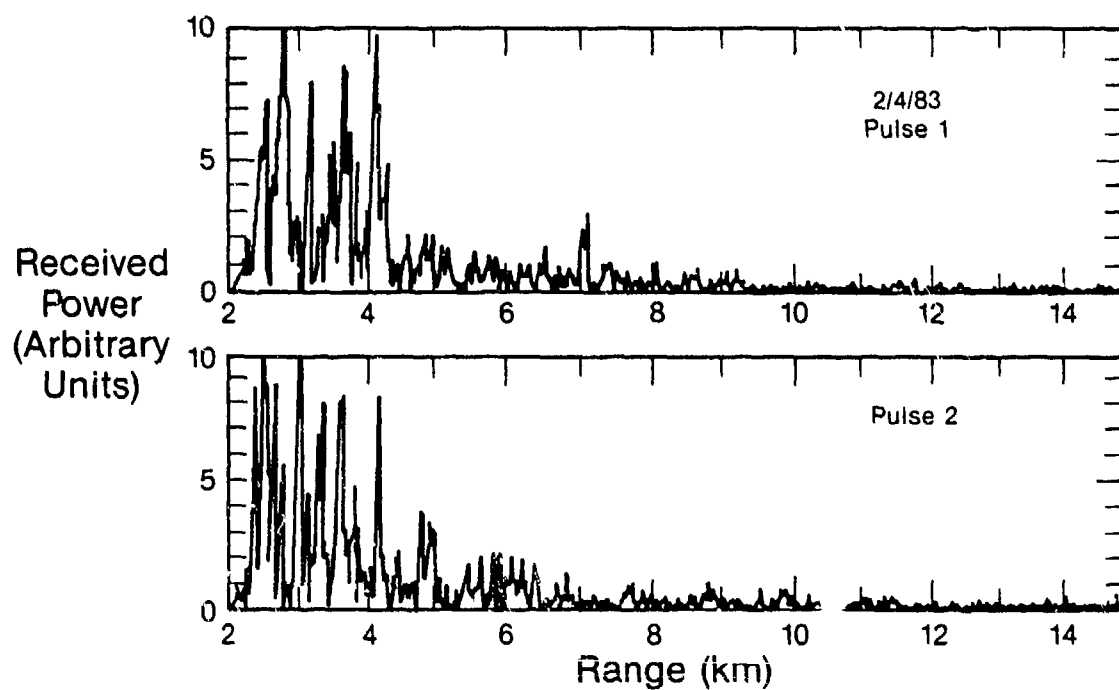illustrated in Figs. 4-11 and 4-12, which show the measured histograms

Fig. 4-10 – Power versus range calculated from two individual returns in 2/4/83 data set showing effect of speckle.
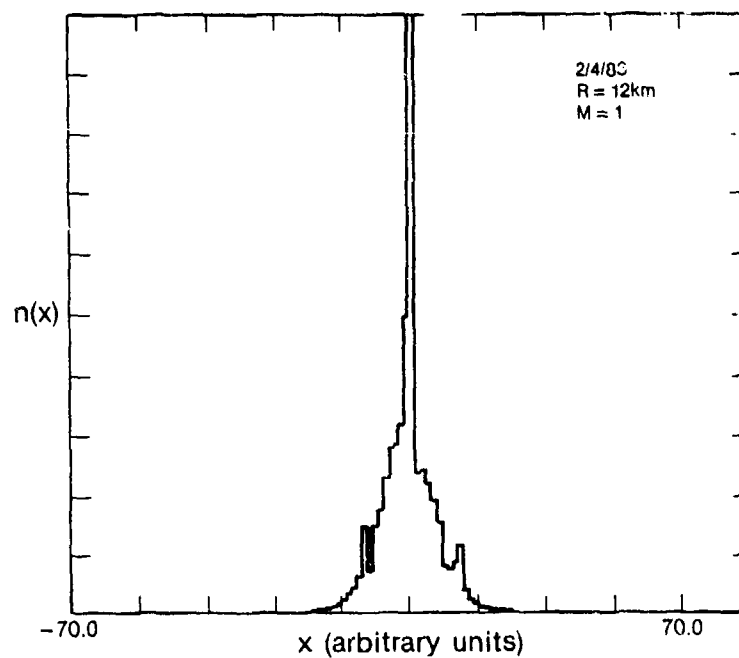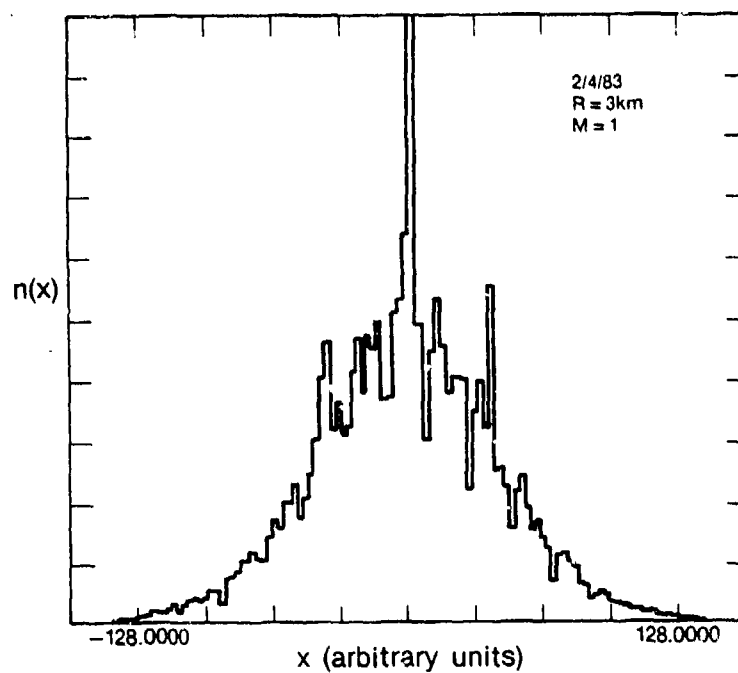
Fig. 4-11 - Histogram of in-phase baseband signal for returns from 3 and 12 km ranges showing approximate Gaussian distribution of raw signal.
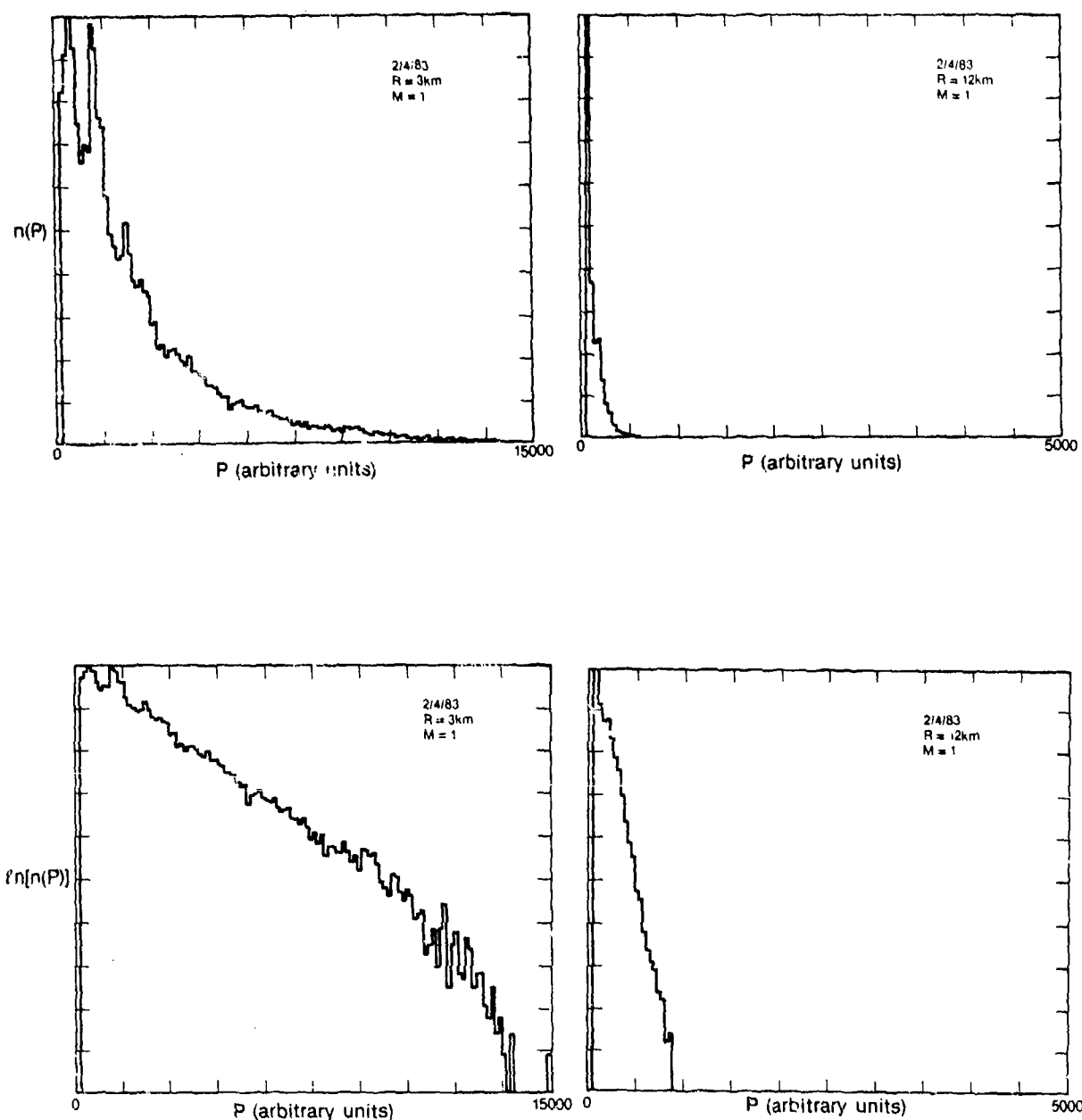
185

Fig. 4-12 - Normalized histogram of received power from 3 and 12 km ranges
plotted on both linear (top) and log (bottom) scales. Straight line
on log scale indicates approximately exponential distribution.

186

of raw return (Fig. 4-11), power (Fig. 4-12) and log power (Fig. 4-12) from the two ranges. The raw returns from both ranges follow the Gaussian distribution characteristic of the random walk model. Note that the presence of additional signal in the 3 km case only broadens the histogram, it does not alter its shape. This is shown in the power histograms as well, where both high and low CNR signals show good approximation to a negative exponential distribution. In the plots of the log of the distribution, the straight line is a good indication of an exponential distribution. The difference between high and low CNR is evident only in the spreading of the histogram, not in the shape.

Negative exponential statistics predict that the normalized standard deviation of the instantaneous power measurements $\sigma_{\hat{P}}/\langle\hat{P}\rangle$ will be unity at all CNRs. The calculated standard deviations of the power measurements from 3 and 12 km ranges were found to be 1.06 and 1.01 respectively, which agree quite well with the theory as additional verification of the random walk model. Although the 3 and 12 km signals exhibit similar fluctuation statistics, the effect of low CNR on measurement accuracy is brought to light when one considers the normalized standard deviation of backscattered-signal power $\hat{P}_3$, rather than the total measured power $\hat{P}$. For a single pulse the signal power is calculated from

$$\hat{P}_s = \hat{P} - \overline{P}_n \tag{4.21}$$

Since $\overline{P}_N$ is a constant (its uncertainty is assumed to be negligible), the normalized standard deviation of a single-sample power estimate can be calculated from Eq. (3.22) as

187

$$\frac{\sigma_{\hat{P}_s}}{\langle \hat{P}_s \rangle} = \left\{ \frac{\langle (\hat{P}_s + \hat{P}_N)^2 \rangle}{\langle \hat{P}_s^2 \rangle} \right\}^{1/2} . \qquad \qquad \cdot (4.22)$$

Thus the normalized standard deviation of an instantaneous backscattered power measurement from 3 km, where CNR = 20 dB, equals unity as expected since noise is negligible. The 12 km-range backscattered power measurements, on the other hand, have a much higher normalized other hand, have a much higher normalized standard deviation ($\sigma_{\hat{P}_s \text{NORM}}$ = 5) since fluctuations due to shot noise dominate the speckle-induced uncertainties when CNR is -6 dB. It is apparent in Eq. (4.22) that shot noise fluctuations become significant when CNR < 0 dB.

Obviously, single-sample estimates of backscattered signal power are of little value even at high CNR's, and much worse when the CNR falls appreciably below 0 dB. The standard deviation of the estimate in a single return can be reduced by averaging or filtering the instantaneous power measurements in the return over some time interval. As discussed in Sec. C and illustrated in Fig. 4-7, lengthening the observation (averaging) window length or filter temporal response reduces the range resolution, since the pulse propagates in range during the averaging interval. Thus, a trade-off exists between the required range resolution and the necessary estimate accuracy. When both sufficient accuracy and range cannot be obtained from a single pulse return multiple pulse averaging must be employed. This is almost always the case with pulsed heterodyne systems.

The efficiency of intra-pulse power averaging is a function of the autocovariance function of the rec..ive3 signal, as well as the receiver averaging time or lowpass filter response. Figure 4-13 shows the measured normalized autocovariance function of measured power B_p' from the 3 km and 12 km ranges, calcualted frcm

$$B_p^\wedge(\ell) = \frac{1}{I_1 - I_2} \sum_{i=I_1}^{I_2} \hat{P}(i)\ \hat{P}(i+\ell) - \frac{1}{I_1 - I_2} \sum \hat{P}(i) \sum \hat{P}(i+\ell) \qquad (4.23)$$

$$B_p'(\ell) = B_p^\wedge(\ell)/B_p^\wedge(0)$$

and averaged over 1000 pulses. Since the functions were calculated over a 6.7 μs time interval, the pulse actually translated 1 km during the course of the measurements. The covariance fractions shown contain both signal and noise components, as is evident in the 12 km returns. The effect of the wideband noise in the 12 km return is to add an impulse to the autocovariance function of the backscattered signal.

Since the 3 km returns exhibit high SNR, noise effects in measured $B_p'(\tau)$ from that range were negligible. The backscattered signal component of the normalized autocovariance functions from both short and long ranges exhibits correlations to time-lags beyond 1 μs. This correlation, which physically means that the signal fluctuations occur at longer time scales than the wider bandwidth noise fluctuations, determines the effectiveness of intra-pulse averaging.
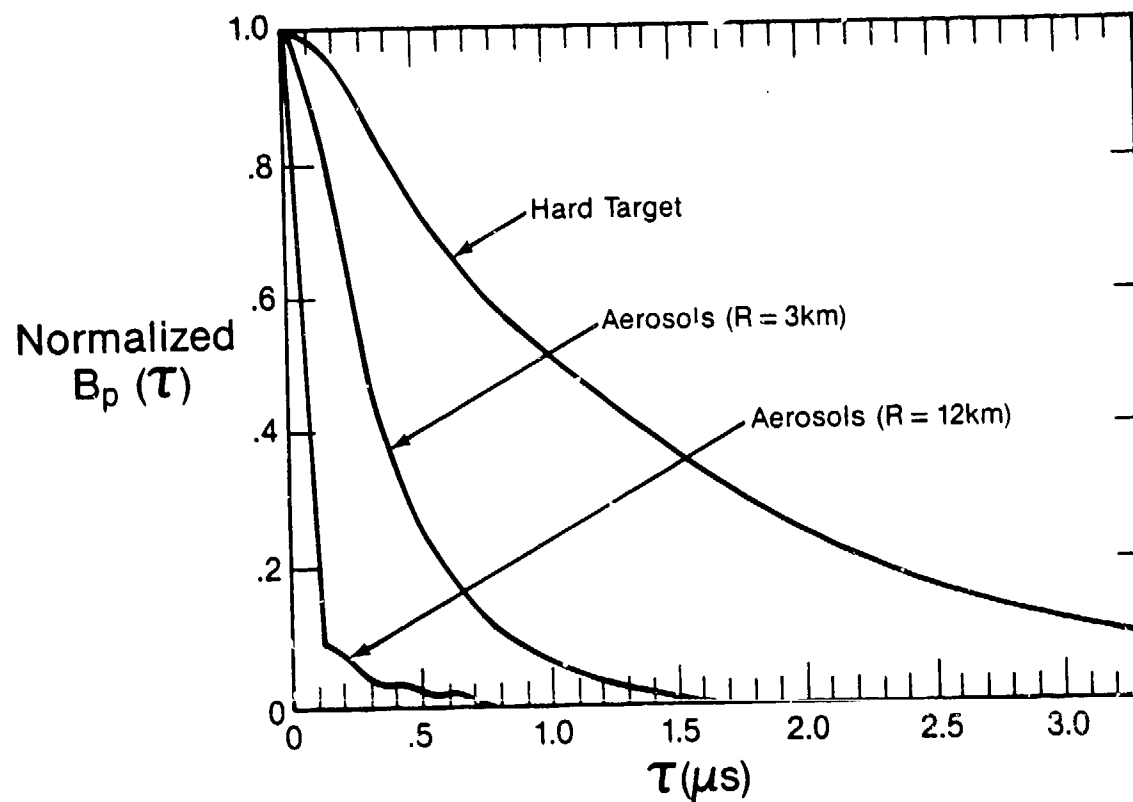
189

Fig. 4-13 – Normalized autocovariance function of total power in return signal from 3 and 12 km ranges. Also plotted is autocovariance function of lidar transmit pulse.

Figure 4-13 also shows the measured normalized autocovariance func-
tion $B_p^{\Lambda'}(\tau)$ for returns reflected off a stationary sandpaper-covered
calibration disk. The measured $B_p^{\Lambda'}(\tau)$ from the atmospheric returns
show shorter correlation times those that calculated from the disk-

reflected returns, due to velocity variations (turbulence) within the
pulse volume.

The velocity turbulence spectrum in the measure ent volume can be
estimated by solving for $\vec{R}_V(\tau)$ in Eq. (4.16) to a first approximation.
If we assume that chirp effects in the pulse are negligible, as dis-
cussed in Section C, and that mean velocity is constant over the effec-
tive measurement volume, then the phase of the correlation function can
be ignored such that

$$R_V(\tau) = \frac{\left|\vec{R}_{E}(\tau)\right|}{\left|\vec{R}_{E_t}(\tau)\right|} .\qquad (4.24)$$

Figure 4-14 shows the envelope of the estimated autocorrelation
functions of the turbulent velocity spectrum for the 3 and 12 km
returns as calculated from Eq. (4.24). A stored version of the disc
return was used as the pulse reference $\vec{R}_{E_t}(\tau)$. Also shown in the fig-
ures are least-squares fits of Gaussian functions to each calculated
$\left|\vec{R}_V(\tau)\right|$. Although the measured functions are obviously not truly
Gaussian, a rough estimate of the atmospheric velocity spread can be
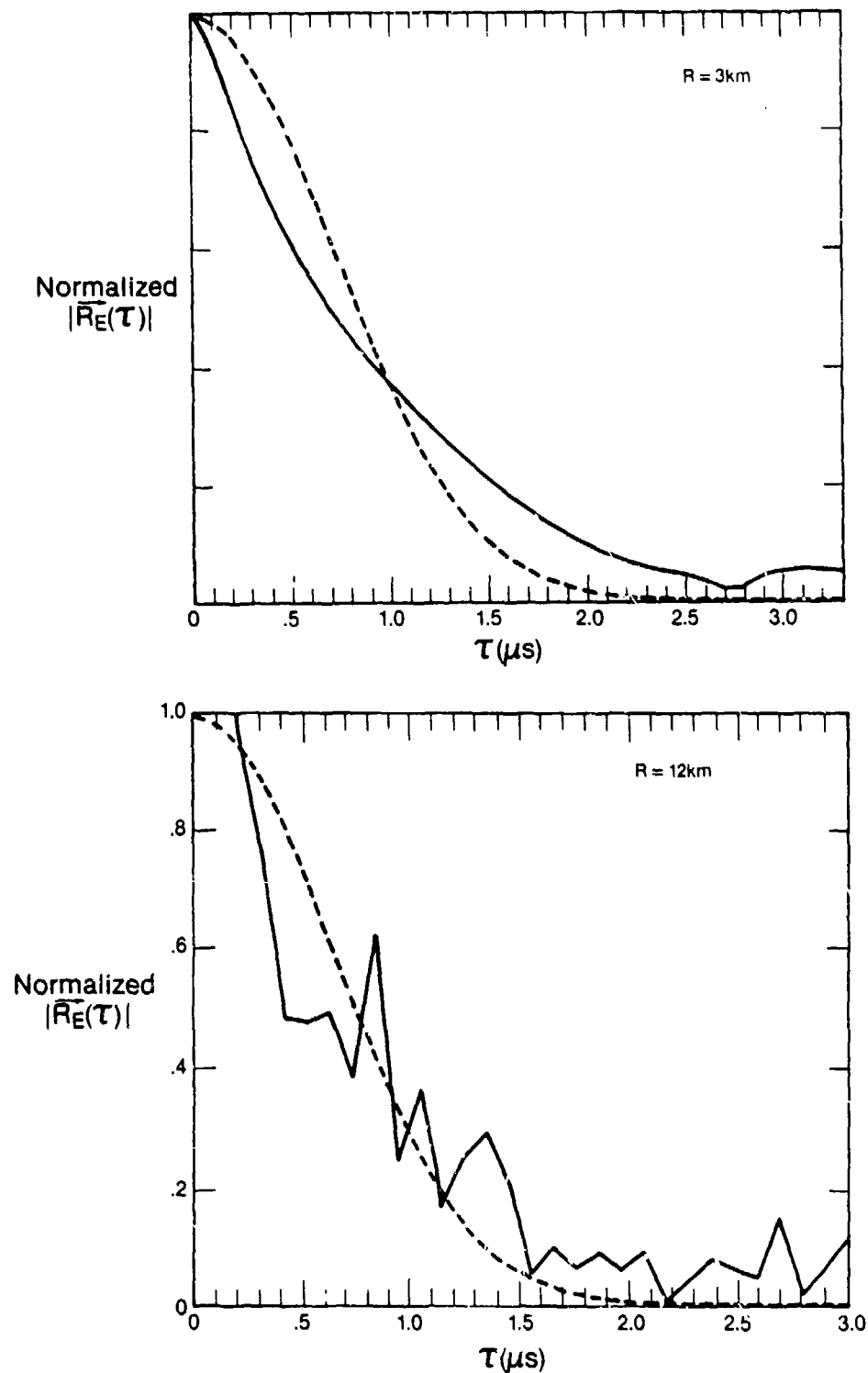obtained from the standard deviation of the fitted curve. The velocity

191

Fig. 4-14 - Magnitude of estimated velocity turbulence complex autocor-
relation function, calculated from Eq. (4.24) for 3 and 12 km
returns. Dotted line is best-fit Gaussian curve to calculated
response.

distributions estimated in this manner show spreads of approximately 1 m s^{-1}, which generally agree with observations of wind fluctuations in the troposphere. The calculated 3-km velocity distribution is slightly wider than that at 12 km, as might be expected when comparing wind measurements from the boundary layer with those from the free atmosphere. Although this example indicates the potential of measuring velocity turbulence and other parameters associated with velocity distribution, more analysis of the technique is required to determine sensitivity of the technique.

When individual samples in a single pulse return are block-averaged, the normalized measurement standard deviation reduces more rapidly with increased number of samples if the signal correlation times are short. In Fig. 4-15 the normalized variance of the average power measurement is plotted versus the number of points averaged for returns from the two ranges. The measurement variance decreases rather slowly for the 3-km returns, since the returns are correlated over time scales approaching 1 μs and the equivalent number of independent samples is small. For the 12-km data, the normalized standard deviation drops rapidly for 1 and 2 pulse averages, then less sharply as additional points are included. This behavior results from the additional effect of the noise in the 12-km data. Because individual noise samples are uncorrelated, averaging just a few samples of the 12 km returns quickly decreases that part of variance due to the noise. The variance due to signal fluctuations is relatively unaffected for
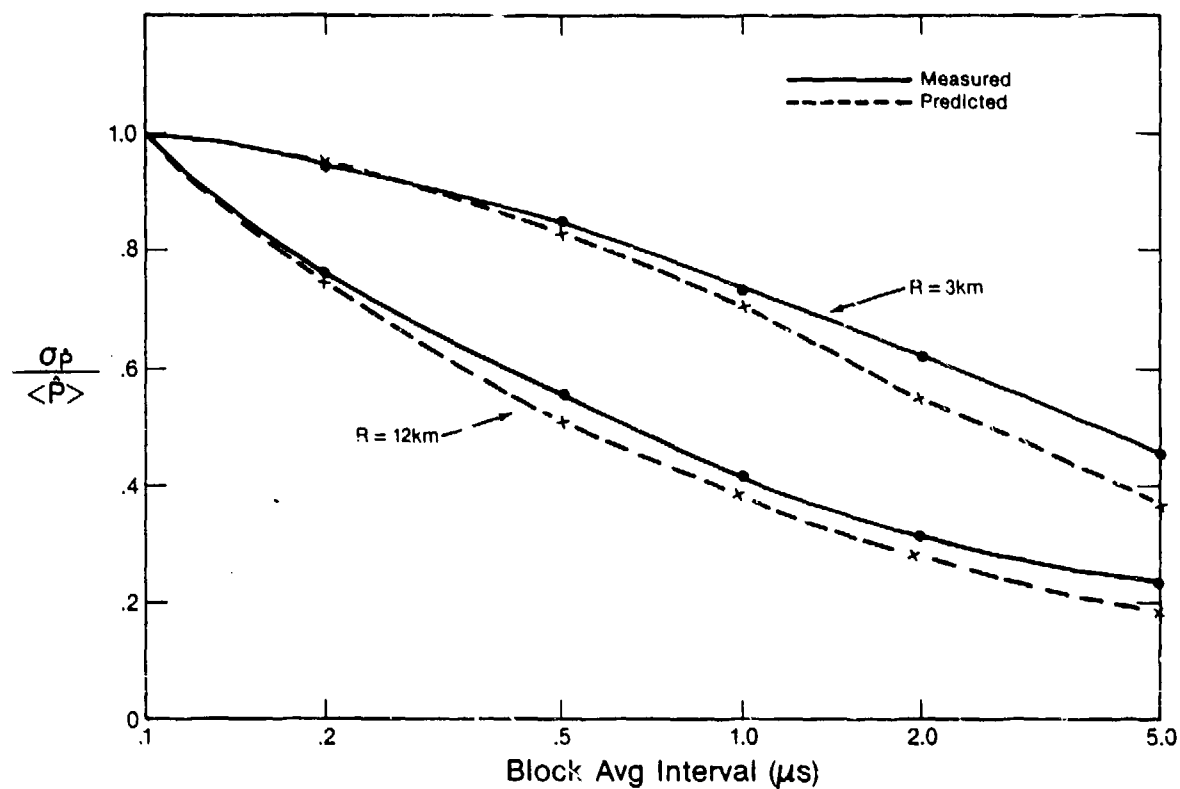
193

Fig. 4-15 - Normalized variance of single-pulse power estimates versus
length of intra-pulse block averaging interval. Dotted lines
indicate predicted performance from Eq. (4.25).

short intervals since these fluctuations are highly correlated over .1
- .2 µs. Since noise effects average out qui 'ly, the error eventually
becomes dominated by signal fluctuations. In this region the charac-
teristic shape of the σ_{NORM} curve is similar for both high and low CNR
cases. In many coherent lidar applications 3.3 µs time windows are
used in data analysis, since this produces a range resolution (Fig.
4-7) which is roughly equivalent to $c\Delta t/2$. It is seen from Fig. 4-15
that the expected normalized standard deviation of a single-pulse
measurement given such a window is approximately 0.25 at 20 dB CNR and
1.0 at −6 dB CNR. It is obvious from the figure that pulse-to-pulse
averaging is necessary in addition to this intra-pulse smoothing to
reduce the uncertainties to acceptable values (typically <10%). Since
the uncertainty is larger in the low CNR data, more pulses must be
averaged to obtain the same output normalized error.

The results in Fig. 4-15 can be compared with uncertainties pre-
dicted using the observed correlation functions of the returns. The
reduction in normalized variance for a block averaged data set of M
samples is estimated from

$$\left.\frac{\sigma_{\hat{P}}^{2}}{\langle \hat{P} \rangle^{2}}\right|_{M \text{ samples}} = \left.\frac{\sigma_{\hat{P}}^{2}}{\langle \hat{P}^{2} \rangle}\right|_{1 \text{ sample}} \times \frac{1}{m_{eff}} \qquad (4.\text{-}5)$$

where

$$m_{eff} = M/[1 + 2 \sum_{i=1}^{M} \frac{M-i}{M} R_p^{\circ}(k)] .$$

Equation (4.25) is adapted from Eq. (3.24) which is appropriate for continuous data. In Fig. 4-15 the calculated variance of the averaged returns is shown by the dashed lines. Since the predicted vs. measured points generally agree quite well, Eq. (4.25) can be used to estimate the normalized variance of an estimate after intra-pulse averaging, given the composite signal correlation function.

The reduction in variance obtained by intra-pulse averaging is also apparent in the histogram of single-pulse power estimates. Figure 4-16 shows histograms of the power estimates when the returns are block averaged over a 5 μs time window. The distributions are seen to resemble the higher-order chi-square distributions predicted for summations of exponentially-distributed (order 2 chi-square) random variables. Theoretically, the order of the chi-square distribution increases by 2 for every independent exponentially distributed sample averaged.

In Chapter III, the tradeoff between signal bandwidth and measurement uncertainty was discussed. In general, when CNR is high, the optimum strategy is to increase the transmit signal bandwidth by chirping or shortening the pulse. This increases the fluctuation rate (decreases the correlation time) so that intra-pulse averaging is more effective due to more number of independent samples in the interval. It was shown in Chapter III that when the receiver incorporates a
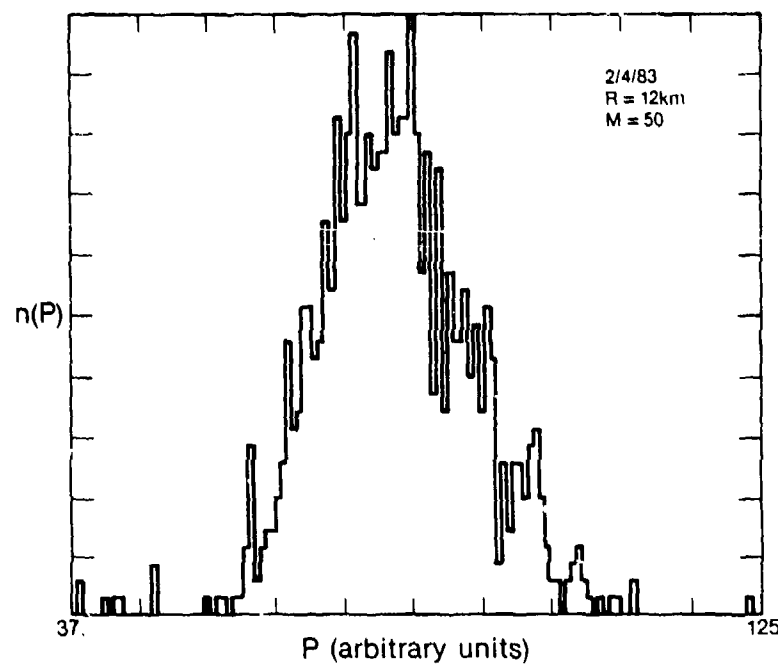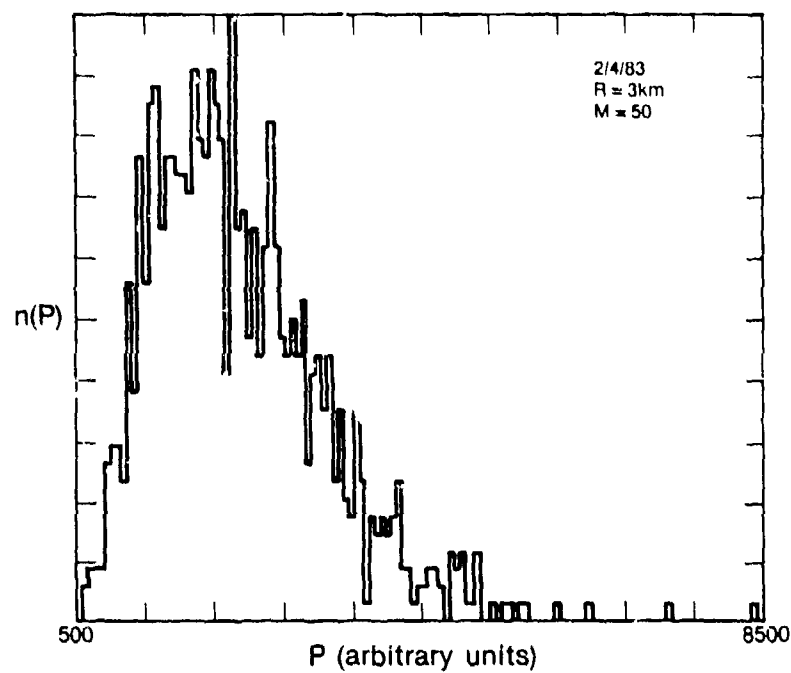
196

Fig. 4-16 – Histogram of single-pulse power estimates calculated using 5.0 µs intra-pulse block average.

matched filter, such that signal bandwidth equals noise bandwidth, the variance of the averaged signal is minimized when CNR $\approx$ 1 (assuming transmit energy holds constant as bandwidth broadens). This conclusion must be modified when a wider bandwidth receiver is used, such as in the NOAA Doppler lidar, because correlation times of the signal and noise components differ. The minimum error case becomes

$$CNR_{opt} \approx \frac{m_s}{m_n} \tag{4.26}$$

where m_s and m_N are the effective number of independent samples of the signal and noise over the averaging interval calculated from Eq. (4.25).

These results clearly show that the relatively long pulse length and narrow pulse bandwidth of the WPL lidar system limit the effectiveness of intra-pulse signal averaging. Even at high CNR, $\sigma_{\hat{P}_{NORM}}$ for a single-pulse power estimate is on the order of 0.5 when the averaging occurs over a 500 m equivalent range gate; the estimate is even worse for low CNR. Thus, averaging of $\hat{P}$ at given ranges over multiple pulses becomes necessary to reduce the expected estimate error to an amount.

Averaging of pulse-to-pulse estimates brings with it a potential problem of stationarity. In the interval between pulses, and over the total multi-pulse interval, characteristics of the backscatter and propagation medium will vary. In many analyses of DIAL measurement capability, such as the one performed in Chapter III, the fluctuations in

198

the received signal power estimate were assumed to be independent and
stationary, such that averaging of multipulses reduced the normalized
standard deviation of a single pulse estimate by $1/\sqrt{N}$, where N is the
number of pulses averaged. A recent study at Lincoln Laboratory [119]
examined the pulse-to-pulse statistics of returns from a hard diffuse
target using both coherent and incoherent detection. It was observed
that for both types of detection, the pulse-to-pulse fluctuations exhi-
bited long-term correlation (time scale on the order of minutes) which
reduced the effectiveness of averaging. These fluctuations were attri-
buted to the effects of turbulence and water vapor absorption along the
propagation path. Additionally, by using two lasers pulsing simulta-
neously at different CO_2 wavelengths, they showed that the long-term
fluctuations in backscattered signal at the two wavelengths were corre-
lated. As a result the standard deviation of the ratio of the two
power measurements, as used in Eq. 3.1, decreased faster with addi-
tional pulses than those of either of the measurements taken singly.
This result illustrated the potential improvement to be gained by
simultaneous transmission of the on-line and off-line wavelengths in a
DIAL measurement.

Since the results described in [119] were for returns from hard
targets only, NOAA lidar data samples were analyzed to make similar
measurements of pulse-to-pulse statistics of aerosol backscattered
returns. Figure 4-17 shows a long-term time series of the average
measured signal power from 3 km range analyzed over a 0.5 km (3.3 µs)

interval. In a single-pulse measurement speckle and shot noise fluc-
tuations will dominate any long-term measurement variations. Five
single pulse measurements were averaged for each data point plotted in
Fig. 4-17. The time series clearly shows long-term fluctuation in the
measured backscattered signal power measurement. Such fluctuation
could result from the atmospheric effects discussed in [119] as well as
from temporal variations in laser transmit power or system sensitivity.
Although the time-scale of the fluctuations (~ 2-3 minutes) is similar
to that in the monitored transmit signal energy, such a time scale is
also consistent with that which would occur due to the advection of 0.5
km scale-size eddies of transmission or backscatter inhomogeneities
across the transmit/receive path.

Figure 4-18 shows the measured normalized autocovariance function
$B_p^{\hat{}}{}'(\tau)$ of the 5-pulse averaged measurement. The impulse at zero lag
in $B_p^{\hat{}}{}'(\tau)$, due to the uncorrelated white fluctuations, accounts for
approximately 40% of the variance after averaging 5 pulses. As more
pulses are averaged the contribution in variance due to the white seg-
ment reduces as $1/\sqrt{N}$ leaving the residual, long-term correlated fluc-
tuation term. These fluctuations occur so slowly that much longer time
segments than the 5-minute segment in Fig. 4-18 are probably necessary
to obtain a sufficient number of independent samples to reduce this
error term. These results are similar to those observed in [119] in
the analysis of hard target returns. The net effect of the correlation
is to limit the potential accuracy to be gained in estimation of the
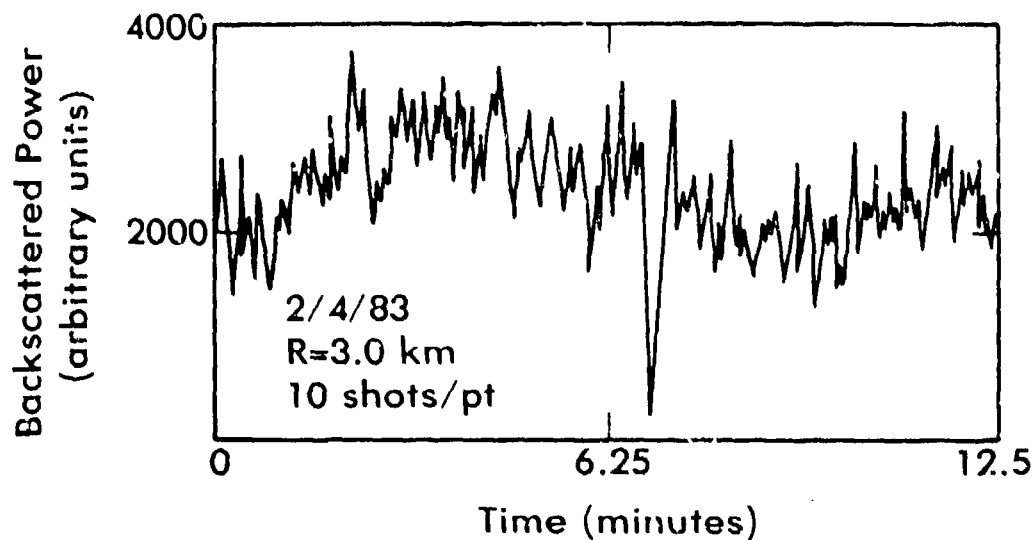mean power through pulse-to-pulse averaging.

200

Fig. 4-17 – Time series of returns from 3.0 km range gate showing
long-term variability. Each point represents an average of
5 single-pulse estimates. A uniform 3.3 μs averaging window
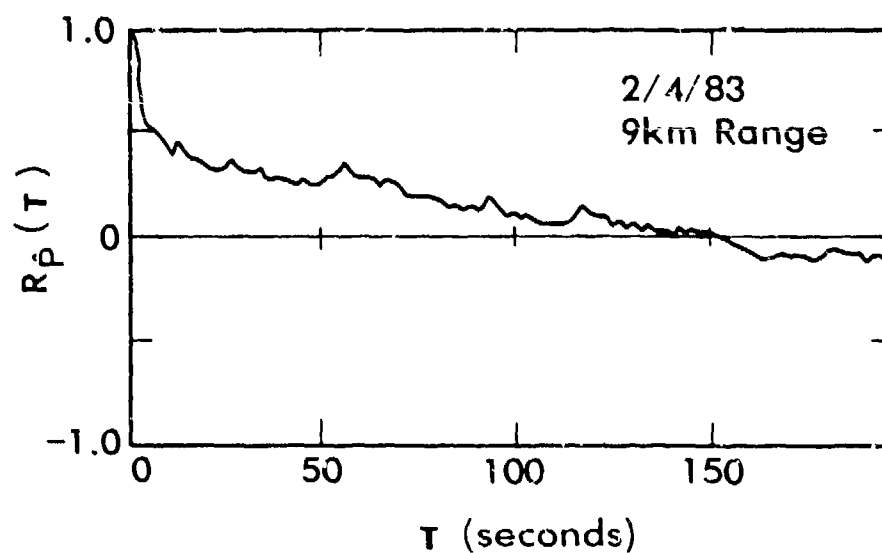was used for the single-pulse power estimate.

Fig. 4-18 – Autocorrelation function of time series in Fig. 4-17, show-
ing long-term drift in received backscatter power estimate.

201

This limitation is illustrated in Fig. 4-19, which snows the measured reduction in normalized standard deviation $\sigma_{P_{NORM}}$ versus number of pulses averaged for measurements on different days at both high and low CNR. The curves all show the same "leveling off" in the averaging efficiency due to long term fluctuations. After averaging 100 pulses the observed $\sigma_{P_{NORM}}$ is substantially greater than would be predicted if pulse-to-pulse fluctuations were independent. Menyuk et al. [119] concluded that this inherent limitation on measurement accuracy has important implications in the design and selection of system operating parameters.

Although detrimental to overall DIAL capability, the effect of long-term power measurement fluctuations is diminished for the range-resolved case if fluctuations in the measurements used in the ratio terms in Eq. (3.1) are correlated. This is seen in Eq. (3.2), where the correlation terms reduce the error from that predicted when the four power measurements (two wavelengths at two ranges) are independent. Since the NOAA lidar must be manually tuned between laser lines, DIAL measurements were taken by averaging a large number of pulses at one wavelength, then tuning to the other wavelength and repeating the procedure. As a result, one would not expect to see the correlation between fluctuations of the different wavelengths reported by Menyuk et al., whose measurements were simultaneous. These data can be used, however, to examine the correlation between fluctuations in power received during the two DIAL measurements from ranges R_1 and R_2 at the
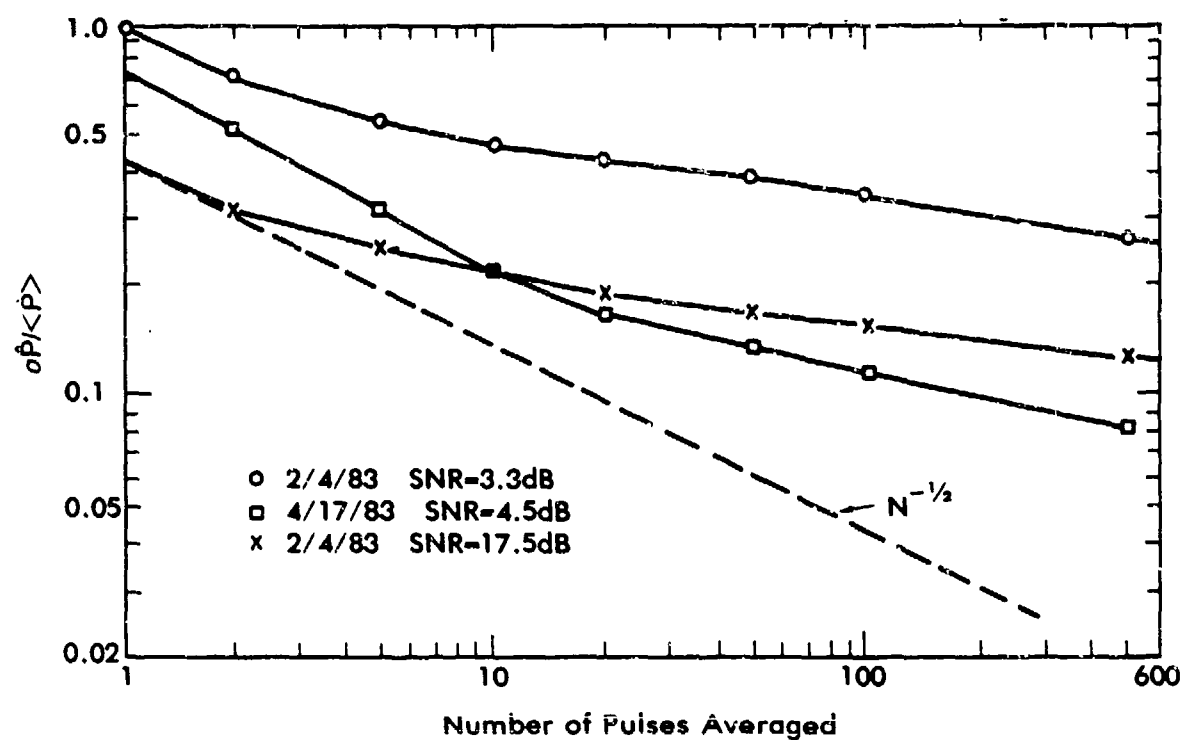
202

Fig. 4-19 – Reduction in normalized variance of multi-pulse averaged
power estimate versus number of pulses averaged.

same wavelength. Figure 4-20 shows a time series of average power received from ranges of 2.5-3.0 km and 3.0-3.5 km. As in the previous analysis, 5 pulses were averaged per point. The degree of correlation between the signals is immediately obvious. The correlation coefficient between the two time series can be calculated from

$$\rho[P(R_1),P(R_2)] = \frac{cov(\hat{P}(R_1)\ \hat{P}(R_2))}{\sigma_{\hat{P}(R_1)}\ \sigma_{\hat{P}(R_2)}} \ . \qquad (4.27)$$

Calculations of correlation coefficients for this and other data sets consistently showed values as high as 0.95 for the case where 10 or more pulses were averaged per point. This value decreased as the number of pulses averaged decreased, since the relative contributions of the white, uncorrelated fluctuation to the total variance were higher for smaller number of pulses. Once the number of pulses averaged was large enough such that the white fluctuations were negligible, the calculated correlation coefficient remained constant at a relatively high value, usually greater than 0.9. This is shown in Fig. 4-21.

Since the long-term fluctuations of measured power from adjacent ranges were highly correlated, the ratio of the measured powers was relatively unaffected by the long term fluctuations. This is illustrated graphically in Fig. 4-22, which shows the reduction in the normalized standard deviation of measurements of the ratio $\hat{r} = (\hat{P}3 \text{ km}/\hat{P}2.5 \text{ km})$ versus number of points averaged before ratioing.
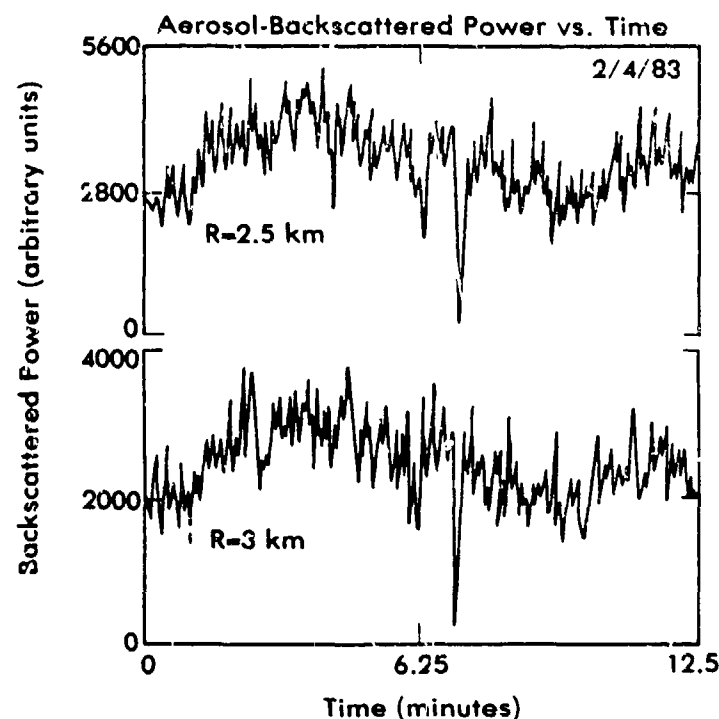
204

Fig. 4-20 - Time series of returns from adjacent range gates. Filtering parameters were the same as in Fig. 4-17.
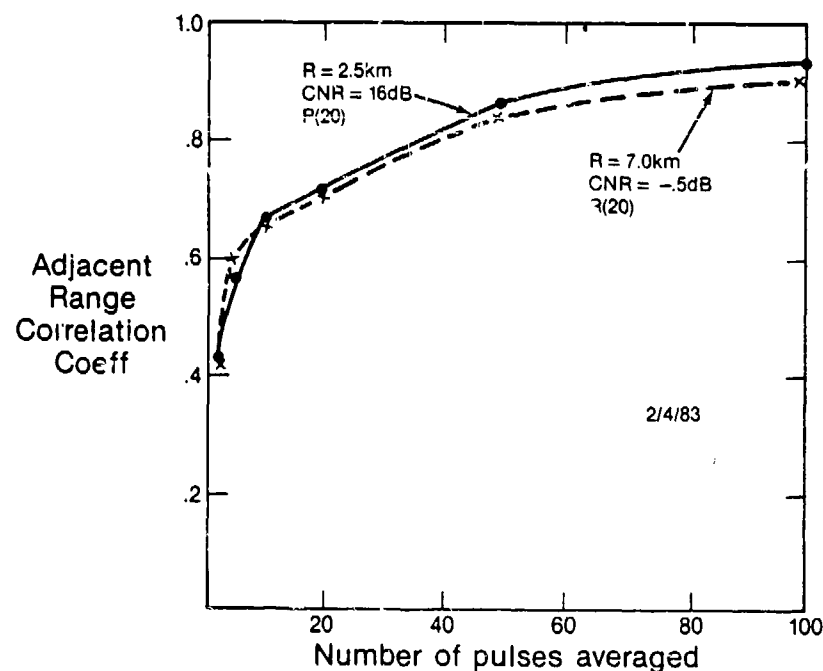

Fig. 4-21 - Correlation coefficient of fluctuations in adjacent received power estimates from 2.5 km and 7.0 km ranges versus number of pulses averaged.

205

Unlike the single-range power estimate, $\sigma_{r_{NORM}}$ decreases very close to

the predicted $N^{-1/2}$ behavior for up to 200 pulses. Thus, the effect

of long-term fluctuations is less than would be expected if the

fluctuations were independent from range-to-range. This is shown in

Fig. 4.22, which also shows $\sigma_{r_{NORM}}$ that is predicted when the long-

term fluctuations are independent from range to range. The improve-

ment gained because of the range-to-range correlation amounted to 80%

when 100 pulses were averaged.

It is important to reemphasize a point discussed earlier regarding

the source of the received signal fluctuations. Since output pulse

energy was not monitored during the measurements, the long-term fluc-

tuations could have been contributed by systematic as well as

atmospheric effects. Thus, the range-to-range correlation shown in

these results may not be indicative of that due strictly to atmospheric

processes, although the preceding discussion of pulse volume averaging

indicates that all but the longest length-scale eddies should be spa-

tially filtered. Analysis of additional data with exact monitoring of

system parameters is required before more definitive conclusions can be

drawn regarding correlation of atmospherically induced fluctuations in

aerosol-backscattered returns. However, these results indicate that

such careful monitoring of system performance is not critical in range-

resolved DIAL measurements. Since the important parameter is power

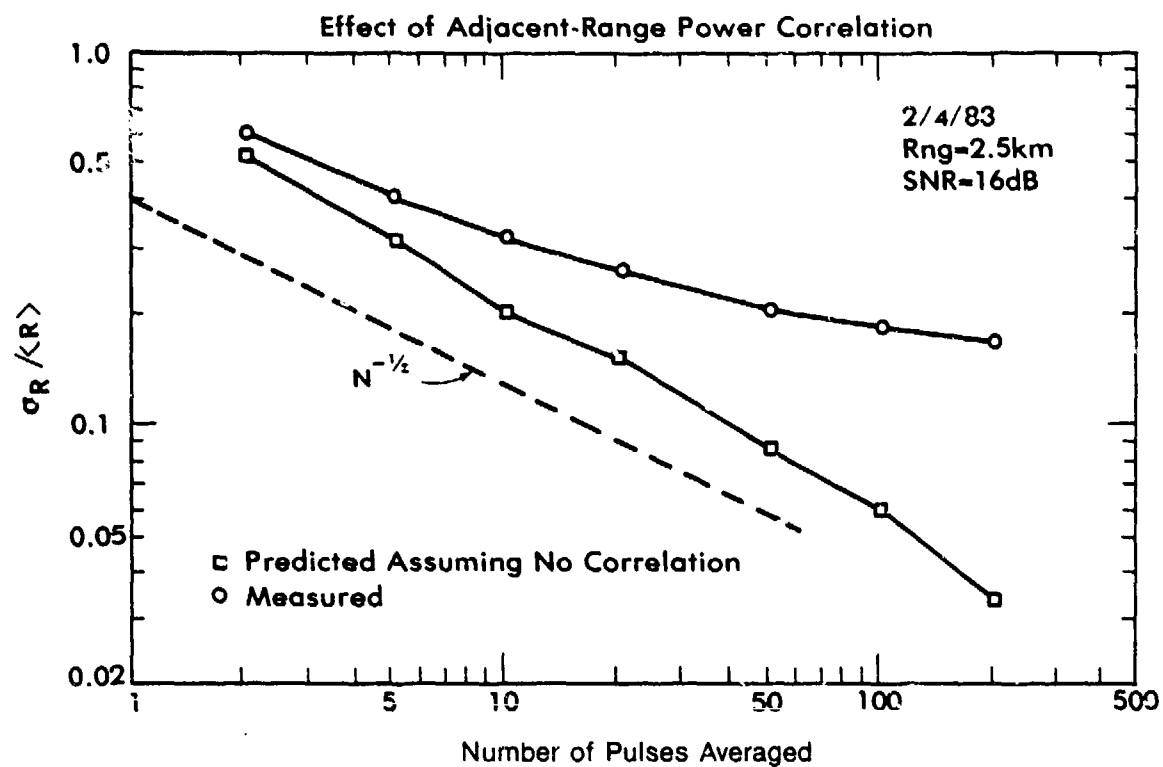attenuation across the range cell, the ratioing inherent in the DIAL

206

Fig. 4-22 — Reduction in standard deviation of adjacent-range power
ratio estimate versus number of pulses averaged before ratioing.
Also plotted is predicted performance assuming range-to-range
fluctuations are uncorrelated.

calculation provides a self-normalization which effectively removes the errors caused by systematic variability. Such is not the case in path-integrated measurements from hard targets. With this type of measurement, long-term systematic variability has a potentially significant impact on measurement accuracy, since no self-normalization exists.

Finally, the bias which exists when estimating backscattered power ratios for short data samples is examined. In our measurements, we first estimate the backscattered power from ranges of interest for each pulse, then average the power estimates from each range over multiple pulses. Assuming stationarity exists over the total pulse averaging period, the distribution of the individual power estimates follows a chi-square of order 2m, where m is the total number of independent samples given by

$$m = m_{eff} \, M \, .$$
(4.28)

In Eq. (4.28) m_{eff} is the number of independent samples in a single pulse calculated from Eq. (4.25), and M is the effective number of independent pulses.

Rye [120] examined the bias and variance of ratio estimates for small m as a function of numerator and denominator CNR and mean ratio. He determined that in most cases for m < 100 the estimator

208

$$Z = \frac{1}{N} \sum_{i=1}^{N} [\ln (\frac{\hat{P}_1}{\hat{P}_2})_i] \qquad (4.29)$$

resulted in less variance and smaller bias than the estimator

$$F = \ln [\frac{1}{N} \sum_{i=1}^{N} (\frac{\hat{P}_1}{\hat{P}_2})_i] \qquad (4.30)$$

where $\hat{P}_1$ and $\hat{P}_2$ were formed from the short data sequences. For m > 100 the bias in the ratio estimate was typically negligible.

Figure 4-23 shows measurements taken with the NOAA lidar of the ratio of backscattered power from adjacent range gates versus number of points averaged before ratioing. This is equivalent to Rye's F estimator. The appearance of a bias is evident for a small number of pulses at both low and high CNR values. These curves agree qualitatively with the results of Rye, although a more careful matching of parameters to those used by Rye is necessary for a detailed comparison. In general, the results show that the 10-pulse averaged ratio comes within 5% of the long-term (1000 pulse) averaged ratio value at 0 dB CNR. Because of the effects on intra-pulse averaging, 10 pulses actually corresponded to at least 20 independent samples of the power fluctuations.

Although some improvement was seen to exist in bias behavior with increasing CNR (decreasing range), the effect was not notably dramatic. This is most likely because CNR is already enhanced by intra-pulse
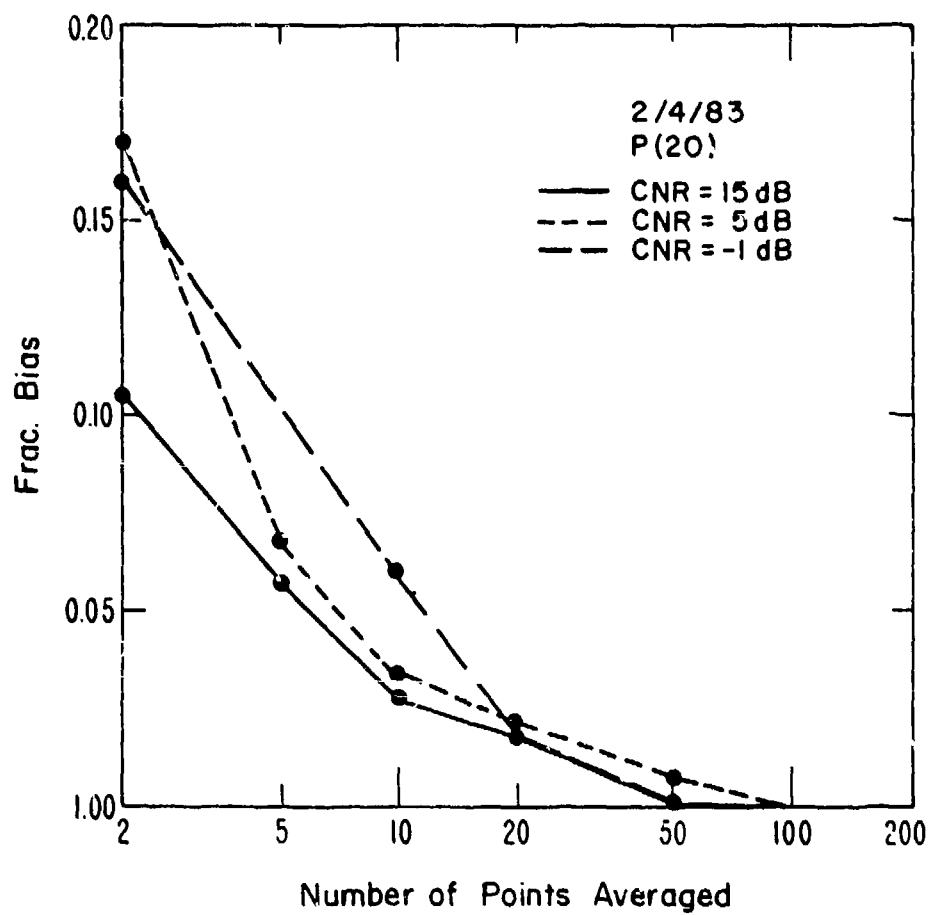
Fig. 4-23 - Mean estimate of adjacent-range ratio estimate versus
number of pulses averaged before ratioing.

averaging. The 3.3 µs average (33 samples) smoothes out noise fluctuations such that

$$CNR_o = CNR_1 \times \sqrt{m_n} \qquad\qquad (4.31)$$

where m_n is the effective number of independent noise samples. Since the noise bandwidth was 10 MHz, individual noise samples were uncorrelated and m_n was equal to the total number of points averaged. Thus, averaging produced an immediate 7.5 dB improvement in CNR, such that even 0 dB input CNR yielded a single pulse estimate with relatively little detection noise. Since speckle noise dominated the uncertainty at all but the lowest CNR values, little improvement was gained by increasing CNR.

Returns from the NOAA lidar show substantial long-term range-to-range correlation, consequently there is little advantage in averaging short data records before ratioing. However, if pulses were shorter, or if subsequent measurements show that most of the measured correlation was due to systematic variations, the optimum averaging interval might be shortened considerably. Under such conditions the potential bias and variance become important parameters to consider in choosing system parameters and estimator techniques.

E. SUMMARY

The measurements in this chapter are important for quantifying the expected errors in the DIAL measurements due to certain systematic and

211

atmospheric effects. Analysis of system properties such as pulse characteristics and long-term stability showed that the NOAA system was not exactly optimum for all types of DIAL measurements. The relatively long transmit pulses, as described in Sec. B, limit range resolution to a minimum 300 m and preclude effective intra-pulse averaging. By decreasing pulse duration and/or increasing bandwidth, the correlation time of the return signal can be shortened. This gives more independent samples of backscattered power per unit time, which improves the estimate of mean power obtained at high CNR from a single pulse.

Longer-duration pulses reduce system range resolution because the propagating pulse is spread over a longer region in space. This can be a advantage in sequentially-tuned DIAL measurements such as those described in the next chapter. In sequentially-tuned measurements the statistical properties of the aerosol distribution at a given range should be equivalent for both wavelength measurements. If the aerosol homogeneities are a passive-addition to the turbulence field, most of the energy in the spatial aerosol fluctuation spectrum will be at the longer wavelengths. Hence, by employing long pulses, which are equivalent to a narrow band spatial filter, one can reduce the variability in the averaged returns due to aerosol variability, as shown in Eq. (4.4). As illustrated in Fig. 4-7, the 3 μs NOAA lidar pulse should ideally average out spatial inhomogeneities below about 0.5 km in scale size.

Due to the nature of the system the key pulse characteristics of the NOAA lidar are essentially fixed. Thus, the pulse length cannot be

easily shortened should better range resolution or intra-pulse speckle averaging be desired. In Section C. the potential of employing a matched filter receiver to improve range resolution was examined by calculating the radar ambiguity function. It was concluded, since little obvious improvement could be gained, that the chirp in the transmit pulse tail is relatively insignificant in limiting system performance.

An important result in the chapter described the statistical characteristics of the aerosol-backscattered return and the effectiveness of intra-pulse averaging. The returns were shown to closely follow a Rayleigh phasor model with respect to both the shape of the distribution and the calculated normalized variance. Although the nature of the distribution was independent of CNR, the normalized standard deviation of the estimate and averaging effectiveness depended strongly on the relative portion of noise present. At low CNR, initial values of normalized standard deviation were high, but averaging over short intervals was more effective. An expression based on the power autocovariance function to estimate measurement uncertainty after averaging was shown to closely follow the actual results.

Because intra-pulse averaging of power fluctuations was relatively ineffective for the NOAA system pulse, the effectiveness of multi-pulse averaging was examined. It was found that fluctuations at single ranges showed significant long term correlation over time scales of 2 minutes or more. This correlation means that the uncertainty does not

213

decrease by $N^{-1/2}$, which would be the case if the pulse-to-pulse fluc-
tuations were independent, and defines limitations in averaging
multiple pulses to measure mean backscattered power from a single
range, such as in backscatter coefficient measurements.

When comparing returns from adjacent ranges, however, it was found
that the fluctuations were for the most part highly correlated. This
was significant for DIAL measurements, since the key parameter to esti-
mate is the ratio of power estimates from adjacent ranges rather than
the absolute powers themselves. The effect of the correlation was to
produce an $N^{-1/2}$ decrease in the ratio estimate with increasing pulses,
despite the fact that the numerator and denominator estimates in the
ratio improved individually at a slower rate. No conclusions were
offered as to the cause of the high correlation in signals from adja-
cent ranges, although systematic variations were almost certain to have
been at least partially responsible.

The results described in this chapter were useful in defining the
range-filtering function used in DIAL data analysis, and predicting the
expected error versus CNR and range resolution. These facets of the
problem, as well as actual water vapor measurements, are described in
the next chapter.

V. COHERENT DIAL WATER VAPOR MEASUREMENTS

In this chapter a series of water vapor measurements taken during late 1982 and the first half of 1983 is discussed. These measurements are the major contribution of this dissertation. Although many of the results in the previous two chapters provide essential building blocks for modeling and predicting coherent DIAL measurement capability, the actual measurements must be performed to provide proof of the concept. The experiments reported here are the first reported attempts to make range-resolved coherent DIAL measurements of species concentration. As such, the results offer quantitative data on the operational advantages and disadvantages of the well-discussed coherent DIAL technique.

The organization of the chapter is as follows. Section A discusses the experimental procedure used in collecting data for the measurements, while Section B describes the analysis of the digitized data sets. As in the previous chapter, almost all analysis of raw data was performed by the computer. Because of the large errors potentially present in specification of the water vapor absorption cross section (ACS) at the two laser frequencies, Section C is devoted to a discussion of that parameter, including the assumptions employed when specifying ACS for the actual concentration measurements. Section D describes the important DIAL water vapor measurements. The cases described in Section D are representative of the data characteristics in those measurement sets which are not directly discussed. Since one

215

benefit of coherent DIAL is the potential capability to measure velocity as well as concentration, combined DIAL/Doppler measurements are examined in Section E. Results of analysis of actual lidar returns, as well as simulated performance capabilities are presented in this section to show the tradeoffs in specifying a system to perform such a dual function. The results of the measurements are summarized and interpreted in Section F.

A. EXPERIMENTAL PROCEDURE

The DIAL measurements required measurement of backscattered radiation at two wavelengths. Since switching transmitter output wavelength among the various CO_2 lasing lines in the NOAA lidar involved manually tuning the laser-cavity diffraction grating, rapid switching between absorbing and non-absorbing wavelengths was not possible. Thus, the method of data collection was to digitize and store returns from a succession of pulses at one wavelength, then manually tune the transmitter and LO cavity to the other wavelength and repeat the procedure. Prior to beginning a measurement, the approximate settings of the grating-micrometer on each lasing line were found by tuning the cavity and observing the output frequency of each laser using an Optical Engineering spectrum analyzer. During the course of the measurements, line selection was performed by adjusting each laser grating to the pre-recorded micrometer setting for the given wavelength, then peaking the output power from each laser. This method

216

worked relatively well. Total time to tune and peak both transmitter and LO laser outputs was usually on the order of 3-4 minutes.

Because of a desire to estimate variability in the individual water vapor estimates, during each measurement sequence at least 3 separate data sets on each of the absorbing and non-absorbing wavelengths were gathered when possible. A typical measurement sequence went as follows:

Measurement Number	Procedure
1.	Tune to absorbing line and gather a multiple pulse data set.
	Tune to non-absorbing line and gather a multiple-pulse data set.
2.	Maintain operation on non-absorbing line; gather a multiple pulse data set.
	Tune to absorbing line, gather a multiple pulse data set.
3.	Maintain operation on absorbing line; gather a multiple pulse data set.
	Tune to non-absorbing line; gather a multiple pulse data set.
4.	Alternate steps 2 and 3.

The method of data sampling employed was identical to that described in Section IV for power measurements. The backscattered in-phase and quadrature baseband signals were digitized at a 10 MHz rate for 100-200 µs following pulse transmission and stored on magnetic tape. Most measurements were made at elevation angles less than 45° to provide better height resolution, since $\Delta h = \Delta R \sin\theta$, where θ is elevation angle. At shallow elevation angles, the radial component of the

217

horizontal wind can produce significant Doppler shift in the backscattered signal, hence IF bandwidth was kept at ± 5 MHz (equivalent to the Doppler shift from ± 25 m s^{-1} radial wind component) for all measurements. If vertical measurements were taken, such that the radial component of horizontal wind was approximately zero, IF bandwidth could have been reduced to slightly more than the ~ 375 kHz backscattered signal bandwidth. Such a reduction in receiver bandwidth would improve CNR at a cost of degraded height-resolution assuming the transmit pulse duration was left unchanged.

Prior to commencement of a measurement sequence, a careful optical alignment was performed on the system. Following alignment the measurements were taken as rapidly as possible, in order to minimize effects of atmospheric nonstationarities on the measurement statistics. Unless serious degradation was observable in signal quality, no subsequent realignments were performed over the course of the measurement sequence. It was observed that, in general, system sensitivity did not decrease noticeably even when the system was continuously tuned between lines. This is consistent with the observations described in Chapter IV where deliberate severe misalignments produced a maximum 3 dB loss in sensitivity. By avoiding realignment between line switches, measurement sequences were made as short as possible. Although some drift undoubtedly occurred, absolute calibration of the signals at the two wavelengths was not important for the range-resolved concentration measurements.

A typical data set for a single measurement consisted of returns from 500-1000 pulses at each of the two laser wavelengths. The number of pulses per data set was selected to balance the contradictory objectives of providing maximum averaging of speckle and noise fluctuations, and minimizing the total measurement time. By averaging 500 pulses per wavelength the normalized variance of the range-to-range ratio estimate due to speckle is reduced to less than 5% of the single pulse value, yet the entire measurement, including line-tuning of both lasers, can still be performed in under 5 minutes. Use of 500-1000 pulses (requiring 50-100 s when laser prf is 10 Hz) also provides a reasonable match to the time required for a pulse-volume-sized eddy of atmospheric backscatter inhomogeneity to advect across the scattering volume. Consequently, for typical wind conditions more than one independent sample of the large-scale aerosol backscatter should have been included in the estimate of backscattered power from each range. This would have tended to reduce errors from differential backscatter caused by the presence of different, pulse-sized eddies at the two reference ranges.

For almost all measurements the R(20) line ($\lambda = 10.247$ μm) and R(18) lines ($\lambda = 10.260$ μm) of the $00^\circ 1 - 10^\circ 0$ transition were used for the absorbing and non-absorbing wavelengths, respectively. In addition to being adjacent in the CO_2 spectrum, these lines provide a high differential absorption cross-section in the 10.6 μm CO_2 band. Another good absorbing line exists near P(40) ($\lambda = 10.81$ μm), however,

219

limitations on the total movement of grating mountings in both the TE and LO cavities prevented operation on this line.

When very moist conditions exist along the transmit/receive path, the R(20) laser radiation can be severely attenuated over ranges as short as a few km. Under these conditions the resulting large differential attenuation between the two lines will improve the close-in measurement accuracy; however, the rapid fall-off in signal on the R(20) line severely limits maximum measurement range. In the DIAL measurements described, the elevation angle was varied to obtain maximum signal vs. range on the R(20) line. Under this criterion, the "best" elevation angle was usually between 20° and 45°. In a typical atmosphere, both water vapor and aerosol backscatter coefficient decrease with height. Thus, at high elevation angles, the rapid decrease in aerosol with range is the dominant effect in limiting system range capability, since the path-integrated attenuation due to moisture is usually quite minimal. Conversely, at very shallow elevation angles both water vapor and backscatter levels are high even at longer ranges. In this situation the exponential effect of the water vapor absorption usually dominates, especially under moist conditions, and signal fall-off with range on the R(20) line is often quite steep. For our measurements, the best sensitivity versus range usually occured somewhere between the two elevation angle extremes.

Measurements of either dew point wet-and-dry-bulb temperatures, and/or humidity were recorded immediately outside the lidar trailer on

220

most days to provide an estimate of atmospheric water vapor con-
centration at the surface. Such measurements gave useful concentration
values for comparison with the DIAL estimates made along a horizont-
ally-pointing path. During June, moisture profiles were obtained con-
currently with the lidar measurements by rawinsondes launched adjacent
to the lidar trailer. Comparisons of these two measurements are
discussed in detail in Section D.

B. METHOD OF ANALYSIS

Magnetic tapes containing the digitized DIAL measurement data were
analyzed on a Data General Eclipse minicomputer. The data array for
each lidar pulse consisted of 500 to 1000 complex (in-phase and
quadrature) samples of the backscattered signal. Since the sampling
rate was fixed at 10 MHz, the pulse propagated 15 m between each
sampled point. Maximum range in the digitized backscattered returns
varied between 15 and 30 km depending on the number of samples taken.

The first step in reduction of the data was to ca̲ ulate, for each
digitized return, the average power in each complex sample by the
previously-discussed summation of the in-phase and quadrature com-
ponents. This produced single-pulse power versus range profiles.
Since, as was shown in Chapter IV, single-pulse power estimates have
large uncertainties caused by speckle, it was necessary to average
multiple returns. The optimum averaging interval for DIAL measure-
ments, where the ratio of backscattered power measurements from two

221

ranges must be computed, is that which maximizes the correlation between the averaged power measurements from the two reference ranges. Since the data analyzed in Chapter IV showed a monotonically increasing correlation coefficient as number of pulses averaged increased, the returns at each wavelength were averaged over the entire data set (typically 500 - 1000 pulses) before computing the ratios. Only a single ratio estimate was obtained per line, thus the question of how to best average the ratios (i.e., whether to average the log ratios or take the log of the average ratio; see Chapter IV and Rye [120]) was not important. When 500 pulses were averaged to produce mean power profiles, the fluctuations due to speckle and shot noise were substantially reduced. Noise effects at longer ranges were still signficant after averaging.

Since the raw detector-output signal contained energy from shot noise as well as from the backscattered energy, the estimate $\hat{P}_i = X_i^2 + + Y_i^2$ where X and Y are the in-phase and quadrature components, was biased. This bias was removed by forming an estimate of the total noise power and subtracting this estimate from the computed total power of each point in the profile. As described in Chapter IV noise power was calculated from a "noise gate", defined as a distant range from which no backscattered signal was present. Selection of the location of the "noise range-gate" was made from observation of the signal on the oscilloscope monitor. This method worked quite well, although care had to be taken to ensure that a long-range cloud or some other high-reflectivity target did not intrude into the noise gate.

The mean noise power was averaged over the same number of pulses as was the signal estimate, then subtracted point-by-point from the average signal profile. This technique assumes stationarity of the noise signal (i.e., that the statistical properties of the noise within the noise gate are identical to those of the noise at all other ranges). Figure 5-1 shows a plot of average system noise power versus range. Since very little variation with range is apparent, the stationarity assumption is probably valid.

Despite averaging large numbers of pulses, the effect of noise-induced fluctuations was generally significant at longer ranges. To further smooth the profile a finite-impulse-response (FIR) filter was employed on the data sequence. Response of the filter was approximately matched to the range resolution as determined by the transmit pulse shape. The smoothing filter impulse response was formed by truncating the ideal discrete lowpass filter response

$$h_f(\tau) = \text{sinc}\left(\frac{\tau}{\tau_f}\right) \tag{5.1}$$

at the first zero crossings. Filtering completely eliminated the white fluctuations in the profile such that only the longer scale fluctuations remained. Based on the discussion in Chapter IV, range resolution calculated from the filter response and the pulse shape is on the order of 0.5 km for the filtered profile.
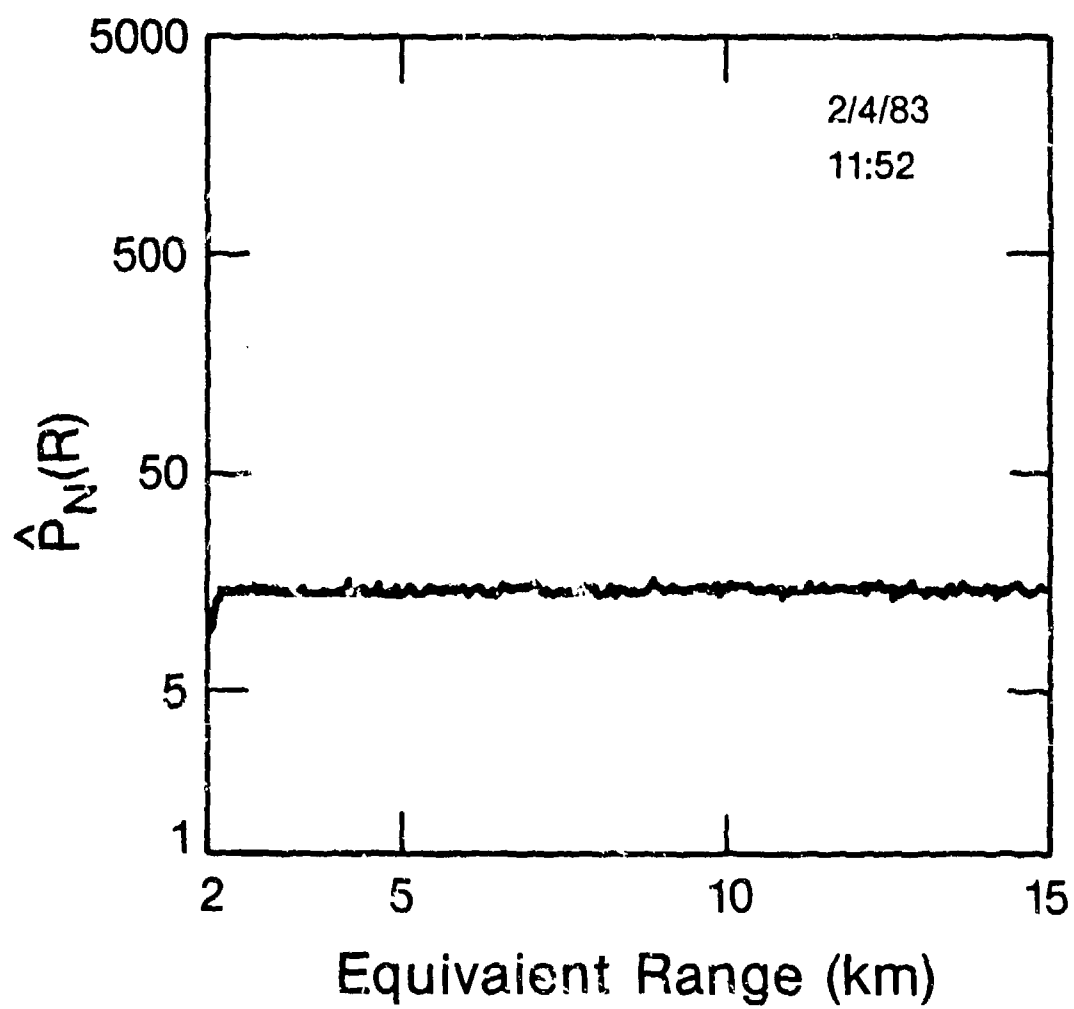
Following filtering, the ratio

223

Fig. 5-1 - Average system noise power versus range.

$$\hat{r}\left(R + \frac{\Delta R}{2}\right) = \frac{\hat{P}_s(R)}{\hat{P}_s(R + \Delta R)} \tag{5.2}$$

was calculated for the data set at each wavelength. In general, since $R(20)$ is the absorbed wavelength, $\hat{r}(R + \Delta R/2)$ was higher on the $R(20)$ line than on the $R(18)$ line, because of the increased attenuation across the range cell. The total integrated path absorption eventually causes the $R(20)$ signal to fall below threshold at ranges where the $R(18)$ signal is still relatively strong; thus, at some range the $R(20)$ ratio reduces to near unity. Since at this range the $R(18)$ ratio is higher, the absence of $R(20)$ signal produces the same result as a negative species concentration. This marks the maximum range of the measurement.

The species concentration is calculated from

$$\rho\left(R + \frac{\Delta R}{2}\right) = \frac{1}{2\bar{K}_m \Delta R} \left[\ln \hat{r}_{R20} \left(R + \frac{\Delta R}{2}\right) - \ln \hat{r}_{R18} \left(R + \frac{\Delta R}{2}\right) \right] \tag{5.3}$$

where ΔR is the absorption cell length and $\bar{K}_m(R + \Delta R/2)$ is the differential absorption cross-section at range $(R + \Delta R/2)$. For these calculations ΔR was defined to be the distance between the centers of the range-weighting function assuming constant backscatter at times τ_1 and $\tau_1 + \Delta t$, where Δt was generally 6.7 μs. As discussed previously, inhomogeneities in the radial backscatter can effectively change ΔR, introducing error into the measurement.

225

A key parameter in Eq. (5.3) is the differential absorption cross section $\overline{K}_m(R)$. As discussed in chapter III, errors in $\overline{K}_m(R)$ can produce systematic errors of as much as 20% or so in the DIAL measurements. Because of the remote nature of the measurement, assumptions must be included in specification of $\overline{K}_m$. The following section is devoted to a discus ion of these assumptions.

C. ABSORPTION CROSS-SECTION ESTIMATION

The absorption-cross-section (ACS) estimation problem for remote measurements is significant. First, one must know the species absorption spectrum with a resolution equal to the transmitter (in this case, 10 MHz) given certain standard environmental parameters such as temperature, total pressure, and gas partial pressure. Then, the change in ACS as these environmental parameters vary must be established. Finally, even in cases where ACS behavior with environment is precisely known, errors will still be introduced in remote measurements because the environmental parameters such as temperature and pressure at the measurement point cannot be precisely monitored. In the case of DIAL water vapor profiles using the R(20)/R(18) line pair, uncertainties in each of the above factors contributes to measurement errors.

Over the past 15 years or so, much has been reported in the literature on absorption cross-sections of various molecular species at CO_2 laser wavelengths. This research coincides with an increased awareness of DIAL techniques for species modeling. Consequently, data

on absorption cross-sections in the 9-11 μm spectral region for a
number of common atmospheric pollutants or hazardous gases are reaso-
nably abundant. In most cases, the reported values of ACS are in
reasonable agreement for a given species.

When the species of interest is water vapor, however, a noted
disparity exists between reported values of ACS. Absorption by water
vapor is somewhat unique because of the so-called water vapor con-
tinuum. The existence of a continuum has been postulated as a means of
explaining experimental observations which show water vapor absorption
to be greater than predicted by conventional models (i.e., Lorentz).
Although there seems to be general agreement regarding the existence of
the continuum, there is as yet no definitive model to explain its
dependence on temperature and pressure. Consequently current models of
water vapor absorption in the 8-12 μm region rem. n largely empirical.

Because of this uncertainty, work on specification of water vapor
absorption at CO_2 wavelengths appears to be continuing. Since the pri-
mary interest here is absorption on the R(20)/R(18) line pair, the
literature was surveyed for data on measurements at these wavelengths.
The work most often quoted is that by Shumate et al. [121], where a
spectrophone was used to measure absorption in air and nitrogen by
water vapor at three partial pressures (5.0, 10.0, and 15.0 torr).
Total pressure during the measurements was 760 torr; temperature was
300 K. At 10 torr partial pressure the measured absorption coef-
ficients on the R(20) line were 9.9×10^{-t} cm^{-1} when a nitrogen

background was used and 11.0×10^{-6} cm^{-1} for an air background. These values correspond to absorption cross-sections of 7.52×10^{-4} atm^{-1} cm^{-1} and 8.36×10^{-4} atm^{-1} cm^{-1}, respectively. Measurements taken by Shumate et al. at the other two partial pressures indicated a roughly linear dependence in absorption coefficient with concentration.

Later measurements by Nordstrom et al. [122] and Peterson et al. [123] were in good agreement with those reported by Shumate et al. Nordstrom et al. using a long path absorption cell, measured the R(20) absorption coefficient to be 9.86×10^{-6} cm^{-1} for 10 torr of water vapor mixed to atmospheric pressure with an 80:20 mixture of nitrogen and oxygen. Peterson et al. studied water vapor broadened by nitrogen only. Employing both a spectrophone and a white cell, their measurements corresponded to an absorption coefficient of 10×10^{-6} cm^{-1} for 10 torr of water vapor. Although Peterson et al. did not present data on the dependence of absorption with water vapor partial pressure, their stated observation of a quadratic dependence of continuum absorption versus concentration agreed qualitatively with that observed by Shumate et al.

This general agreement among the previous groups on ACS value for the R(20) line of approximately 8.6×10^{-4} atm^{-1} cm^{-1} is disputed in work reported by Ryan et al. [124]. Ryan et al. used a spectrophone to measure water vapor absorption on lines of CO_2 isotopes $^{13}C^{16}O_2$ and $^{14}C^{16}O_2$ as well as on $^{12}C^{16}O_2$. On the R(20) line, they measured an absorption coefficient of 5.36×10^{-6} cm^{-1}, which is about half of the

228

value measured by Shumate et al. Although aware of the discrepancy with previous work, Ryan et al. offered no explanation, stating that the careful attention paid to potential error sources during their measurements would be expected to produce accurate estimates. On the subject of dependence of the absorption coefficient on species partial pressure, their results were in much better agreement with those of Shumate et al. Both observed a linear variation with no apparent quadratic term.

Results of the measurements discussed above are presented in Fig 5-2, along with absorption as predicted from the 1978 version of the widely-used AFGL absorption model [39]. Absorption coefficients measured by Shumate et al., Nordstrom et al., and Peterson et al. are approximately a factor of 3 greater than those predicted by the AFGL model; even the lower value measured by Ryan et al. is 1.5 times as great as the AFGL calculated value. Thus, a rather wide range of values is available from which to choose. When processing our measurements, as described in the next section, water vapor concentrations were calculated using both the Shumate et al. and Ryan et al. cross-section. As will be shown, the larger value generally produced the better estimate.

The measurements described above were all performed at pressures and temperatures close to standard. In actual profiling applications, where one would like to estimate concentrations to altitudes of as much as 5 km, the variations of temperature and pressure with height and
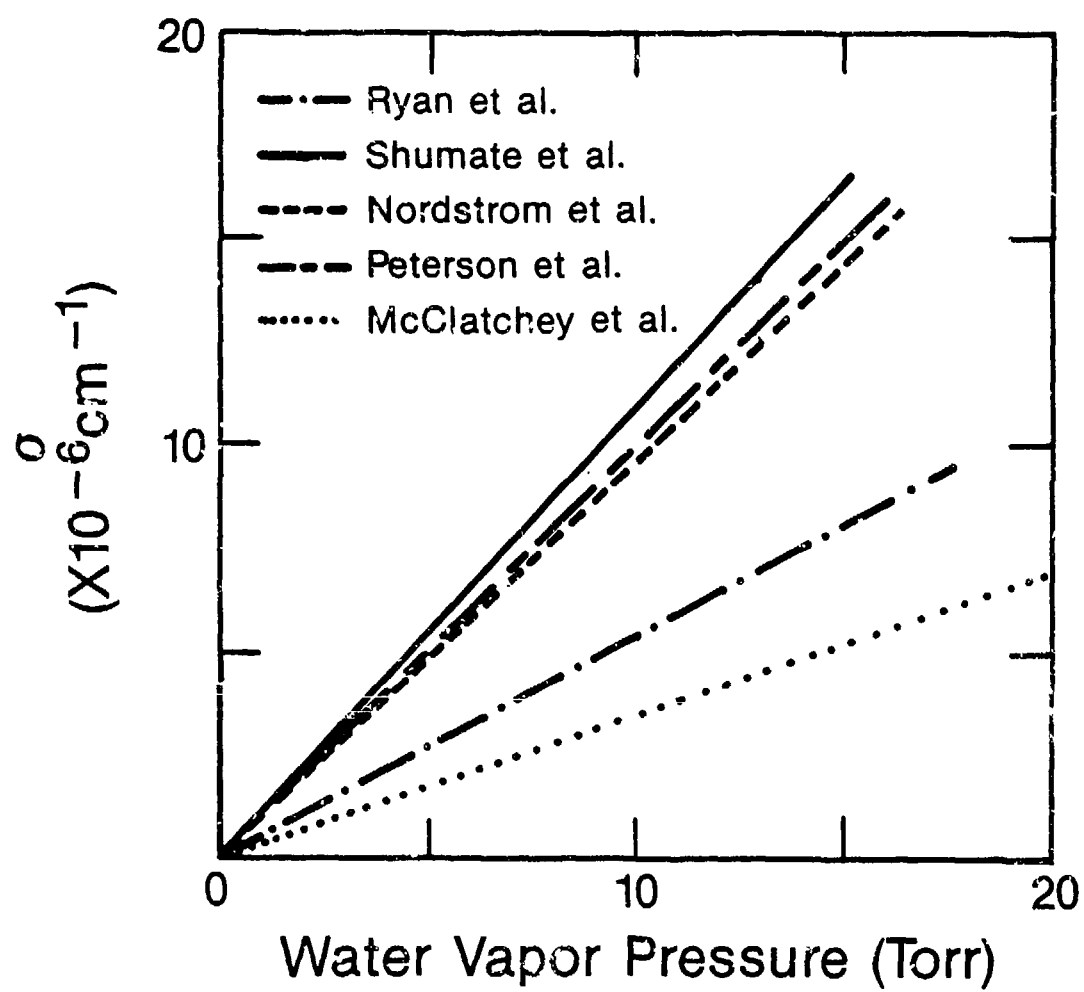
Fig. 5-2 - Absorption coefficient on R(20) line versus water vapor
partial pressure as measured by different authors.

their effect on absorption cross-section must be considered. As dis-
cussed in Chapter III, inaccuracies in estimating this parameter can be
major sources of error in water vapor measurements.

To examine the pressure and temperature dependence of the water
vapor absorption cross-section on the R(20) line, parameters from the
AFGL model were used. From Eqs. (3.54) and (3.55), the ACS can be
written as

$$\bar{K}_\nu(T,\rho) = K_\nu(T_o,\rho_o) \frac{\alpha(T,p)[(\nu-\nu_o)^2 + \alpha^2(T_o,n_o)]}{\alpha(T_o,p_o)[(\nu-\nu_o)^2 + \alpha^2(T,p)]} \exp\left[\frac{1.439E''(T-T_o)}{T\,T_o}\right]$$

(5.4)

where $\bar{K}_\nu(T_o,p_o)$ is the ACS at standard temperature and pressure and
other rms were previously defined in Chapter III. Figure 5-3 shows the
predicted variation in ACS versus temperature at three atmospheric
pressures, assuming $\bar{K}_\nu(T_o,p_o)$ is that calculated from Shumate et al.,
and other parameters are those used in the AFGL line parameter com-
pilation.

The curves indicate both a temperature and pressure dependence in
the predicted ACS. Pressure uncertainty effects are in reality rather
small, as first discussed in Chapter III, since typical deviations in
the pressure at a given height only vary by at most a few percent from
the climatological models. The ACS error is much more strongly
affected by potential uncertainties in temperature, as is obvious in
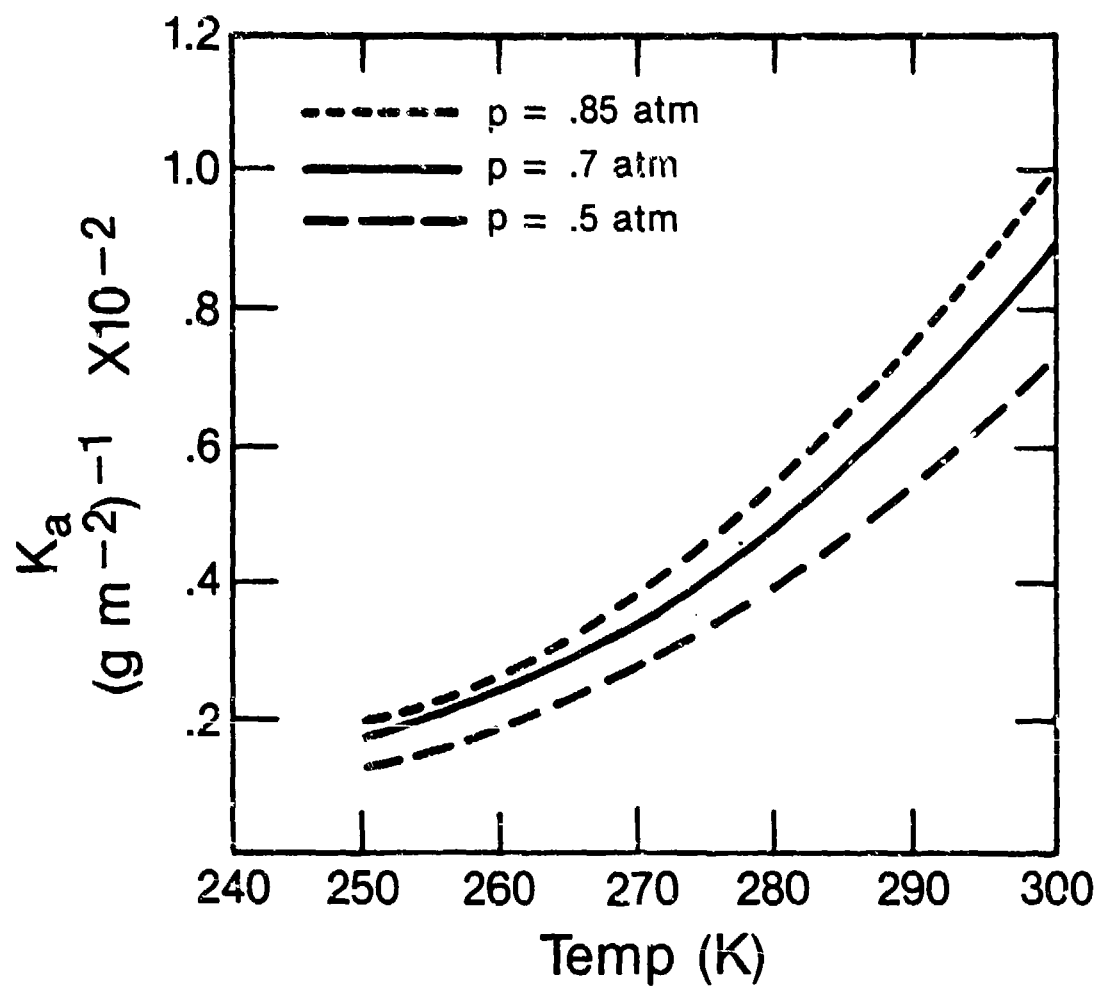
231

Fig. 5-3 - R(20) absorption cross-section temperature-dependence computed using McClatchey model, assuming $K(T_o, p_o)$ measured by Shumate et al., [121].

Fig. 5-3. For example, at 850 mb pressure the ACS is predicted to
decrease by a factor of 5 as the temperature varies between 300 K and
250 K. Although a 50 K error in temperature estimation is unlikely,
errors on the order of 10° or more are certainly possible, especially
when the temperature aloft must be estimated a priori from the ground
with no additional information. Consequently, one must in this case
start with a reasonable estimate of temperature in order to estimate
water vapor.

One method of estimating temperature aloft is to employ seasonal
climatological means. This technique is probably unacceptable even in
the upper troposphere since passage of transient eddies can cause as
much as a 5 K deviation from the seasonal mean. The situation is even
worse in the boundary layer, where inversions or local effects can pro-
duce significant deviations from seasonal means.

A second method is to use profiles measured by the nearest rawin-
sonde launch. Although this should be better than using the climatolo-
gical means, the method is again unreliable near the ground. To
account for behavior in the boundary layer, the profile might be
adjusted based on the surface temperature. Obviously an extensive
study could be undertaken on the best method of estimating temperature
profiles for DIAL measurements. In our case since only three measure-
ments of elevated water vapor profiles were attempted, an empirical
method was used. It was assumed that the temperature lapse rate in the
lower 3 km was either standard or convective, based on observation of

233

weather conditions and time of day. If the convective assumption was made, as would be the case on a hot summer afternoon, a temperature lapse rate of 10 K/km below 3 km, and 6 K/km above 3 km was assumed. This agreed reasonably well with observations from rawinsonde launches at the Boulder Atmospheric Observatory (BAO), site of the summertime DIAL measurements, and of Denver Airport (Fig. 5-4). Maximum deviation between the convective model and any of the measured profiles is less than 2 K. Under non-convective conditions a single lapse rate of 7 K/km was assumed from the ground upward. Thus, to estimate ACS the surface temperature was measured and the appropriate lapse rate applied. Note that a general implementation of this technique would have to take into account inversions, where temperature increases with height. This would be especially true for morning measurements. However, since all of the profile measurements took place on clear afternoons, the potential presence of inversions was neglected.

After analyzing the actual DIAL measurements, as described in the next section, the lidar estimates using the Ryan et al. ACS showed a consistent tendency to be biased high when compared to moisture measurements from other sources. Because of this tendency, values of ACS computed by Shumate et al. were generally employed. Even when this higher value was used, overestimates still occurred in the profile estimates at the higher altitudes. This seemed to imply that the predicted temperature and pressure dependence of the ACS, as computed from Eq. (5.4), was not correctly modeling ACS behavior. No published data
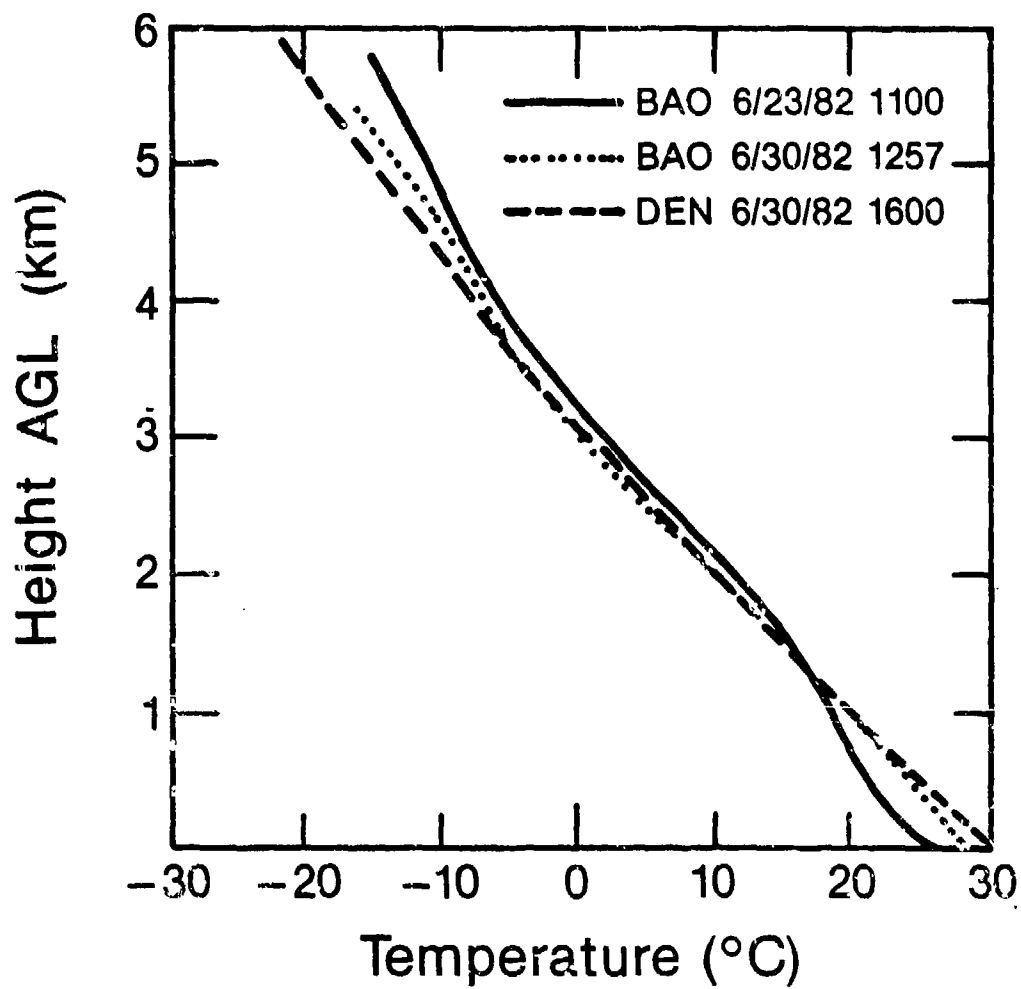
234

Fig. 5-4 – Temperature lapse rate measured on two different summer days (3 observations).

on R(20) ACS values at other than standard conditions were found with which to compare the model predictions.

In their discussion of the discrepancy between their measurements and the AFGL-predicted ACS on the R(20) line, Shumate et al. state that the separation $\Delta\nu$ between the H_2O and CO_2 line centers could be less than assumed in the model. If such were the case, the ACS pressure dependence would be less than that computed in the AFGL model. Shumate et al.'s hypothesis was taken a step further by calculating the value of $\Delta\nu$ necessary to obtain their observed ACS, assuming other line parameters were unchanged. The resulting value of $\Delta\nu$ is .04 cm^{-1}, compared to .08 cm^{-1} assumed in the AFGL model. Given the modified $\Delta\nu$ the dependence of ACS on pressure and temperature can then be computed. Figure 5-5 shows the resulting curves. Comparing with Fig. 5-3 it is seen that ACS is expected to change much less versus pressure with the smaller $\Delta\nu$. Temperature dependence also decreases, albeit very slightly. Because it produced better agreement with observations, the smaller $\Delta\nu$ value was used to calculate ACS temperature and pressure dependence. As is shown in the next section, the results, though better, still appear to be biased high.

D. RESULTS

Because of heavy use of the NOAA lidar for a multitude of research tasks, the DIAL data set was limited to 9 cases roughly evenly spaced during the period from October 1982, through June 1983. Since water
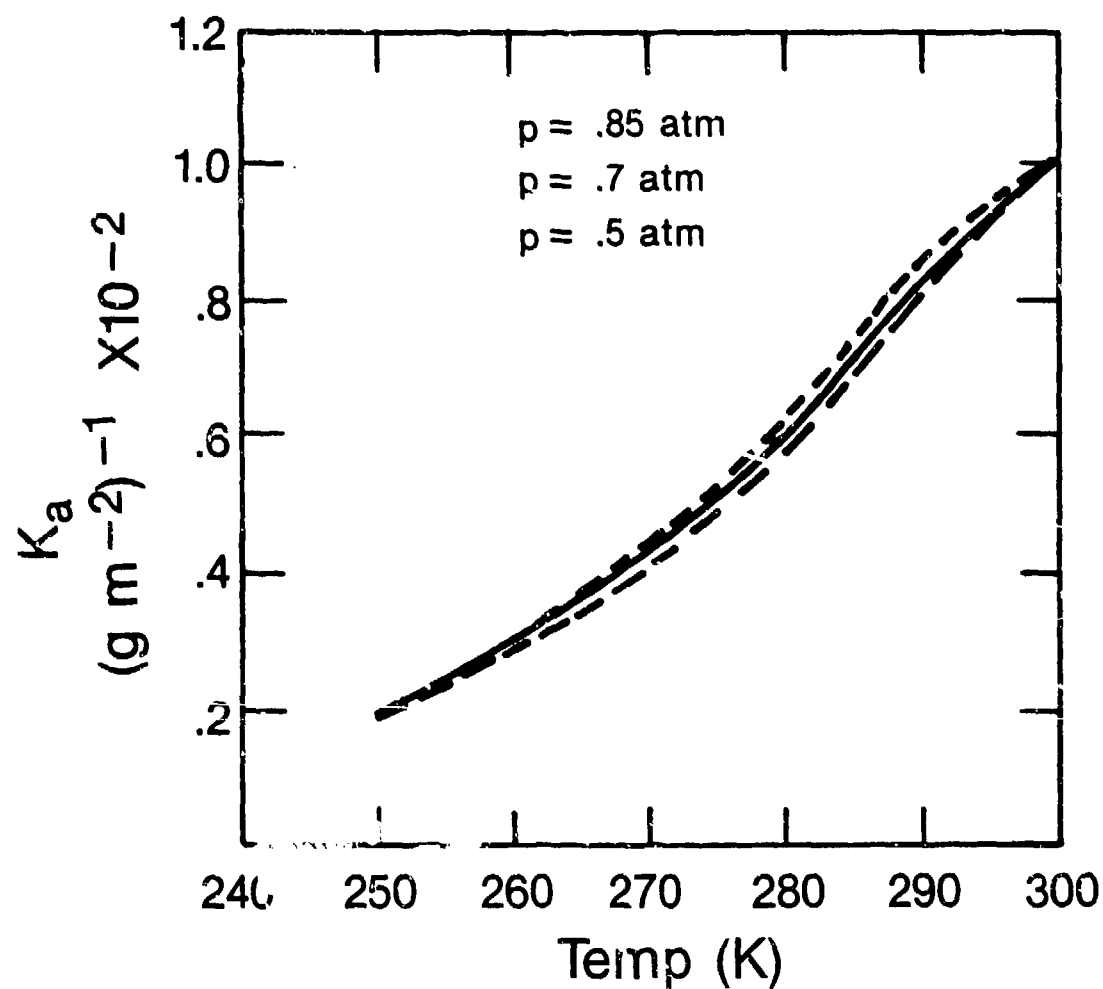
236

Fig. 5-5 – R(20) absorption cross-section temperature-dependence using adjusted McClatchey model, where Δy was decreased to reconcile model output and Shumate et al., observation.

237

vapor concentration typically falls off sharply with height during the winter months, measurements between October and March were performed with the lidar pointing roughly horizontally. Such measurements poten-tially enable examination of spatial structure in water vapor con-centration, as well as having ground-based humidity sensors available for comparison. Also, backscatter coefficients were usually of suf-ficient magnitude within the boundary layer and lower troposphere that measurements to beyond 10 km were possible. Such is not usually the case for wintertime vertical measurements, when both backscatter coef-ficient and water vapor concentration both tend to decrease rapidly within a few km of the surface. During spring and summer, when both elevated moisture levels and backscatter coefficients increased, ver-tical profile measurements were performed by directing the lidar beam at steeper elevation angles.

In order to avoid repetition while still emphasizing the important points in the measurement results, two wintertime, one spring, and two summertime measurement cases are discussed in detail. These cases are, in general, characteristic of the cases which, in the interest of bre-vity, will not be discussed.

1. February 4, 1983 Measurement

DIAL measurements on this day were made following the series of runs to gather data on return characteristics discussed in Chapter IV. The lidar was elevated at approximately 5° elevation and pointed toward

the east. Four measurements were taken over a period of approximately 1 hour; each measurement consisted of 1000 shots sampled at each wavelength.

Figure 5-6 shows the averaged power versus range from each measurement. The apparent presence of backscatter inhomogeneities causes fluctuations in the power profiles over scale sizes of 0.5 km or greater. These fluctuations, which vary in intensity and range from one measurement set to the next, are indicative of a constantly changing backscatter medium. Since both the R(20) and R(18) returns are affected, the fluctuations are probably not caused by water vapor variability, which would tend to cause fluctuations only in the R(20) return.

It is interesting to observe the increase in the intensity fluctuations in Fig. 5-6 as time proceeds. Although some inhomogeneties are present, the 13:27 measurements show a relatively smooth profile, which is consistent with the observation discussed in Chapter IV that the intensity-versus-range profile measured during the 20 minute data-gathering segment at 12:25 did not show significant 1-km scale fluctuations. In the 13:35 measurement, however, a rather sharp discontinuity can be seen in the R(20) range profile at approximately 6 km range (the R(20) data set was actually taken at 13:46). This apparent inhomogeneity continues to be present at both wavelengths of the 13:59 measurement. At this time the entire profile has acquired noticeably more structure than in the 13:35 measurement taken 1/2 hour early. The
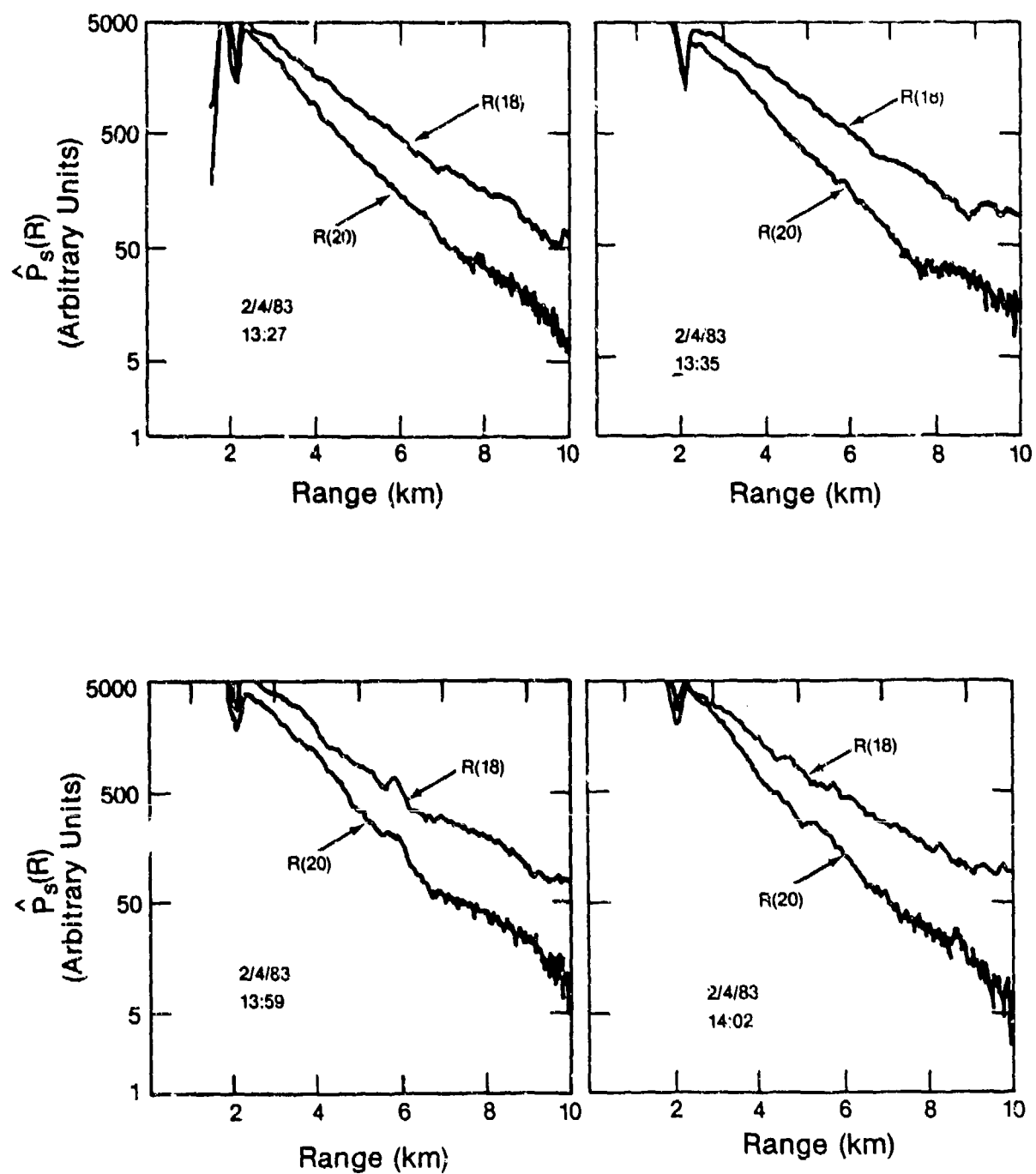
Fig. 5-6 - Averaged power versus range profiles for consecutive measurements on February 4, 1983.

13:59 and 14:02 R(20) measurements differed by only 3 minutes, yet a definite change can be seen in the profile structures. Such a rapidly-changing backscatter environment is generally not conducive to accurate sequentially-tuned DIAL measurements.

Because of their large scale size, the effects of the inhomogeneities are not altogether filtered by the lowpass filter (Fig. 5-7). Although all detection noise is apparently eliminated, the fluctuations due to the inhomogeneities remain in the filtered profiles, as well as in the profiles of ratio $\hat{P}_s(R)/\hat{P}_s(R + \Delta R)$ (Fig. 5-8). The presence of the abrupt increase (decrease) in the filtered power profile at around 6 km range causes a full wave oscillation in the ratio profile, since the power ratio relative to the next range is increased (decreased and the ratio relative to the preceding range is decreased (increased). This is seen in Fig. 5-8, where the backscatter inhomogeneity at 6 km range produces a sharp decrease in the $\hat{P}_s(5 \text{ km})/\hat{P}_s(6 \text{ km})$ ratio, and a sharp increase in the $\hat{P}_s(6 \text{ km})/\hat{P}_s(7 \text{ km})$ ratio. The effect of this inhomogeneity on the ratio increases dramatically between 13:35 and 14:02.

Figure 5-9 shows the estimated water vapor concentrations for each of the four measurements, calculated using both the ACS measured by Shumate et al. and the lower value reported by Ryan et al. Both estimates are corrected for temperature using Eq. (5.4). Figure 5-10 shows the mean of the four measurements, as well as the surface moisture measured at BAO (25 km away). No local measurements were taken on this
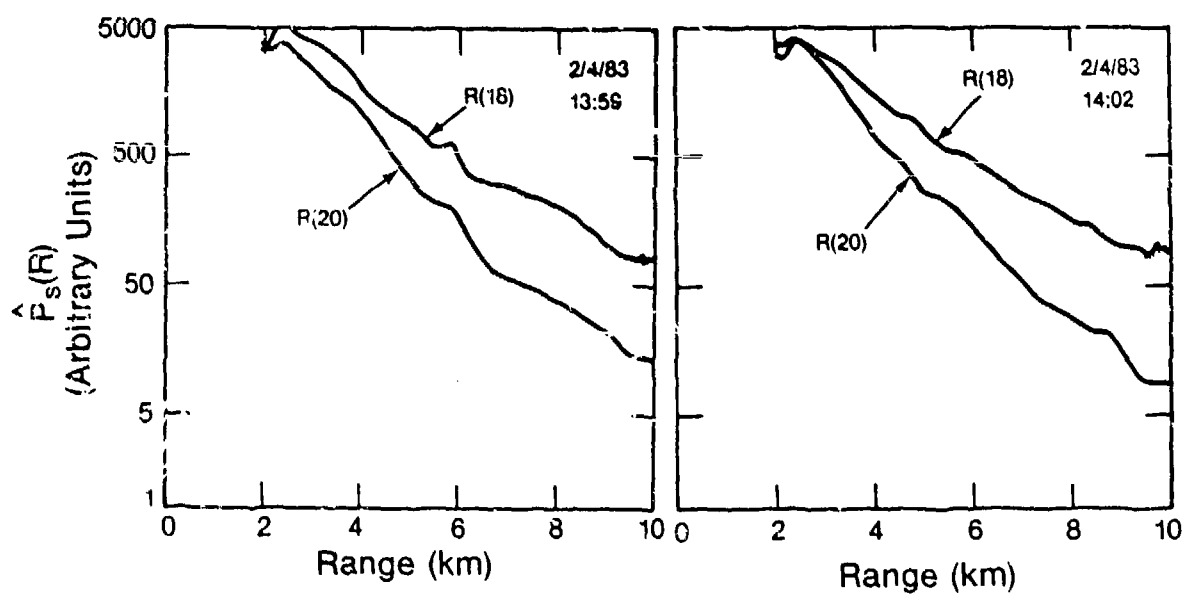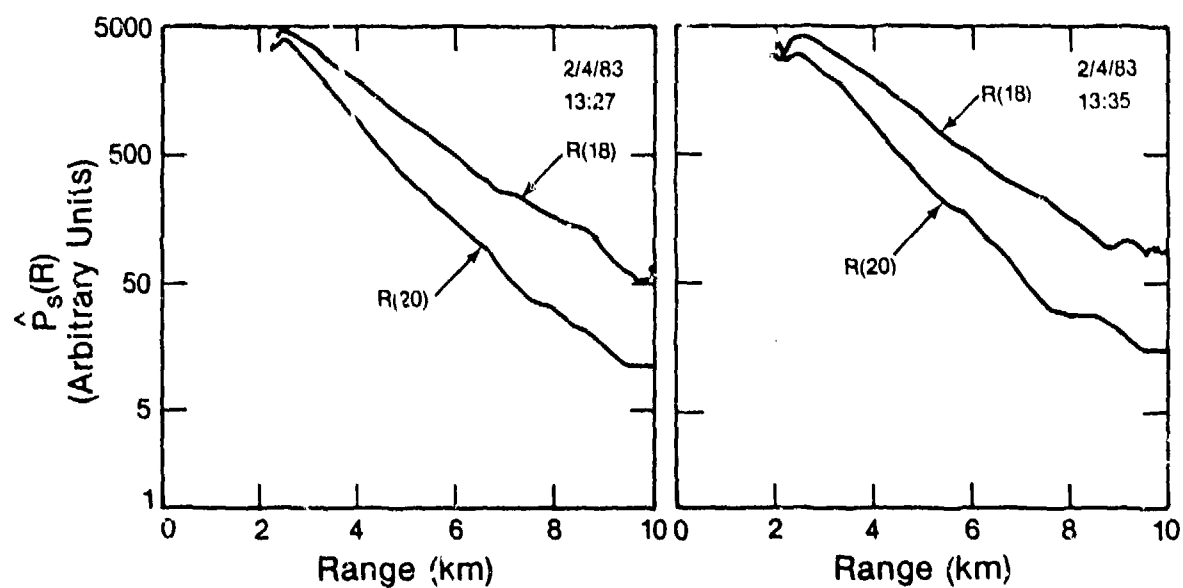
241

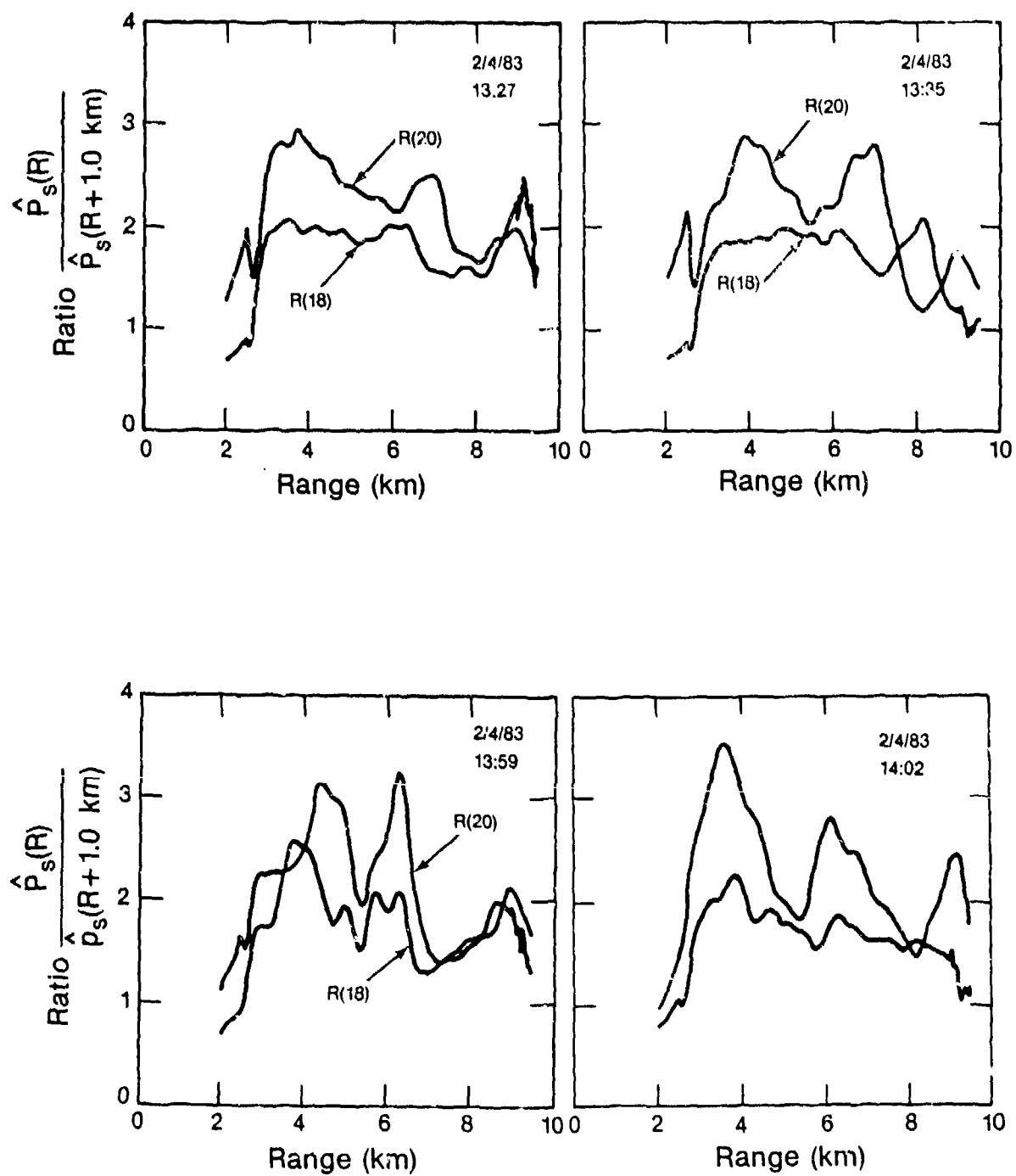Fig. 5-7 - Range-filtered averaged power versus range profiles for consecutive measurements on February 4, 1983.

Fig. 5-8 - Ratio of adjacent range power measurements versus range
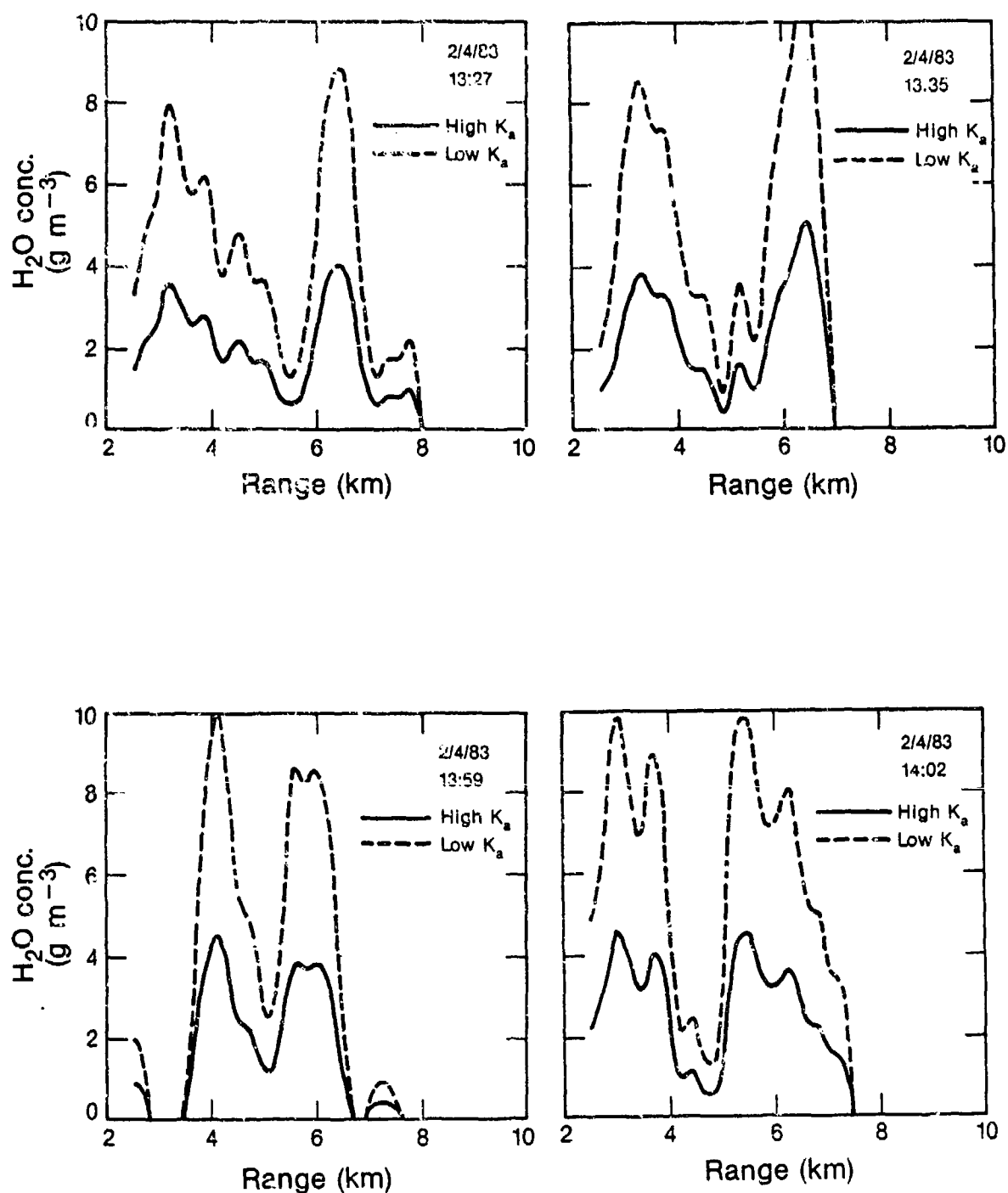for February 4, 1983, measurements.

Fig. 5-9 – Concentration measurements from February 4, 1983, data calculated using Shumate et al., (solid line) and Ryan et al., (dashed line) absorption cross-section values.

day. The temperature-corrected Shumate et al. ACS value which was used in Fig. 5-10 produced a profile whose mean more closely approximated the measured water-vapor concentrations. The oscillations due to the previously-discussed backscatter inhomogeneities which show up in the individual lidar measurements are also readily apparent in the mean. Because the data were taken at an elevation angle of 5°, some decrease in water vapor with range, as seen in the trend of Fig. 5-10, might be expected.

By calculating the mean CNR vs. range profiles for the R(18) and R(20) measurements, a rough estimate of the expected standard deviation in the concentration estimate due to speckle and noise can be obtained from

$$\sigma_{\bar{\rho}}(R + \frac{\Delta R}{2}) = \frac{1}{2\bar{K}_m \Delta R N^{1/2}} \left[\frac{\sigma_{\hat{r}_a}^2}{\langle \hat{r}_a \rangle^2} + \frac{\sigma_{\hat{r}_w}^2}{\langle \hat{r}_w \rangle^2} \right]^{1/2} \tag{5.5}$$

where the subscripts denote measurements at the absorbing and nonabsorbing (wing) wavelengths, and

$$\frac{\sigma_{\hat{r}}^2}{\langle \hat{r} \rangle^2} \simeq \left[\frac{1}{\sqrt{m_s}} + \frac{1}{[CNR(R-\Delta R]\sqrt{m_n}} \right]^2 + \left[\frac{1}{\sqrt{m_s}} + \frac{1}{CNR(R+\Delta R)\sqrt{m_n}} \right]^2. \tag{5.6}$$

In Eq. (5.6) m_s and m_n are the number of intrapulse independent samples over the low-pass filter response time calculated from Eq. (3.24). Figure 5-11 shows the estimated standard deviation of the concentration measurement calculated from Eqs. (5.5) and (5.6) as well as the observed standard deviation in the four measurements. The observed
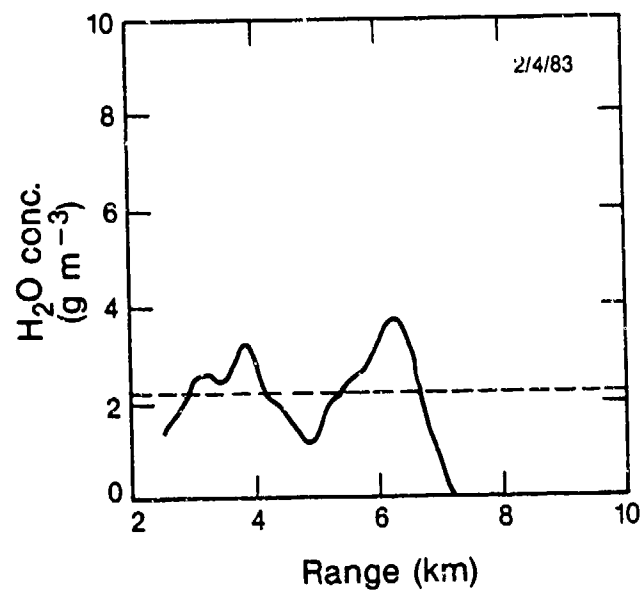
245

Fig. 5-10 - Mean of February 4 concentration measurements. Dashed line is ground measurement taken at BAO tower site.
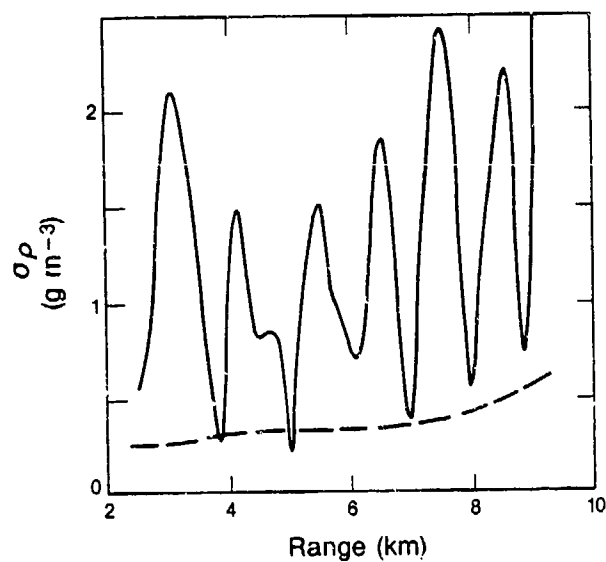

Fig. 5-11 - Standard deviation of February 4, 1983, concentration measurements (solid line) and estimated portion of standard deviation due to speckle and noise.

246

standard deviation shows a notable oscillation, due most likely to the radial advection of specific regions of aerosol inhomogeneity regions during the course of the measurement. The mean of the oscillating standard deviation vs. range plot in Fig. 5-11 is approximately 1.0 $g-m^{-3}$ which is about five times greater than the predicted uncertainty due to speckle and detection noise. This implies that other factors, most likely the backscatter variability, are dominating the speckle term, which is generally assumed to be the limiting factor in coherent DIAL measurements.

2. March 23, 1983 Measurements

A measurement set taken on March 23, 1983 at the Table Mountain field site was similar to the February 4 measurement in that the lidar was again directed approximately horizontal. In this case, however, the lidar pointed toward a north-south running ridge just to the west of the lidar field site. The return from the ridge at both wavelengths is apparent at a range of 8 km in Fig. 5-12, which shows the 1000-pulse-averaged unfiltered profiles. Since the ridge acts as a hard target, the entire pulse power profile can be seen as a function of apparent range.

Although only two measurements were taken on this day, the power versus range profile appears to show less of the one-half-km scale variations than were seen in the February 4 data. Based on the assumption that the fluctuations in the earlier data set were due to aerosol
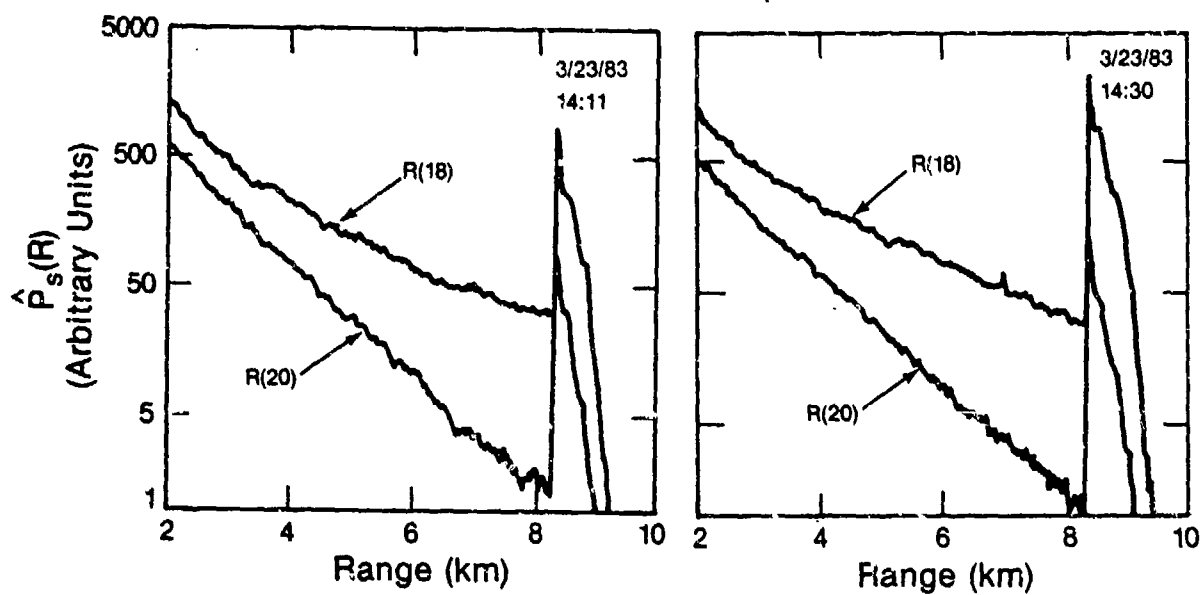
247

Fig. 5-12 – Averaged power versus range profiles for March 23, 1983, measurements.

inhomogeneities, this would tend to indicate better mixing of the aerosol in the boundary layer on March 23.

This observation of less fluctuation is confirmed in Fig. 5-13, which shows the ratio of averaged received power across the measurement cell versus range for the two measurements. It is seen that much more consistency between the two measurements than existed in the February 4 data. The two ratio profiles are very close to being identical. Such behavior is indicative of a nearly stationary data set over the course of the two measurements (approximately 25 minutes). It was assumed that the variations in the February 4 data set were caused primarily by the presence of large regions of aerosol inhomogeneities which were slowly advected across and along the beam. If this assumption is correct, the atmosphere on March 23 was either very well-mixed, such that significant large scale backscatter inhomogeneities did not exist; or alternately, the winds were so light that any significant regions of backscatter inhomogeneity did not advect across the beam during the measurement. In any event, the profiles at the two wavelengths exhibited much less variability with range.

Figure 5-14 shows the individual and 2-measurement-averaged lidar water vapor profile estimates. The surface reference for this case is a point measurement taken 25 km away at the Boulder Atmospheric Observatory. These and all ensuing DIAL concentrations were calculated using the higher (Shumate) value ACS only. The two measurements agree to within 1 $g-m^{-3}$ out to a range of about 6 km. In addition to
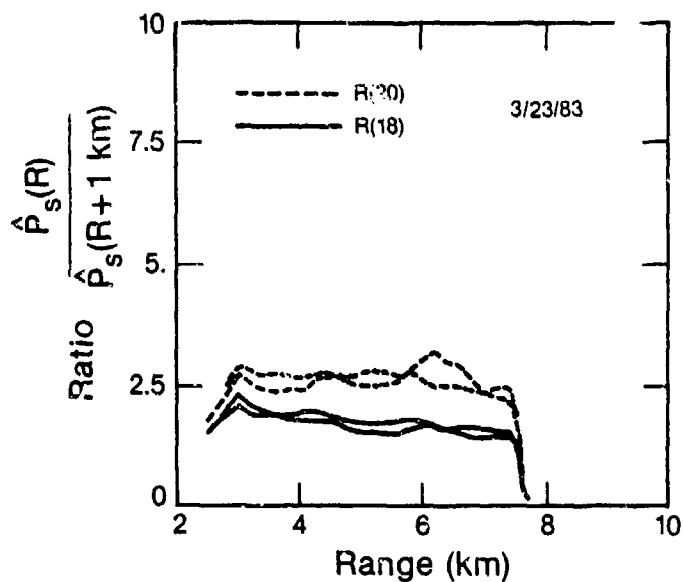
249

Fig. 5-13 - Adjacent-range
power ratios versus range
on R(20) (dashed) and R(18)
(solid) laser wavelengths
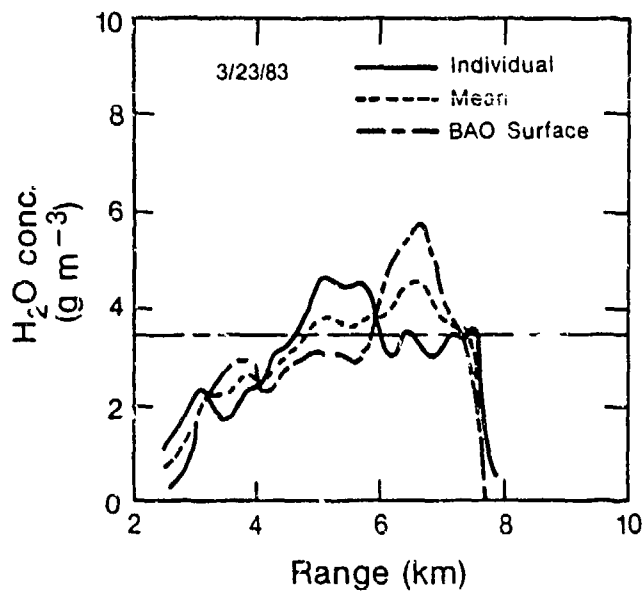for March 23, 1983,
measurements.

Fig. 5-14 - Individual and mean
concentration measurements
for March 23, 1983, data.
Long dashed line is BAO
mean surface measurement.

250

fluctuations, both of the March 23 profiles show a slight increase in water vapor concentration with range. Such behavior might be caused by the beam's increasing proximity to the ground, since the land slopes up toward the foothills as a function of range. Humidity could conceivably be higher just above the surface due to evaporation. As in the February 4 case, the Shumate ACS value gave an estimate much closer to the surface-measured water vapor concentration than did the Ryan et al. value. Although reasonable, the estimat: appears to be biased slight high relative to that from the hygrometer.

When the observed versus predicted measurement standard deviations are compared (Fig. 5-15), it is again seen that the measured σ_ρ is, in a mean sense, roughly 3-4 times higher than that predicted due to speckle and noise. Since there were only two values in the observed data set, the statistyical sample on the standard deviation estimate is obviously rather poor; however, by "eyeball averaging" in range one can rather easily estimate the mean in the estimate of σ_ρ. The observed mean is substantially less than that of the February 4 data set.

As a final note on this data set, it is interesting to observe the effect of the distant ridge on the measurement data. Since the ridge is a solid target with a relatively high reflection coefficient compared to that of the atmospheric aerosol, the return power as shown in Fig. 5-12 increases sharply when the pulse encounters the hill. The power reflected back at the leading edge is proportional to the transmit power at the leading edge of the pulse, rather than the total
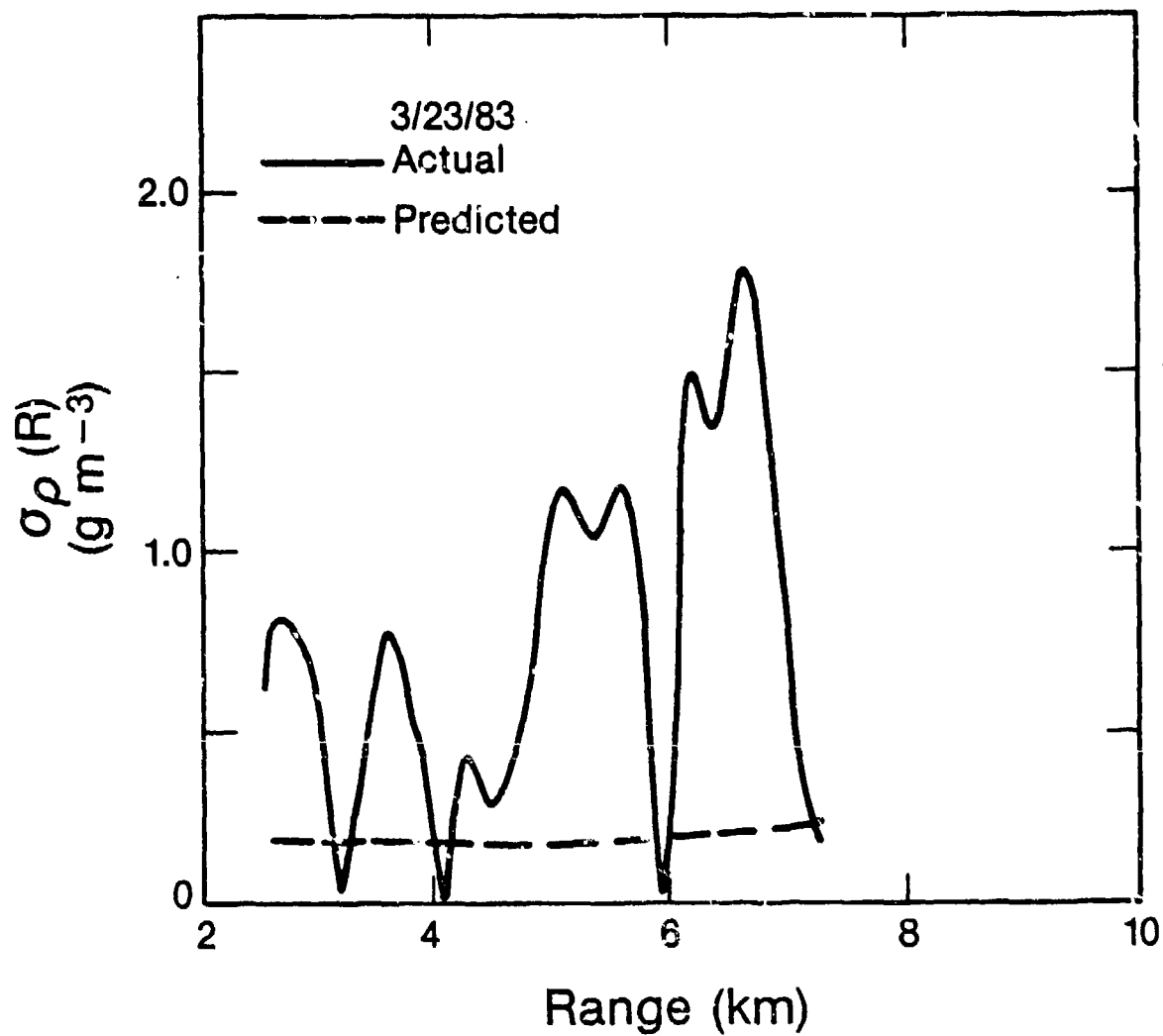
251

Fig. 5-15 - Observed standard deviation for March 23, 1983, measurements. Dashed line is estimated standard deviation due to speckle and noise.

energy in the pulse as in a distributed target. As a result, it is of little value to look at ranges beyond the edge of the hill-reflected pulse in order to calculate the power ratio $\hat{P}(R)/\hat{P}(R+\Delta R)$, since the ratio suddenly dips well below unity at both wavelengths as seen in Fig. 5-13.

The presence of the hill does provide an opportunity to estimate path-averaged concentration from the equation

$$\bar{\rho} = \frac{1}{2\bar{K}R} \left[\ln \frac{\hat{P}_a(R)}{\hat{P}_w(R)} \right] \tag{5.7}$$

where $\hat{P}_w(R)$ and $\hat{P}_a(R)$ are the returns from the hill at the nonabsorbing and absorbing wavelength respectively. Since the output signal was not monitored during these measurements it was assumed that energy output on both lines was approximately equal (other measurements have found this to be generally true). Substituting the appropriate values into Eq. (5.7), and using the larger ACS value, a concentration of 2.5 cm^{-3} was calculated, which is slightly less than both the mean of the range-resolved measurement profile and the point surface measurement.

3. May 4, 1983 Measurements

The data set taken on May 4, 1983, provided the first opportunity to attempt actual vertical profiling of water vapor. The day was clear and relatively warm; measured surface temperature was 17°C at the lidar van. During these measurements the lidar was parked at the National

Bureau of Standards in Boulder. Data were taken with the beam pointed southeast and elevated at an angle of 20°. A series of 5 measurements comprised the data set.

Figure 5-16 shows a sample of signal power versus height at the two wavelengths. A signal is detectable on the R(20) line to approximately 2.5 km above ground level (AGL), corresponding to a slant range of approximately 7 km. It is interesting to note that the fall-off in backscattered signal with range on both the R(18) and R(20) lines is less than in either the February 4 or March 23 data sets. Such a behavior implies a higher backscatter coefficient along the lidar transmit/receive path, which is somewhat unusual in light of the observation that the February and March measurements were taken at lower elevation angles, where one would typically expect higher turbidity. During the previous two springs, lidar backscatter levels in the middle and upper troposphere were observed to be higher than at other times of the year. This, coupled with the fact that Boulder is situated in a valley whose sides rise a few hundred meters to both the south and east, might explain stronger signals in the May 4 data.

The decreased signal attenuation versus range is apparent in the plot of $\hat{r}(R)$ in Fig. 5-17. On the reference R(18) line, mean signal decrease over 1 km was approximately 2.5 dB, compared to approximately 4 dB in the March 23 data and 3 dB in the February 4 data. The ratio plot shows reasonably good repeatability over the course of the five data runs. Variations in both ratio estimates were less than about 10% up to about 2.1 km height (~6 km range).
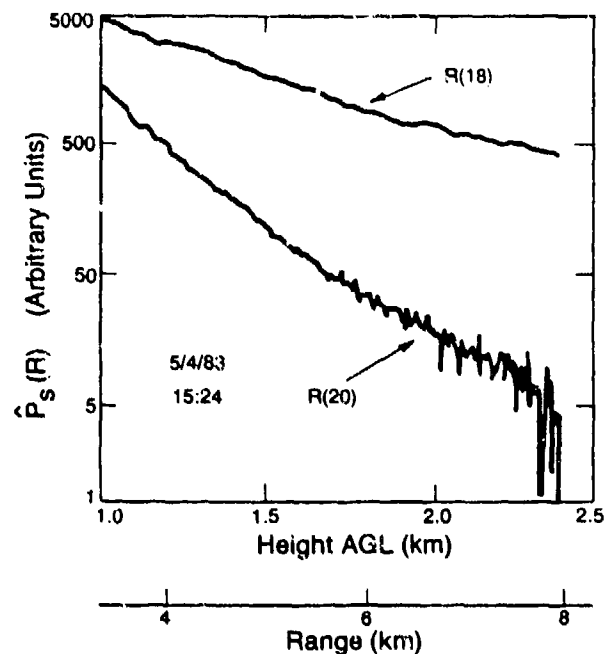
254

Fig. 5-16 - Averaged signal
power versus height (upper
scale) and range (lower
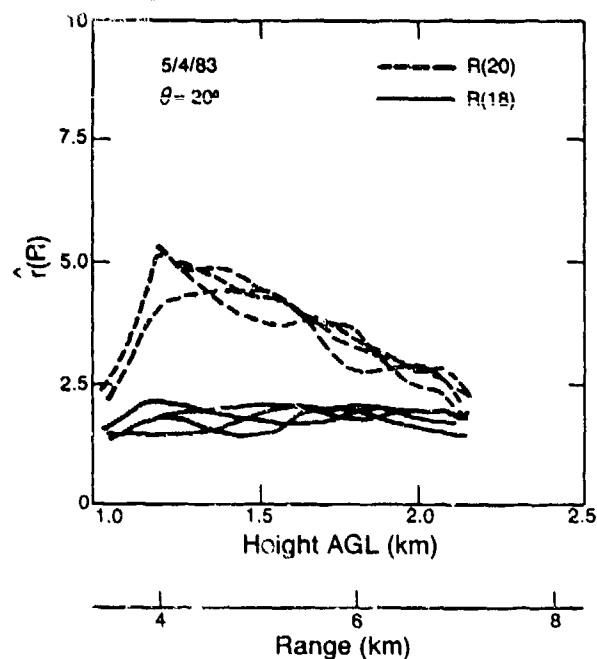scale) for one of May 4,
1983, measurement sets.

Fig. 5-17 - Adjacent range power
ratios versus range on R(20)
(dashed) and R(18) (solid)
laser wavelength for May 4,
1983, measurements.

Since this was a profile measurement, it was necessary to adjust the absorption cross section to account for the changes in temperature and pressure with increasing height. A standard lapse rate of 7°C/km above the surface, where the temperature was 17°C, was assumed. Although this was slightly less than the actual lapse rate measured by the 5 pm Denver rawinsonde, maximum temperature deviation from the rawinsonde profile was less than 2°C below 3 km.

The resulting concentration measurements (Fig. 5-18) show the same consistency that was present in the ratio plots. The mean of the measurement (dashed line in Fig. 5-18) indicates that a rather sharp decrease in water vapor concentration exists between 1.5 and 2 km above ground level. This discontinuity does not show up in either the morning or evening Denver rawinsonde soundings which are also shown in the figure. However, since height resolution of the soundings is rather poor in this region, such a sharp break in the profile could easily be missed.

Of more concern is the apparent bias in the measurements. Despite the good repeatability, each of the individual lidar measurements overestimates the moisture concentration when compared to either one of the rawinsonde profiles. There seems to be two separate but consistent sensor-dependent data sets, in which the lidar measurements agree among themselves, the rawinsonde measurements agree among themselves, but the two sets disagree with each other. The rawinsondes, which were displaced from the lidar measurement in both time and space, are
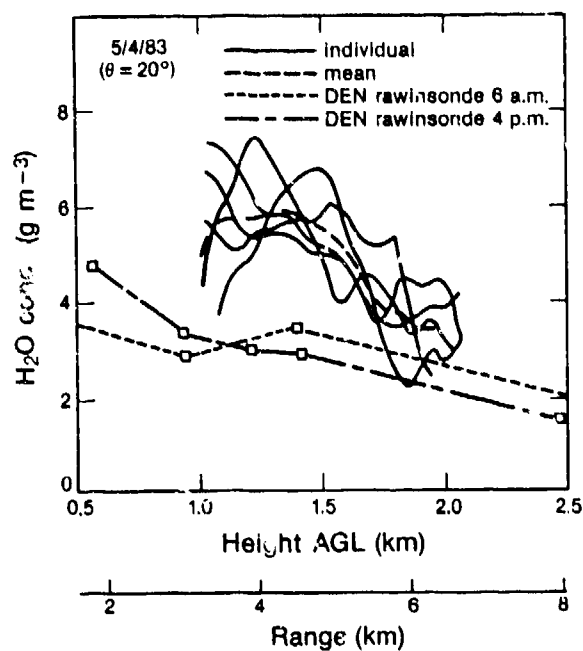
256

Fig. 5-18 - Concentration estimates for May 4, 1983, measurements. Also shown are a.m. and p.m. Denver rawinsonde moisture soundings.
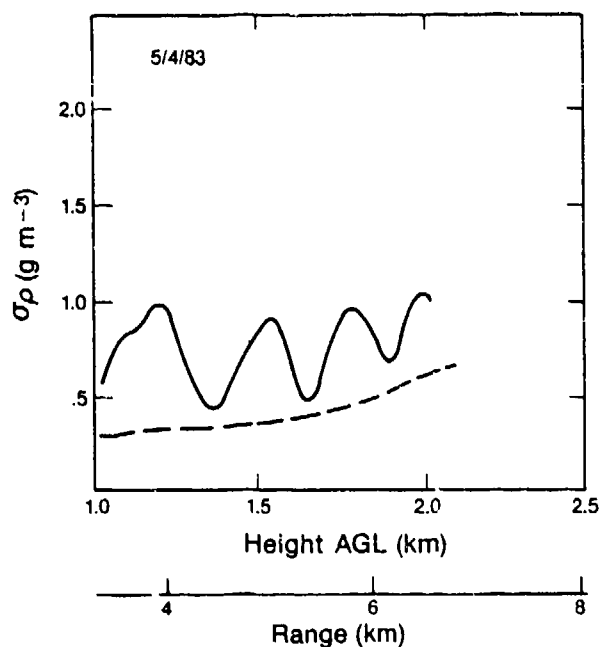
Fig. 5-19 - Measured (solid) and noise- and speckle-produced (dashed) estimate standard deviation for May 4, 1983, measurements.

certainly not an ideal comparison source. Hoehne [125] estimated accuracy of rawinsondes by comparing the measurements from two sondes tied to the same balloon and found that dew-point depression errors were on the order of $3.5°C$. Such errors correspond to concentration errors of approximately $2 \ g\text{-}m^{-3}$, which is significant. However the reasonable agreement between the two sondes gives cause to believe that the lower moisture readings are not caused by a few statistically inaccurate data points. Thus one is, in essence, left with an apparent bias between the two sensors which could be caused by spatial and temporal differences, resolution differences, or any number of other factors.

Comparing the observed standard deviation of the individual measurements to the predicted value (Fig. 5-19) assuming that speckle and shot noise dominate the error term, the observed error is again seen to be greater than the predicted error, in this case by a factor of about 2. Thus, other noise sources, such as aerosol inhomogeneities, were of approximately the same order as the speckle noise.

The actual mean standard deviation of the measurement was on the order of $0.75 \ g\text{-}m^{-3}$, which gives a normalized measurement error of approximately 15%. This would be quite acceptable were it not for the bias terms.

4. June 23, 1983 and June 30, 1983 Measurements

The final measurements to be discussed were taken on June 23 and June 30, 1983 under nearly identical summertime conditions. During these measurements the lidar was located at the Boulder Atmospheric Observatory (BAO), approximately 25 km east of Boulder. Because a balloon-launch facility was available at the BAO, rawinsonde launches timed to coincide with the lidar measurements were arranged. These simultaneous measurements potentially offered the best comparison data set of the entire measurement program.

The increased moisture present in the summer atmosphere was apparent in the measurements, especially on June 23. On this day the signal fall-off with range on the R(20) line due to low-level moisture was such that the maximum range attainable at a 45° elevation angle was only 4.2 km. Although this limited range capability was caused primarily by attenuation, system performance was further degraded due to unusually low lidar transmit energies. Measured output energy was only about 40-50 mJ per pulse on the R(20) line, which is more than 3 dB below the normal system pulse energy of 100-130 mJ. The July 30 data set was similarly degraded by low transmit energies, however, the decreased moisture levels on that day enable system maximum range to be extended to approximately 6.3 km at 45° elevation angle.

Figure 5-20 shows the ratios of adjacent range power estimates for the two lines for both measurement sets. The high attenuation on June

23 is evident in the R(20) ratio value, which peaks at value of 5, equivalent to nearly 7 dB of attenuation per km. The June 23 R(20) ratio estimates show much more variability than those computed from the June 30 data. Although this increased variability could be a result of turbulent eddies of water vapor advecting through the measurement volume, a more likely candidate is the decreased CNR of the measurements due to the high extinction. Since in these measurements the reference (R(18)) ratios stayed reasonably constant, backscatter variability is probably not the reason for the lack of measurement consistency.

As was discussed in Section C, in order to calculate the variation of ACS with height the temperature profile was modeled with a simple convective model for lapse rate. Based on this extrapolation of the surface temperature, the estimated ACS on June 23 was approximately $0.72 \times 10^{-4} \ g^{-1} \ m^2$ at 2 km height and $0.41 \times 10^{-4} \ g^{-1} \ m^2$ at 4 km height. For the June 30 data the adjusted ACS was estimated to be $0.81 \times 10^{-4} \ g^{-1} \ m^2$ at 2 km height and $0.46 \times 10^{-4} \ g^{-1} \ m^2$ at 4 km height. Thus, for both days estimated ACS decreased by about 40% over a few km.

Figure 5-21 shows the actual concentration measurements for both days, as well as the comparison rawinsonde measurements. Also plotted are the evening Denver rawinsonde measurements, to provide an example of rawinsonde variability. As in the ratio plots of Fig. 5-20, the concentration measurements on June 23 show large variability. Each individual measurement differed by such a large extent that no obvious
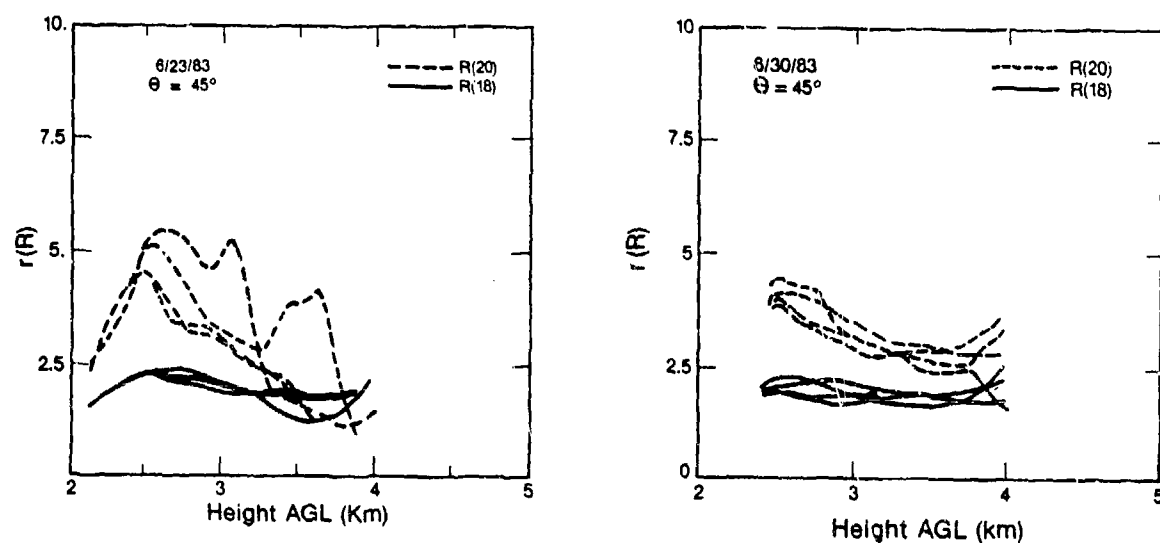
Fig. 5-20 - Adjacent-range power ratios for June 23, 1983, and June 30, 1983, measurements.
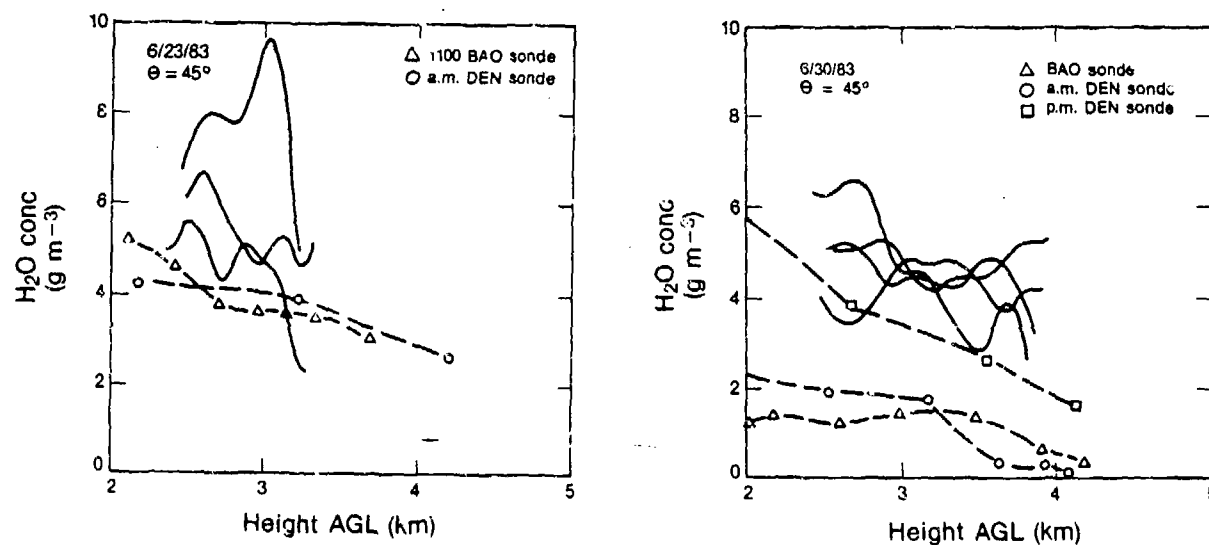

Fig. 5-21 - Concentration measurements and rawinsonde soundings for June 23, 1983, and June 30, 1983, measurements.

261

trend can be discerned within the 2 km to 3 km range where estimates were attempted. Again, as in the May 4 data set, the estimates were consistently higher than those from the closest rawinsonde launches for both the June 23 and June 30 cases. This was also the case with the June 30 data, as seen in Fig. 5-21. In the June 30 case the data show more internal consistency between measurements, and a trend of slightly decreasing moisture with height can clearly be discerned. However, even though the mean moisture estimate is lower than that of the June 23 data, as would be expected in a drier atmosphere, the measurements are still biased high relative to the rawinsondes. This consistent bias in each of the elevated measurements is discussed in more detail in the next section.

In previous cases the degree of fluctuation between the individual concentration measurements was always greater than predicted by Eq. (5.5), which assumes that speckle and detection noise dominate the measurement. In the June 23 measurements, however, the observed deviation was approximately equivalent to the predicted value as seen in Fig. 5-22. Since the June 23 returns were characterized by low CNR, this seems to indicate that CNR effects in the error process were dominant relative to the differential backscatter processes, which appear to have dominated the other measurments. It also suggests, for these measurements, a potential limit, on errors due to differential backscatter of on the order of 2 $g-m^{-3}$. Presumably this could be improved by simultaneous transmission at the two wavelengths.
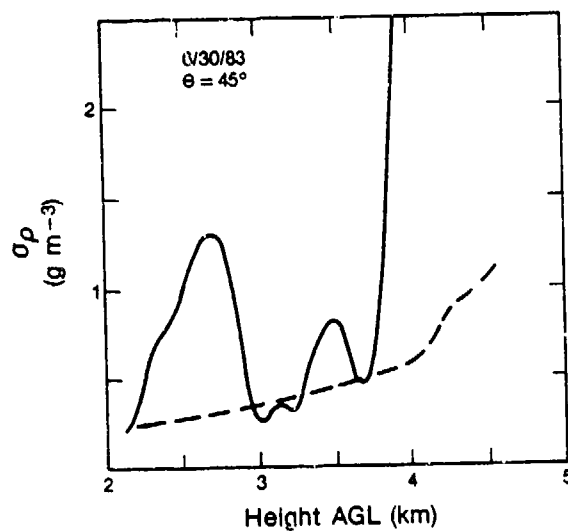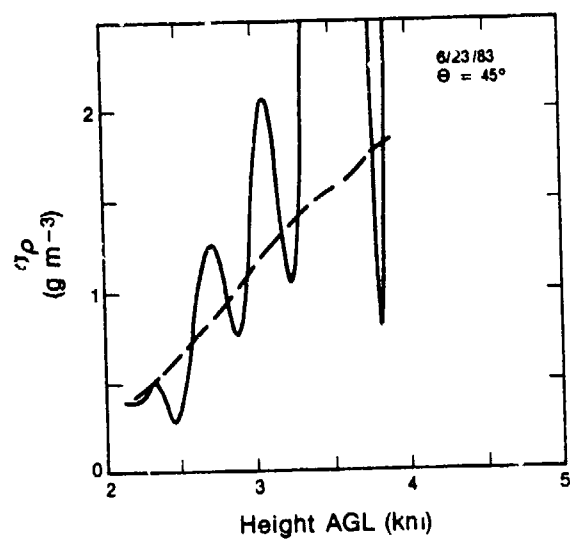
Fig. 5-22 – Observed measurement standard deviation, plus standard
deviation due to speckle and noise for June 23, 1983, and
June 30, 1983, data sets.

Since the June 23 measurements were limited in range due to attenuation by the rather high level of water vapor present, the feasibility of using the R(12)/R(18) line pair for the differential measurement was examined. This pair has been suggested for use in regions where high humidity limits operation on the R(20) line. The differential ACS for this pair, from the measurements of Shumate et al., is approximately $.68 \times 10^{-4}$ atm^{-1} cm^{-1} at standard temperature and pressure. Given an H_2O concentration of 10 $g-m^{-3}$, expected differential attenuation over 1 km is approximately 10% or about 0.5 dB.

Analysis of the data taken on the R(12) and R(18) lines showed almost identical profiles of backscattered power versus range. No apparent difference could be detected in the absorption on each line over range increments as long as 3 or 4 km. It can be concluded from this result that atmospheric moisture content was not sufficiently high to warrant operation on this line pair. Apparently, moisture levels such as those found in the tropics, where water vapor concentration is on the order of 18 $g\ m^{-3}$, would be necessary to obtain noticeable differential attenuation.

E. RADIAL VELOCITY ESTIMATES

The primary reasons usually set forth for performing coherent DIAL measurements using CO_2 lasers are (1) increased sensitivity available through heterodyne detection, and (2) presence of many absorbing species at these wavelengths. Another potentially important advantage of

coherent DIAL is the capability to measure radial wind velocity as well as species concentration within the measurement volume. In the case of water vapor, measurements of velocity and concentration might be used to study phenomena such as moisture convergence and advection for precipitation studies. When the species of interest is potentially toxic, such measurements could provide remote detection of the hazardous substance, as well as indications of the time available before the substance is carried back toward the sensor by the prevailing winds. This capability could be useful in tactical battlefield situations.

To demonstrate this capability the radial velocity versus range was calculated from the May 4 R(18) and R(20) returns. The velocity was determined using the pulse-pair algorithm; this algorithm turns out to be non-optimal for the NOAA lidar parameters. Despite this, good single-pulse estimates of velocity were obtained out to the limiting range of the DIAL measurement, as shown in Fig. 5-23, on the non-absorbed R(18) wavelength. Because the R(20) wavelength encounters more attenuation, single pulse estimates on that line exhibit a rather large variability at ranges beyond a few km. By averaging 1000 pulses, however, good estimates are obtainable on that line to beyond the maximum DIAL measurement range.

In Chapter III, and again in Chapter IV, optimization of the lidar pulse length to minimize the concentration estimate error due to the combined effects of speckle and shot noise was discussed. In the
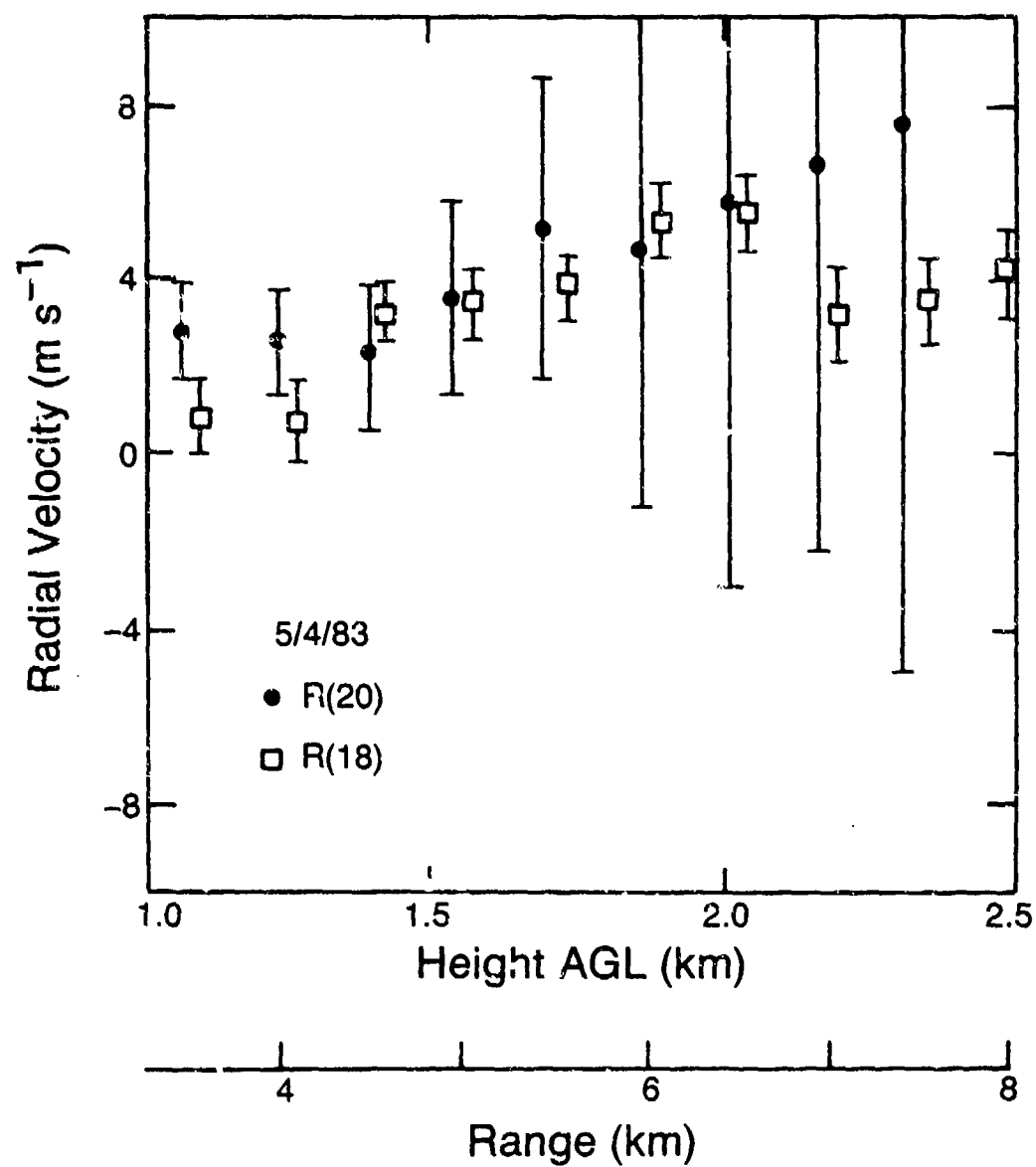
Fig. 5-23 – Mean and standard deviation of single-pulse velocity estimates calculated from R(20) and R(18) returns in May 4, 1983, data sets.

absence of other criteria, the general technique is to reduce pulse duration until speckle and shot noise terms are approximately equivalent. When velocity estimates are also desired, a new constraint is added to the problem, since the increase in signal bandwidth which comes about as the pulse duration is reduced tends to degrade the velocity estimate.

This problem was examined using the simulation described in Chapter III. Figure 5-24 shows the uncertainty in a single-pulse velocity measurement as a function of pulse duration τ_p, where signal bandwidth is assumed to be $1/\tau_p$. Energy per pulse is presumed to be held constant. Two sets of curves are plotted; one set assumes maximum range resolution is desired; i.e., a single velocity measurement is obtained every $c\tau_p/2$ m. The other family of curves assumes a range resolution of 1 km, such that m_v velocity estimates are averaged per range gate, where $m_v = 1000/(c\tau/2)$. It is seen that pulses could be shortened to the order of 100 ns and still produce single-pulse velocity uncertainties of less than 5 m s^{-1} (1 km range resolution). Since a DIAL measurement would certainly require multiple pulses, averaged velocity estimates would be reduced to well below 1 m s^{-1} when 100 or so pulses are averaged. Therefore, given a 1 J transmitter, acceptable velocity measurements are probably obtainable when pulses are shortened to improve DIAL estimates.

Figure 5-25 shows the predicted corresponding DIAL power measurement error as a function of pulse duration, again assuming the

267

RADIAL VELOCITY MEASUREMENT UNCERTAINTY
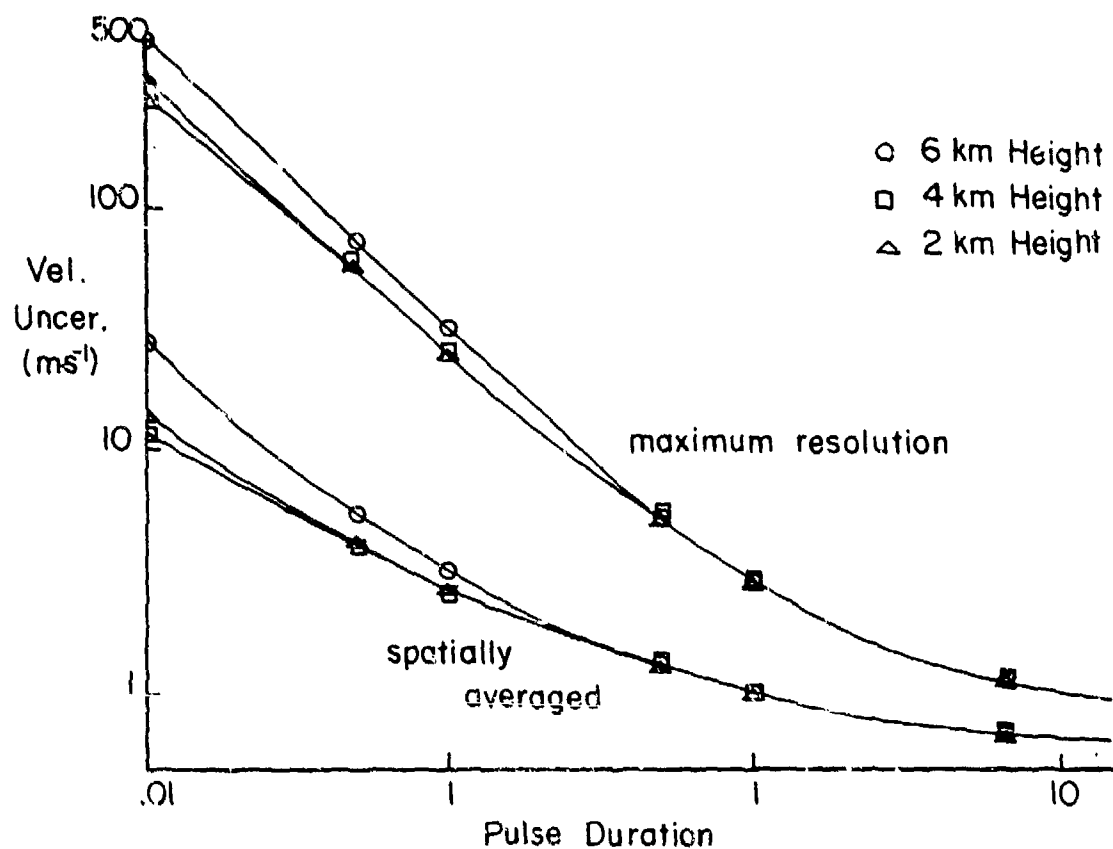
Fig. 5-24 - Predicted uncertainty in single-pulse velocity estimate versus pulse duration, assuming system and atmospheric model parameters described in Chapter III.

DIAL POWER MEASUREMENT UNCERTAINTY

Single Pulse

○ 6 km Height
△ 4 km Height
□ 2 km Height
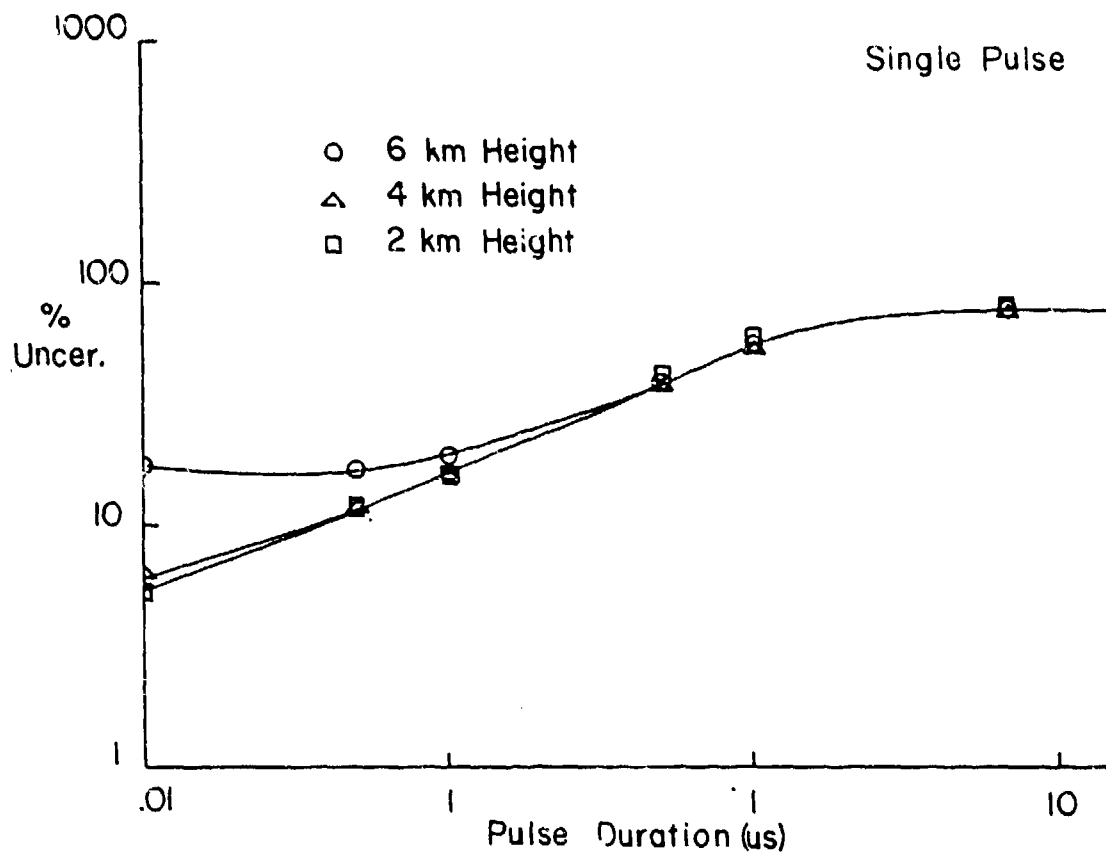
Fig. 5-25 - Predicted single-pulse DIAL measurement uncertainty versus pulse duration, assuming system and atmospheric model parameters described in Chapter III.

simulation parameters used in Chapter III. It is seen that 100 ns pulses provide a factor of 5 or so reduction in single-pulse power estimate error (range resolution is assumed to be 1 km). Since predicted errors are still on the order of 10%, multiple pulse averaging would still be required.

In summary, the results from both the analysis of real data and performance simulation indicate that combined DIAL/Doppler measurements are potentially feasible. Experience shows that the concentration measurement is the harder to make; good velocity measurements were easily obtained from the June 23 data set even though the concentration measurements are somewhat uncertain. Thus the problem becomes one of initially determining the accuracy or utility of the concentration measurement; then, given an acceptable set of system parameters, examining the potential accuracy of the velocity measurement.

F. SUMMARY

The cases discussed in this chapter were examined over a wide range of conditions. Measurements were taken along both elevated and vertical paths; in winter and summer conditions; and on returns from both aerosols and hard targets. This diverse data set produced information on the robustness of the coherent DIAL technique and its sensitivity to different measurement environments. A number of important, if somewhat preliminary, conclusions can be drawn from these examples.

On the positive side, the advantage in sensitivity of coherent detection is aptly demonstrated. Range-resolved measurements were obtained to ranges of 10 km at low elevation angles and to heights of 4 km above ground level (AGL). This was substantially better than the reported incoherent measurements to 500 m height using a 2-J laser [66]. For meteorological applications measurements to 4 km AGL, corresponding to approximately 5.6 km above sea level, are probably more than adequate, since most of the significant moisture structure occurs below 700 mb (3 km). When moisture content is high, such as occurred during the June 23 measurement, attenuation on the R(20) line will limit overall system profiling capability. Under drier conditions limitation is due to the combination of decreasing backscatter and integrated water vapor absorptions.

The two measurement sets taken with the beam pointing horizontally showed good mean agreement with other ground-based sensors used for comparison. Although fluctuations in the estimates were apparent, especially in the February 4 data set, the mean of the individual estimates averaged over range generally showed good agreement with comparison sensors. Such was not the case in the profile estimates. In comparisons with rawinsondes, the lidar concentrations were universally higher than the sonde values. Rawinsondes are far from ideal comparison sensors. In addition to the known rms errors which introduce an equivalent uncertainty of more than 1 g-m^{-3} to the concentration estimates, many of the comparison sondes were launched from 20-40 km

away, with time displacem s of as much as 5 hours. At the least,
comparisons made under   n conditions have to be viewed with reaso-
nable skepticism.

Despite the potential problems with such comparisons, the con-
sistent lidar overestimate of the concentration gives strong evidence
that some bias does exist. Even when the larger of the two previously-
discussed ACS values was used, hj- tended to produce a smaller con-
centracion estimate, the estimates were consistently higher than the
values measured by the sondes. The degree of the overestimate ranged
from about 1.4 to as much as 2 times the concentration measured by the
comparison sensor.

Potential sources of such bias are errors in the estimate of the
differential ACS, additional absorption on the R(20) line by an inter-
fering species, systematic variability in system response versus range
on the two laser lines, consistent differences in on-line and off-line
back atter coefficients, or a range weighting effect which would tend
to produce a longer ΔR than is assumed in the calculation. Of these,
the most likely source is probably the ACS. The values reported by
both Ryan et al. and Shumate et al. were used to calculate the con-
centrations since they appeared to be well documented in the litera-
t   Both tended toward overestimation of the concentration. An ACS
of 1.5×10^{-3} atm^{-1} cm^{-1} reported by Schnell et at. [126], which is
nearly twice as large as that of Shumate et al. and 4 times as large
as Ryan et al., produces estimated H_2O concentrations for the profile

272

measurements which are closer to those measured by the sonde. The horizontal measurements are then underestimated, however.

In addition to the uncertainties in the water vapor absorption coefficient at atmospheric pressure and room temperature, its variability with temperature is another potential source of error. In the calculations the AFGL model was used to estimate line strength for the water vapor absorption line at the R(20) wavelength. The model predicts a strong temperature dependence, such as to produce in a factor of 2 change in ACS with a 25°C variation in temperature. By including this effect in the calculations of ACS aloft, an ACS value is employed which is much less than the values measured at standard temperature and pressure. If the effect of temperature on linestrength is smaller than that predicted using AFGL model, the estimates would tend to be biased high at upper levels. This is consistent with the observations.

There does not appear to be any typical atmospheric background species which would consistently produce the observed overestimate. Using the AFGL model, the potential effect of ozone was examined. The predicted absorption coefficient, even at high concentrations, was less than .006 km^{-1} on the R(20) wavelength. Such a value should be negligible in its effect on concentration measurements.

Equally unlikely as sources of measurement bias are differential systematic effects. As discussed previously, some overall change in system response might reasonably be expected when moving between the

273

R(18) and R(20) lines due to misalignment or non-optimal LO bia.   ch

changes would inject some uncertainty into the absolute calibration on

each of the system wavelengths. Since these measurements were range-

resolved, however, the calibration would have to vary systematically

versus range as well as wavelength to produce the observed consistent

bias. The existence of such a characteristic seems highly improbable.

One candidate explanation might be differential backscatter coef-

ficients at the two laser frequencies. Petheram [103] examined the

effect of humidity on backscatter coefficients at CO_2 wavelength for

measurement of ozone and ethylene, and found that changes due to aero-

sol hydration could cause measurement errors. However, for this effect

to be significant in the measurements, the backscatter coefficients at

the two wavelengths would have to vary differentially with range. Such

an effect could possibly occur in measurements at slant elevation

angles, where discrete aerosol layers often exist at different heights.

Again, however the effect would have to be consistently present in all

the measurements to produce the observed estimate bias.

In addition to bias, most of the measurements contained significant

oscillation in the concentration estimate from range-to-range and

measurement to measurement. Such behavior was almost certainly due to

advection of aerosol inhomogeneities into and out of the scattering

volume throughout the course of the measurement. Most models attempt-

ing to predict coherent DIAL feasibility, including the one described

in Chapter III, assume that speckle and shot noise effects dominate the

error. Except for the low CNR case of June 23, the data indicate that a significant atmospheric variability error term, on the order of 1-2 $g-m^{-3}$, exists on top of the speckle error term. Presumably this error would be reduced for simultaneous measurements.

Fluctuation errors were quite large in the February 4 data, taken on a winter day when concentrations were low. Such a characteristic is not unexpected, since the logarithmic nature of the estimation process tends to enhance fluctuations. This is shown in Fig. 5-26, which plots the mean concentration $\bar{\rho}$ versis adjacent range power ratio $\hat{r}_{R(20)}$ on the R(20) line. For this example $\hat{r}_{R(18)}$ is assumed to be 1.7, typical of observed values in the measurements. At low concentrations, indicated by low values of $\hat{r}_{R(20)}$, the slope $d\bar{\rho}/d\hat{r}$ is quite large, such that slight variations in $\hat{r}$ cause large fluctuations in $\bar{\rho}$. As concentration and ratios increase the slope decreases, hence the concentration estimate becomes less sensitive to noise in the $\hat{r}$ estimate. Note that the curve changes as ACS is varied. Ideally one would like to operate in a region where $d\bar{\rho}/d\hat{r}$ is low given the expected range of concentrations. Assuming that the ACS can be chosen freely (most likely requiring a continuously tunable lidar system) this implies maximizing ACS subject to the constraint of not attenuating the signal to such a degree that the ratio estimate is unacceptably noisy. The tradeoffs inherent in optimizing ACS were examined for a spaceborne lidar by Remsburg and Gordley [127].

In Chapter IV it was postulated that spatial averaging, due to the relatively long pulse length and the advection of different aerosols

275
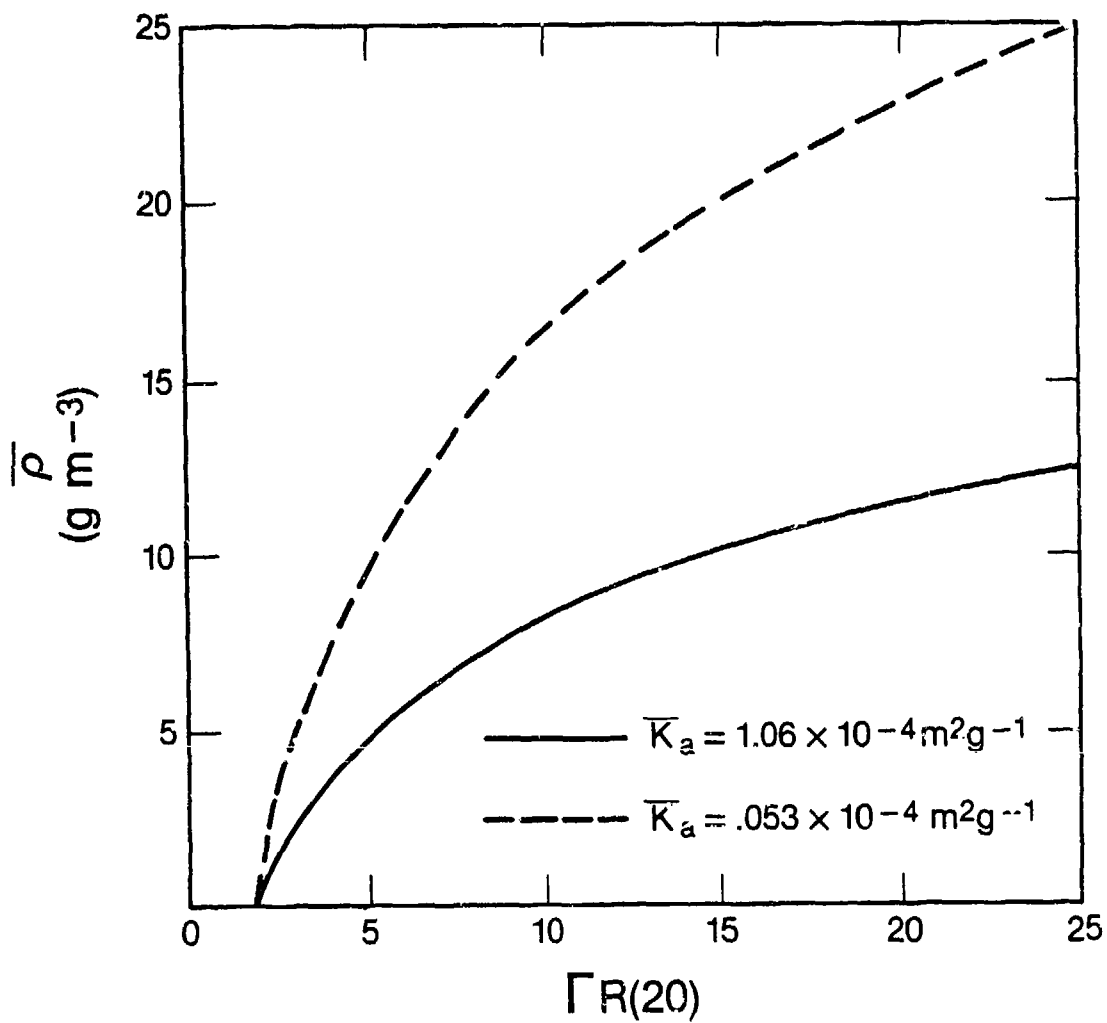
Fig. 5-26 - Mean concentration (assuming a 1 km measurement cell) versus R(20) adjacent range power ratio, assuming R(18) adjacent range power ratio = 1.7.

276

across the beam during the measurement, might tend to average out these long term fluctuations. The data indicate that such averaging is not sufficient, probably due to the presence of large, nonstationary inhomogeneities in the aerosol field whose effects are not averaged out over the 1-2 minute data sampling interval. A more efficient method of processing the data from multiple runs is probably to average the power profiles over all runs, then calculate the concentration from the single pair of averaged profiles. This would reduce effects due to high $\overline{d\rho}/\hat{dr}$ at small concentrations. Another possibility is to scan the lidar beam during the measurement, in order to increase the effectiveness of spatial averaging. Such a technique would not work, however, if clouds were randomly present anywhere within the volume of interest. In general, these results seem to reinforce the need for simultaneous on-line and off-line measurements. Even when pulses are long and averaging time is significant, aerosol fluctuations appear for the most part to ultimately determine accuracy for the sequential type measurements described.

As shown in the analysis of the previous section, combined simultaneous DIAL/Doppler measurements are probably feasible. Such a capability could be particularly useful for detection and tracking of chemical agents in the battlefield environment. The battlefield problem is simplified because the system has only to detect the presence of toxic agents, as opposed to making exact concentration measurements. As a result, the DIAL constraints might be relaxed somewhat to obtain better

277

wind velocity estimates. Such estimates would probably have other uses in the battlefield scenario.

Since, in general, the measurements indicate that DIAL estimates are more difficult than wind velocity measurements, it is recommended that a proposed combined system be first analyzed in terms of its species-measuring capability. Once such a feasibility is established, the Doppler measuring capability and potential tradeoffs can then be examined.

These measurements were done on water vapor primarily because the system was easily tunable in the range of the R(20) and R(18) line pairs. Additionally, the presence of some water vapor in the atmosphere was guaranteed, eliminating the need for special absorption cells. In the next chapter these results are interpreted in terms of the general coherent DIAL measurement problem. The measurements are also compared with predicted capabilities scaled from the results of Chapter III, and conclusions regarding the overall feasibility of the technique are discussed.

VI. DISCUSSION OF RESULTS

Results of this research clearly show that the advantages of co-
herent DIAL in the 9-11 μm spectral region exist in practice as well as
principle. The 100 mJ/pulse NOAA lidar produced concentration measure-
ments to ranges of 1C km using only the atmospheric aerosol as a back-
scattering source. This range capability is much better than has been
reported for incoherent CO_2 DIAL systems, where maximum ranges were
typically only 2-3 km despite the use of multiple-joule transmit puses.
The ability for coherent DIAL systems to measure radial wind velocities
was also demonstrated. Using identical data sets, radial velocity
measurements were obtained from ranges beyond the maximum range for
species measurements. The capability for simultaneous measurement of
species concentration and radial velocity offers the potential to study
species transport and diffusion with a single instrument.

When the simulation results described in Chapter III are adjusted
to acount for the differences between the assumed system parameters and
the NOAA system parameters, they compare reasonably well with the
experimental results. Carrier-to-noise ratio is the key parameter
determining species measurement capability when speckle and quantum-
noise dominate the error. The assumed system parameters in the simula-
tion (1 J/pulse, .5 m optics, 10% system efficiency, 200 kHz bandwidth)
should produce a CNR approximately 37 dB higher than that obtained with
the NOAA system (.1 J/pulse, .3 m optics, 2.5% system efficiency, 10

279

MHz bandwidth). Comparing the predicted CNR value at 2 km range with the observed CNR for the February 4, 1983 data set, it can be shown that the observed value is 28 dB less than the value predicted in the simulation. However, 5 dB must be subtracted from the observed value to compensate for the backscatter difference between the surface and 2 km, since simulated results assumed vertical propagation paths while actual measurements were taken along horizontal paths. The resulting 33 dB discrepancy is only slightly less than the 37 dB attributable to system differences.

Since scaling relationships relating CNR to system parameters are reasonably straightforward, the degree of agreement between the predicted and measured system performance is for the most part a measure of the validity of the assumed atmospheric models. One should be cautioned, however, from interpreting the agreement described above as a validation of the atmospheric models used in the simulation. Since the data in the models were based on wide-area climatological means, exact agreement between the predicted result and a single local measurement is probably somewhat fortuitous. Before simulation results can be accepted with reasonable confidence, more corroborating data is needed to validate or improve the atmospheric models, especially at higher altitudes. Even when more accurate models exist, however, they will still most likely predict performance only in a mean sense. Randomness in the atmosphere will continue to provide variability to local measurements.

In estimating the species concentration error, the simulation assumed that uncertainties in the backscattered power measurement due to speckle and detection noise were key parameters. The validity of this assumption for coherent systems was shown in the experimental observations described in Chapter IV. At high CNR's, uncertainty due to speckle was shown to dominate the received power measurement error; while at low CNR, the detection noise was more important. Since in both cases the instantaneous power measurements were characterized by exponentially-distributed random processes, both intra-pulse and multi-pulse averaging were necessary to reduce the error in the estimate of the mean. The optimum intrapulse averaging strategy is seen to be very much a function of the dominant error source. When speckle dominates, one wants to increase signal bandwidth by chirping or sh :tening the transmit pusle. Conversely, when detection noise is dominant, the optimum configuration maximizes CNR by minimizing signal and receiver bandwidth. It is important to note that, in general, reducing the speckle error increases the noise-produced error, and vice versa.

In addition to the speckle and noise-produced errors, additional uncertainty in measured power was seen to exist as a result of long-term fluctuations. These effects were not included in the simulation. The existence of such fluctuations necessitates long averaging times in order to remove residual uncertainties in the species concentration measurement. Measurements with the NOAA lidar showed that these fluctuations could be as much as 30% of the mean over time scales of 5-10 minutes. Causes for this variability include fluctuations in

atmospheric backscatter and transmission characteristics as well as drifts in the system transmit energy or receiver sensitivity. Because range-resolved DIAL measurements entail calculating ratios of powers (e.g., Eq. 31), detrimental effects of long-term power fluctuations on concentration measurement accuracy are less if the fluctuations from adjacent range-gates are correlated. Our measurements showed correlation coefficients as high as .9 existed between long-term power fluctuations from ranges separated by 0.5 km. Such high correlation probably indicates that fluctuations are due to a combination of system variability, changing transmission path properties, and advection of large regions of aerosol (>1 km) which tend to encompass both range gates. More experiments are planned to try to identify the source of these fluctuations.

Although the on-line and off-line power measurements in the DIAL experiments were often separated by as much as 10 minutes, effects of changing atmospheric properties were typically not sufficiently significant to totally dominate the speckle errors. For the most part, the errors attributed to atmospheric variability added less than 1 $g-m^{-3}$ of uncertainty over that predicted from speckle and turbulence. The rather long effective measurement cell length, produced by the convolution of the transmit pulse and the receiver low pass filter response, probably was beneficial because of its filtering effect on the small-scale spatial variations in mean backscatter level. Because the large-scale fluctuations, which were not filtered, require relatively long times to advect into and out of the paths, their detrimental

effect is reduced even over measurement time scales of 10 minutes.
Shortening the pulse, which has the advantage of improving range resolution as well as increasing speckle averaging effectiveness, will probably produce an increase in the errors due to inhomogeneities.
Effects are worse when the spatial variability in backscatter is highly structured, as in the February 4, 1983 data set.

Based on these results, those error sources that need to be addressed to improve measurement capability apply equally to incoherent as well as coherent DIAL. In addition to backscatter variability, which suggests the need for simultaneous on and off-line transmission, the primary source of systematic uncertainty was postulated to be specification of the exact absorption cross-section. As pointed out in Chapter V, reported measurements of absorption cross-sections on the R(20) line under near standard conditions vary by as much as a factor of 3. Since very little measurement data exists on temperature and pressure variability of this line, theoretical expressions had to be used to correct for temperature and pressure variations along the path. Specification of temperature and pressure within the measurement volume is difficult for vertical profiling, since no in situ measurements are available. In general, one would like to select operating wavelengths where the temperature and pressure variabilities are minimized, however, other factors such as line strength or presence of interfering species must also be considered. Because of these inter-related effects it is recommended that multi-parameter optimization be carefully carried out to select operating wavelengths. Having selected the

wavelengths, carrying out a careful measurement program to characterize absorption under a variety of temperature and pressure conditions is essential.

When the DIAL research was begun, it was assumed that fluctuations and decoherence due to refractive-index turbulence would be significant sources of measurement error. Subsequently, results of simulations assuming vertically pointing measurements, as well as field measurements and modifications to propagation theory, have tended to downgrade the effects of turbulence. Under many measurement conditions, such as along elevated paths, turbulence effects can be completely neglected. However, turbulence must still be considered when long-range, horizontal measurements are desired, such as in the battlefield hazardous gas sensing application. Integrated turbulence under such conditions may be sufficiently high so as to degrade measurements.

Although the results of this research show the overall feasibility of DIAL measurements using heterodyne CO_2 lidars, they also raise a number of questions which require additional investigation. In order to resolve such questions, future measurements should be made using more advanced systems. Ideally a next-generation research DIAL system would have some or all of the following capabilities:

1. Variable delay between on-line and off-line transmit pulses ranging from simultaneous to as much as 1 s or more.

2. Capability to adjust pulse-length from 10 ns to 10 μs.

3. Tail clipping to eliminate long pulse tails from TE lasers.

4. Capability to transmit at high pulse repetition frequencies.

5. Incorporation of high-pressure laser transmitters and LO lasers to provide maximum tunability across the 9-11 μm range.

6. Capability to switch easily between direct and heterodyne detection modes.

7. Multi-detector element array to study effects of spatial averaging.

Advanced capabilities such as those listed above would enable questions to be resolved regarding such matters as: atmospheric variability, speckle averaging, spatial averaging of backscatter inhomogeneities, trade-offs in operating wavelength selection, and direct versus heterodyne detection DIAL measurement accuracy. Such a system should also incorporate sufficient signal processing or data sampling capability to examine DIAL species versus Doppler velocity measurements. By using the research lidar to quantitatively determine the primary DIAL error sources and resulting optimum system configurations which minimize their effects, sufficient information could be obtained to develop specifications for lower cost, special-purpose operational DIAL systems.

None of the stated performance capabilities for such a research system necessitates technological breakthrough. Simultaneous or near simultaneous operation requires dual-pulsed transmitters and receivers;

such systems have been developed at Lincoln Laboratories and the University of Hull. Pulse length and tail clipping can be controlled by an intra-cavity plasma switch; pulse duration is also controllable by varying the percentage of nitrogen within the gain cell. A high pulse rate laser has been proposed by SRI in a coherent DIAL system to measure ammonia concentrations in smokestack emissions; design of the system is commencing in early 1984. High pressure CO_2 laser research has been performed at Laser Development Corporation [128] and at Hull University [129]; a commercially available high-pressure laser has been advertised by Laser Application Limited. Although stability specifications for such lasers are not available at the present time, their very existence opens the way for potential incorporation into coherent systems. Similarly, high performance multi-element detector arrays have been developed and are commercially available from a number of sources.

In conclusion, the work described in this dissertation has been an important first step in showing sensitivity and multi-purpose advantages of coherent DIAL. Since most of the experimental data was collected with a system optimized for Doppler wind velocity measurements, however, a number of questions on ultimate measurement capability remain to be answered. It is important to continue the research effort through the use of better-designed systems in order to answer these questions. As a goal, one can dream of a scanning DIAL-Doppler system capable of measuring both species concentration and radial velocity once per second in 250 m range gates out to 10-20 km range. Such

286

a system could produce two-dimensional pictures of species concentration, velocity and concentration flux covering 700 km^2 or so once every 5-10 minutes. The technology is available now, only the stated mission and resources are lacking.

APPENDIX A: APERTURE AVERAGING IN COHERENT LIDAR SYSTEMS

In this analysis the notation of Gardner [86] is followed. Consider a uniformly-spaced array of detectors upon which the backscattered return is imaged. If each detector is uniformly irradiated with a local oscillator field, then the capacitively-coupled output from each detector is proportional to the optical field amplitude and phase at the detector. Assume that the individual optical detector outputs are square-law detected and combined to produce a power estimate. The power estimate is then

$$\hat{P} = \sum_{k=1}^{N} \hat{P}_k \qquad (A.1)$$

where $\hat{P}_k$ is power estimate from each detector. If the size of each detector is small relative to the imaged scale size of the speckles, and detection noise is negligible, then Eq. (A.1) can be approximated by

$$\hat{P} = \int \eta I(\rho) w(\rho) d^2\rho \qquad (A.2)$$

where η is detector quantum efficiency, $w(\rho)$ is the aperture weighting function, $I(\rho)$ is optical intensity, and $d^2\rho$ indicates that the integral is calculated over the total aperture. The mean of the power estimate is

$$\langle \hat{P} \rangle = \eta \langle I(\rho) \rangle \int_{-\infty}^{\infty} w(\rho) d^2\rho \quad .$$

The measurement standard deviation is calculated from

$$\sigma_{\hat{P}}^2 = \langle \hat{P}^2 \rangle - \langle \hat{P} \rangle^2 \tag{A.3}$$

where

$$\langle \hat{P}^2 \rangle = \eta^2 \iint I(\rho_1) I(\rho_2) w(\rho_1) w(\rho_2) d^2\rho_1 d^2\rho_2$$

$$= \eta^2 \iint I(\rho_1) I(\rho_1 + r) w(\rho_1) w(\rho_1 + r) d^2\rho_1 d^2 r$$

$$= \eta^2 \left[\langle I^2 \rangle \int B_I'(r) R_w(r) d^2 r + \langle I \rangle^2 \int R_w(r) d^2 r \right] . \tag{A.4}$$

where $B_I'(r)$ is the autocovariance function of intensity normalized so that $B_I'(0) = 1$ the variance is

$$\sigma_{\hat{P}}^2 = \eta^2 \langle I^2 \rangle \int B_I'(r) R_w(r) d^2 r \quad . \tag{A.5}$$

If the received signal is assumed to fit the Rayleigh phasor model, the normalized variance of the power estimate given a single speckle is unity. For multiple speckles the number of independent samples m is equivalent to the inverse of the normalized variance:

$$m = \frac{\langle \hat{P} \rangle^2}{\sigma_{\hat{P}}^2} = \frac{\left[\langle I \rangle \int w(r) d^2 r \right]^2}{\langle I^2 \rangle \int B'(r) R_w(r) dr} \quad . \tag{A.6}$$

The above analysis is valid when the number of detectors is much greater than m_s, the effective number of independent samples across the aperture. For a limited number of detectors evenly spaced across the

aperture, the number of independent samples = N, such that the final

result is

$$m_s = m \qquad m < N$$
$$\quad = N \qquad m < N \, .$$

APPENDIX B: TEMPORAL AVERAGING OF POWER FLUCTUATIONS

1. Heterodyne Detection

Consider the schematic of Fig. 3-1. The detector output signal
passes through an IF filter, which limits the noise power, and into a
complex demodulator. The complex demodulator generates baseband in-
phase and quadrature components $x_R(t)$ and $x_Q(t)$ composed of signal and
noise processes. Since $x(t)$ is joint Gaussian $x_R(t)$ and $x_Q(t)$ are
uncorrelated Gaussian random processes. Because of this, we can exa-
mine the effects of each component independently. Denoting

$$x_R(t) = s(t) + n(t) \tag{B.1}$$

where s and n are contributions due to backscattered signal and noise
respectively. Both $s(t)$ and $n(t)$ are assumed to be stationary, zero-
mean Gaussian random processes. Then

$$y_R(t) = s^2(t) + 2s(t)\, n(t) + n^2(t). \tag{B.2}$$

After lowpass filtering

$$\hat{P}_R(t) = \int_{-\infty}^{\infty} h(t-\tau)\, y_R(\tau)\, d\tau \tag{B.3}$$

where $h_f(t)$ is the lowpass filter impulse response. Similarly

$$\hat{P}_Q(t) = \int_{-\infty}^{\infty} h(t-\tau) \, y_Q(\tau) \, d\tau . \qquad (B.4)$$

The signal power estimate is formed by taking the total power esti-
mate $\hat{P}(t)$ and subtracting the contribution due to noise. It is assumed
here that the mean system noise power is a constant and can be accura-
tely estimated by observing the noise for a sufficient period of time
to reduce the uncertainty in the estimate to a negligible value. Under
this assumption the signal power estimate is

$$\hat{P}_s(t) = \hat{P}(t) - \bar{P}_n \qquad (B.5)$$

where $\hat{P}(t) = P_R(t) + P_Q(t)$ and $\bar{P}_n$ is the mean noise power. To find the

normalized variance of the estimate we must compute the first and
second moments. The first moment is

$$
\begin{aligned}
\langle \hat{P}_s(t) \rangle &= \langle \hat{P}(t) \rangle - \bar{P}_n \\
&= \langle P_R(t) \rangle + \langle P_Q(t) \rangle - \bar{P}_n \qquad (B.6)
\end{aligned}
$$

$$= 2[\langle s^2(t) \rangle + \langle n^2(t) \rangle] \int_{-\infty}^{\infty} h(t-\tau) d\tau - \bar{P}_N$$

$$= \langle P_s(t) \rangle + \langle P_n(t) \rangle - \bar{P}_n \qquad (B.7)$$

$$= \langle P_s(t) \rangle$$

which shows that the estimator is unbiased. To calculate the second
moment of $P_s(t)$ we first calculate the second moment of $P_R(t)$

$$\langle P_R^2(t) \rangle = \int_{-\infty}^{\infty} R_{y_R}(\tau) \, R_h(\tau) d\tau \qquad (B.8)$$

where $R_{y_R}(\tau)$ is the autocorrelation function of $y(\tau)$ and $R_h(\tau)$ in the

292

self-convolution of the filter impulse response $h_f(t)$. The autocorrelation of $y_R(t)$ is computed from

$$R_{y_R}(\tau) = \langle \{s^2(t)+2s(t)n(t)+n^2(t)\}\{s^2(t+\tau)+2s(t+\tau)n(t+\tau)+n^2(t+\tau)\} \rangle \quad (B.9)$$

which is

$$R_{y_R}(\tau = \mu_s^2 + \mu_n^2 + 2\mu_s \cdot + 2R_s^2(\tau) + 2R_n^2(\tau) + 4R_s(\tau)R_n(\tau) \quad (B.10)$$

where we have made the substitutions $\mu_s = \langle s^2(\tau) \rangle$, $\mu_n = \langle n^2(t) \rangle$ and $R_s(t)$, $R_n(t)$ are the autocorrelation functions of the signal and noise components. Then

$$\langle P_R^2(t) \rangle = [\mu_s^2 + \mu_n^2 + 2\mu_s\mu_n] \int_{-\infty}^{\infty} R_{y_R}(\tau)d\tau$$

$$+ \int_{-\infty}^{\infty} R_{y_R}(\tau) [2R_s^2(\tau) + 2R_n^2(\tau) + 4R_s(\tau)R_n(\tau)]d\tau . \quad (B.11)$$

Since $\bar{P}_n$ is a constant, the variance of $\hat{P}_s$ is calculated from

$$\sigma_{\hat{P}_s}^2(t) = \sigma_{\hat{P}(t)}^2$$

$$= 2\sigma_{P_R}^2(t)$$

$$= 2[\langle P_R^2(t) \rangle - \langle P_R(t) \rangle^2] \quad (B.12)$$

which is computed to be

293

$$\sigma_{\hat{P}_s(t)}^2 = 4\mu_s^2 \int_{-\infty}^{\infty} R_h(\tau) \, R_s'^2(\tau) d\tau$$

$$+ 4\mu_n^2 \int_{-\infty}^{\infty} R_h(\tau) \, R_n'^2(\tau) d\tau \qquad \text{(B.13)}$$

$$+ 8\mu_s\mu_n \int_{-\infty}^{\infty} R_h(\tau) \, R_s'(\tau) \, R_n'(\tau) d\tau$$

where the prime denotes a normalized autocorrelation function and the normalized variance is thus

$$\frac{\sigma_{\hat{P}_s(t)}}{\langle P_s(t)\rangle^2} = \frac{1}{m} + \frac{2}{m_c} \frac{1}{SNR} + \frac{1}{m_n} \frac{1}{CNR^2} \qquad \text{(B.14)}$$

where $CNR = \mu_s/\mu_n$ and

$$m_s = \frac{\int_{\infty}^{\infty} R_h(\tau)d\tau}{\int_{-\infty}^{\infty} R_h(\tau) \, R_s'^2(\tau) \, d\tau} \qquad \text{(B.15a)}$$

$$m_n = \frac{\int_{\infty}^{\infty} R_h(\tau)d\tau}{\int_{-\infty}^{\infty} R_h(\tau) \, R_s'^2(\tau) \, d\tau} \qquad \text{(B.15b)}$$

$$m_c = \frac{\int_{\infty}^{\infty} R_h(\tau)d\tau}{\int_{-\infty}^{\infty} R_h(\tau) \, R_s'(\tau) \, R_n'(\tau)d\tau} \qquad \text{(B.15c)}$$

2. Direct Detection

Consider the model of Fig. 3-3, where $v(t)$ is the output of the detector due to signal power, background power and noise. It is assumed that $n(t)$ is zero-mean Gaussian and contains effects of all

noise terms, including background quantum noise, and further assumed
that mean background power is constant, such that

$$v(t) = S(t) + n(t) + B \tag{B.16}$$

where $S(t)$ is the signal due to backscattered irradiance, $n(t)$ is noise
and B is a d.c. level due to background irradiance to estimate the
signal power the background contribution is subtracted, i.e.,

$$\hat{P}_S(t) = \hat{P}(t) - \bar{P}_B \tag{B.17}$$

where $\hat{P}(t)$ is the signal at the output of the lowpass filter, the mean
of $\hat{P}_s(t)$ is

$$\langle P_s(t) \rangle = \langle S(t) \rangle \int_{-\infty}^{\infty} h(\tau)d\tau$$

$$+ B \int_{-\infty}^{\infty} h(\tau)d\tau - P_B \tag{B.18}$$

defining $\qquad \bar{P}_B = B \int_{-\infty}^{\infty} h(\tau)d\tau$

then $\qquad \langle \hat{P}_s(t) \rangle = \langle S(t) \rangle \int_{-\infty}^{\infty} h(\tau)d\tau .$ $\qquad$ (B.19)

To compute the normalized variance we need the second moment of $\hat{P}_s(t)$

$$\langle \hat{P}_s^{\,2}(t) \rangle = \langle \{ \hat{P}(t) - \bar{P}_B \}^2 \rangle \tag{B.20}$$

we first find $\langle \hat{P}_s^{\,2}(t) \rangle$, i.e.,

$$\langle \hat{P}_s{}^2(t) = \int_{-\infty}^{\infty} R_v(\tau) \; R_f(\tau) d\tau \qquad (B.21)$$

where $R_v(\tau)$ is the autocorrelation function of $v(t)$ and $R_f(\tau)$ is the self-convolution of the filter impulse response. The term $R_v(\tau)$ is computed from

$$R_v(\tau) = \langle \{S(t) + B + n(t)\}\{S(t+\tau) + B + n(t+\tau)\}\rangle$$

$$= R_s(\tau) + 2B\langle S(t)\rangle + B^2 + R_n(\tau) \qquad (B.22)$$

which can be written in terms of autocovariance functions as

$$R_v(\tau) = B_s(\tau) + \langle S(t)\rangle^2 + 2B\langle S(t)\rangle + B^2 + B_n(\tau) \; . \qquad (B.23)$$

The second moment is thus

$$\langle \hat{P}^2(t)\rangle = \int R_f(\tau) \; [B_s(\tau) + B_n(\tau)]d\tau$$

$$+ [\langle S(t)\rangle + B]^2 \int R_f(\tau)d\tau \qquad (B.24)$$

and the second moment of $\bar{\hat{P}}_s(t)$ is

$$\langle \hat{P}_s{}^2(t)\rangle = \int R_f(\tau) \; [B_s(\tau) + B_n(\tau)]d\tau + [\langle S(t)\rangle + B]^2 \int R_f(\tau)d\tau$$

$$- 2[B + \langle S(t)\rangle] \int h_f(\tau)d\tau + \bar{P}_B{}^2 \; . \qquad (B.25)$$

The variance of $\hat{P}_s(t)$ is, from Eq. (B.25)

$$\hat{\sigma_{P_s}}(t) = \int R_f(\tau) \, [B_s(\tau) + B_n(\tau)] d\tau$$

$$= \sigma_s^2 \int R_f(\tau) \, B_s'(\tau) d\tau \qquad (B.26)$$

$$+ \sigma_n^2 \int R_f \, B_n'(\tau) d\tau$$

where the primes indicate normalized autocovariance functions. The normalized variance can thus be written

$$\frac{\sigma_{\hat{P}_s}^2(t)}{\langle \hat{P}_s(t)\rangle^2} = \frac{\sigma_s^2}{\langle S^2\rangle} \frac{\int R_f(\tau) \, B_s'(\tau) d\tau}{\int R_f(\tau) d\tau}$$

$$+ \frac{\sigma_n^2}{\langle S^2\rangle} \frac{\int R_f(\tau) \, B_n'(\tau) d\tau}{\int R_f(\tau) d\tau} \; . \qquad (B.27)$$

If the fluctuations in signal level are caused primarily by speckle, then $\sigma_s^2 = \langle S^2\rangle$ and Eq. (B.27) becomes (where spatial averaging effects are included)

$$\frac{\sigma_{\hat{P}_s}^2(t)}{\langle \hat{P}_s(t)\rangle^2} = \frac{1}{m_a \, m_t} + \frac{1}{CNR^2} \qquad (B.28)$$

where

$$m_t = \frac{\int R_f(\tau) \, B_s'(\tau) d\tau}{\int R_f(\tau) d\tau} \; , \qquad (B.29)$$

and CNR is the voltage carrier to noise ratio at the filter output. Eq. (B.28) includes the effects of spatial averaging, where m_a is given by Eq. (3.6).

297

REFERENCES

1. W.E.K. Middleton and A.F. Spilhaus, _Meteorological Instruments_, Toronto: Univ. of Toronto Press, 1953.

2. R.M. Hardesty, K. Elmore, and M. Jackson, "A comparison of radar and lidar wind measurements made during the JAWS program," _Preprints 21st Radar Meteor. Conf._ (Edmonton, Alta.) p. 584, September 1983.

3. J. Rothermal, C. Kessinger, and D.L. Davis, "Dual Doppler lidar measurement of winds in the JAWS experiment," submitted to J. Atmos. and Ocean Tech., February 1984.

4. W.B. Grant and R.D. Hake, "Calibrated remote measurements of SO_2 and O_3 using atmospheric backscatter," _J. Appl. Physics_, vol. 46, no. 7, p. 3019, July 1975.

5. J.G. Hawley, "Characterization of the EPRI Differential Absorption Lidar (DIAL) System," EA-1267, Final Report, Project 862-14, Electric Power Research Institute, Palo Alto, CA, December 1979.

6. R.T. Thompson, J.M. Hoell, and W.R. Wade, "Measurements of SO_2 absorption coefficients using a Tuneable Dye Laser," _J. Appl. Physics_, vol. 46, no. 7, p. 3040, July 1975.

7. E.V. Browell, "Remote sensing of tropospheric gases and aerosols with an airborne DIAL system," in _Optical and Laser Remote Sensing_, D.K. Killinger and A. Mooradian, eds, Berlin: Springer-Verlag, 1983.

8. K. Frederiksson, B. Galle, K. Nystrom, and S. Svanberg, "Mobile Lidar system for environmental probing," _Appl. Opt._, vol. 20, no. 24, p. 4181, December 1981.

9. W.S. Heaps and T.J. McGee, "The NASA/Goddard balloon-borne lidar system," in _Optical and Laser Remote Sensing_, D. K. Killinger and A. Mooradian, eds, Berlin: Springer-Verlag, 1983.

10. J.B. Laudenslager, I. Stuart McDermid, and Thomas J. Pocala, "Development of compact excimer lasers for remote sensing," in _Optical and Laser Remote Sensing_, D. K. Killinger and A. Mooradian, eds, Berlin: Springer-Verlag, 1983.

11. T. Srinivasan, H. Egger, T.S. Luk, H. Pummer, and C.K. Rhodes, "Progress in dye and excimer sources for remote sensing," in _Optical and Laser Remote Sensing_, D. K. Killinger and A. Mooradian, eds, Berlin: Springer-Verlag, 1983.

12. K.W. Rothe, H. Wather, and J. Werner, "Differential-absorption measurements with fixed-frequency IR and UV measurements," in *Optical and Laser Remote Sensing*, D.K. Killinger and A. Mooradian, eds, Berlin: Springer-Verlag, 1983.

13. K. Frederiksscn, B. Galle, K. Nystrom, and S. Svanberg, "Lidar system applied in atmospheric pollution monitoring," *Appl. Opt.*, vol. 18, no. 17, p. 2998, September 1979.

14. W.B. Grant, R.D. Hake, Jr., E.M. Liston, R.C. Robbins, and E.K. Proctor, Jr., "Calibrated remote measurement of NO_2 using the differential absorption technique," *Appl. Opt.*, vol. 24, no. 11, June 1974.

15. G. Megie, J. Pelon, J. Lefere, C. Cohen, and P.H. Flamant, "Ozone and water vapor monitoring using a ground-based lidar system," in *Optical and Laser Remote Sensing*, D.K. Killinger and A. Mooradian, eds, Berlin: Springer-Verlag, 1983.

16. R.M. Schotland, "Some observations of the vertical profile of water vapor by means of a laser optical radar," *Proc. Fourth Symposium on Remote Sensing of Environment*, p. 273, (Ann Arbor, MI) 1966.

17. T. Kobayashi, M. Hiroma, and H. Inaba, "Remote monitoring of NO_2 molecules by differential absorption using optical fiber link," *Appl. Opt.*, vol. 20, no. 19, p. 3279, October 1981.

18. N. Menyuk, D.K. Killinger, and W. DeFeo, "Remote sensing of NO_2 using a differential absorption lidar," *Appl. Opt.*, vol. 19, no. 19, p. 3282, October 1979.

19. H. Shimzu, Y. Sasano, N. Takeuchi, O. Matsudo, and M. Okuda, "A mobile computerized laser radar system for observing rapidly varying meteorological phenomena," *Opt. Quant. Electr.*, vol. 12, no. 2, p. 159, March 1980.

20. E.E. Uthe, N.B. Nelson, and W.L. Jimison, "Airborne lidar plume and haze analyzer (ALPHA-1), *Bull. Am. Meteor. Soc.*, vol. 61, no. 9, p. 1035, September 1980.

21. D.J. Brassington, "Differential absorption lidar measurements of atmospheric water vapor using an optical parametric oscillator source," *Appl. Opt.*, vol. 21, no. 24, p. 4411, August 1982.

22. R.L. Byer, T. Kane, J. Eggleston, and S.Y. Long, "Solid state laser sources for remote sensing," in *Optical and Laser Remote Sensing*, D.K. Killinger and A. Mooradian, eds, Berlin: Springer-Verlag, 1983.

23. S.E. Taylor and E.L. Thomas, "Derivative monitoring of atmospheric species with pulsed leadsoft diode lasers," Tech. Dig. CLEO '83 (Baltimore, MD), Paper THP1, May 1983.

24. P.F. Moulton and A. Mooradian, "Broadly tunable CW operation of Ni: MgF_2 and $CO:MGF_2$ lasers," App. Phys. Lett., vol. 35, no. 11, p. 838, December 1979.

25. B.A. Greene, D. Masters, B.J. Rye, and E.L. Thomas, "Antenna considerations in atmospheric backscatter coherent lidar, in Tech. Dig. Coherent Laser Radar for Atmospheric Sensing (Aspen, CO), paper TuB3, July 1980.

26. D.C. Spears, "IR Detectors: Heterodyne and Direct," in Optical and Laser Remote Sensing, D.K. Killinger and A. Morradian, eds, Berlin: Springer-Verlag, 1983.

27. R.T.H. Collis and P.B. Russell, "Lidar measurement of particles and gases," in Laser Monitoring of the Atmosphere, E.D. Hinkley, ed., Berlin: Springer-Verlag, 1976.

28. F.E. Goodwin and M.E. Pedinoff, "Application of CCl_4 and CCl_2: CCl_2 ultrasonic modulators to infrared optical heterodyne experiments," Appl. Phys. Lett., vol. 8, no. 3, p. 60, February 1966.

29. A.V. Jelalian and R.M. Huffaker, "Laser Doppler techniques for remote wind velocity measurements," Dig. Specialist Conference on Molecular Radiation (Huntsville, AL), October 1967.

30. T.R. Lawrence, D.J. Wilson, C.E. Craven, I.P. Jones, R.M. Huffaker, and J.A.L. Thomson, "A laser velocimeter for remote sensing," Rev. Sci. Inst., vol. 43, no. 3, p. 512, March 1972.

31. L.J. Sullivan, "Firepond Laser Radar," Electro/81 Conference Record, Session 34, 1981.

32. A.B. Gschwendtner, R.C. Harney, and R.J. Hull, "Coherent IR radar technology," in Optical and Laser Remote Sensing, D.K. Killinger and A. Mooradian, eds, Berlin: Springer-Verlag, 1983.

33. J.W. Bilbro, "Atmospheric laser Doppler velocimetry: an overview," Opt. Eng., vol. 19, no. 4, p. 533, July/August 1980.

34. W.D. Jones, J.W. Bilbro, S.C.Johnson, H.B. Jeffreys, L.Z. Kennedy, and C. A. Dimorzio, "Design and calibration of a coherent lidar for measurement of atmospheric backscatter," paper presented at SPIE 25th Tech. Symposium (San Diego, CA), August 1981.

35. W.F. Herget, R. Rollins, M.C. Krause, and K.N. Shaw, "The EPA laser-Doppler velocimeter for remote measurement of wind or stack plume velocity," Tech. Dig. Coherent Laser Radar for Atmospheric Sensing (Aspen, CO), July 1980.

36. R.M. Hardesty, "Measurement of winds, backscatter and return signal properties using pulsed coherent lider," Tech. Dig. Eleventh ILRC (Madison, WI), June 1982.

37. H.J. Pfeifer, "Possibilities and limitations of remote cross-wind velocity measurements with Frinzi type laser Doppler anemonetry," Tech. Dig. Coherent Laser Radar for Atmospheric Sensing (Aspen, CO), July 1980.

38. R.M. Schotland, "The determination of the vertical profiles of atmospheric gases by means of a ground-based optical radar," Proceedings of the Third Symposium on Remote Sensing of the Environment (Ann Arbor, MI), 1964.

39. R.A. McClatchey, W.S. Benedict, S.A. Clough, D.E. Burch, R.F. Calfee, K. Fox, L.S. Rothmon, J.S. Garing, "AFCRL atmospheric absorption line parameters compilation," AFCRL-TR-73-0096 (Bedford, MA), January 1973.

40. R.M. Schotland, "Errors in the lidar measurement of atmospheric gases by differential absorption," J. Appl. Meteor., vol. 2, no. 1, p. 71, February 1974.

41. V.E. Derr and C.G. Little, "A comparison of remote sensing of the atmosphere by optical, radio, and acoustic radar techniques," Appl. Opt., vol. 9, no. 9, p. 1970, September 1970.

42. H. Kildal and R.L. Byer, "Comparison of laser methods for the remote detection of atmospheric pollutants," Proc. IEEE, vol. 59, no. 12, December 1971.

43. K.W. Rothe, U. Brinkmann, and H. Walther, "Applications of tunable dye lasers to air pollution detection: measurements of atmospheric NO_2 concentration by differential absorption," Appl. Phys., vol. 3, p. 115, 1974.

44. J. Kuhl and H. Spitschan, "A frequency doubled dye laser with a servo-tuned crystal," Opt. Commun., vol. 13, no. 1, p. 6, January 1975.

45. T. Hennigsen, M. Garbung, R.L. Byer, "Remote measurement of CO by parametric tunable laser," Appl. Phys. Lett., vol. 24, no. 5, p. 242, March 1974.

46. R.T. Ku, E.D. Hinkley, and J.O. Sample, "Long-path monitoring of atmospheric carbon monoxide with a tunable diode laser system," Appl. Opt., vol. 14, no. 4, p. 854, April 1975.

301

47. T. Kobayashi and H. Inaba, "Infra-red heterodyne laser radar for remote sensing of air pollutants by range-resolved differential absorption," Opt. and Quant. Electron., vol. 7, no. 4, p. 319, July 1975.

48. R.T. Menzies and M.S. Shumate, "Remote measurements of ambient air pollutants with a bistatic laser system," Appl. Opt., vol. 15, no. 9, September 1976.

49. E.R. Murray, R.D. Hake, Jr., J.E. van der Laan and J.G. Hawley, "Atmospheric water vapor measurements with a infrared (10-µm) differential absorption lidar system," Appl. Phys. Lett., vol. 28, no. 9, p. 542, May 1976.

50. E.R. Murray and J.E. van der Laan, "Remote measurement of ethylene using a CO_2 differential-absorption lidar," Appl. Opt., vol. 17, no. 5, p. 814, March 1978.

51. E.R. Murray, J.E. van der Laan, and J.G. Hawley, "Remote measurement of HCl, CH_4, and N_2O using a single-ended chemical laser system," Appl. Opt., vol. 15, no. 12, p. 3140, December 1976.

52. W. Wiesemann, R. Beck, W. Englisch, and K. Gurs, "In-flight trial of a continuous laser remote sensing system," Appl. Phys., vol. 15, p. 257, 1978.

53. R.T. Menzies, "Atmospheric monitoring using herodyne detection techniques," Opt. Engin., vol. 17, no. 1, p. 44, Jan/Feb 1978.

54. M.S. Shumate, W.B. Grant, and R.T. Menzies, "Remote measurement of trace gases with the JPL laser absorption spectrometer," in Optical and Laser Remote Sensing, D.K. Killinger and A. Mooradian, eds, Berlin: Springer-Verlag, 1983.

55. J. Boscher, W. Englisch, and W. Wiesemann, "Foreign gas interference and differential albedo effects in CO_2 laser long path absorption monitoring," Tech. Dig. Coherent Laser Radar for Atmospheric Sensing (Aspen, CO), July 1980.

56. W. Englisch and W. Wiesemann, "Remote sensing of atmospheric trace gases by differential absorption spectroscopy," Proc. OST Conf., ESA Special Publication ESA-SP-134, p. 465, (Toulouse, France), 1978.

57. K. Asai, T. Itabke, and T. Igarashi, "Range-resolved measurements of atmospheric ozone using a differential-absorption CO_2 laser radar," Appl. Phys. Lett., vol. 35, no. 1, p. 60, July 1979. 1978.

58. R.W. Fegley and C.M. Penney, "An attempt to measure atmospheric ozone with ultraviolet lidar," NOAA Technical Memorandum ERL ARL-75, (Silver Spring, MD), December 1978.

59. J. Pelon and G. Megie, "Ozone vertical distribution using a ground-based active remote sensing technique," Nature, vol. 299, no. 5879, p. 134, September 1982.

60. E.V. Browell, A.F. Carter, S.T. Shipley, R.J. Allen, C.F. Butler, M.N. Mayo, J.H. Siurter, Jr., and W.M. Hall, "NASA multipurpose airborne DIAL system and measurements of ozone and aerosol profiles," Appl. Opt., vol. 22, no. 4, p. 522, February 1983.

61. E.V. Browell, T.D. Wilderson, and T.J. McIlrath, "Water vapor differential absorption lidar development and evaluation," Appl. Opt., vol. 18, no. 20, p. 3474, October 1979.

62. E.V. Browell, "Lidar measurements of tropospheric gases," Opt. Eng., vol. 21, no. 1, p. 128, Jan/Feb, 1982.

63. V.V. Zuev, V.E. Zuev, Y.S. Makushkin, V.N. Maricher, and A.A. Mitsel, "Laser sounding of atmospheric humidity: experiment," Appl. Opt., vol. 22, no. 23, p. 3742, December 1983.

64. D.K. Killinger and N. Nenyuk, "Remote probing of the atmosphere using a CO_2 DIAL system," IEEE J. Quant. Electron., vol. QE-17, no. 9, p. 1917, September 1981.

65. J.L. Bufton, T. Itabe, and D.A. Crotemund, "Airborne remote sensing measurements with a pulsed CO_2 DIAL system," in Optical and Laser Remote Sensing, D.K. Killinger and A. Mooradian, eds, Berlin: Springer-Verlag 1983.

66. P.W. Baker, "Atmospheric water vapor differential absorption measurements on vertical parths with a CO_2 lidar," Appl. Opt., vol. 22, no. 15, p. 2257, August 1983.

67. S. Lundquist, C.-O. Falt, U. Persson, B. Marthinsson and S.T. Eng, "Air pollution monitoring with a Q-switched CO_2-laser radar using heterodyne detection, Appl. Opt., vol. 20, no. 14, p. 2534, July 1981.

68. M. Endemann and R.L. Byer, "Remote single-ended measurements of atmospheric temperature and humidity at 1.77 μm using a continuously tunable source," Opt. Lett., vol. 5, no. 10, p. 452, October 1980.

69. J.B. Mason, "Lidar measurement of temperature: a new approach," Appl. Opt., vol. 14, no. 1, p. 16, January 1975.

70. A. Rosenberg and D.B. Hogan, "Lidar technique of simultaneous temperature and humidity measurements: analysis of Mason's method," Appl. Opt., vol. 20, no. 19, p. 3286, October 1981.

71. G.K. Schwemmer and T.D. Wilkerson, "Lidar temperature profiling: performance simulations of Mason's method," Appl. Opt., vol. 18, no. 21, p. 3539, November 1979.

72. C.K. Korb, G.K. Schwemmer, and M. Dombrowski, "Atmospheric pressure and temperature profiling using near IR differential absorption lidar," in Optical and Laser Remote Sensing, D.K. Killinger and A. Mooradian, eds, Berlin: Springer-Verlag, 1983.

73. R. Greco, "Atmospheric lidar multi-user instrument system definition study," G.E. Space Division, Final report on contract NAS-1-15476, (Philadelphia, PA), 1980.

74. G. Megie and R.T. Menzies, "Complementarity of UV and IR differential absorption lidar for global measurements of atmospheric species," Appl. Opt., vol. 19, no. 7, p. 1173, April 1989.

75. T.J. Kane, B. Zhou, and R.L. Byer, "The potential for coherent Doppler wind velocity lidar using Neodymium lasers," submitted to Appl. Opt.

76. R.M. Hardesty, "A comparison of heterodyne and direct detection CO_2 DIAL systems for ground-based humidity profiling," NOAA Technical Memorandum ERL WPL-64, (Boulder, CO), October 1980.

77. F.R. Faxvog and H.W. Mocker, "Rapidly tunable CO_2 TEA laser, Appl. Opt., vol. 21, no. 22, p. 3986, November 1982.

78. J.W. Goodman, "Some fundamental properties of speckle," J. Opt. Soc. Am., vol. 66, no. 11, p. 1145, November 1976.

79. M. Born and E. Wolf, Principles of Optics, New York: Macmillan, 1964.

80. P. Beckmann, Probability in communication engineering, New York: Harcourt Brace and World, 1965, 511 pp.

81. K. Ostberg, "Differential absorption lidar: effects of speckle noise," FOA Reports, vol. 13, no. 1, p. 1 (Stockholm, Sweden) 1979.

82. C.S. Gardner and G.S. Mecherle, "Speckle noise in direct-detection lidar systems," RRL Publication No. 495 (Urbana, IL), April 1978.

83. A. Yariv, Quantum Electronics, New York: Holt, Rinehard and Winston, 1976.

84. W.L. Wolfe, ed., Handbook of Military Infrared Technology, Washington, DC: Office of Naval Research, 1965.

85. R.M. Huffaker, ed., "Feasibility study of a satellite-borne lidar global wind monitoring system," NOAA Technical Memorandum ERL WPL-37, (Boulder, CO), 1978.

86. C.S. Gardner and A.M. Saleh, "Speckle noise in differential absorption lidar systems," RRL Publication No. 496, (Urbana, IL), October 1978.

87. Clifford, S.F., "Physical properties of the atmosphere in relation to laser probing," Opt. and Quant. Elec., vol. 8, no. 2, p. 95, March 1976.

88. R.L. Fante, "Electromagnetic beam propagation in turbulent media," Proc. IEEE, vol. 63, no. 12, p. 1669, December 1980.

89. V.I. Tatarski, The Effects of the Turbulent Atmosphere on Wave Propagation, Springfield, VA: U.S. Dept. of Commerce, Nat. Tech. Info. Serv., 1971.

90. S.F. Clifford, T. Wang, and T.R. Lawrence, "Refractive turbulence effects on lidar systems," NOAA Technical Memorandum ERL WPL-48 (Boulder, CO) 1980.

91. R.L. Philips and L.C. Andrews, "Measured statistics of laser light scattering in atmospheric turbulence," J. Opt. Soc. Am., vol. 71, no. 12, p. 1440.

92. S.S.R. Murty, "Laser Doppler systems in atmospheric turbulence," NASA TM X-73354, (Marshall Space Flight Center, AL), November 1976.

93. A. Thomson and M.F. Dorian, "Heterodyne detection of monochromatic light scattered from a cloud or moving particles," General Dynamics Convair Division (San Diego, CA) 1967.

94. D.L. Fred and G.E. Meyers, "Evaluation of r_0 for propagation down through the atmosphere," Appl. Opt., vol. 13, no. 11, p. 2620, November 1974.

95. S.M. Wandzura, "Meaning of quadratic structure functions," J. Opt. Soc. Am., vol. 70, no. 6, p. 745, June 1980.

96. S.F. Clifford and S. Wanzura, "Monostatic heterodyne lidar performance: the effect of the turbulent atmosphere," Appl. Opt., vol. 20, no. 3, p. 514, February 1981.

305

97. J.F. Holmes, J.R. Kerr, M.A. Lee, and M.E. Fossey, "Experimental pulsed laser remote crosswind measurement system - feasibility study and design," Report No. FA-TR-76065, Frankford Arsenal (Philadelphia, PA) November 1976.

98. J.H. Shapiro, B.A. Capron, and R.C. Harney, "Imaging and target detection with a heterodyne detection optical radar," Appl. Opt. vol. 20, no. 19, p. 3292, October 1981.

99. A.G. Kjelaas, P.E. Nordal, and A. Bjerkestrand, "Scintillation and multiwavelength coherence effects in a long-path absorption spectrometer," Appl. Opt., vol. 17, no. 2, p. 277, January 1978.

100. D.M. Gaks, R.F. Calfee, D.W. Hansen, and W.S. Benedict, "Line parameters and computed spectra for water vapor bands at 2.7 μm," NBS monograph 71, 1964.

101. G.K. Yue, G.S. Kent, U.O. Farrukh, and A. Deepak, "Modeling atmospheric aerosol backscatter at CO_2 laser wavelengths. 3: Effects of changes in wavelength and ambient conditions," Appl. Opt., vol. 22, no. 11, p. 1671, June 1983.

102. R.T.H. Collis and P.B. Russell, "Lidar measurement of particles and gases by elastic backscattering and differential absorption," in Laser Monitoring of the Atmosphere, E.D. Hinkley, ed., Berlin: Springer-Verlag, 1976.

103. J.C. Petheram, "Differential backscatter from the atmospheric aerosol: the implications for IR differential absorption lidar," Appl. Opt., vol. 20, no. 22, p. 3941, September 1981.

104. M.J. Post, "Experimental measurement of atmospheric aerosol inhomogeneities," Opt. Lett., vol. 2, no. 6, p. 166, June 1978.

105. Elterman, L., "UV, visible, and IR attenuation for altitudes to 50 km," Environ. Res. Paper 285, Air Force Cambridge Research Laboratories (Bedford, MA) 1968.

106. R.A. McClatchey, R.W. Fenn, J.E.A. Selby, F.E. Volz, J.S. Garing, "Optical Properties of the Atmosphere," Envir. Res. papers, No. 411, Air Force Cambrdige Research Laboratory (Bedford, MA), 1972.

107. R.E. Hufnagel, "Variations of atmospheric turbulence," Tech. Dig. Tropical Meeting on Optical Propagation through turbulence (Washington, DC) 1974.

108. A.H. Oort and E.M. Rasmussen, "Atmospheric circulation statistics," NOAA Professional Paper 5, (Washington, DC) 1971.

109. L. Lading, personal communication.

306

110. M.J. Post, R.A. Richter, R.M. Hardesty, T.R. Lawrence, F.F. Hall, Jr., "National Oceanic and Atmospheric Administration's pulsed coherent infrared DOPPLER lidar - characteristics and data. Proc. SPIE, vol. 300, p. 65, July, 1981.

111. B.J. Rye, "Primary abberation contribution incoherent backscatter heterodyne lidar returns," Appl. Opt., vol. 21, no. 5, p. 839, March 1982.

112. D. Willetts and M.R. Harris, "An investigation into the origin of frequency sweeping in a hybrid TEA CO_2 laser," J. Phys. D, vol. 15, no. 1, p. 51, January 1982.

113. S.R. Byron, P.E. Cassady, T.A. Snotias, D.C. Quimby, and S.E. Moody, "Chirp analysis for pulsed CO_2 laser oscillators," Tech. Dig. 2nd Topical Meeting on Coherent Laser Radar: Technology and Applications, paper TuD4-1 (Aspen, CO) August 1980.

114. D.S. Zrnic, "Estimation of spectral moments for weather echoes," IEEE Trans. Geosci. Electron., vol. GE-17, no. 4, p. 133, October 1979.

115. M.J. Post, R.A. Richter, R.J. Keeler, R.M. Hardesty, T.R. Lawrence, and F.F. Hall, "Calibration of coherent lidar targets," Appl. Opt. vol. 19, no. 16, p. 2828, August 1980.

116. R.M. Hardesty, R.J. Keeler, M.J. Post, and R.A. Richter, "Characteristics of coherent lidar returns from calibration targets and aerosols," Appl. Opt., vol. 20, no. 21, p. 3763, November 1981.

117. M.I. Skolnik, Introduction to Radar Systems, New York: McGraw-Hill, 1962.

118. M.J. Post, F.F. Hall, R.A. Richter, and T.R. Lawrence, "Aerosol backscattering profiles at $\lambda = 10.6$ μm," Appl. Opt., vol. 2, no.13, p. 2442, July 1982.

119. N. Menyuk, D.K. Killinger, and C.R. Menyuk, "Limitations of signal averaging due to temporal correlation in a laser remote-sensing measurements," Appl. Opt., vol. 21, no. 18, p.3377, September 1982.

120. B.J. Rye, "Estimation of differential irradiance in incoherent backscatter lidar with square-law detection," submitted to J. Appl. Meteor.

121. M.S. Shumate, R.T. Menzies, J.S. Margolis, and L.G. Rosengren, "Water vapor absorption of carbon dioxide laser radiation," Appl. Opt., vol. 15, no. 10, p. 2480, October 1976.

307

122. R.J. Nordstrom, M.E. Thomas, J.C. Peterson, E.K. Damon, and R.K. Long, "Effects of oxygen addition on pressure-broadened water vapor absorption in the 10 µm region," $\underline{Appl}$. $\underline{Opt}$., vol. 17, no. 17, September 1978.

123. J.C. Peterson, M.E. Thomas, R.J. Nordstrom, E.K. Damon, and R.K. Long, "Water vapor-nitrogen absorption at CO_2 laser frequencies," $\underline{Appl}$. $\underline{Opt}$., vol. 18, no. 6, p. 834, March 1979.

124. J.S. Ryan, M.H. Hubert, and R.A. Crane, "Water vapor absorption at isotopic CO_2 laser wavelengths," $\underline{Appl}$. $\underline{Opt}$., vol. 22, no. 5, p. 711, March 1983.

125. W.E. Hoehne, "Precision of National Weather Service Upper Air Measurements," Test and Evaluation Division, NOAA TM T & ED-16 (Sterling, VA) August, 1980.

126. W. Schnell and G. Fischer, "Carbon dioxide laser absorption coefficients of various air pollutants," $\underline{Appl}$. $\underline{Opt}$., vol. 14, no. 9, p. 2058, September 1975.

127. E.E. Remsburg and L.L. Gordley, "Analysis of differential absorption lidar from the Space Shuttle," $\underline{Appl}$. $\underline{Opt}$., vol. 17, no. 4, p. 624, February 1978.

128. J.S. Levine, M. Guerra and A. Javan, "Development of tunable high pressure CO_2 laser for lidar measurements of pollutants and wind velocities," NASA Contractor Report 3274 (Langley Research Center, VA) 1980.

129. J.W. van Dijck, J.C. Petheram and B.J. Rye, "A multi-atmospheric carbon dioxide laser for use in differential absorption," $\underline{Proc}$. $\underline{SPIE}$, vol. 415, p. 100, (Arlington, VA) 1983.